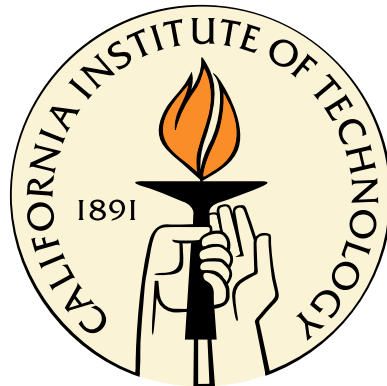


# Applications of nuclear resonant scattering to further our understanding of Earth's interior

Thesis by  
Dongzhou Zhang

In Partial Fulfillment of the Requirements  
for the Degree of  
Doctor of Philosophy



California Institute of Technology  
Pasadena, California

2016  
(Defended December 4, 2014)



而世之奇伟瑰怪非常之观，常在于险远，而人之所罕至焉；故非有志者，不能至也。

— 王安石，游褒禅山记（1054 A. D.）

Translation: The (geological) wonders are usually far away and difficult for people to reach.

Only the most determined can make it.

— Wang Anshi, after visiting the Baochan Mountain in 1054 A.D.

# Acknowledgments

First and foremost, I would like to thank my advisor, Professor Jennifer Jackson. My background was in condensed matter physics, and when I began my Ph.D., you firmly encouraged me to explore the new field of high pressure mineral physics. You were always there to help, when I prepared my first diamond anvil cell, conducted my first synchrotron experiment, and heated my first sample with laser. In my third year, you insightfully inspired me to start the melting project, years before other groups dived into this field. Your endless encouragement and support has helped me overcome countless difficulties during the development of the FasTeR spectrometer. Without your strong support, I could not have made it to the final list of the CSC scholarship. In addition, I benefitted a lot from your mentorship beyond science, from learning the sophisticated details in language, to overcoming the huge cultural barrier. Life in your high pressure mineral physics group is really a joyful and wonderful journey, and I am indeed grateful for that.

I would also like to thank those people who made my challenging experiments possible. First I'd like to thank Dr. Wolfgang Sturhahn. You generously taught me how to use CONUSS, PHOENIX and MINUTI, and how to adjust the timing window in the beamline with the small screwdriver. You were always there to help during the most difficult time of my experiments, and you always gave me the best solution. Many thanks to the physicists in Sector 3: Dr. Jiyong Zhao, Dr. Ercan Alp, Dr. Thomas Toellner, Dr. Michael Hu, Dr. Ahmet Alatas and Dr. Wenli Bi. You made Argonne my "second home" besides Pasadena, and made my heart warm during the coldest winters in the windy city. I am very grateful for being able to work with the best "synchrotron crew" in the world: Dr. Bin Chen, Dr. Caitlin Murphy, Dr. June Wicks, Dr. Aaron Wolf, Rachel Miller and Natalia Solomatova. Your passion and wisdom inspired me during every beamtime, and conducting experiments with you was a lot of fun. Caitlin helped to synthesize the precious thin Fe-Ni foils, without which I couldn't have done the second half of my thesis.

I am extremely lucky to study in the world's best geophysics department. I would like to first acknowledge my thesis committee for navigating my thesis work. I would like to thank Professor Rob Clayton, not only for being my academic advisor for years, but also for teaching me how to process seismic data and link them with sound speeds of materials, so that I could connect mineral physics experiments with the real-world seismograms. I attended Professor Mike Gurnis's geodynamics class

three times, once as a student and twice as a teaching assistant. I thank Mike for giving me a vivid picture of the dynamic deep earth, which makes the abstract melting curves more concrete. Professor Paul Asimow's Ge101 class was the first geology class that I had ever attended. Discussions with Paul helped me dig more into the geological and geochemical aspects of my research, as well as link my diamond anvil cell experiments with shock-wave experiments and theoretical calculations.

Many thanks also go to other faculty members who have taught me. I thank Professor Joann Stock for teaching me plate tectonics and field geophysics, and helping me with my second oral project on the earthquake surface ruptures. Thanks to Professor George Rossman for the class of spectroscopy in mineralogy, which I will continue to explore in my career. Professor Thomas Heaton and Professor Donald Helmberger taught me seismology classes, which made me understand how my experimental work can help seismologists. Lectures from Professor Andrew Ingersoll and Professor David Stevenson inspired me to look beyond Earth into other planets. In addition, I'd like to thank the field trip leaders: Professor Joseph Kirschvink showed me how the Baja-California peninsula evolved with time. Professor Jean-Philippe Avouac took me to Greece in the division enrichment trip, where I got a chance to feel the real subduction among the Aegean Isles. Professor Jason Saleeby took me to the Pahoehoe trip, and the journey from the rain forest to the volcano caldera was an unforgettable memory.

I am very fortunate to have many wonderful collaborators and colleagues around the world, and I learned a lot from them. Dr. Guoyin Shen, Dr. Yue Meng, Dr. Vitali Prakapenka, Dr. Mark Rivers and Dr. Yanbin Wang always gave me helpful suggestions when I was caught in some experimental problems at the APS. Dr. Jinyuan Yan was always supportive when I needed help on X-ray diffraction at the ALS. Dr. Yuming Xiao helped a lot with the Mössbauer data collection at the HPCAT. Dr. Razvan Caracas provided important phonon density of states calculations to complement my NRIXS study on enstatite. I am very grateful to all of you for your help with my research. I also want to thank Dr. Tao Chen, Dr. Sinan Akciz and Dr. Ken Hudnut for the help with the LiDAR project. I am very glad to see the paper finally coming out after the long time.

I'd like to thank my officemates – Dr. Ravi Kanda, Dr. Michelle Selvans, Dr. Dan Bower, Dr. Zhongwen Zhan, Yingdi Luo, Chris Rollins, Rachel Miller and Albert Chan. You made South Mudd 358 a nice room to stay. By flying between Pasadena and Argonne, I got the privilege to know a lot friends on both sites. Dr. Jeffrey Thompson, Dr. Thomas Ader, Dr. Zhongwen Zhan, and Dr. Sara Dougherty always work together with me on differential departmental activities in my first 4 years. I thank the Chinese students and scholars in both the Seismolab and the APS – Dr. Lijun Liu, Dr. Daoyuan Sun, Dr. Bin Chen, Dr. Ting Chen, Dr. Shengji Wei, Dr. Lingsen Meng, Dr. Yihe Huang, Dr. Risheng Chu, Dr. Zhongwen Zhan, Dr. Yu-Nung Lin, Dr. Wei Leng, Dr. Fan-Chi Lin, Dr. Tao Chen, Dr. Han Yue, Junle Jiang, Zhihong Tan, Dunzhu Li, Yiran Ma, Yingdi Luo, Junjie Yu, Xiaolin Mao, Kangchen Bai, Dr. Lili Gao, Dr. Lifen Yan, Dr. Wenli Bi,

Dr. Zhicheng Jing, Dr. Ligang Bai, Dr. Cheng Ji and many others – for being supportive when I was homesick. In addition, I would like to thank the current and former supporting staffs: Sarah Gordon, Julia Zuckerman, Donna Mireles, Kimberly Baker-Gatchalian, Mike Black, Scott Dungan, Elizabeth Boyd, Leticia Calderon, Viola Carter and Dian Buchness.

My experience in the states has been enriched by numerous friends out of the Caltech campus, and it is a pity that I can't list all of them here. I would like to thank Xiaoman Lin, Ming Chen, Pengfei Zang, Langechuan Liu, Chenyu Xu and many others for sharing the emotions, life experiences and wonderful memories with me either in person or through various communication technologies. Last but not least, I would like to thank my family. I am deeply indebted to my parents, my grandparents and my in-laws, who have given, and will continue to give me endless support. Special thanks go to my wife, Zhiying Ma. Our incredible journey started in Chicago on a beautiful fall weekend, and then we shared many wonderful memories with each other. After years of traveling back and forth, it turns out that the windy city is still the best place for both of us, and I can't wait to start our next adventure together in Chicago.

---

I thank the California Institute of Technology, the Chinese Scholarship Council and NSF (NSF-EAR-0711542, CAREER EAR-0956166, EAR-1316362) for support of this research. Use of the Advanced Photon Source is supported by the U.S. D.O.E., O.S., O.B.E.S. (DE-AC02-06CH11357). Use of the Advanced Light Source is supported by the U.S. D.O.E., O.S., O.B.E.S. (DE-AC02-05CH11231). Sector 3 operations and the gas-loading system at GSE-CARS are supported in part by COMPRES under NSF Cooperative Agreement EAR 06-49658. Use of HP-CAT is supported by DOE-BES, DOE-NNSA, NSF, and the W.M. Keck Foundation.

# Abstract

The elastic and the thermodynamic properties of minerals under extreme P-T conditions are of general importance to the geodynamic modeling and the interpretation of seismic-wave observations. An accurate laboratory determination of these properties provides constraints to determine the composition and temperature of Earth's interior. In this thesis, I focus on the application of nuclear resonant scattering, an advanced synchrotron based spectroscopic technique, to further our understanding of candidate materials in Earth's interior. Specific examples include enstatite, which is an abundant mineral in the mantle, and iron-nickel alloy, which is believed to be the major component of the core. Our nuclear resonant scattering experiments is complemented with other synchrotron based techniques, such as diffraction.

Nuclear resonant scattering is capable of detecting subtle changes in the mineral's hyperfine parameters, and can therefore be sensitive to the transitions occurring in minerals under pressure. For example, we explore the site-specific hyperfine behavior of iron in a  $^{57}\text{Fe}$ -enriched powdered enstatite sample using nuclear resonant scattering and diamond-anvil cells in two independent experiments. The  $(\text{Mg}_{0.980}\text{Fe}_{0.020(5)})(\text{Mg}_{0.760}\text{Fe}_{0.240})\text{Si}_2\text{O}_6$  sample is pressurized up to 36 GPa at ambient temperature. In one experiment, NaCl is used as the pressure-transmitting medium, and in the other experiment, Ne surround the sample. Analyses of both data sets reveal a change in the trend or discontinuity in the hyperfine parameters around 10 GPa, indicative of a structural transformation in enstatite. However, the detailed behaviors of the iron sites with pressure appear to depend on the local stress conditions provided by the different pressure media.

Nuclear resonant scattering is also used to measure the elastic properties of iron-bearing enstatite at high pressures. The behavior of synthetic powdered  $^{57}\text{Fe}$ -enriched  $(\text{Mg}_{0.980}\text{Fe}_{0.020(5)})$ - $(\text{Mg}_{0.760}\text{Fe}_{0.240})\text{Si}_2\text{O}_6$  is explored by X-ray diffraction (XRD) and nuclear resonance inelastic X-ray scattering (NRIXS). The *Pbca*-structured enstatite sample is compressed in fine pressure increments for our XRD measurements. One structural transition between 10.1 and 12.2 GPa is identified from the XRD data. The XRD reflections observed for the high-pressure phase are best matched with space group  $P2_1/c$ . The partial phonon density of states (DOS) is derived from the raw NRIXS data up to 17 GPa, and from the low-energy region of the DOS, the Debye sound velocity is determined. We use the equation of state determined from XRD and Debye sound velocity to compute

the isotropic compressional and shear wave velocities of enstatite at different pressures. We combine density-functional theory with nuclear resonant scattering to understand the local site symmetry of the Fe atoms in our sample. We compare our experimental results with seismic observations to understand large lateral variations in shear wave velocities in the upper mantle.

Recently, nuclear resonant scattering has been shown to be a powerful probe in determining the solid-liquid boundary of iron-bearing materials. To capture the sample’s transient temperature fluctuations and reduce uncertainties in melting temperatures, we have developed a Fast Temperature Readout (FasTeR) spectrometer in-line with nuclear resonant scattering measurements under extreme conditions at Sector 3-ID-B of the Advanced Photon Source at Argonne National Laboratory. Dedicated to determining the sample’s temperature near its melting point, FasTeR features a fast readout rate (about 100 Hz), high sensitivity, large dynamic range and well-constrained focus. FasTeR is capable of reading out temperatures about 1 to 2 magnitudes faster than the conventional CCD spectrometer, without sacrificing accuracy, and is especially suitable for dynamic measurements at extreme conditions.

By combining nuclear resonant scattering with the laser heated diamond anvil cell and the FasTeR spectrometer, we have determined the melting temperatures of *fcc*- and *hcp*-structured iron and iron-nickel alloy at high pressures. We find that the melting curve of Fe is slightly higher than the melting curve of  $\text{Fe}_{0.9}\text{Ni}_{0.1}$ , but the difference is smaller than the uncertainty. We calculate the  $\gamma$ - $\epsilon$ -l triple point of  $\text{Fe}_{0.9}\text{Ni}_{0.1}$  to be  $116\pm 5$  GPa and  $3260\pm 120$  K, and  $110\pm 5$  GPa and  $3345\pm 120$  K for Fe. With the  $\gamma$ - $\epsilon$ -l triple points of Fe and  $\text{Fe}_{0.9}\text{Ni}_{0.1}$ , and the thermophysical parameters of *hcp*-Fe determined from a NRIXS measurement, we compute the high pressure melting curves of *hcp*-structured Fe and  $\text{Fe}_{0.9}\text{Ni}_{0.1}$ . The extrapolated  $\text{Fe}_{0.9}\text{Ni}_{0.1}$  melting curve provides an estimate for the upper bound of Earth’s inner core-outer core boundary temperature of  $5500\pm 200$  K. The temperature within the liquid outer core is then approximated with an adiabatic model, which constrains the upper bound of the temperature at the core side of the core-mantle boundary to be  $4000\pm 200$  K. We discuss a potential melting point depression caused by light elements and the implications of the presented core-mantle boundary temperature on phase relations in the lowermost part of the mantle.

# Contents

<b>Acknowledgments</b>	<b>iv</b>
<b>Abstract</b>	<b>vii</b>
<b>List of figures</b>	<b>xiii</b>
<b>List of tables</b>	<b>xv</b>
<b>1 Introduction</b>	<b>1</b>
1.1 Iron and Earth's deep interior . . . . .	1
1.2 High pressure-high temperature experiments . . . . .	4
1.2.1 The diamond anvil cell . . . . .	4
1.2.2 Generating high temperature in diamond anvil cells . . . . .	6
1.3 Scope of thesis . . . . .	8
<b>2 Experimental Methods</b>	<b>11</b>
2.1 Static compression with the diamond anvil cell . . . . .	11
2.2 Experiments using synchrotron radiation . . . . .	17
2.2.1 X-ray powder diffraction . . . . .	17
2.2.2 Nuclear resonant scattering of synchrotron radiation . . . . .	20
<b>3 Local structure variations observed in orthoenstatite at high-pressures</b>	<b>26</b>
3.1 Introduction . . . . .	26
3.2 Experimental procedures . . . . .	28
3.2.1 Sample preparation . . . . .	28
3.2.2 Synchrotron Mössbauer spectroscopy . . . . .	28
3.2.3 Pressure uncertainties . . . . .	29
3.3 SMS data evaluation and results . . . . .	30
3.3.1 CONUSS with a Beam-Search algorithm . . . . .	30
3.3.2 En87-NaCl . . . . .	32

3.3.3	En87-Ne . . . . .	36
3.4	Discussion . . . . .	36
3.4.1	Influence of different pressure media . . . . .	36
3.4.2	Local structure variations in orthopyroxene at high-pressures . . . . .	38
<b>4</b>	<b>Elasticity and lattice dynamics of enstatite at high pressure</b>	<b>41</b>
4.1	Introduction . . . . .	41
4.2	Methodology . . . . .	43
4.2.1	X-ray diffraction . . . . .	43
4.2.2	Nuclear resonant inelastic X-ray scattering . . . . .	44
4.2.3	First-principles calculations . . . . .	47
4.3	Results . . . . .	47
4.3.1	X-ray diffraction . . . . .	47
4.3.2	Nuclear resonant inelastic X-ray scattering and first-principles calculations . . . . .	51
4.3.3	Geophysical implications . . . . .	57
<b>5</b>	<b>Fast temperature spectrometer for samples under extreme conditions</b>	<b>62</b>
5.1	Introduction . . . . .	62
5.2	Instrumentation . . . . .	64
5.2.1	Experimental set-up . . . . .	64
5.2.2	Fast temperature readout spectrometer (FasTeR) . . . . .	66
5.2.3	Calibration . . . . .	67
5.2.4	FasTeR sampling frequency . . . . .	71
5.2.5	Simulating FasTeR . . . . .	73
5.3	Melting of $^{57}\text{Fe}_{0.9}\text{Ni}_{0.1}$ at high pressure . . . . .	75
5.4	Conclusions . . . . .	79
<b>6</b>	<b>Temperature of Earth's core constrained from melting of Fe and <math>\text{Fe}_{0.9}\text{Ni}_{0.1}</math> at high pressures</b>	<b>80</b>
6.1	Introduction . . . . .	80
6.2	Experiments . . . . .	82
6.2.1	Sample preparation . . . . .	82
6.2.2	Synchrotron Mössbauer spectroscopy measurements . . . . .	84
6.3	Results and Discussion . . . . .	88
6.3.1	Thermal contribution to the pressure . . . . .	88
6.3.2	Melting temperature determination . . . . .	89
6.3.3	Melting curves of the <i>fcc</i> -phases and triple points . . . . .	91

6.3.4	Melting curves of the <i>hcp</i> -phases . . . . .	92
6.3.5	Implications for the temperature in Earth's core . . . . .	95
6.4	Conclusion . . . . .	98
<b>7</b>	<b>Concluding remarks</b>	<b>99</b>
7.1	Earth's upper mantle . . . . .	99
7.2	Cores of terrestrial planets . . . . .	101
<b>A</b>	<b>Appendix</b>	<b>103</b>

# List of Figures

<b>Chapter 1</b>	<b>1</b>
1.1 Mineral volume fractions of the Earth. . . . .	2
1.2 Average global seismic models. . . . .	3
1.3 Typical diamond anvil cell and its components. . . . .	5
1.4 Scales of interest in this thesis. . . . .	9
<b>Chapter 2</b>	<b>10</b>
2.1 Diamond anvil cells and their components. . . . .	12
2.2 Typical diamond anvil assembly and sample loading. . . . .	12
2.3 Aligning diamonds. . . . .	14
2.4 Principles of X-ray powder diffraction . . . . .	18
2.5 Experimental setup for nuclear resonant scattering experiments. . . . .	22
<b>Chapter 3</b>	<b>25</b>
3.1 Representative SMS time spectra for En87-NaCl and En87-Ne at different pressures. .	34
3.2 The best-fit hyperfine parameters derived from the time spectra of En87-NaCl. . . . .	35
3.3 The best-fit hyperfine parameters derived from the time spectra of En87-Ne. . . . .	37
3.4 High-pressure observations and reported transition pressures from experiments using orthopyroxene with different Fe/(Fe+Mg) ratios at 300 K. . . . .	40
<b>Chapter 4</b>	<b>40</b>
4.1 Select XRD patterns of enstatite at different pressures. . . . .	45
4.2 Unit cell volume as a function of pressure for En87. . . . .	45
4.3 Confidence ellipses in $K_T$ and $K'_T$ for the fit of the BM3 EOS to the En87 P-V data.	46
4.4 Select NRIXS spectra and partial projected phonon density of states of En87 at different pressures. . . . .	48

4.5	The DFT calculated phonon DOS and measured Fe-partial projected phonon DOS for OEN at ambient pressure. . . . .	49
4.6	Debye sound velocity determination of En87 at 10.5 GPa. . . . .	54
4.7	Sound velocities of enstatite at different pressures. . . . .	55
4.8	Comparison of calculated shear wave velocities from candidate upper mantle petrological models with seismic profiles. . . . .	60
<b>Chapter 5</b>		<b>61</b>
5.1	Design of the experimental set-up for laser-heating, nuclear resonant scattering, x-ray diffraction, and FasTeR at beamline 3-ID-B of the Advanced Photon Source at Argonne National Laboratory. . . . .	65
5.2	Measured wavelength-dependent channel transmission of the optical bandpass filters for FasTeR. . . . .	68
5.3	Calibration of intensity ratios from theoretical calculations and the tungsten standard lamp, and comparison with measured laser-heated hotspot. . . . .	69
5.4	Comparison between the temperature read by the CCD spectrometer and FasTeR. . . . .	70
5.5	FasTeR's time resolution tested with an optical chopper. . . . .	72
5.6	Transient temperature fluctuation as a function of laser power captured by the FasTeR system but not the CCD spectrometer. . . . .	72
5.7	Demonstration of the SIMFaster code. . . . .	74
5.8	Temperature and normalized delayed counts as functions of the laser power. . . . .	76
5.9	Determining the melting temperature of $\text{Fe}_{0.9}\text{Ni}_{0.1}$ at $P_{300K}=29\pm 2$ GPa. . . . .	77
<b>Chapter 6</b>		<b>79</b>
6.1	Determining the pressures of samples with XRD . . . . .	83
6.2	Comparison of the pressures of pre-heated samples and post-melted samples. . . . .	83
6.3	SMS spectra of $^{57}\text{Fe}_{0.9}\text{Ni}_{0.1}$ and $^{57}\text{Fe}$ at high pressures and high temperatures. . . . .	85
6.4	Temperature and normalized delayed counts as functions of the laser power . . . . .	87
6.5	Constraining the thermal contribution of pressure using high P-T XRD data. . . . .	89
6.6	Determining the melting point of $\text{Fe}_{0.9}\text{Ni}_{0.1}$ and Fe samples at high pressures. . . . .	90
6.7	Melting points of <i>fcc</i> -structured Fe and $\text{Fe}_{0.9}\text{Ni}_{0.1}$ sample at high pressures. . . . .	91
6.8	Phase diagram and phase boundaries of Fe and $\text{Fe}_{0.9}\text{Ni}_{0.1}$ . . . . .	95
6.9	Proposed thermal profiles of Earth's interior and melting points of minerals. . . . .	96

# List of Tables

<b>Chapter 2</b>	<b>10</b>
2.1 List of Mössbauer isotopes with nuclear transitions that are feasible for nuclear resonant scattering experiments at Sector 3 at the Advanced Photon Source. Values come from <i>Sturhahn (2004)</i> . . . . .	21
<b>Chapter 3</b>	<b>25</b>
3.1 Comparison with previous conventional Mössbauer spectroscopy measurements of $(\text{Mg,Fe})_2\text{Si}_2\text{O}_6$ orthopyroxene at ambient temperature and pressure. . . . .	31
3.2 The error correlation matrix for the fitted parameters at ambient pressure (En87-NaCl), as reported by CONUSS . . . . .	31
3.3 The best-fit parameters for the two sites model from the SMS time spectra evaluation for En87-NaCl: $(\text{Mg}_{0.980}\text{Fe}_{0.020(5)})(\text{Mg}_{0.760}\text{Fe}_{0.240})\text{Si}_2\text{O}_6$ . . . . .	33
3.4 The best-fit parameters for the one site model from the SMS time spectra evaluation for En87-NaCl: $(\text{Mg}_{0.980}\text{Fe}_{0.020(5)})(\text{Mg}_{0.760}\text{Fe}_{0.240})\text{Si}_2\text{O}_6$ . . . . .	35
3.5 The best-fit parameters for the two sites model from the SMS time spectra evaluation for En87-Ne: $(\text{Mg}_{0.980}\text{Fe}_{0.020(5)})(\text{Mg}_{0.760}\text{Fe}_{0.240})\text{Si}_2\text{O}_6$ . . . . .	38
<b>Chapter 4</b>	<b>40</b>
4.1 Unit cell volumes of the OEN phase and the HP phase as a function of pressure. . . . .	51
4.2 Unit cell volume, isothermal bulk modulus and its pressure derivative of orthoenstatite ( <i>Pbca</i> ) at room pressure and temperature from different experimental studies. . . . .	52
4.3 Thermodynamic parameters of the $^{57}\text{Fe}$ -participating vibrations of En87 determined from NRIXS spectra at different pressures measured at 300 K. . . . .	53
4.4 Thermodynamic parameters determined from the DFT computed phonon DOS, calculated at 0 K and 300 K using PHOENIX. . . . .	53
4.5 Elastic parameters of En87 determined from this study using XRD and NRIXS at different pressures. . . . .	55

4.6	Thermoelastic parameters of minerals used in the finite strain model. . . . .	58
<b>Chapter 6</b>		<b>79</b>
6.1	Experimental results and melting points of $\text{Fe}_{0.9}\text{Ni}_{0.1}$ determined by synchrotron Mössbauer spectroscopy. . . . .	93
6.2	Experimental results and melting points of Fe determined by synchrotron Mössbauer spectroscopy. . . . .	93
<b>Appendix</b>		<b>102</b>
A.1	Detailed experimental information of all high pressure experiments in this thesis. . . .	104

# Chapter 1

## Introduction

### 1.1 Iron and Earth's deep interior

To better constrain and simulate the physical and chemical processes within the Earth, more knowledge about the materials that build this planet is needed. From cosmochemical, seismological and mineralogical studies, we have determined some general pieces of information about the Earth's deep interior (e.g., *Dziewonski and Anderson 1981; McDonough and Sun 1995; Anderson 2007; Frost 2008; Fiquet et al. 2008*). Earth has four major layers: a relatively thin crust (0-35 km), a silicate mantle (35-2900 km), a liquid metallic outer core (2900-5100 km) and a solid metallic inner core (5100-6370 km) (Figure 1.1). The mantle, outer core and inner core make up > 99 wt% of Earth's total mass, and are therefore most critical in determining the processes inside the Earth's deep interior. Major mineralogical components vary with the depth. In the upper mantle, the most abundant minerals are olivine ( $(\text{Mg,Fe})_2\text{SiO}_4$ ), garnet ( $(\text{Mg,Fe,Ca})_3\text{Al}_2\text{Si}_3\text{O}_{12}$ ), orthopyroxene ( $(\text{Mg,Fe})_2\text{Si}_2\text{O}_6$ ) and clinopyroxene ( $(\text{Mg,Ca})_2\text{Si}_2\text{O}_6$ ) (*Ringwood, 1979, 1991*). In the transition zone (410-660 km), the most abundant minerals become wadsleyite ( $(\text{Mg,Fe})_2\text{SiO}_4$ ), ringwoodite ( $(\text{Mg,Fe})_2\text{SiO}_4$ ) and majorite ( $(\text{Mg,Fe,Ca})_3(\text{Mg,Si,Al})_2\text{Si}_3\text{O}_{12}$ ) (*Liu and Bassett, 1975; Ringwood, 1991*). In the lower mantle, the dominating mineral component is bridgmanite ( $(\text{Mg,Fe,Al})(\text{Si,Al})\text{O}_3$ ) (*Tschauner and Ma (2014)*), coexisting with ferropericlase ( $(\text{Mg,Fe})\text{O}$ ) and calcium-perovskite ( $\text{CaSiO}_3$ ) (*Liu, 1975; Ringwood, 1991*). The core is made up of iron alloyed with 5-10 wt% nickel, plus ~10 wt% light elements (*McDonough and Sun, 1995; Li and Fei, 2003; Fiquet et al., 2008*). The candidate light elements in the core include hydrogen, carbon, oxygen, silicon, sulphur and magnesium (*Stevenson, 1981; Li and Fei, 2003; Fiquet et al., 2008*). The existence and abundance of these minerals inside Earth is determined from high pressure-high temperature experiments on the stability fields and elasticities of different minerals (*Ringwood, 1979; Bass and Anderson, 1984; Duffy and Anderson, 1989; Ringwood, 1991*), as well as seismic observations (Figure 1.2, *Dziewonski and Anderson 1981; Kennett et al. 1995*). For example, the olivine→wadsleyite→ringwoodite→bridgmanite+ferropericlase transitions account for the 410-520-660 km seismic discontinuities (*Liu, 1975; Duffy and Ander-*

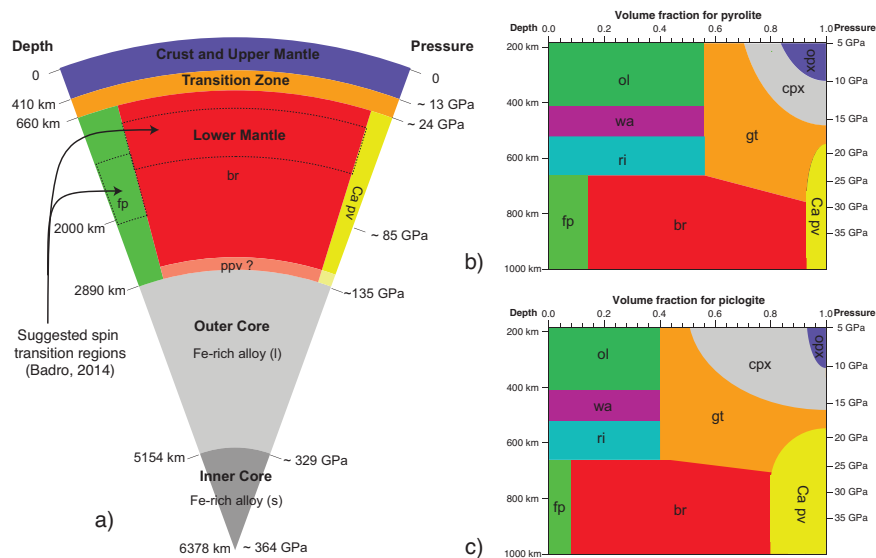


Figure 1.1: a): Proposed mineral volume fractions of the Earth. Dashed regions: suggested spin transition regions of ferropericlase and bridgmanite (*Badro*, 2014).  $\text{Fe}^{2+}$  cations in ferropericlase and bridgmanite are at high spin state above the spin transition regions, and at low spin state below these regions. Post-perovskite is shown in the bottom part of the lower mantle (*Murakami et al.*, 2004). b): Proposed mineral volume fractions of the pyrolitic Earth between 200 and 1000 km in depth (*Frost*, 2008). c): Proposed mineral volume fractions of the piclogitic Earth between 200 and 1000 km in depth (*Ita and Stixrude*, 1992). ol: olivine ( $(\text{Mg,Fe})_2\text{SiO}_4$ ); cpx: clinopyroxene ( $(\text{Mg,Ca})_2\text{Si}_2\text{O}_6$ ); opx: orthopyroxene ( $(\text{Mg,Fe})_2\text{Si}_2\text{O}_6$ ); gt: garnet ( $(\text{Mg,Fe,Ca})_3\text{Al}_2\text{Si}_3\text{O}_{12}$ ); wa: wadsleyite ( $(\text{Mg,Fe})_2\text{SiO}_4$ ); ri: ringwoodite ( $(\text{Mg,Fe})_2\text{SiO}_4$ ); fp: ferropericlase ( $(\text{Mg,Fe})\text{O}$ ); br: bridgmanite ( $(\text{Mg,Fe,Al})(\text{Si,Al})\text{O}_3$ ); Ca pv: calcium perovskite ( $\text{CaSiO}_3$ ); ppv: post-perovskite ( $(\text{Mg,Fe,Al})(\text{Si,Al})\text{O}_3$ ).

*son*, 1989; *Ringwood*, 1991). The disappearance and re-appearance of seismic shear velocity at the Earth's core-mantle boundary and inner core-outer core boundary indicate that the outer core is liquid whereas the inner core is solid (*Lehmann*, 1936; *Dziewonski and Anderson*, 1981; *Anderson*, 2007).

Iron is the most abundant element in the Earth's interior (*McDonough and Sun*, 1995; *Anderson*, 2007). It is the major component of Earth's core, which makes up  $\sim 16\%$  by volume and  $\sim 32\%$  by mass of the planet. In major mantle components like olivine, orthopyroxene, majorite garnet, ferropericlase and bridgmanite, iron contributes to  $\sim 10\%$  of the total cations in the crystal (*Frost*, 2008; *Fiquet et al.*, 2008). Iron is involved in many important geophysical phenomena. Adding iron may decrease the sound velocities of certain mantle components such as pyroxene and ferropericlase (*Jackson et al.*, 2006, 2009; *Antonangeli et al.*, 2011; *Chen et al.*, 2012; *Wicks et al.*, 2010), while the bulk modulus of bridgmanite is not strongly sensitive to Fe content (*Dorfman et al.*, 2013). Denser than the mantle silicates, iron accumulates into the center of Earth during its evolution (*Labrosse et al.*, 2007; *Rubie et al.*, 2007), which determines the Earth's mass distribution and moment of inertia. The flow of the conducting liquid outer core generates the geomagnetic field, and shields

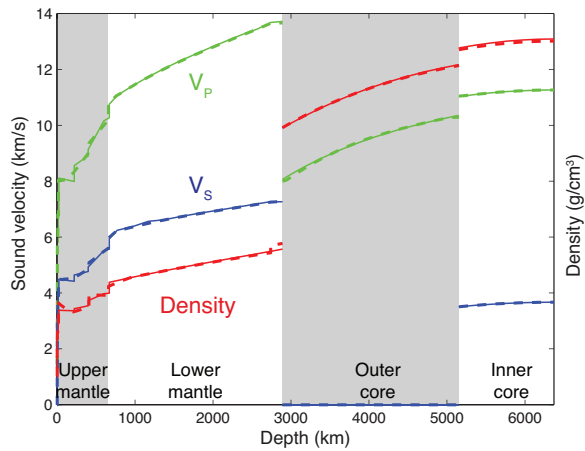


Figure 1.2: Average global 1D seismic models. Solid curves: PREM (*Dziewonski and Anderson, 1981*). Dashed curves: AK135 (*Kennett et al., 1995*). Red curves: density ( $\text{g/cm}^3$ ). Green curves: compressional seismic velocity ( $\text{km/s}$ ). Blue curves: shear seismic velocity ( $\text{km/s}$ ).

human beings from the harmful cosmic particles. In the lower mantle, iron endures a spin crossover (*Sturhahn et al., 2005; Badro, 2014*), in which the  $\text{Fe}^{2+}$  cation transforms from high spin state to low spin state. Experiments have shown that this spin crossover occurs in ferropericlase ( $(\text{Mg,Fe})\text{O}$ ), however the effects in bridgmanite ( $(\text{Mg,Fe,Al})(\text{Si,Al})\text{O}_3$ ) remain inconclusive (see *Badro (2014)*, and references therein). This spin crossover influences the elastic moduli of materials at high pressure (*Lin et al., 2005; Antonangeli et al., 2011; Chen et al., 2012*), but it might not have effects on compressional or shear sound velocities, because the changes in bulk and shear moduli are cancelled by the change in density (*Antonangeli et al., 2011; Badro, 2014*). Another important topic is the partitioning of iron between different mantle components. Experiments suggest that in simplified  $\text{MgO-FeO-SiO}_2$  systems, iron preferentially partitions into ferropericlase relative to bridgmanite at lower mantle conditions, with the partitioning coefficient  $K_D = (\text{Fe/Mg})_{Mg-Br}/(\text{Fe/Mg})_{Fp}$  ranging from 0.1 to 0.3 (*Ito and Takahashi, 1989; Nakajima et al., 2012*). However, in more complex systems that contain Al, the partitioning coefficient  $K_D$  increases to  $\sim 0.35\text{-}0.9$  due to the coupled incorporation of  $\text{Fe}^{3+}$  and  $\text{Al}^{3+}$  for  $\text{Mg}^{2+}$  and  $\text{Si}^{4+}$  in bridgmanite (*Frost and Langenhorst, 2002; Prescher et al., 2014*). This partitioning influences the bulk elasticity of this region, because iron-rich ferropericlase has an extremely low shear velocity at high pressure (*Wicks et al., 2010*) and it thus may be a component of the ultra-low velocity zones near the core-mantle boundary (*Wicks et al., 2010; Bower et al., 2011*). Recent study suggests that the bridgmanite may disassociate into two phases at lower mantle conditions: one is an iron-depleted bridgmanite phase, and the other is a new phase that is iron-rich and hexagonal in structure, named the H-phase (*Zhang et al., 2014*). As iron is a critical player in many deep earth phenomena, knowledge of its behavior in different phases at the conditions of Earth's deep interior is important to mineral physicists, seismologists, and geodynamicists.

The motivation of this thesis is to study two regions of the Earth. The first region is in the upper mantle, around 300 km depth. Some seismic studies suggest that there is a seismic discontinuity called the "X-discontinuity" in this region, which is still not well constrained (*Woodland, 1998; Deuss and Woodhouse, 2002; Akashi et al., 2009*). The structural transition of iron-bearing orthopyroxene ( $(\text{Mg,Fe})_2\text{Si}_2\text{O}_6$ ) has been suggested as an explanation for the "X-discontinuity" (*Woodland, 1998; Kung et al., 2004; Akashi et al., 2009*), though other components such as mantle water content (*Jacobsen et al., 2010*) or phase transitions involving silica (*Woodland, 1998*) may also explain the origin of this discontinuity. We use nuclear resonant scattering to constrain orthopyroxene's structural transition and the sound velocity change associated with this transition. The second region of interest is the core. The major component of the outer core is thought to be an iron-nickel alloy. Currently, the constraints on the temperature of the core are not comparable with its geophysical significance. The melting points of iron and iron-nickel at the pressure of Earth's inner-core outer-core boundary are suggested as the upper bounds of the temperature at this depth (*Jackson et al., 2013; Anzellini et al., 2013*). It is possible to calculate the temperature profile of the outer core through an adiabatic model, thus constrain the upper bound temperature of the core-mantle boundary. Nuclear resonant scattering is capable of constraining the melting points of iron-bearing materials at high pressures, and we will apply this method to determine the melting points of iron and iron-nickel alloy at high pressures, so as to help constrain the temperature regime of Earth's core-mantle boundary region.

## 1.2 High pressure-high temperature experiments

### 1.2.1 The diamond anvil cell

Different from the surface of the Earth, the interior of Earth is under both high pressures (up to  $\sim 360$  GPa) and high temperatures (up to  $\sim 6000$  K). Therefore, to study the behaviors of materials in the conditions of the Earth's deep interior, one must subject the sample to conditions at or approaching those of the deep Earth. Currently there are three major ways to generate the high pressure-high temperature environment in mineral physics experiments. The first method is shock compression (e.g., *Brown and McQueen 1986; Yoo et al. 1993; Ahrens et al. 2002; Nguyen and Holmes 2004*). This method uses a gas gun to accelerate projectiles and impact the sample on the target. During the impact process, the sample can be compressed to extremely high pressures and temperatures. The second method is large volume press (e.g., *Wang et al. 1998; Kung et al. 2004; Stewart et al. 2007; Chen et al. 2008*). In this method, a sample of  $\sim 0.1$  mm<sup>3</sup> size is placed in the center of a press, and hundreds to thousands tons of static force is exerted on the sample to generate high pressure. The advantage of this method is the relatively large sample size. Up to now, the upper limit of pressures that large volume presses can reach is 110-125 GPa (*Kunimoto and Irifune, 2010*;

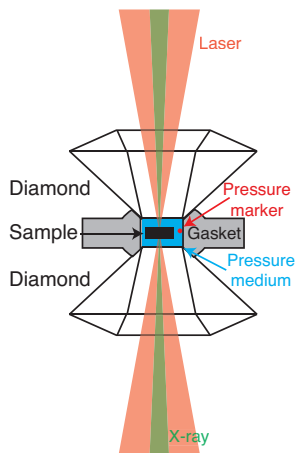


Figure 1.3: Selected regions of a typical diamond anvil cell, representing a small part of the components.

*Yamazaki et al.*, 2014).

The third, and most ubiquitous method to reach high P-T condition is the diamond anvil cell (e.g., *Jayaraman* 1983; *Zhang et al.* 2011, 2013a). Diamond is one of the strongest materials on the Earth, and it can hold a large pressure (up to hundreds of GPa) without being cracked, thus diamond is selected to form the pressure vessel. The diamonds used in diamond anvil cells have a small but flat tip, called the "culet". Since the pressure  $P = F/A$ , where  $F$  is the force and  $A$  is the area that  $F$  is exerted on, given a certain force, the smaller the area is, the larger the pressure one can achieve. Typical culets have shapes of 8 or 16 sided polygons, and their diameters range from 50 to 500  $\mu\text{m}$ . For a diamond with culet's diameter of 100  $\mu\text{m}$ ,  $\sim 800$  N force is needed to get a pressure of 100 GPa.

Diamond anvil cell has many advantages to serve as the pressure vessel for high pressure experiments. The diamond anvil cell-based experiments can provide a pressure-temperature range of higher than 350 GPa and 5500 K (*Tateno et al.*, 2010), or up to 640 GPa at room temperature (*Dubrovinsky et al.*, 2012). Diamond is transparent to visible light and relatively transparent to X-rays, so it is possible to use both visible and X-ray methods to probe a sample in the diamond anvil cell. The diamond anvil cell can provide a static pressure environment, and compared with other pressure vessels it is very portable, which is convenient for synchrotron-based measurements.

A typical diamond anvil cell assembly contains two diamonds with the same culet, and a gasket in between to hold the pressure from the side (Figure 1.3) (*Jayaraman*, 1983). The gasket can be made of hard metals like rhenium and stainless steel (*Jayaraman*, 1983), or other non-metal materials such as cubic boron nitride (*Wang et al.*, 2011; *Du et al.*, 2013a). For certain experiments that require collecting scattered X-ray photons from the side of the diamond anvil cell, X-ray transparent materials such as beryllium and amorphous boron are used to make gaskets (*Zhang et al.*, 2013a). The gasket is pre-indented to  $\sim 30$   $\mu\text{m}$  to increase stability, and a hole is drilled in the center of the

indentation to hold the sample. The gasket hole can be drilled by mechanical drill, electric discharge machine or laser mill (*Jayaraman, 1983; Zhang et al., 2013a*). The diamonds are glued on backing plates with epoxy. The backing plates are made of hard materials such as tungsten carbide or cubic boron nitride. There are openings on the backing plates for the transmission of X-ray. The backing plates, together with the diamonds on top of them, are fixed and aligned in the body of the diamond anvil cell with set screws. An example of the diamond anvil cell assembly is shown in Figure 1.3. The sample chamber is formed by the two diamond culets and the hole in the gasket. In addition to the sample, the sample chambers are typically filled with pressure media and a pressure marker. Pressure media are often soft materials like NaCl or compressed noble gases (*Zhang et al., 2011*). For laser heating experiments, thermal insulators like KCl and corundum ( $\text{Al}_2\text{O}_3$ ) are used (*Boehler, 1993; Jackson et al., 2013*). Pressure markers like gold (*in-situ*), platinum (*in-situ*) and ruby sphere (*ex-situ*) are usually placed in the gasket hole close to the sample to determine the pressure (e.g., *Heinz and Jeanloz 1984; Mao et al. 1986; Holmes et al. 1989*). In addition, *in-situ* X-ray diffraction of the sample can be combined with the sample's equation of state to constrain the pressure (e.g., *Anzellini et al. 2013; Zhang et al. 2013a*). More details on the specific DAC preparations related to this thesis are provided in Chapter 2.

### 1.2.2 Generating high temperature in diamond anvil cells

In high pressure experiments conducted using the diamond anvil cells, there are essentially three ways to reach high temperatures in the diamond anvil cell: laser heating (*Shen et al., 2001, 2005; Meng et al., 2006; Prakapenka et al., 2008*), resistive heating (*Bassett et al., 1993; Du et al., 2013a; Zha et al., 2008*) and shock-wave loading of precompressed samples *Loubeyre et al. (2004); Jeanloz et al. (2007)*. The latter method permits unique states of matter to be probed at high pressures and temperatures. However, the sample is typically destroyed, thus presenting reproducibility challenges *Jeanloz et al. (2007)*. Heating by infrared lasers permits temperatures characteristic of Earth's deep interior (up to and exceeding 6500 K) to be reached. Although resistive heating alone presents challenges in generating temperatures higher than 2000 K at high pressures (*Bassett et al., 1993; Du et al., 2013a; Zha et al., 2008*), thermocouple-based temperature determinations provide fairly accurate and precise sample temperatures. Laser heating can be implemented in most diamond anvil cell designs, while special gaskets, additional heaters and associated controllers are required for resistive heating (*Bassett et al., 1993; Du et al., 2013a; Zha et al., 2008*). Laser heating is therefore often employed in high pressure experiments where temperatures greater than about 1200 K are desired.

Laser heating does present challenges. The temperature distribution in laser heating experiments can be inhomogeneous (*Boehler, 2000; Campbell, 2008*). Some recent progress have been made to increase the spatial homogeneity, including laser heating from both sides (*Shen et al., 2001;*

*Prakapenka et al.*, 2008), combining different laser modes (*Shen et al.*, 2001), and adjustable laser geometry with beam-shaping optics (*Prakapenka et al.*, 2008). The second and less discussed challenge is the stability of laser heating over a defined time period. The sample’s temperature in a laser heating experiment can fluctuate faster than in resistive heating experiments. Previous studies have documented temperature fluctuations of several hundred Kelvins (*Jeanloz and Heinz*, 1984; *Jeanloz and Kavner*, 1996; *Dewaele et al.*, 2007, 2010; *Anzellini et al.*, 2013) at a minimum of tens of Hz (*Jeanloz and Heinz*, 1984) during continuous wave laser heating. Experiments have shown that small ( $\sim 0.2\text{-}3\%$ ) temporal fluctuations in laser power are followed by large fluctuations in the temperature of the sample (*Jeanloz and Heinz*, 1984). It is also suggested that melting of the thermal insulation layer (*Dewaele et al.*, 2010), changes in the thermal conductivity in the sample chamber (*Geballe and Jeanloz*, 2012) and changes in the laser coupler’s reflectivity (*Geballe and Jeanloz*, 2012) may contribute to these large temperature fluctuations. Such fluctuations are not favorable for reliable temperature determinations of a laser-heated sample, and will inevitably increase the error of the temperature measurement.

There are a few approaches to address unstable temperature readouts in laser-heated diamond anvil cell experiments. Closed-loop laser power feedback systems have proved to be effective in reducing the temperature fluctuation at a constant laser power (*Heinz et al.*, 1991; *Shen et al.*, 2001). However, this method is not suitable for experiments that involve ramping up the laser power every few seconds, such as that done for melting studies. For these types of experiments, it is preferred to determine the temperature of the sample at a frequency higher than: the sample’s temperature fluctuations and the accumulation time needed to diagnose certain material properties. Currently, most temperature determination systems in laser-heated diamond anvil cell experiments use charge-coupled device (CCD) chips as detectors. The CCD chip is either used in a spectrometer to fit the measured intensities to a temperature using Planck’s law (*Shen et al.*, 2001; *Zhao et al.*, 2004; *Prakapenka et al.*, 2008), or used to monitor the spatial distribution of the hotspot temperature by measuring the intensities of different wavelength bands (*Campbell*, 2008; *Du et al.*, 2013b). However, most conventional CCD chips are intrinsically slow. The readout time is on the order of  $10\ \mu\text{s}$  per CCD pixel, and CCD chips for spectrometers usually have  $10^5$  pixels (*Reed*, 1992). Therefore, in most CCD-equipped laser-heated diamond anvil cell experiments, the temperature readout frequency is at best on the order of 1 Hz (e.g., *Dewaele et al.* 2007, 2010 and *Anzellini et al.* (2013)). For laser-heated diamond anvil cell experiments involving rapid temperature changes, a high-frequency temperature readout system is highly desirable. We have developed a new **F**ast **T**emperature **R**eadout (FasTeR) spectrometer dedicated to experiments involving rapid temperature changes in the sample near its solidus. More details on the FasTeR spectrometer are provided in Chapter 3.

### 1.3 Scope of thesis

This thesis summarizes all my experimental work on high pressure mineral physics in the past 6 years. Chapter 2 gives the detailed review of how those experiments were conducted. In Chapter 2, I describe how to prepare the diamond anvil cell so that we exert high pressure on the sample, and how the synchrotron-based experiments, namely X-ray diffraction, synchrotron Mössbauer spectroscopy and nuclear resonant inelastic X-ray scattering, are carried out.

The elastic and the thermodynamic properties of minerals under extreme conditions are of general importance to the geodynamic modeling and the interpretation of seismic-wave observations, and an accurate laboratory determination of these properties will provide constraints on the composition and temperature of Earth's interior. In Chapters 3-6, I will focus on the application of nuclear resonant scattering to further our understanding of candidate materials in Earth's interior.

Enstatite is an abundant silicate mineral in the upper mantle, and it endures a structural transition at high pressures. Nuclear resonant forward scattering (also known as Synchrotron Mössbauer spectroscopy) is capable of detecting subtle changes in the mineral's hyperfine parameters, and can therefore be sensitive to the transitions occurring in minerals under pressure. In Chapter 3, we discuss the site-specific hyperfine behavior of iron in a  $^{57}\text{Fe}$ -enriched powdered enstatite sample using synchrotron Mössbauer spectroscopy in two independent experiments with different pressure media (NaCl and Ne). The  $(\text{Mg}_{0.980}\text{Fe}_{0.020(5)})(\text{Mg}_{0.760}\text{Fe}_{0.240})\text{Si}_2\text{O}_6$  sample is pressurized up to 36 GPa at ambient temperature. Analyses of data sets reveal a discontinuity in the hyperfine parameters at around 10 GPa, indicative of a structural transformation in enstatite. We also discuss the detailed behaviors of the iron sites with pressure and its relation with the local stress conditions provided by the different pressure media.

In Chapter 4, we use nuclear resonant inelastic X-ray scattering and X-ray diffraction to determine the elastic properties of iron-bearing enstatite at high pressures. The behavior of the same synthetic powdered  $^{57}\text{Fe}$ -enriched  $(\text{Mg}_{0.980}\text{Fe}_{0.020(5)})(\text{Mg}_{0.760}\text{Fe}_{0.240})\text{-Si}_2\text{O}_6$  enstatite studied in Chapter 3 is explored. The *Pbca*-structured enstatite sample was compressed in fine pressure increments for our XRD measurements and one structural transition between 10.1 and 12.2 GPa is identified from the XRD data. The partial phonon density of states (DOS) is derived from the raw nuclear resonant inelastic X-ray scattering (NRIXS) data up to 17 GPa, and from the low-energy region of the DOS, the Debye sound velocity is determined. We use the equation of state determined from XRD and Debye sound velocity from NRIXS to compute the isotropic compressional and shear wave velocities of enstatite at different pressures. We combine density-functional theory with nuclear resonant scattering to understand how the local site symmetries of the Fe atoms affect the total phonon DOS. We compare our experimental results with seismic observations to speculate on the origin of large lateral variations in shear wave velocities in the upper mantle.

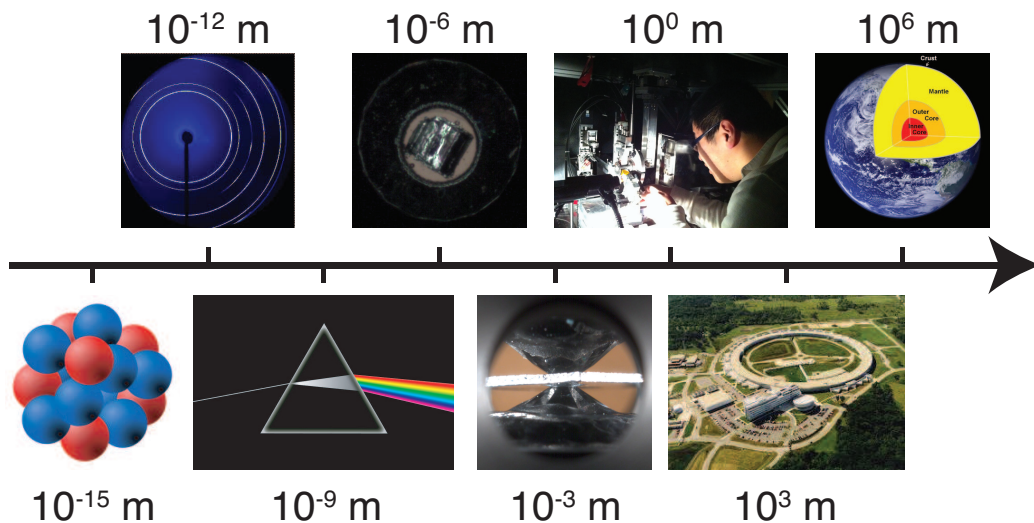


Figure 1.4: Scales of interest in this thesis.  $10^6$  m: typical diameter of terrestrial planets.  $10^3$  m: typical diameter of third-generation synchrotron radiation.  $10^0$  m: magnitude of researcher’s height.  $10^{-3}$  m: dimension of diamond anvil cell.  $10^{-6}$  m: typical dimension of sample in high pressure experiments.  $10^{-9}$  m: magnitude of photon’s wavelength used in the experiments.  $10^{-12}$  m: typical magnitude of sample’s lattice parameter.  $10^{-15}$  m: typical diameter of nuclei.

Recently, nuclear resonant scattering has been shown to be a powerful probe in determining the solid-liquid boundary of iron-bearing materials (*Jackson et al.*, 2013). To capture the sample’s transient temperature fluctuations and reduce uncertainties in melting temperatures, we develop a Fast Temperature Readout (FasTeR) spectrometer in-line with nuclear resonant scattering measurements under extreme conditions at Sector 3-ID-B of the Advanced Photon Source at Argonne National Laboratory. Chapter 5 describes the FasTeR system in detail. Dedicated to determining the sample’s temperature near its melting point, FasTeR features a fast readout rate (about 100 Hz), high sensitivity, large dynamic range and well-constrained focus. FasTeR is capable of reading out temperatures about 1 to 2 magnitudes faster than the conventional CCD spectrometer at the same beamline, without sacrificing accuracy, and is especially suitable for ultrafast time-resolved measurements at extreme conditions.

By combining nuclear resonant scattering with the laser heated diamond anvil cell and the FasTeR spectrometer, we have developed a novel methodology to probe the melting points of iron-bearing materials at high pressures. Chapter 6 focuses on the application of this methodology to core-related materials. We determine the melting temperatures of *fcc*-structured iron and iron-nickel alloy at high pressures. Our results combined with newly reported thermal equations of state provide new constraints on the melting curves of iron and iron-nickel. Following this chapter, there is a final conclusion chapter which summarizes this thesis.

This thesis covers a broad range of length scales (Figure 1.4). In order to study properties of the terrestrial planets’ interior (typical diameter:  $10^6$  m), high pressure experiments are carried out in

the synchrotron (typical accelerator ring diameter:  $10^3$  m) by researchers (magnitude of height:  $10^0$  m). Diamond anvil cells are used (typical size:  $10^{-3}$  m) to compress the sample (typical size:  $10^{-6}$  m). The photons used in the experiments have wavelenghtes in the order of  $10^{-9}$  m. The lattice parameters (in the order of  $10^{-12}$  m) and the excitation of nuclei (typical diameter:  $10^{-15}$  m) of the sample are studied in the experiments. Using different length scales, this thesis helps to provide new constraints on the materials inside Earth and other terrestrial planets.

## Chapter 2

# Experimental Methods

The data presented in this thesis were collected at 3rd generation synchrotron radiation facilities in the United States. The majority of our experiments were conducted at the Advanced Photon Source at Argonne National Laboratory, Argonne, Illinois. A portion of the X-ray diffraction measurements were carried out at the Advanced Light Source at Lawrence Berkeley National Laboratory, Berkeley, California. Sample preparations were performed prior to each experiment in the Diamond Anvil Cell Laboratory at the California Institute of Technology, Pasadena, California, and at the Advanced Photon Source. Data analysis, interpretation and related software development were conducted at the California Institute of Technology and at the Advanced Photon Source. Detailed experimental runs are tabulated in Chapters 3-6 and the Appendix.

### 2.1 Static compression with the diamond anvil cell

Many different diamond anvil cells have been designed to meet the requirements of various experimental geometries and setups (Figure 2.1). For high pressure X-ray diffraction and synchrotron Mössbauer spectroscopy measurements, symmetric diamond anvil cells are typically used. The symmetric diamond anvil cell features symmetric openings of  $57^\circ$  on both sides in the axial direction, which is helpful to capture as much scattered photons as possible. The components involved in a complete symmetric diamond anvil cell assembly are: 1 piston, 1 cylinder, 2 diamonds, 2 backing plates, mounting epoxy, 8 aligning screws, 2 set screws, mounting putty, 1 gasket (typically rhenium), and 4 tightening screws. There is no difference between putting the piston side or the cylinder side toward the downstream direction of the incident X-ray beam, unless one uses different backing plates for piston and cylinder sides. Different from SMS and X-ray diffraction, the nuclear resonant inelastic X-ray scattering technique requires a panoramic diamond anvil cell. The main features of a panoramic diamond anvil cell are the large "windows" cut out of the cylinder, so that detectors can be brought in very close ( $\sim 5$  mm) to the compressed sample without compromising the ability to apply a uniform force to the sample chamber and, in turn, generate pressure. The components

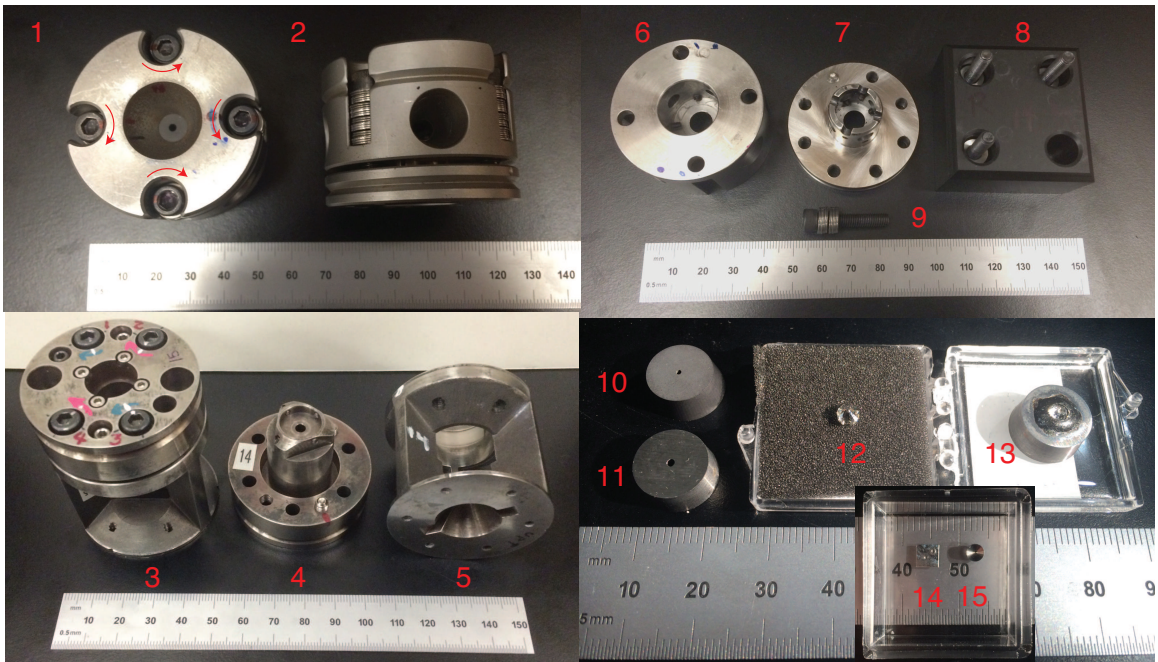


Figure 2.1: Diamond anvil cells and their components. 1: symmetric diamond anvil cell assembly, top view. Arrows indicate the tightening direction of the screws; 2: symmetric diamond anvil cell assembly, side view; 3: panoramic diamond anvil cell assembly designed and machined at Caltech; 4: piston part of a panoramic diamond anvil cell; 5: cylinder part of a panoramic diamond anvil cell (laid down to show the opening); 6: piston part; 7: cylinder part; 8: tightening screws and box holder; 9: tightening screw with spring washers; 10: cBN backing plate; 11: WC backing plate; 12: diamond (0.25 carat); 13: diamond mounted on WC backing plate; 14: Re gasket with pre-indentation; 15: Be gasket with pre-indentation.

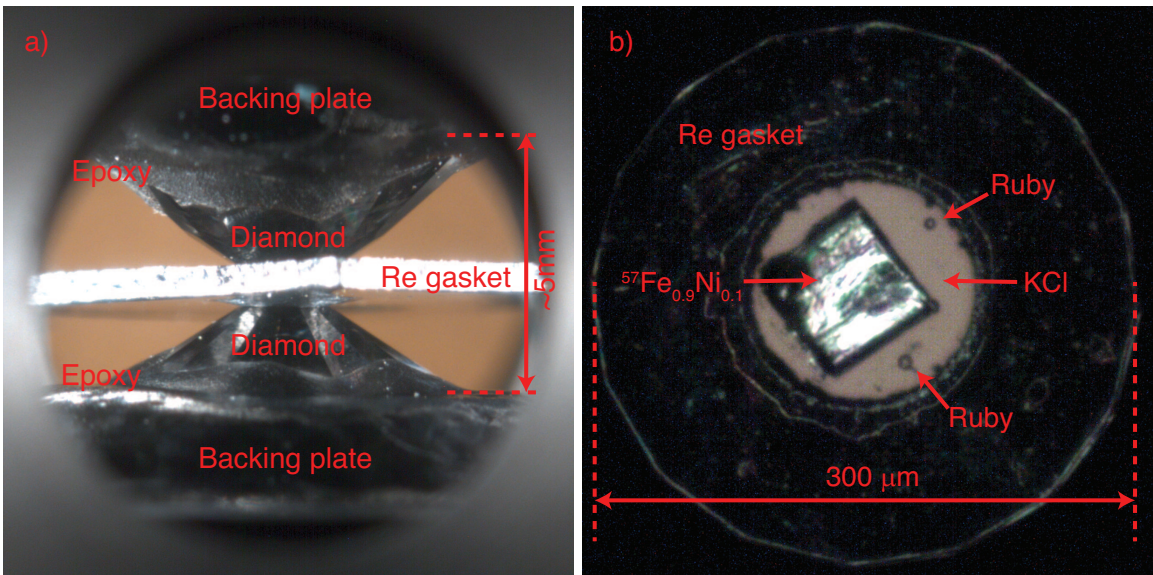


Figure 2.2: a): a typical diamond anvil assembly. b): a diamond anvil loaded with  $^{57}\text{Fe}_{0.9}\text{Ni}_{0.1}$  sample. Ruby spheres are used as pressure markers, and KCl serves as both pressure medium and thermal insulator.

involved in a complete panoramic diamond anvil cell assembly are: 1 piston, 1 cylinder, 2 diamonds, 2 backing plates, mounting epoxy, 10 aligning screws, 2 set screws, mounting putty, 1 X-ray transparent gasket (beryllium), 1 boron epoxy insert, and 4 tightening screws. The Caltech designed panoramic diamond anvil cell features a slotted opening angle of  $100^\circ$ . For a panoramic diamond anvil cell, the cylinder side should be placed toward the downstream direction of the incident X-ray beam in order to maximize the angular access for diffraction.

#### *Mounting diamonds*

To prepare a diamond anvil cell for high pressure experiments, one begins by mounting the diamonds to the backing plates. Gem quality single crystal diamonds that are  $\sim 2$  mm thick are used because of their high moduli ( $K_S = 442$  GPa,  $\mu = 575.8$  GPa), hardness ( $10^4$  kg/mm<sup>2</sup>) and yield strength ( $>110$  GPa), translucency at optical and typical X-ray energies (attenuation length: 3.7 mm at 14.4 keV and 13.1 mm at 30 keV), and good thermal conductivity, all of which are essential for performing experiments at high-pressure and temperature conditions. Backing plates are commonly made from tungsten carbide (WC) and cubic boron-nitride (cBN), which also have large bulk moduli (WC: 470 GPa; cBN: 400 GPa) and hardness values (WC: 2000 kg/mm<sup>2</sup>; cBN: 4500 kg/mm<sup>2</sup>). A significant difference between WC and cBN is that at typical X-ray energies, WC is highly absorbing while cBN is relatively transparent. At 14.4 keV, the attenuation length for cBN is 5.2 mm, whereas the attenuation length for WC is only 4.6  $\mu$ m, so the X-ray absorption of WC is about 1000 times higher than cBN. A cBN backing plate is therefore necessary on the downstream side of the diamond anvil cell for X-ray diffraction measurements, in order to maximize the range of accessible diffraction angles.

To mount a diamond on the backing plate, both components are thoroughly cleaned, and a mounting jig is used to align and secure the diamond in the center of the backing plate, centered over a hole pre-drilled in the backing plate. A mixture of Stycast 2651 resin and a catalyst in a ratio of 100:7 by weight (prepared immediately before diamond mounting) is used to fix the diamond on the backing plate. The epoxy should cover the girdle of the diamond and fill in between the girdle and the backing plate, but it shouldn't seep between the bottom of the diamond and the backing plate in order to maximize the stability of the anvil. When the epoxy is in place, the backing plate is placed on a heating plate at a temperature of  $\sim 80^\circ\text{C}$  for at least 8 hours to harden the epoxy.

#### *Alignments*

Once the diamonds have been secured to their backing plates, they are positioned and fixed in the piston and cylinder sides of the diamond anvil cell using the aligning screws, which hold the backing plates flush against the base of the diamond anvil cell. The sides of the backing plate are usually tilted, so that the forces from the aligning screws have components to tighten the backing plate against the piston/cylinder part (Figure 2.3a). For a typical symmetric diamond anvil cell, the piston and the cylinder are each equipped with four aligning screws. In order to align the

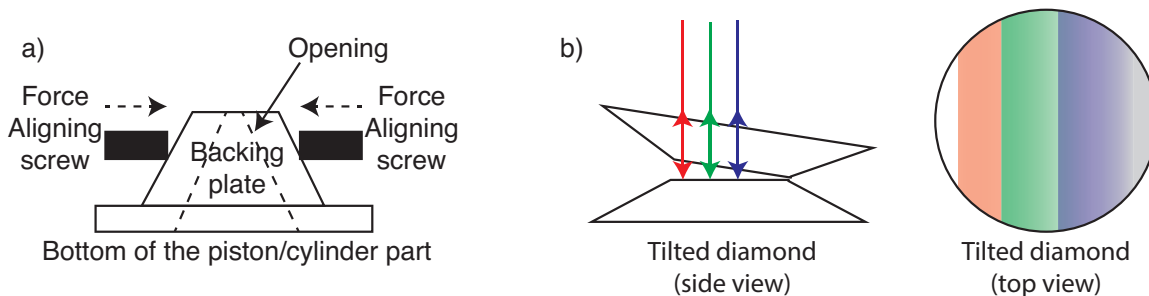


Figure 2.3: a): Fixing the backing plate with aligning screws. b): Interference fringes between tilted diamond culet surfaces.

diamonds in such a symmetric diamond anvil cell, first one needs to secure the diamond as close to the center of the piston side as possible, and then adjust the aligning screws on the cylinder side while looking through the piston-side diamond using a high-magnification microscope to align the culets with respect to each other. By looking through the microscope while the diamond anvil cell is rotated  $90^\circ$  around its axis (Figure 2.1, #2), one can fix the spacing between the opposing culets and perform this alignment procedure at a variety of spacings, from 1 mm to  $< 10 \mu\text{m}$ . Finally, the alignment of the diamonds is confirmed while they are in contact with each other and the outlines of both culets match each other. The parallelism of the culets is checked by investigating the optical interference fringes. If there is a degree of non-parallelness, then there is a small air wedge between the two culets (Figure 2.3b). The reflection of light with wavelength of  $\lambda$  is enhanced at the air wedge thicknesses  $h = \frac{2n-1}{4}\lambda$ , where  $n = 1, 2, 3, \dots$ . Therefore, when the diamonds are tilted, one can see the interference fringes changing from blue to red periodically. When the two diamonds are in close contact to each other and they are parallel, the culet's image is uniformly grey. If  $\geq 2$  full fringes are visible, the alignment process should be repeated, or a new orientation of the piston with respect to the cylinder can be chosen. For the panoramic diamond anvil cell, the cylinder is equipped with six aligning screws, while the piston has four. Therefore, common practice is to first secure the diamond on the cylinder side, and then adjust the aligning screws on the piston side. All other aligning procedures for the panoramic diamond anvil cell are similar to those of the symmetric diamond anvil cell.

#### *Gasket preparation*

The next step is to prepare a gasket, which will serve as the sample chamber in the diamond anvil cell. Many materials can be used to make gaskets. For X-ray diffraction, either stainless steel or rhenium gaskets are typically used. For SMS experiments, one can only use rhenium (Re) gaskets, because stainless steel generates a strong background from its  $^{57}\text{Fe}$  component which overwhelms the sample's signal. The Re gasket is pre-cut to a  $5 \text{ mm} \times 5 \text{ mm}$  square shape with a thickness of  $200 \mu\text{m}$ . For NRIXS experiments, beryllium (Be) gaskets are used. Be is a hazardous material, and it is much softer than Re (bulk moduli:  $K_{SBe} = 130 \text{ GPa}$ ,  $K_{SRe} = 370 \text{ GPa}$ ; shear moduli:

$\mu_{Be} = 132$  GPa,  $\mu_{Re} = 178$  GPa), which makes diamond anvil cell preparations difficult and limits the pressure range over which the sample chamber remains stable. However, the scattered photons in an NRIXS experiment must pass through the gasket with minimal absorption to reach radially positioned detectors, so the more common, X-ray absorbing gasket materials like stainless steel and Re cannot be used. We use specially designed Be gaskets that are 3 mm in diameter and machined with a  $\sim 400$   $\mu\text{m}$  flat area in center that is  $\sim 100$   $\mu\text{m}$  thick. The smaller diameter results in less absorption of scattered photons, while the flat area in the center allows for the gasket to rest stably in a horizontal position on the diamond culets during final indentation.

Preparation of a gasket for high-pressure experiments involves pre-indenting the gasket and drilling a hole in the center of it. For Be gaskets, there is a third step of applying an insert made of a stiff, low-atomic number material, e.g., boron-epoxy, cBN, or diamond. A plastic mounting putty is used to support the gasket during indentation and one marks the orientation of the gasket before drilling. To pre-indent the gasket, one begins by supporting it on a ring of mounting putty and centering a flat area of the gasket over the culets. Indenting the gasket to a thickness of  $\sim 35$ - $45$   $\mu\text{m}$  work-hardens it prior to the experiment, resulting in an increased resistance to further deformation during the experiment and improves the chances of achieving higher pressures. A sample chamber is produced by drilling a hole in the center of the pre-indentation. For Re gaskets, the hole can be drilled by mechanical drill, electrical discharge machining or laser drilling machine, and the drill hole diameter should be  $\sim 1/3$  of the culet diameter. For Be gaskets, because a stiff insert needs to be filled into the hole to hold pressure, the drill hole diameter should be  $\sim 1/2$ - $2/3$  of the culet diameter. The hole in the gasket is thoroughly cleaned.

The stiff insert reinforces the shape and size of the sample chamber in the Be gasket and avoids rapid thinning of the sample and chamber during compression. For high-pressure NRIXS experiments, we use a boron-epoxy insert material because it is less absorbing at the relevant X-ray energies ( $\sim 14.4$  keV) than cBN and diamond. To make the boron-epoxy, one mixes amorphous boron (Alfa Aesar; 99% pure; part No. 11337;  $\sim 1$  g for each boron-epoxy preparation), epoxy part A and epoxy part B (Epoxy Technology; part No. 353ND) in a ratio of 3.5:1:0.1 by weight with acetone on a glass slide or a mortar and pestle until they are well combined. This procedure is done under a fume hood right before the first insert is to be loaded. If the boron-epoxy dries out, it tends to lose mechanical flexibility. One then loads a small piece of the boron-epoxy into the drilled hole in the Be gasket and compresses it between the diamonds. The insert should fill the entire hole; spilling over onto the gasket material is not acceptable because the soft Be gasket is easily indented by the hard insert at high pressure, which usually is not good for stabilizing the cell assembly. Finally, a fine-tipped tungsten loading needle is used to drill a smaller hole in the boron-epoxy insert, which will serve as the sample chamber. A tungsten needle is used because one must avoid  $^{57}\text{Fe}$  contamination, which may happen if a stainless steel loading needle is used.

### *Sample loading*

The next step is to load the sample, the pressure marker and a pressure-transmitting medium into the sample chamber. Primary samples studied in this thesis are 95%  $^{57}\text{Fe}$  enriched, as this isotope enrichment allows for optimal counting rates. Depending on the concentration of  $^{57}\text{Fe}$  in the sample and desired pressure range, the sample typically has a optimal starting thickness between 10 to 30  $\mu\text{m}$ . This optimal sample thickness assures reasonable counting rates for our experiments, while preventing unnecessary absorption of the forward scattering signal and significant sample thinning during compression. In all of our experiments, the samples are loaded in the center of the culets and not in contact with the gaskets or insert materials, to maximize sample chamber stability and minimize heat loss during heating (for Mössbauer melting experiments). When necessary, a few ruby ( $\text{Al}_2\text{O}_3$ ) spheres are loaded as secondary pressure markers, so the pressure can be monitored off-line without X-rays. The placement of the ruby sphere is tricky. First, the ruby sphere should be placed close to the sample, so as to eliminate the influence of the pressure gradient within the sample chamber. Ruby is a relatively absorbing material at  $\sim 14.4$  keV (attenuation length: 470  $\mu\text{m}$ ). For NRIXS experiments, ruby may reduce the counting rate of the inelastic signal, so the ruby spheres should be placed away from the directions of detectors. In laser heating experiments, ruby might react with the sample at high temperatures, so the ruby spheres are loaded close to, but not in contact with the sample. In some experiments, the pressure in the sample chamber is also monitored using the high-frequency Raman edge of the diamond at the center of the culet (*Akahama and Kawamura, 2006*). When it is possible to collect X-ray diffraction patterns of our sample, our final reported pressures are based on our *in-situ* measured unit cell volumes of the sample and do not depend on the diamond edge or ruby fluorescent gauges.

The loading of pressure transmitting media varies with experiments. Pressurized noble gasloading facilities are available in the Diamond Anvil Cell Laboratory at Caltech, and at the GeoSoilEnviro-CARS (GSECARS) sector of the Advanced Photon Source (*Rivers et al., 2008*). Pressurized noble gases provide the most hydrostatic environment at pressures higher than 10 GPa (*Jacobsen et al., 2008; Zhuravlev et al., 2010; Zhang et al., 2011*), and is therefore preferable for X-ray diffraction and nuclear resonant scattering experiments at room temperature. The pressurized noble gases are loaded after the sample and rubies are loaded. The pressure transmitting medium is different for Mössbauer melting experiments. Because diamond is a good thermal conductor, thick solid pressure media are required to isolate the sample from the diamonds. For high temperature experiments, KCl plates are used and serve as both the pressure-transmitting medium and the thermal insulator. The KCl plate is made by placing KCl grains between two parallel diamond culets in a cell and compressing. Desired KCl plate thicknesses are 10-15  $\mu\text{m}$ . Two KCl plates are loaded between the sample and the culets on both sides to form a sandwich-like structure (Figure 1.3). The procedures for loading this sandwich-like configuration are slightly different from loading noble gases. First, a

KCl plate that fits the gasket hole size is loaded in the center of the hole; then the sample is placed on top of the KCl plate in the center; finally, a second KCl plate is loaded centered right above the sample. When one closes the diamond anvil cell, the sample is sealed by KCl and thus isolated from the gasket or diamond culets. KCl is transparent to the 1064 nm infrared laser, and the sample can be laser-heated to high temperatures ( $>2000$  K). All experiments described in this thesis were performed with pressure transmitting media. Neon was used for high pressure X-ray diffraction and nuclear resonant scattering studies on enstatite at 300 K, and KCl was used for the Mössbauer melting experiments on Fe and  $\text{Fe}_{0.9}\text{Ni}_{0.1}$ .

To close the diamond anvil cell and increase the pressure, one uses the tightening screws (Figure 2.1 #9). In most of the symmetric and panoramic diamond anvil cells, there are four tightening screws, two of them are right-handed, and the other two are left-handed. Each pair of left-handed and right-handed screws are on opposite sides in the diamond anvil cell (Figure 2.1 #1), and when increasing pressure, one should turn a right-handed and left-handed tightening screw on opposite sides simultaneously with the same angle, so as to apply uniform forces to the diamonds, which improves the stability of the sample chamber with compression. Sometimes 3-pin diamond anvil cells are used in experiments. To generate high pressure in 3-pin diamond anvil cells, in each pressure step one should turn the 3 tightening screws with the same small angular increment ( $\sim 1^\circ/\text{turn}$ ) to achieve a uniform force as much as possible. The mounting putty is removed once the diamond anvil cell engages pressure to avoid: the absorption of the nuclear resonant inelastically scattered photons, and any potential contamination during Mössbauer melting experiments.

## 2.2 Experiments using synchrotron radiation

### 2.2.1 X-ray powder diffraction

#### *Principles*

Powder X-ray diffraction is a relatively mature technique for high pressure research. It has been broadly used to constrain and determine the crystal structure of the sample at high pressures (e.g., Zhang *et al.* 2012, Zhang *et al.* 2013a, Lavina *et al.* 2014 and Zhang *et al.* 2014) and to determine the sample's pressure *in-situ* (e.g., Dewaele *et al.* 2006; Murphy *et al.* 2013; Komabayashi *et al.* 2012). The loss of the diffraction peaks and appearance of diffuse scattering has also been used to constrain the sample's melting point (e.g., Anzellini *et al.* 2013). X-ray diffraction is an elastic and coherent scattering process that can be described by Bragg's law (Figure 2.4 inset):

$$2d\sin\theta = n\lambda \tag{2.1}$$

where  $d$  is the distance between crystallographic planes,  $\lambda$  is the wavelength of the incident X-ray,  $\theta$

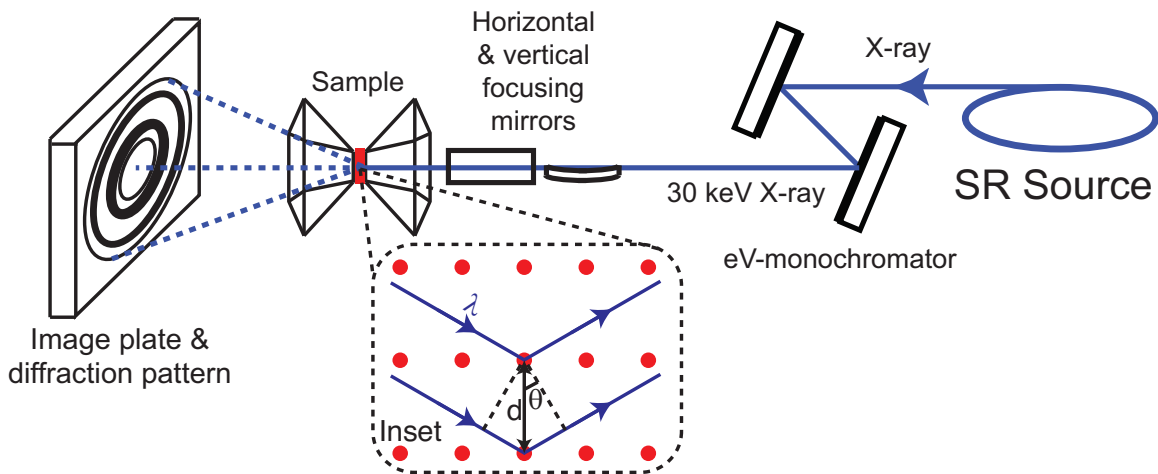


Figure 2.4: Principles and instrumentation of X-ray powder diffraction experiments at Sector 12.2.2 (ALS). X-ray photons (30 keV, 0.4133 Å) from the synchrotron source are first filtered by monochromator to eV bandwidth, and then focused to  $\sim 10 \times 10 \mu\text{m}^2$  on the sample. At Sector 3-ID-B (APS), the X-ray photons have a energy of 14.4125 keV ( $\lambda = 0.8603 \text{ \AA}$ ) and a bandwidth of 1 meV. The diffracted photons are collected by the image plate. Inset: the principle of diffraction (Bragg's law):  $n\lambda = 2d\sin\theta$ .

is the diffraction angle and  $n = 1, 2, 3, \dots$  (Bragg 1913, 1967). Each X-ray diffraction pattern provides the intensity of the scattered X-ray photons as a function of  $\theta$ , and with  $\lambda$  fixed by the beamline monochromator, one can calculate the  $d$ -spacing for different Miller indices, and obtain the unit cell volume of the sample.

#### Experiments

One of the principal hardware components for synchrotron based powder X-ray diffraction at both sector 12.2.2 at the Advanced Light Source and 3-ID-B at the Advanced Photon Source is the MAR3450 image plate, which features low background and high sensitivity and allows for high-statistical quality with low-energy ( $E < 100 \text{ keV}$ ) X-ray diffraction. Sector 12.2.2 is equipped with a Si(111) monochromator, which has an energy range of 6 to 40 keV, and a sample-detector distance of  $\sim 200 \text{ mm}$ . For our experiments in the symmetric diamond anvil cell, we used  $E = 30 \text{ keV}$  ( $\lambda = 0.4133 \text{ \AA}$ ), and determined the sample-detector distance with high accuracy using a  $\text{LaB}_6$  standard. Together with a X-ray transparent cBN backing plate in the downstream position and angular opening in the diamond anvil cell of  $57^\circ$ , one has access to a maximum  $2\theta$  range of  $\sim 30^\circ$  ( $0.8 \text{ \AA} \leq d \leq 25 \text{ \AA}$ , the upper bound comes from the beam-stop).

Sector 3-ID-B is optimized for nuclear resonant scattering experiments, and is also equipped for in-line X-ray diffraction. The MAR3450 image plate is positioned between the sample stage and the forward scattering detector, and can be moved in and out of the X-ray path to allow for in situ X-ray diffraction before and after an nuclear resonant scattering experiment (Figure 2.5). The incident energy for this in situ X-ray diffraction is dictated by the nuclear resonant scattering technique,

which requires an incident X-ray energy equal to that of the nuclear resonant energy of  $^{57}\text{Fe}$  ( $E = 14.4125 \text{ keV}$ ,  $\lambda = 0.86025 \text{ \AA}$ ). The sample-detector distance is  $\sim 300 \text{ mm}$ , and is determined during each experimental run from the calibration procedure using a  $\text{CeO}_2$  standard. This suggests a maximum  $2\theta$  of  $28.5^\circ$  ( $d \geq 1.75 \text{ \AA}$ ), which would corresponds to the maximum pressure at which the (101) diffraction peak for  $\epsilon\text{-Fe}$  is accessible of  $\sim 100 \text{ GPa}$ . However, by positioning the MAR3450 image plate at a horizontal offset of 35mm from a centered alignment with the X-ray beam, we were able to increase the maximum accessible  $2\theta$  to  $33^\circ$  ( $d \geq 1.51 \text{ \AA}$ ). This new  $2\theta$  corresponds to a pressure from the (101) diffraction peak of  $\epsilon\text{-Fe}$  that is well beyond that of the center of the Earth (*Murphy et al.*, 2011, 2013).

To carry out the X-ray diffraction measurement, the first step is to remotely locate the sample in the X-ray's focus. This step is usually carried out with a 3-dimensional translation stage system, a zoom camera and a point detector (pin-diode or APD) to measure the X-ray's intensity. The X-ray is first focused on a thin YAG scintillator plate ( $\sim 300 \mu\text{m}$  thick) so that the camera can capture its fluorescent image. The camera is then zoomed in, focused and centered onto the X-ray's fluorescent image on the YAG scintillator plate with the translation stage system and fiducialize the image with the position of the X-rays. Then, the YAG scintillator plate is replaced by the sample in the diamond anvil cell, and we focus and center the sample's image in the camera using the translation stage system while keeping the camera fixed. A diamond correction is then made by moving the sample toward the propagation direction of the X-ray to compensate for the diamond's index of refraction. The value of the diamond correction varies with the diamond height used in the experiment. In our case, the diamonds are  $\sim 2 \text{ mm}$  thick, thus correction is around 1.15 mm. Then, the camera is moved out of the X-ray's path and the point detector is moved in. Then, we scan the sample horizontally and vertically to fine-tune the sample's position relative to the center of the X-ray. This fine-tune step is only possible when the sample's absorption of the incident X-ray is significantly different from the gasket or the pressure medium. In some X-ray diffraction beamlines, the sample position relative to the stage rotation center is also fine-tuned by rotating and scanning the diamond anvil cell horizontally. If the sample's horizontal center doesn't change with and without the rotation, the sample is co-axial with the horizontal rotation axis. The rotation is applied when one needs to increase the  $2\theta$  range of the X-ray diffraction patterns, or to remove strong diffraction peaks of the diamond single crystal.

After placing the sample in the desired location, X-ray diffraction data collection can be started. Usually the data collection starts with erasing the image plate without X-rays (shutters closed) to remove the influence of previous exposures. Then, the X-ray shutter is opened to expose the image plate. Depending on the sample, the X-ray and the detector, the exposure time ranges from a few seconds to tens of minutes. After the exposure, the image plate is read and the diffraction image is saved. The data processing procedures are described in Chapters 4-6.

## 2.2.2 Nuclear resonant scattering of synchrotron radiation

### *Principles*

Due to iron's abundance and importance in the Earth, a wide variety of experimental methods have been developed to investigate iron-bearing minerals' structural, vibrational and thermodynamic properties, among which synchrotron Mössbauer spectroscopy (*Mössbauer*, 1962) or nuclear resonant scattering is of specific interest.

Nuclear resonant scattering of synchrotron radiation is made possible based on two physical principles. First, at the resonant energy of a particular Mössbauer isotope, the scattering cross section of the nuclei can be much larger than that of the electrons. For electronic scattering, the Thomson-scattering cross section for electromagnetic radiation by a point charge is given by

$$\sigma_T = \frac{8\pi}{3} \left( \frac{q^2}{mc^2} \right)^2 \quad (2.2)$$

Where  $\sigma_T$  is the Thomson-scattering cross section,  $q$  is the charge,  $m$  is the mass of the particle, and  $c$  is the speed of light. For non-resonant incident X-ray, the scattering strength of the nucleus compared to the electron shell is then reduced by a factor of  $(Zm/M)^2 \approx 10^{-7}$ , where where  $m$ ,  $M$  are the masses of the electron and nucleus, and  $Z$  is the atomic number (*Sturhahn*, 2004). However, for "resonant X-rays", the nuclear resonant cross section becomes

$$\sigma_N = \frac{\lambda^2}{2\pi} \frac{1}{1 + \alpha} \frac{2I' + 1}{2I + 1} \quad (2.3)$$

Where  $\lambda$  is the wavelength of the resonant photon,  $\alpha$  is the internal conversion coefficient, and  $I$ ,  $I'$  are the spins of the nuclear ground and excited state. Take  $^{57}\text{Fe}$  as an example ( $\alpha = 8.6$ ,  $I = 1/2$  and  $I' = 3/2$ ), at its resonant energy (14.4125 keV), the nuclear resonant cross section  $\sigma_N = 2.56$  Mb,  $\sim 450$  times larger than the electronic cross section (*Sturhahn and Jackson*, 2007). Second, compared with the electronic energy levels, the nuclear energy level bandwidth is much narrower, and as a result of the Heisenberg's relationship ( $\tau\Gamma = \hbar$ ), the lifetime of nuclear resonant transition can be much larger than the electronic transition (*Sturhahn*, 2004; *Sturhahn and Jackson*, 2007). For  $^{57}\text{Fe}$ , the bandwidth of the nuclear resonant transition energy level ( $\Gamma$ ) is 4.66 neV, and its lifetime ( $\tau$ ) is 141 ns. The long lifetime of the nuclear resonant transition makes it possible to remove electronic scattering processes from the observed signal using a mechanism called "time-discrimination", that is, collecting only the scattered photons that are delayed after a certain amount of time ( $\sim 20$  ns) from the incident X-ray bunch (*Sturhahn and Jackson*, 2007). This delayed signal is dominated by photons from nuclear resonant scattering. The isotopes that can be measured with the nuclear resonant scattering techniques at Sector 3 at the Advanced Photon Source of the Argonne National Laboratory are listed in Table 2.1 (*Sturhahn*, 2004). At Sector 30 of the APS,  $^{119}\text{Sn}$  can be measured

Table 2.1: List of Mössbauer isotopes with nuclear transitions that are feasible for nuclear resonant scattering experiments at Sector 3 at the Advanced Photon Source. Values come from *Sturhahn* (2004)

Isotope	$E_0$ (keV)	$\lambda$ (Å)	$\tau$ (ns)	Strength
$^{83}\text{Kr}$	9.404	1.32	212	0.2
$^{57}\text{Fe}$	14.4125	0.86	141	1
$^{151}\text{Eu}$	21.541	0.58	14	0.63
$^{119}\text{Sn}$	23.88	0.52	25.7	6.7
$^{161}\text{Dy}$	25.651	0.48	40.5	1.2

$E_0$ : transition energy.  $\tau$ : lifetime for the excited nuclear state. The strength for each isotope is estimated by  $\Gamma\sigma_n/\sigma_e$  and then divided by the value for  $^{57}\text{Fe}$ , where  $\Gamma$  is the width of the excited nuclear state,  $\sigma_n$  is the nuclear resonant cross section, and  $\sigma_e$  is the photoelectric resonant cross section.

now. Nuclear resonant scattering can only be carried out at the APS, because it has the optimal bunch structure (153 ns interval between two X-ray bunches for top-up mode) and spectral flux ( $10^{15}$  photon  $\text{sec}^{-1} \text{ev}^{-1}$  at 14.4 keV). In comparison, the time interval between two bunches in ALS is only 2 ns, and the spectral flux at 14.4 keV is only  $10^{11}$  photon  $\text{sec}^{-1} \text{ev}^{-1}$ . The high spectral flux from the APS significantly reduces the data collecting times, the required amount of sample containing the Mössbauer isotope, and pressure gradients in the measured data, making high-quality high-pressure nuclear resonant scattering measurements of iron-bearing samples possible (e.g., *Sturhahn* 2004; *Sturhahn and Jackson* 2007; *Zhang et al.* 2011).

The nuclear resonant scattering technique includes two independent methods: synchrotron Mössbauer spectroscopy and nuclear resonant inelastic X-ray scattering. Both methods capture the delayed photons scattered by the resonant nuclei. Synchrotron Mössbauer spectroscopy detects the delayed photons in the forward direction, and the spectrum is time-resolved (0.05ns resolution). Synchrotron Mössbauer spectroscopy provides information like hyperfine parameters and magnetic properties similar to conventional Mössbauer spectroscopy, but eliminates the  $^{57}\text{Co}$  source broadening to the spectra.

Recently, synchrotron Mössbauer spectroscopy has been applied to detect the solid-liquid boundary of Fe at high pressure (*Jackson et al.*, 2013). The physical parameter of interest is the dimensionless Lamb-Mössbauer factor:

$$f = e^{-k^2 \langle x^2 \rangle} \quad (2.4)$$

where  $k$  is the wave vector of the incident resonant X-ray photon, and  $\langle x^2 \rangle$  is the mean-square displacement of the resonant nuclei. The Lamb-Mössbauer factor is a finite value for solid material, and drops to zero for liquids (*Mössbauer*, 1962). By monitoring the Lamb-Mössbauer factor as a function of temperature, it is possible to constrain the melting points of Mössbauer isotope-bearing materials under extreme conditions using synchrotron radiation (*Jackson et al.*, 2013). Chapters 5 and 6 explore this method further and apply it to compressed Fe and  $\text{Fe}_{0.9}\text{Ni}_{0.1}$ .

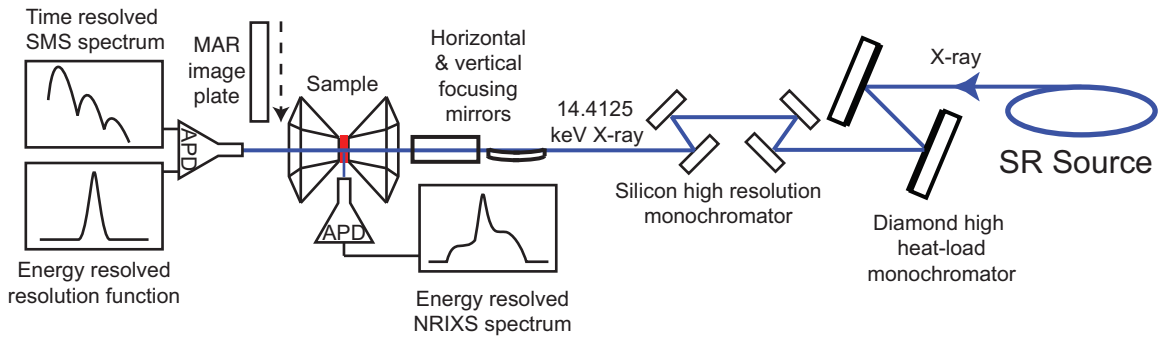


Figure 2.5: Basic experimental setup for nuclear resonant scattering experiments at 3-ID-B (AP-S). SR: synchrotron radiation source; Diamond high heat-load monochromator filters the X-ray to eV bandwidth. Silicon high resolution monochromator filters the X-ray to  $\sim 1$  meV bandwidth. Horizontal and vertical focusing mirrors focus the X-ray beam to  $10 \times 11 \mu\text{m}^2$ . APD: avalanche photo diode detector used to collect scattered photons. MAR image plate: detector used to collect diffraction patterns. The MAR image plate can be moved in and out of the X-ray path.

In the case of nuclear resonant inelastic X-ray scattering (NRIXS), the scattering process is inelastic and incoherent. NRIXS captures the scattered photons perpendicular to the propagation direction of the incident X-ray as well as scattered photons in the forward direction, and the collected spectra are energy-resolved (1 meV resolution). Nuclear resonant inelastic X-ray scattering provides information concerning the vibrational dynamics of materials, and can be used to measure the sound velocities of materials (*Zhang et al.*, 2013a; *Murphy et al.*, 2013). In comparison with experimental techniques that have also been used to probe sound velocities, such as Brillouin spectroscopy, ultrasonic interferometry, and impulsive stimulated light scattering, nuclear resonant inelastic X-ray scattering provides additional information via the partial projected phonon density of states, such as the mean-square displacement of the iron atoms and average force constant of the iron sub-lattice (*Sturhahn*, 2004; *Jackson et al.*, 2009; *Zhang et al.*, 2013a). A high energy resolution X-ray monochromator and time discrimination are necessary to conduct nuclear resonant scattering experiments, because the energy width of the nuclear resonant level is on the order of neV ( $\Gamma = 4.66$  neV for  $^{57}\text{Fe}$ ), whereas the best energy resolutions of X-ray optics are in the  $100 \mu\text{eV}$  regime (*Toellner*, 2000). Increasing the energy resolution improves the quality of nuclear resonant scattering data, and avoids the detector to be saturated by photoelectric background. The high energy resolution monochromator determines the energy resolution of nuclear resonant inelastic X-ray scattering experiments.

#### *General sample preparation*

A brilliant, continuous spectrum of photons is produced by insertion devices at 3rd-generation synchrotron radiation sources, such as the Advanced Photon Source. To select out the X-rays with the necessary energy for NRS experiments, the beam first passes over a diamond (111) high-heatload monochromator, which selects for a narrow band of wavelengths around the nuclear transition energy

of  $^{57}\text{Fe}$  with a resolution ( $\Delta E$ ) of  $\sim 1$  eV. Next, the beam passes over a Si multireflection high-resolution monochromator, which selects an X-ray energy of 14.4125 keV with  $\Delta E \sim 1$  meV (*Toellner*, 2000). Finally, the beam is focused onto the sample using Kirkpatrick-Baez mirrors, which produce a focused spot size of  $\sim 10 \mu\text{m} \times 11 \mu\text{m}$ . Delayed scattered photons from nuclear resonances are detected by avalanche photodiode (APD) detectors positioned radially around and close to the sample in the case of NRIXS. In addition, the energy resolution function is determined via a fourth APD, which is placed in the forward-scattering direction. In the case of SMS experiments, there is only one APD used downstream from the sample. An X-ray diffraction image plate can be moved into and out of the beam's path to collect in situ X-ray diffraction.

The following procedures for collecting a nuclear resonant scattering dataset are specific to Sector 3-ID-B of the Advanced Photon Source, and assumes that the X-ray beam is already optimally aligned and focused. In addition, it assumes the monochromator has been tuned so that the energy of the incident X-rays is near the nuclear resonance energy of  $^{57}\text{Fe}$  (14.4125 keV). Finally, it assumes the placement of an APD detector in the forward scattering position, which will measure the energy resolution function during the NRIXS experiment.

The first step is to prepare the diamond anvil cell to be mounted on the sample stage. Similar to X-ray diffraction, before the X-ray shutter is opened, one initially locates the sample using a microscope that has been aligned with the X-ray spot in all dimensions. Once the sample is approximately focused in the aligning microscope, a diamond correction is made to account for the index of refraction of the diamond. After recording the approximate position of the sample, one can open the X-ray shutter and check whether any delayed signal is being registered on the APDs. If there is little to no signal, the first step is to tune the monochromators to ensure the energy of the beam is on resonance, i.e., 14.4125 keV. The fine-tune of energy can be assisted by inserting a large piece of  $^{57}\text{Fe}$  foil into the X-ray's path, so that one is sure that there is resonant material in the X-ray focus, and then optimize the delayed counts in the downstream APD. Once the energy of the X-rays have been optimized, one can scan the position of the sample stage in the horizontal and vertical directions, to align a very reproducible spot on the sample that has high counting rates; this often corresponds to the center of the sample. The energy of the beam is further tuned to fully optimize the energy of the X-rays and, in turn, the counting rates. Finally, the background that is being measured by the APDs is checked by allowing them to count for 100 seconds at an energy that is 200 meV below the resonance energy, because the background is minimized on the anti-Stokes side. If the number of background counts is too high ( $> 0.1$  Hz), then it is likely that the timing window of the detectors needs to be adjusted because photons are spilling over from the prompt signal (electronic scattering). Specific experimental procedures are different for the time-resolved SMS measurement to determine hyperfine parameters, the energy-resolved NRIXS measurement, and SMS melting.

*Synchrotron Mössbauer spectroscopy*

For SMS measurements, after the general sample alignment, the timing window of the detectors should be checked to ensure optimal counting rate and minimal noise for SMS. The timing window is usually  $\sim 15$ - $140$  ns. The timing window should be chosen to remove the prompt signal as much as possible. If timing windows are correct but the noise signal remains without any incident X-rays, the detector itself likely needs to be replaced or repaired. It is also important to check whether any noise is being detected by the APD while the X-ray shutter is closed, since this could add significant background to the dataset. If there are significant counts on the detector, the detector should be checked to ensure it is optically sealed. After that, one can start the procedures of SMS data collection.

For SMS measurements, one should use the MCA counter to collect the integrated time-resolved signal. During the data collection, one should tune the energy so that the delayed counts are maximized, while the electronic prompt signal is not saturating the APD (prompt  $< 6,000,000$  Hz). If the prompt signal is saturating the APD, an aluminium absorber should be inserted to protect the APD. Usually the SMS collection time is between 5 minutes and 1 hour. Sometimes a thin stainless steel foil is inserted in the downstream direction of the sample to constrain the isomer shift. Details about the SMS data processing with CONUSS software package are described in Chapter 3.

*Nuclear resonant inelastic X-ray scattering*

Before the NRIXS measurement, the putty that supported the Be gasket during indentation and sample loading must be removed in order to maximize the counting rates, since leftover putty will absorb scattered photons. Next, it is recommended that a mark be made on the diamond anvil cell to note upward direction, for consistency between measurements. For NRIXS measurements, the three APD detectors should be positioned as close to the sample as possible ( $\sim 5$  mm away). Similar to SMS measurements, it is important to check whether any noise is being detected by the APDs while the X-ray shutter is closed, since this could add significant background to the dataset. If there are significant counts on any of the detectors, the detectors should be checked to ensure they are optically sealed, or electrically insulated from the diamond anvil cell and not being torqued. Then, one needs to adjust the timing window. For NRIXS, the timing window is usually  $\sim 25$ - $130$  ns. Finally, the sample mount can be placed in the path of the X-ray beam, to begin the procedures of NRIXS data collection.

To begin an NRIXS measurement, the parameters of a single scan are assigned, including the energy range around the nuclear resonance energy to be scanned; the number of points to be collected over that energy range (i.e., the energy step size); and the amount of time for data collection at each energy step. The energy can drift over time due to temperature changes, so a scan time of  $\sim 1$  hour is ideal. This allows for the optimization of the energy between scans to ensure a high-quality dataset. Finally, individual scans are summed together after as many scans as are necessary to produce

the desired number of counts have been collected. Details about the NRIXS data processing with PHOENIX software package are described in Chapter 4.

### *SMS melting*

Similar to NRIXS measurement, the putty is also suggested to be removed for SMS melting experiments to avoid pollution of the sample. Then, it is recommended to mark the upward direction of the sample. For melting experiments with rectangular shaped sample, the upward direction must be parallel to one pair of the sample's edges, which is important to aligning the X-ray with the laser hotspot. The diamond anvil cell can then be secured in the sample holder. After that, there is another step to set up an ion-chamber right in front of the downstream APD to measure the X-ray's flux after interacting with the sample. The timing window of SMS melting experiment is usually  $\sim 15$ -140 ns. Similarly, it is also important to check whether any noise is being detected by the APD while the X-ray shutter is closed.

The major setup of the SMS melting experiment is similar to that of the room temperature SMS measurement, except for setting up a laser power scan before melting. In a melting measurement, one scans the laser power from low to high values until very high temperatures are reached, and record the temperature of the sample, the integrated delayed counts per 3 seconds, and the ion-chamber's reading. 300 K SMS spectra are collected before and after melting on the same sample spot, and one high temperature SMS spectrum is collected right before melting to constrain the effective thickness of the sample. Details of the SMS melting experiments and data procession with SIMX software can be found in Chapters 5-6.

## Chapter 3

# Local structure variations observed in orthoenstatite at high-pressures

### 3.1 Introduction

The pyroxene group is an abundant mineralogical component in the Earth's top 400 km silicate shell and exists in the Earth in two major forms: orthopyroxene (Opx) and clinopyroxene. The common space group for Opx is  $Pbca$ , although experiments and theoretical simulations show the possibility of other forms, such as phases with space group  $Pbcn$ ,  $Cmca$ ,  $Ibca$  or  $P2_1ca$  (Yang and Ghose, 1995; Jackson *et al.*, 2004; Jahn, 2008). Clinopyroxene (Cpx) can be further divided into low-pressure clinopyroxene (LP-Cpx, with space group  $P2_1/c$ ) and the non-quenchable high-pressure clinopyroxene (HP-Cpx, with space group  $C2/c$ ). Although some of these symmetries of Ca-poor pyroxene have been demonstrated in both laboratory and natural occurrences, Opx is one of the most abundant. Opx comprises anywhere from 5% to 40% by volume of rocks in the Earth's crust and upper mantle (e.g., Ringwood 1979; Anderson 2007). The structural transitions observed in pyroxenes at elevated pressures and temperatures have been thought to provide explanations of geophysical observations in the upper mantle, such as the "X-discontinuity" at approximately 240 to 340 km depth (8 to 11 GPa and  $\sim 1350$  to  $1450$  °C) (Woodland, 1998; Akashi *et al.*, 2009) and low-velocity regions (Jackson *et al.*, 2004; Reynard *et al.*, 2010). However, seismological studies indicate that the depth of the "X-discontinuity" cannot be explained by a single Clapeyron slope (Deuss and Woodhouse, 2002), and several studies on Opx at high-pressures have yielded different results regarding the micro- and macroscopic details of the transition. In the iron-rich end-member,  $Fe_2Si_2O_6$  ferrosilite, a  $Pbca$  to  $C2/c$  transition was observed to occur at 4.2 GPa and 300 K (Hugh-Jones *et al.*, 1996). In other iron-rich Ca-poor pyroxenes,  $Pbca$  is also thought to transform into  $C2/c$  at high-pressures (Hugh-Jones *et al.*, 1994, 1996; Woodland and Angel, 1997; Woodland, 1998). In Mg-rich orthopyroxenes or orthoenstatites (Oen), the observations have been much more diverse. A

---

<sup>0</sup>Revised over what was previously published as Zhang *et al.* (2011)

Raman spectroscopy study on orthoenstatite  $\text{Mg}_2\text{Si}_2\text{O}_6$  showed a transition occurred at 9 GPa and 300 K and suggested that the new Raman pattern was consistent with a transition to  $C2/c$  (Hugh-Jones *et al.*, 1997). Results on  $\text{Mg}_2\text{Si}_2\text{O}_6$  using X-ray diffraction (Kung *et al.*, 2004; Lin *et al.*, 2005), ultrasonics (Kung *et al.*, 2004, 2006), and Raman spectroscopy (Lin, 2003; Lin *et al.*, 2005) claim the observed high-pressure behavior in  $\text{Mg}_2\text{Si}_2\text{O}_6$  is not consistent with a structural transition to  $C2/c$ , however the symmetry of the high-pressure phase could not be unambiguously determined. Recent molecular dynamics simulations and first principles electronic structure calculations suggest that at room-temperature,  $Pbca$ -structured  $\text{Mg}_2\text{Si}_2\text{O}_6$  may produce metastable displacive transitions to  $P2_1ca$  (at  $\sim 9$  GPa) and  $Pbca$  at  $P > 20$  GPa (Jahn, 2008). These symmetries, however, have not been experimentally identified. Due to the relative abundance of Opx in the upper mantle and potential to explain geophysical observations, a better understanding of its high-pressure behavior is needed.

Investigations on the pressure-dependences of the site specific behavior of  $\text{Fe}^{2+}$  cations in pyroxenes can provide insight to the nature of its phase transitions and can be accurately attained using Mössbauer spectroscopy. Conventional Mössbauer spectroscopy determines the hyperfine parameters and has been applied to understand pyroxenes under ambient pressure conditions (e.g., Domeneghetti and Steffen 1992; Pasternak *et al.* 1992; Dyar *et al.* 2007; Klima *et al.* 2007; Jackson *et al.* 2009). Due in part to the large sample volumes required, limited photon flux and long measuring times, only one high-pressure study was carried out on iron-bearing pyroxenes using conventional Mössbauer spectroscopy (e.g., McCammon and Tennant 1996). In this particular study, the pressure response of iron's hyperfine parameters in  $\text{Fe}_2\text{Si}_2\text{O}_6$  clinoferrosilite ( $P2_1/c$ ) was measured to 4 GPa (McCammon and Tennant, 1996). A structural transition to  $C2/c$  was concluded based on the observation of a step-like discontinuity of the hyperfine parameters between 1.33 and 1.74 GPa, pressures consistent with a structural transition observed in a previous X-ray diffraction study on  $\text{Fe}_2\text{Si}_2\text{O}_6$  clinoferrosilite (Hugh-Jones *et al.*, 1994). Synchrotron Mössbauer Spectroscopy (SMS) provides hyperfine parameters similar to conventional Mössbauer spectroscopy, but eliminates the  $^{57}\text{Co}$  source broadening. The high photon brilliance and the high resolution from the 3rd generation synchrotron radiation significantly reduces the data collecting times, the required amount of sample containing the Mössbauer isotope, and pressure gradients in the measured data, making high-quality high-pressure measurements of iron-bearing samples possible (e.g., Sturhahn 2004; Sturhahn and Jackson 2007). For example, high-pressure SMS measurements have been performed on silicates, such as clinopyroxene-structured  $\text{CaFeSi}_2\text{O}_6$  hedenbergite (Zhang *et al.*, 1999) and more iron-dilute silicates (Jackson *et al.*, 2005; Li *et al.*, 2006; Lin *et al.*, 2008; McCammon *et al.*, 2008; Grocholski *et al.*, 2009; Catalli *et al.*, 2010). In this study, we carried out high-pressure SMS studies on  $(\text{Mg},^{57}\text{Fe})_2\text{Si}_2\text{O}_6$  with space group  $Pbca$  as the initial phase. By using NaCl and Ne as different pressure-media in two independent experiments, we also assessed the influence of pressure media on

iron’s local site behavior.

## 3.2 Experimental procedures

### 3.2.1 Sample preparation

Powdered samples of orthoenstatite-structured  $(\text{Mg}_x^{57}\text{Fe}_{1-x})_2\text{Si}_2\text{O}_6$  with  $x = 0.87$  (En87) were prepared as  $\sim 25 \mu\text{m}$  thick pellets for high-pressure synchrotron Mössbauer spectroscopy experiments. The powdered samples in this experiment were taken from the same run that was used in a nuclear resonant scattering study at ambient conditions (*Jackson et al.*, 2009). Two symmetric piston-cylinder diamond-anvil cells (DAC) were loaded with En87 pellets for high-pressure measurements. For each cell, two Type-I diamonds with culets  $300 \mu\text{m}$  in diameter were mounted and aligned to form the anvil. Rhenium gaskets were pre-indented to  $\sim 50 \mu\text{m}$  thick, and a  $100 \mu\text{m}$  diameter hole was drilled in the center of the pre-indentation using an electrical discharge machine. One cell was loaded with the En87 sample and dehydrated NaCl as the pressure-transmitting medium (hereafter referred to as En87-NaCl). A second cell was prepared with En87 and Ne was gas-loaded (*Rivers et al.*, 2008) as the pressure-transmitting medium (hereafter referred to as En87-Ne). In each cell, a few ruby spheres ( $\sim 10 \mu\text{m}$  in diameter) were placed around the En87 pellet to determine the pressure in the sample chamber.

### 3.2.2 Synchrotron Mössbauer spectroscopy

Synchrotron Mössbauer Spectroscopy (SMS) provides detailed information on the hyperfine structure of the  $^{57}\text{Fe}$  cations in materials (e.g., *Sturhahn* 2004). The hyperfine interaction describes the splitting of nuclear energy levels as a result of the hyperfine coupling to atomic or molecular energy levels. The quantities observed which are most relevant to the current study are isomer shift (IS), quadrupole splitting (QS) and the distribution of QS. The IS is proportional to the s-electron density at the nucleus, and hence is indirectly influenced by the d-electron population in the valence shell via shielding effects. The IS thus provides information on the valence or oxidation state of the Fe cations and is always obtained in a relative sense. IS values are obtained by placing a reference absorber with known composition and thickness in the X-ray beam path near the sample. The QS is observed when an electric field of non-cubic symmetry exists around the nuclei. In general, two factors can contribute to the electric field gradient: an electron distribution in the valence shell and/or a nearby lattice environment with non-cubic symmetry. Thus, QS data yield information on local chemical environment and in an independent manner to the isomer shift. The distribution of QS has a similar effect as the full width at half-maximum of an absorption peak in conventional Mössbauer spectroscopy. However, SMS does not suffer "source related broadening", allowing one

to probe the distribution of field gradients caused only by the sample. As the QS indicates the local chemical environment of each iron cation site, the distribution of QS thus shows the variation of the local chemical environment. When the site has abundant local structure variations, usually the corresponding distribution of the QS is large. As explained in previous literature, a single doublet with certain set of IS, QS and distribution of QS in conventional Mössbauer spectroscopy produces a characteristic oscillation in the SMS time spectrum with a periodicity equal to  $2h/QS$ , where  $h$  is the Planck's constant (*Zhang et al.*, 1999). This set of hyperfine parameters is referred as an iron site because it represents a specific polyhedral Fe-containing site in the sample. If there are additional sites present, the composition SMS time spectrum will be a coherent superposition of all oscillations, where the difference in IS corresponds to the relative phase difference between each oscillation component.

The SMS experiments on En87-NaCl and En87-Ne were performed at beamlines 3-ID-B and 16-ID-D, respectively at the APS. Experiments were carried out at ambient temperature. Specific details concerning the experimental set-up have been explained previously (*Sturhahn*, 2004). In our experiment, the prompt broadband X-ray beam from the synchrotron was filtered to 1 meV (in Sector 3-ID-B) and 2 meV (in Sector 16-ID-D) bandwidths using silicon multiple-crystal Bragg reflection monochromators. A Kirkpatrick-Baez mirror system was used to obtain a vertical  $\times$  horizontal focus spot size of  $15 \times 10 \mu\text{m}^2$  at 3-ID-B and  $\sim 40 \times 60 \mu\text{m}^2$  at 16-ID-D at the full width at half maximum. The storage ring was operated in top-up mode with 24 bunches that were separated by 153 ns. An avalanche photo diode detector was placed 100 cm in the downstream direction of the X-ray focus spot to collect coherent elastic photons (the SMS signal). Accounting for detector and bunch separation related effects, we were able to observe nuclear resonant scattering in a time window of 20 to 125 ns following excitation. The isomer shift of the iron sites was determined by placing a  $^{57}\text{Fe}$  enriched stainless steel foil with a physical thickness of  $0.5 \mu\text{m}$  in the X-ray beam path in the downstream direction of the sample. The SMS spectra were collected with and without stainless steel foil with collection times of  $\sim 30$  min per spectrum. We carried out SMS measurements on En87-NaCl from ambient pressure up to 36 GPa with pressure intervals of 1-2 GPa at pressures lower than 20 GPa and pressure intervals of  $\sim 5$  GPa at higher pressures. For En87-Ne, the pressure range was 4.1 to 26.8 GPa with pressure steps of  $\sim 1.5$  GPa.

### 3.2.3 Pressure uncertainties

The pressure was determined offline using the characteristic fluorescence spectral shift of the rubies surrounding the sample (*Mao et al.*, 1986). Spectra were collected on individual rubies surrounding the sample before and after each SMS measurement to document the pressure distribution within the sample chamber and any pressure drift during the SMS measurement. The full width at half maximum (FWHM) of the R1 peak was also determined. These variables were used in our method

to characterize the pressure uncertainty. We report such an uncertainty in the form of a standard deviation. We find that for all pressures investigated, the FWHM of the R1 peak is always larger for the cell loaded with NaCl as a pressure medium than the cell loaded with a Ne pressure medium. For example, the uncertainty in pressure for the cell using NaCl medium is 2.4 GPa at  $\sim 26$  GPa, whereas the largest pressure uncertainty for the cell using Ne medium is only 0.9 GPa at  $\sim 27$  GPa. The level of non-hydrostaticity of the pressure-transmitting media is the cause of the large pressure uncertainties at high-pressures (e.g., *You et al.* 2009).

### 3.3 SMS data evaluation and results

#### 3.3.1 CONUSS with a Beam-Search algorithm

We used the CONUSS software package to evaluate the time spectra of SMS measurements (*Sturhahn*, 2000). It optimizes hyperfine parameters such as IS, QS, distribution of QS, as well as other parameters such as weights of individual sites, thickness, and scaling factor. In addition to a standard least-square algorithm guided by local parameter derivatives, we implemented a Beam-Search algorithm using random trials into CONUSS. This new procedure permitted us to explore a large parameter space and to avoid inconvenient parameter correlations during the search for a local minimum of the least-square sum. We were also able to exclude shallow local minima and reduce the potential for an erroneous identification of such minima as best fits. These complications often impede best-fit attempts using local parameter derivatives, and the Beam-Search algorithm reduced the needed real-time for fitting of the time spectra and increased the reliability of our results. We report the best-fit parameters obtained from this approach with uncertainties given at the 90% confidence level for the last reported significant digit (Tables 3.1-3.5). A correlation matrix for the fitted parameters at ambient pressure is provided in Table 3.2. The correlation matrix gives the normalized covariance between each pair of fitting parameters. Each element in the matrix shows the degree of correlation between the physical properties on the row and column of that element (1 = totally correlated, 0 = totally independent). All the diagonal elements are 1, because each physical property is totally correlated with itself. The correlation matrix is considered into calculate the fitting error.

A well-defined effective thickness allows one to determine the hyperfine parameters within the accuracy of our reported results. The effective thickness,  $\eta$  ( $\eta = \rho\sigma f_{LM}D$ ; *Zhang et al.* 1999; *Sturhahn* 2004), of each sample was calculated prior to the experiments and determined from the CONUSS fitting procedure. The calculation included the Lamb-Mössbauer factor (or recoilless fraction) determined directly from nuclear resonant inelastic X-ray scattering on a sample from the same run charge ( $f_{LM} = 0.73 \pm 0.02$ , *Jackson et al.* 2009) and the initial sample loading thickness of  $D = 23 \pm 0.02 \mu\text{m}$ , producing  $\eta = 9.7 \pm 0.6$ . This value is in excellent agreement with the values

Table 3.1: Comparison with previous conventional Mössbauer spectroscopy measurements of  $(\text{Mg,Fe})_2\text{Si}_2\text{O}_6$  orthopyroxene at ambient temperature and pressure.

	Method	Fe/(Fe +Mg)	M1 IS (mm/s)	M1 QS (mm/s)	M2 IS (mm/s)	M2 QS (mm/s)	Fe <sup>2+</sup> M1 (wt%)
This study	SMS	0.13 <sup>a</sup>	1.191(4)	2.46(5)	1.151(4)	2.22(5)	8(2)
Jackson et al. 2009	MB	0.13 <sup>a</sup>	1.19(1)	2.55(2)	1.16(1)	2.17(1)	8(2)
Pasternak et al. 1992	MB	0.10 <sup>b</sup>	1.179(2)	2.51(1)	1.147(2)	2.22(2)	NR
Dyar et al. 2007	MB	0.10 <sup>c</sup>	1.16	2.55	1.14	2.09	15
		0.20 <sup>d</sup>	1.17	2.47	1.15	2.10	16.5
		0.20 <sup>e</sup>	1.17	2.50	1.15	2.11	15.5
Wang et al. 2005	MB	0.01 <sup>f</sup>	NR	NR	NR	NR	9.3(3)
		0.16 <sup>f</sup>	NR	NR	NR	NR	5.0(3)

Notes: The differences in various reported M1 weights are likely due to different cooling rates of the sample. Values in parentheses indicate the uncertainty in the last significant digit determined by fits of the data. Fe/(Fe+Mg) is the molar fraction of iron to the total number of cations in the sample. The sum of the relative weights of the M1 and M2 sites are constrained to equal 1. The IS for M1 in the first footnote is determined from the spectrum using stainless steel foil as a reference absorber. SMS = synchrotron Mössbauer spectroscopy, MB = conventional Mössbauer spectroscopy, IS = isomer shift ( $\alpha$ -iron reference), QS = quadrupole splitting, and NR = not reported.

<sup>a</sup>  $(\text{Mg}_{0.980}\text{Fe}_{0.020(5)})(\text{Mg}_{0.760}\text{Fe}_{0.240})\text{Si}_2\text{O}_6$ .

<sup>b</sup> Sample synthesized at 1.5 GPa and 900 °C, slow quench.

<sup>c</sup> Sample synthesized at 1 atm and 950-990 °C, rapid quench.

<sup>d</sup> Sample synthesized at 1 atm and 970-980 °C, rapid quench.

<sup>e</sup> Sample synthesized at 1 atm and 950 °C, rapid quench.

<sup>f</sup> Natural sample.

Table 3.2: The error correlation matrix for the fitted parameters at ambient pressure (En87-NaCl), as reported by CONUSS

	M1 weight	M1 QS	M2 IS - M1 IS	M2 QS
M1 weight	1	-0.394	0.665	0.308
M1 QS	-0.394	1	-0.131	-0.855
M2 IS - M1 IS	0.665	-0.131	1	-0.071
M2 QS	0.308	-0.855	-0.071	1

Note: The largest correlation occurs between the QS of the two sites, which is not an unusually high correlation.

determined from CONUSS ( $\eta \approx 10$ ).

The IS values we report are referenced to a-iron in order to readily compare with commonly reported IS values from conventional Mössbauer spectroscopy. At ambient pressure, two iron sites are clearly distinguishable by their hyperfine fields, namely the M1 and M2 octahedral sites, consistent with crystal structural analysis of orthopyroxenes (*Cameron and Papike*, 1981). Within the uncertainties, all the Fe sites in the studied En87 samples can be identified as Fe<sup>2+</sup>. We note that only in the En87-NaCl data set it is possible to fit  $\sim 3\%$  of the total iron as a Fe<sup>3+</sup>-like site without increasing the  $\chi^2$  of the fits. As this site bears negligible weight to the spectra and does not improve the  $\chi^2$ , we exclude Fe<sup>3+</sup> in our fits. The dominant M2 site contributes 92% ( $\pm 2\%$ ) of the spectral weight resulting in the following chemical formula for the studied orthoenstatite (M1)(M2)Si<sub>2</sub>O<sub>6</sub>: (Mg<sub>0.980</sub>Fe<sub>0.020(5)</sub>)(Mg<sub>0.760</sub>Fe<sub>0.240</sub>)Si<sub>2</sub>O<sub>6</sub>. The relative weights of the two sites were fixed to the ambient pressure values for the high-pressure fits. The fitting results we obtained at ambient pressure agree very well with results from previous studies using conventional Mössbauer spectroscopy on a sample from the same run charge (*Jackson et al.*, 2009) and on samples with similar composition and structure (e.g., *Pasternak et al.* 1992; *Dyar et al.* 2007; *Wang et al.* 2005, Table 3.1). The high degree of Fe<sup>2+</sup> ordering observed in our sample using both conventional and synchrotron Mössbauer spectroscopic methods (*Jackson et al.* 2009; this study) is likely due to a relatively slow cooling rate experienced during the quench of our sample (e.g., *Domeneghetti and Steffen* 1992; *Wang et al.* 2005; *Dyar et al.* 2007) and is more comparable to natural orthopyroxenes (*Wang et al.* 2005; *Nestola et al.* 2008).

### 3.3.2 En87-NaCl

A two sites model representing the M1 and M2 Fe<sup>2+</sup> octahedral sites for Fe<sup>2+</sup> is a satisfactory model to fit the SMS spectra of En87-NaCl throughout the pressures investigated (ambient to 36 GPa). However, at pressures greater than 10 GPa, the SMS spectra are fit equally well using only one site to represent the behavior of iron. We discuss both models below.

Two different sets of hyperfine parameters (IS, QS, and QS distribution) were used to represent the two distinct Fe<sup>2+</sup> sites. We report the best-fit hyperfine parameters in Table 3.3. Representative spectra for En87-NaCl are shown in Figures 3.1a and 3.1b with their associated  $\chi^2$  values. Within uncertainties, the QS of both M1 and M2 sites increase with pressure up to 9 GPa (Figure 3.2). At 10.1 GPa, the QS for the M1 site decreases, while the distribution of the QS for both sites decreases. At  $P > 10.1$  GPa, the QS values of the M1 and M2 sites are roughly constant, while the distributions of QS values for the two sites increase and overlap each other (Figure 3.2), reflecting ambiguous local chemical environments for the M1 and M2 sites. The large distributions correlate with the increasing uncertainty in pressure (Table 3.3). Therefore, local structural variations corresponding to a phase transition could be inferred to occur at  $\sim 10$  GPa.

Table 3.3: The best-fit parameters for the two sites model from the SMS time spectra evaluation for En87-NaCl: (Mg<sub>0.980</sub>Fe<sub>0.020(5)</sub>)(Mg<sub>0.760</sub>Fe<sub>0.240</sub>)Si<sub>2</sub>O<sub>6</sub>

Pressure (GPa)	Pressure uncertainty (GPa)	M1 site IS (mm/s)	M1 site QS (mm/s)	Mi site QS distribution (mm/s)	M2 site IS (mm/s)	M2 site QS (mm/s)	M2 site QS distribution (mm/s)
0.0	0.0	1.191(4)	2.46(5)	0.05	1.151(4)	2.22(5)	0.05
1.7	0.2	1.196(5)	2.51(6)	0.06	1.166(5)	2.3(1)	0.12
2.4	0.2	1.22(2)	2.58(6)	0.05	1.17(2)	2.29(7)	0.05
3.0	0.3	1.23(2)	2.49(6)	0.05	1.18(2)	2.3(1)	0.13
4.3	0.4	1.22(2)	2.55(6)	0.05	1.16(2)	2.3(1)	0.12
5.6	0.5	1.19(2)	2.63(9)	0.07	1.15(2)	2.4(1)	0.10
7.4	0.7	1.20(3)	2.63(7)	0.05	1.15(3)	2.4(1)	0.11
9.0	0.8	1.20(2)	2.6(1)	0.08	1.15(2)	2.4(1)	0.13
10.1	0.9	1.14(2)	2.59(6)	0.05	1.16(2)	2.44(7)	0.06
12	1	1.11(1)	2.6(1)	0.08	1.16(1)	2.5(2)	0.12
14	1	1.13(1)	2.72(8)	0.05	1.16(1)	2.5(2)	0.15
17	2	1.15(1)	2.6(1)	0.08	1.16(1)	2.5(2)	0.16
19	2	1.15(2)	2.7(1)	0.05	1.15(2)	2.5(2)	0.13
22	2	1.18(2)	2.7(1)	0.05	1.13(2)	2.4(3)	0.17
26	2	1.12(2)	2.6(1)	0.05	1.12(2)	2.4(3)	0.19
31	3	1.15(3)	2.6(1)	0.05	1.11(3)	2.4(3)	0.19
36	4	1.11(1)	2.6(2)	0.08	1.12(1)	2.4(3)	0.21

Notes: QS = quadrupole splitting, IS = isomer shift ( $\alpha$ -iron reference). The uncertainties are given in parenthesis at the 90% confidence level for the last reported significant digit.

A slight change in trend for the IS values of both M1 and M2 sites around 3 GPa (Figure 3.2b; Table 3.3). This behavior may be due to the start of silicate tetrahedra compression by Si-O bond shortening between  $\sim 4$  and  $\sim 9$  GPa (*Angel and Hugh-Jones, 1994; Hugh-Jones et al., 1997; Taran and Langer, 2003*). The IS of both M1 and M2 sites show relatively small variations with increasing pressure. At  $P > 10$  GPa, the IS values of the M1 and M2 sites fluctuate around a common value of  $\sim 1.15$  mm/s. Such a behavior indicates the s-electron densities in the Fe nuclear position of both M1 and M2 sites become indistinguishable. With the above behavior of IS and QS values at  $P > 10$  GPa, it makes sense to reduce the fitting parameters to a one-site model (i.e.,  $M1 = M2$ ).

We applied the one site model to the datasets at all pressures and examined its validity. The physical assumption of this model is that when the M1 and M2 sites appear indistinguishable, one can allocate one set of hyperfine parameters with a broad QS distribution. In comparison with the two sites model, the one site model does not provide adequate fits to the data below 10 GPa, as indicated by the relatively high fitting  $\chi^2$ . For  $P > 10$  GPa, the fitting  $\chi^2$  of the one-site model is comparable or even slightly smaller than the two sites model (Figure 3.1b). For  $P > 10$  GPa, the QS and IS values for one iron site are approximately the site-occupancy weighted average of the two distinct sites with small negative fitting slopes as a function of pressure (Figure 3.2). The distribution of the QS in the one site model is large, a finding that is consistent with our results assuming two sites.

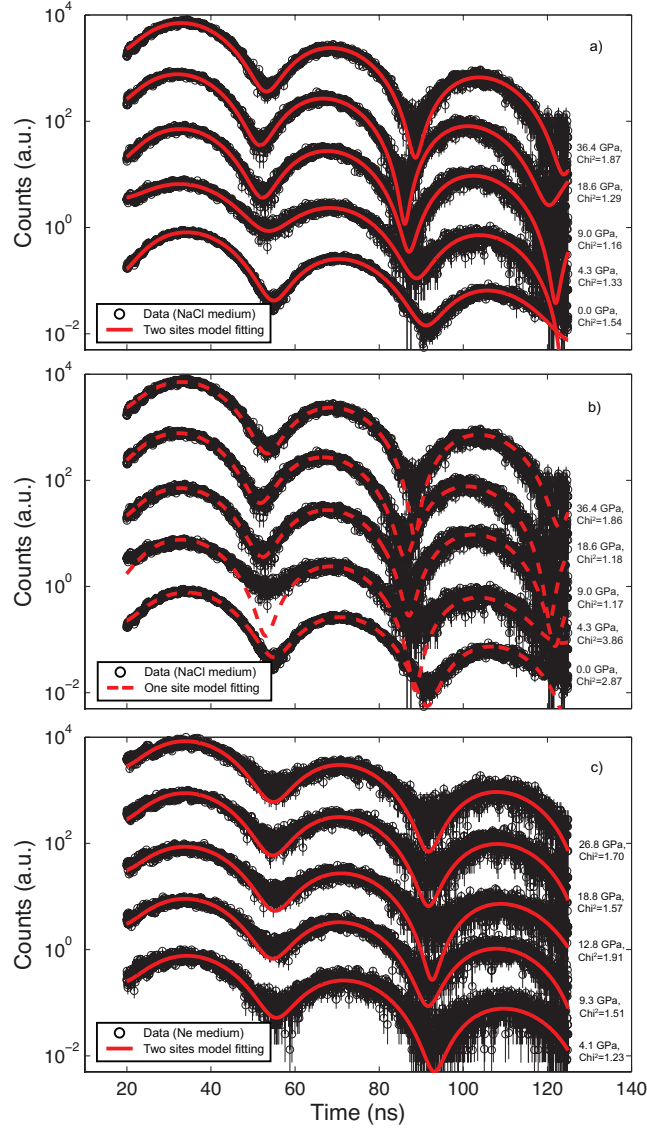


Figure 3.1: Representative SMS time spectra (grey) for En87-NaCl and En87-Ne at different pressures with best-fit parameters associated with the fitting models provided in Table 3.3-3.5. (a) En87-NaCl: best-fit two sites model (red solid lines); (b) En87-NaCl : best-fit one site model (red dashed lines). We find that the one site model fitting is not convincing below 10.1 GPa for En87-NaCl; (c) En87-Ne: best-fit two sites model. For the lowest spectrum in each panel, the actual collected number of events or counts is normalized to one. The other spectra are of similar statistical quality and have been offset by an order of magnitude for clarity. The pressure and fitting  $\chi^2$  are adjacent to each spectrum. The Poisson standard deviation is the uncertainty in counts and shown as vertical bars for each data point.

Table 3.4: The best-fit parameters for the one site model from the SMS time spectra evaluation for En87-NaCl:  $(\text{Mg}_{0.980}\text{Fe}_{0.020(5)})(\text{Mg}_{0.760}\text{Fe}_{0.240})\text{Si}_2\text{O}_6$

Pressure (GPa)	Pressure uncertainty (GPa)	IS (mm/s)	QS (mm/s)	QS distribution (mm/s)
10.1	0.9	1.16(2)	2.5(2)	0.14
12	1	1.16(1)	2.5(2)	0.22
14	1	1.16(1)	2.5(3)	0.30
17	2	1.16(1)	2.5(3)	0.30
19	2	1.15(2)	2.5(3)	0.25
22	2	1.13(2)	2.5(3)	0.21
26	2	1.12(2)	2.5(3)	0.21
31	3	1.11(3)	2.4(3)	0.15
36	4	1.08(1)	2.4(3)	0.17

Notes: Refer to Table 3.3.

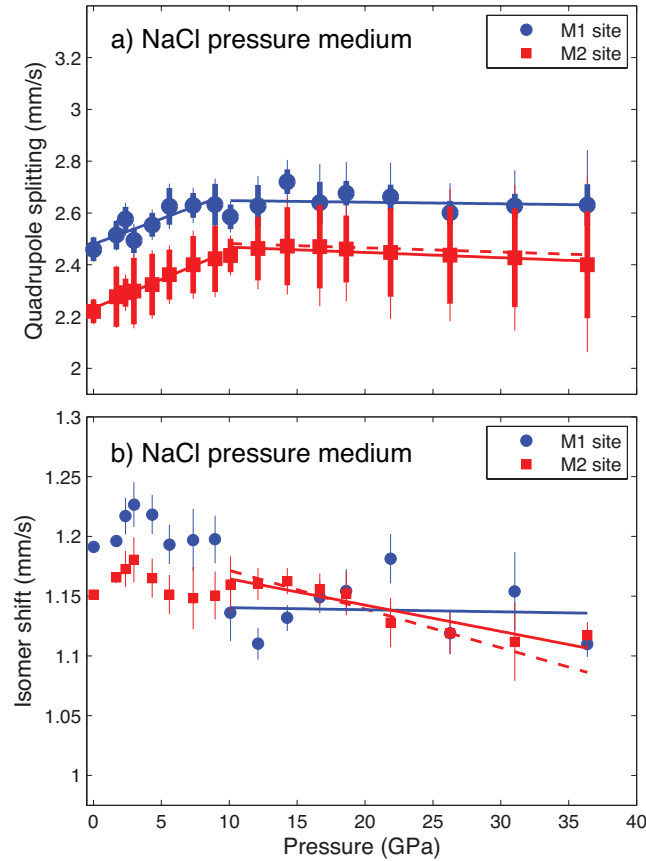


Figure 3.2: The best-fit hyperfine parameters derived from the time spectra of En87-NaCl assuming two distinct iron sites (M1 and M2) (Table 3.3). (a) Quadrupole splitting (QS) as a function of pressure, where the thick bars denote the distribution of QS and the thin bars are the fitting errors. (b) Isomer shift as a function of pressure. Note that the hyperfine parameters from the one-site model (Table 3.4) are not shown for clarity. The least-squares regression lines are guides to the eye for a sub-set of the data: two sites model (solid lines) and one site model (dashed line). Blue symbols are values and linear fits for the M1 site, and red symbols are the values and linear fits for the M2 site.

### 3.3.3 En87-Ne

In the experiments with the cell loaded with Ne as a pressure medium, the two sites model representing the M1 and M2  $\text{Fe}^{2+}$  octahedral sites provides the best fit to the SMS spectra at all pressures investigated (4.1 to 26.8 GPa) (Table 3.5, Figure 3.1c). A one site model was tested on the En87-Ne data set and resulted in non-physical fitting results. It is worth mentioning that the fitted distribution of QS values was always quite small (less than 0.02 mm/s), so we fixed this value to 0.02 mm/s.

The QS for the M1 site is not sensitive to pressure increase and therefore indicates that the local distortion of the M1 site is small at all pressures investigated here. Results from single-crystal X-ray diffraction studies on  $(\text{Mg, Fe})_2\text{Si}_2\text{O}_6$  pyroxene show that the changes in the bond lengths, octahedron volume, and distortion of the M1 site remain small from 4.7 GPa to their highest pressure investigated, 7.5 GPa (*Hugh-Jones et al.*, 1994, 1997). The QS of the M2 site increases with increasing pressure up to 10.1 GPa. At 12.8 GPa, the value drops to  $2.28 \pm 0.05$  mm/s, then continues to increase to 26.8 GPa (Figure 3.3). At  $P > 12.8$  GPa, the QS values of both sites increase at a lower rate than that observed in the lower pressure region. This may indicate a higher resistance to compression in the high-pressure phase, if the observed changes in hyperfine fields between 10.1 and 12.8 GPa are related to a structural transition.

With the exception of the M1 site at pressures lower than 10.1 GPa, the IS decreases with increasing pressure, which indicates an increase of s-electron density likely due to compression. The change of sign in the IS trend with pressure at  $P > 10.1$  GPa might be related to a local structural change.

## 3.4 Discussion

### 3.4.1 Influence of different pressure media

We carried out two independent SMS experiments, where the major difference was the pressure medium used. A softer pressure medium can provide a more hydrostatic environment, whereas a harder pressure medium may accumulate a non-hydrostatic component (*You et al.*, 2009). The degree of non-hydrostatic stress is difficult to measure directly. The shear modulus of the pressure medium serves as a relative indicator of the degree of non-hydrostaticity of the pressure medium. Ne has a shear modulus of 7.2 GPa at 6 GPa pressure (*Shimizu et al.*, 2005), whereas the shear modulus of NaCl at same pressure is 22.8 GPa (*Bartels and Schuele*, 1965). In our experiments, we infer the deviation of pressures within the sample chamber to be proportional to the degree of non-hydrostaticity (*Iizuka et al.*, 2010). The pressure uncertainties for the cell loaded with NaCl are higher than those for the sample loaded with Ne (columns in Table 3.3-3.5), suggesting that the

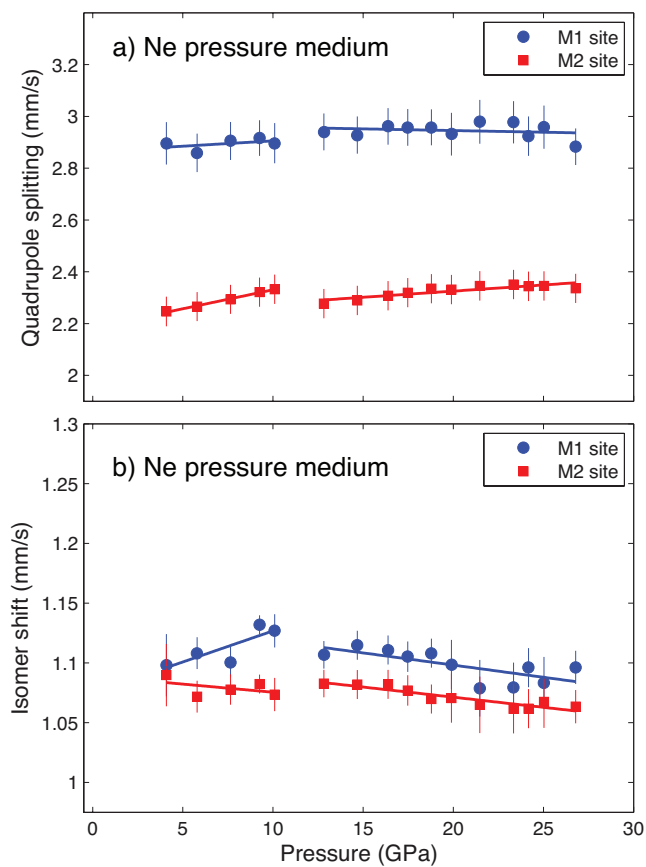


Figure 3.3: The best-fit hyperfine parameters derived from the time spectra of En87-Ne (Table 3.5). (a) Quadrupole splitting (QS) as a function of pressure, where the thin bars are the fitting errors. The distribution of QS is fixed to 0.02 mm/s. (b) Isomer shift as a function of pressure. The symbols have the same meaning as stated in Figure 3.2.

Table 3.5: The best-fit parameters for the two sites model from the SMS time spectra evaluation for En87-Ne:  $(\text{Mg}_{0.980}\text{Fe}_{0.020(5)})(\text{Mg}_{0.760}\text{Fe}_{0.240})\text{Si}_2\text{O}_6$

Pressure (GPa)	Pressure uncertainty (GPa)	M1 site IS (mm/s)	M1 site QS (mm/s)	M2 site IS (mm/s)	M2 site QS (mm/s)
4.1	0.2	1.10(3)	2.90(8)	1.09(3)	2.25(6)
5.8	0.4	1.11(1)	2.86(7)	1.07(1)	2.27(6)
7.7	0.5	1.10(1)	2.91(7)	1.08(1)	2.29(6)
9.3	0.5	1.13(1)	2.92(7)	1.08(1)	2.32(6)
10.1	0.4	1.13(1)	2.90(8)	1.07(1)	2.33(6)
12.8	0.5	1.11(1)	2.94(7)	1.08(1)	2.28(6)
14.7	0.7	1.11(1)	2.93(7)	1.08(1)	2.29(6)
16.4	0.6	1.11(1)	2.96(7)	1.08(1)	2.31(6)
17.5	0.6	1.11(1)	2.96(7)	1.08(1)	2.32(6)
18.8	0.7	1.11(1)	2.96(7)	1.07(1)	2.33(6)
19.9	0.7	1.10(2)	2.93(8)	1.07(2)	2.33(6)
21.5	0.8	1.08(2)	2.98(8)	1.06(2)	2.35(6)
23.4	0.8	1.08(2)	2.98(8)	1.06(2)	2.35(6)
24.2	0.9	1.10(2)	2.92(8)	1.06(2)	2.34(6)
25.0	0.9	1.08(2)	2.96(8)	1.07(2)	2.35(6)
26.8	0.9	1.10(1)	2.88(7)	1.06(1)	2.34(6)

Notes: Refer to Table 3.3.

NaCl pressure medium produces a larger non-hydrostatic stress environment than the Ne medium, an observation consistent with previous studies (e.g., *You et al.* 2009). In each experiment we observe an obvious change in trend or discontinuity in one or more hyperfine parameters around 10 GPa. The major differences between the two experiments are some of the pressure-derivatives of the hyperfine parameters and the observed distribution of QS. The distribution of QS in the NaCl experiment is much larger than that in the Ne experiment. Such an observation implies that, in the case of pyroxene, a broad variation in the local chemical environment is not inherent to pyroxene, but rather due to the sample environment.

### 3.4.2 Local structure variations in orthopyroxene at high-pressures

The isomer shift (IS) is determined by the s-electron density near the  $^{57}\text{Fe}$  nuclei. The primary factors influencing the IS are: 1) the valence number of the Fe cation, and 2) octahedron volume (e.g., *McCammon and Tennant* 1996; *Eeckhout et al.* 2000). If the valence number of Fe cation changes from divalent to trivalent, the IS would decrease from  $\sim 1$  mm/s to  $\sim 0.5$  mm/s (*Eeckhout et al.*, 2000). In our study the IS values for both sites are all around 1 mm/s (Table 3.3-3.5). Therefore, the dominant valence number for the Fe cation in this study is divalent (+2). The IS for most sites decrease with pressure, and is likely due to the anticorrelation between s-electron density

and the IS value (*McCammon and Tennant, 1996*).

The quadrupole splitting (QS) is strongly related to the non-cubic distortion in the Fe<sup>2+</sup>-containing octahedral sites in our experimental context. There are also two components for QS: the valence term which comes from the spatial extension of valence electron clouds, and the lattice term which demonstrates the influence of the nearby ions in the crystal lattice. The valence term will increase with increasing deviation from the initial polyhedral shape, and finally keeps at a maximum value; while the lattice term will continuously but slowly decrease with increasing deviation from the initial polyhedral shape (*Ingalls, 1964; Lin et al., 1993; McCammon and Tennant, 1996; Eeckhout et al., 2000*). For the cell loaded with NaCl as pressure medium and at pressures below 10 GPa, the QS of both M1 and M2 sites increase with pressure. This is likely due to the increase of dominant valence term, which comes from the increase in deviations from the initial polyhedral shape with compression. At 10.1 GPa, the QS of the M1 site drops relative to the low- and high-pressure trends. At pressures larger than 10 GPa, the linear fitting slope of QS of both sites change from positive to slightly negative values, indicating the valence term reached the maximum value and the change of lattice term dominates.

The most obvious feature in the QS measurement in the En87-Ne is one abrupt drop of M2 site QS is detected between 10.1 GPa and 12.8 GPa, indicating a structural transition may be occurring. We found that the M1 QS in En87-Ne is higher than in En87-NaCl. According to previous single crystal diffraction study using DAC with quasihydrostatic methanol-ethanol solution as pressure medium, the M1 octahedron is mostly compressed below 4.76 GPa (volume shrinks from 11.92 Å<sup>3</sup> in room pressure to 11.47 Å<sup>3</sup> at 4.76 GPa), and from 4.76 GPa to 7.50 GPa the volume of M1 octahedron keeps nearly constant around 11.46 Å<sup>3</sup> (*Hugh-Jones et al., 1997*). Therefore, we interpret the higher M1 QS values in En87-Ne as a result of a complete compression of M1 octahedron, which leads to a smaller M1 octahedron volume, a larger electron density to decrease the IS, and a larger valence contribution to raise the QS. Based on single crystal XRD studies up to 7.5 GPa, the M2 octahedron distorts more quickly than the M1 octahedron (*Hugh-Jones et al., 1997*). This observation could explain why the QS of the M2 site increases faster than the M1 site in both experiments (Figs. 2 and 3). One recent theoretical simulation also reveals that the M1 site will remain unchanged during select displacive transitions (*Jahn, 2008*). If these displacive transitions are the origin of the abrupt jump of the hyperfine parameters in En87-Ne, then it can explain why the QS of M1 site has a much smaller change than the QS of M2 site during this transition.

Based on the changes in values and trends of the QS around 10 GPa, there may be a structural transition occurring. The candidates for this transition include *Pbca-Cmca* or *Pbca-Ibca* displacive transitions (*Jackson et al., 2004*), *Pbca-P2<sub>1</sub>ca* or *Pbca-Pbca* displacive transitions (*Jahn, 2008*) or *Pbca-C2/c* reconstructive transition (*Kirby and Stern, 1993; Hugh-Jones et al., 1996, 1997; Kung et al., 2004; Akashi et al., 2009*). The *P2<sub>1</sub>ca* phase and isosymmetric *Pbca* phase haven't been directly

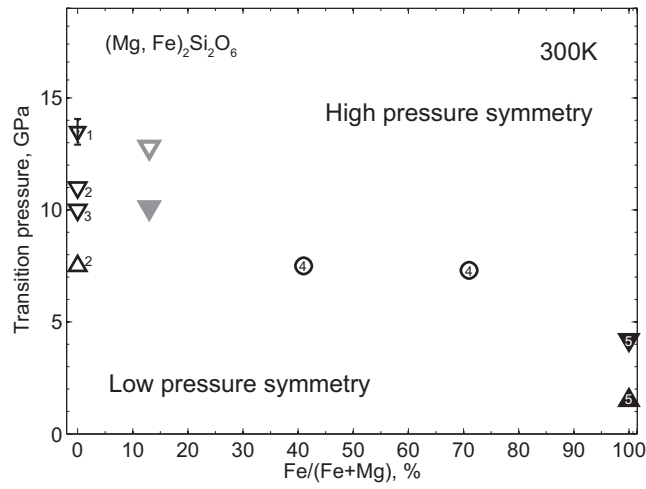


Figure 3.4: High-pressure observations and reported transition pressures from experiments using orthopyroxene with different Fe/(Fe+Mg) ratios as the starting material at 300 K. Each triangle indicates a specific reported phase transition pressure. In studies where the pressure was not high enough to observe a transition, we note where the highest pressure *Pbca* was observed with an open circle. Reverse triangles are transitioning pressures observed on compression, and normal triangles are transition pressures observed on decompression. For the iron-poor studies, the low pressure starting symmetry is *Pbca* and the high pressure symmetry hasnt been determined. For orthoferrosilite, the low pressure starting symmetry is *Pbca* and the high pressure symmetry is *C2/c*; on decompression, the low pressure symmetry was found to be *P2<sub>1</sub>/c*. We plot and list the following results (method, pressure-transmitting medium), 1: *Kung et al. (2004)* (XRD+ultrasonics, NaCl); 2: *Lin (2003)* (Raman, deionized water); 3: *Lin et al. (2005)* (XRD, deionized water); 4: *Hugh-Jones et al. (1997)* (XRD, 4:1 methanol:ethanol solution) 5: *Hugh-Jones et al. (1996)* (XRD, 4:1 methanol:ethanol solution); open gray triangle: this study (SMS, Ne); solid gray triangle: this study (SMS, NaCl).

observed in experiments. One would need X-ray diffraction data on this sample or on a sample with similar composition in this pressure range. The pressure range that we observe a discontinuity in some hyperfine parameters (10.1 to 12.8 GPa) matches with changes observed in an ultrasonics study (13 to 14 GPa) (*Kung et al., 2004*), a Raman spectroscopic study (10 to 11 GPa) (*Lin, 2003*) and an X-ray diffraction study (10.4 GPa) (*Lin et al., 2005*) using Mg<sub>2</sub>Si<sub>2</sub>O<sub>6</sub> orthoenstatite as starting material (Figure 3.4). Our observations are also reasonably consistent with atomistic simulations that predict metastable transitions in *Pbca*-structured orthoenstatite to *P2<sub>1</sub>ca* (9 GPa) or a different *Pbca* phase (14 GPa) (*Jahn, 2008*).

## Chapter 4

# Elasticity and lattice dynamics of enstatite at high pressure

### 4.1 Introduction

The upper mantle plays an important role in Earth's interior, as the interplay between this region and the lithosphere helps drive plate tectonics, which shapes the surface of Earth. The depth region between 250 and 300 km is of specific interest in this study. In this depth range, two general features from seismic observations have been identified. One feature is the horizontal variation in S-wave velocities from different seismic models. These models include global average 1-D models (PREM, *Dziewonski and Anderson* (1981), AK135, *Kennett et al.* (1995)), regional models for the western United States (TNA, *Grand and Helmberger* (1984a)), the eastern North American continent (SNA, *Grand and Helmberger* (1984a)), the North Atlantic Ocean (ATL, *Grand and Helmberger* (1984b)) and the Pacific Ocean (PAC06, *Tan and Helmberger* (2007)). However, little horizontal variation in the P-wave velocity structure for this depth range has been reported among different models, including the comparison amongst global average 1-D models (PREM and AK135), regional models for the tectonically active western United States (mT7, *Chu et al.* (2011)) and the tectonically stable eastern North American continent (CR, *Chu et al.* (2012); S25, *LeFevre and Helmberger* (1989)). These seismological models serve as important constraints on determining the composition of this region, because the elasticity of stable phase assemblages must be consistent with seismic observations. The other feature of interest in this depth range is the seismic X-discontinuity, which is a group of seismic reflections located between 240 and 340 km in depth associated with a shear impedance increase of 3-7.5% (*Deuss and Woodhouse*, 2002; *Revenaugh and Jordan*, 1991). The X-discontinuity is wide-spread, but not global, and is characterized by a large depth variation (*Deuss and Woodhouse*, 2002; *Revenaugh and Jordan*, 1991). The presence of hydrated phases in the upper mantle have been invoked to explain the X-discontinuity (*Revenaugh and Jordan*, 1991; *Jacobsen*

---

<sup>0</sup>Revised over what was previously published as *Zhang et al.* (2013a)

*et al.*, 2010). However, the X-discontinuity has been reported in regions corresponding to the underside of subducted slabs, where hydrated phases are unlikely to be present (*Woodland and Angel*, 1997; *Woodland*, 1998).

(Mg,Fe)<sub>2</sub>Si<sub>2</sub>O<sub>6</sub> enstatite is the second most abundant mineral in peridotite (*Ringwood*, 1991; *Frost*, 2008) containing about 10 to 15% Fe<sub>2</sub>Si<sub>2</sub>O<sub>6</sub>, and is one of the three most abundant components in compositional models of the deep upper mantle (*Bass and Anderson*, 1984; *Irfune and Ringwood*, 1987; *Ringwood*, 1991). The elasticity of orthoenstatite has been used to construct petrological models and compare to mantle seismic velocity structures (e.g., *Bass and Anderson* 1984; *Duffy and Anderson* 1989), and the orthoenstatite (OEN, space group *Pbca*) to high pressure clinoenstatite (HP-CEN, space group *C2/c*) transition has been suggested to explain the X-discontinuity for several reasons. The OEN to HP-CEN transition has a suitable P-T range for the X-discontinuity (~8.5-9.5 GPa along a 1400°C adiabat) (*Woodland and Angel*, 1997; *Woodland*, 1998; *Kung et al.*, 2005; *Akashi et al.*, 2009). Enstatite's abundance in proposed compositional models can explain the existence of X-discontinuity in the underside region of subducted slabs (*Woodland and Angel*, 1997; *Woodland*, 1998). The OEN to HP-CEN/majorite-garnet multivariant transition occurs over a large depth interval and is unlikely to produce a sharp seismic discontinuity, thus potentially explaining the wide variability of the X-discontinuity (*Woodland and Angel*, 1997; *Woodland*, 1998). Further, recent studies on the pressure-induced transitions of OEN have provided new information regarding the high-pressure symmetry of enstatite (*Zhang et al.*, 2011; *Jahn*, 2008; *Zhang et al.*, 2012). Though multi-anvil experiment have shown that Mg<sub>2</sub>Si<sub>2</sub>O<sub>6</sub> HP-CEN phase is the stable phase at 14 GPa and 1000 °C (*Kung et al.*, 2004), a high-pressure study on the vibrational properties of iron-bearing enstatite is still lacking. A better understanding of the high-pressure elastic properties of enstatite with a composition similar to that inferred from petrological observations is needed to make more conclusive statements linking upper mantle seismic structures with the presence of enstatite.

In this study, we present measurements of the elastic properties and lattice dynamics of (Mg,Fe)<sub>2</sub>-Si<sub>2</sub>O<sub>6</sub> enstatite using X-ray diffraction (XRD) and nuclear resonant inelastic X-ray scattering (NRIXS). XRD has been used in the past to determine the crystal structure, unit cell volume and P-V equation of state of enstatite (e.g., *Hugh-Jones and Angel* 1994; *Angel and Jackson* 2002; *Akashi et al.* 2009). NRIXS provides information concerning the lattice dynamics of a phase (*Sturhahn*, 2004), and has also been applied to OEN at ambient conditions (*Jackson et al.*, 2009). Therefore, in comparison with experimental techniques that have also been used to probe the sound velocities of enstatite, such as Brillouin spectroscopy (e.g., *Weidner et al.* 1978; *Duffy and Vaughan* 1988; *Jackson et al.* 1999, 2004), ultrasonic interferometry (*Frisillo and Barsch*, 1972; *Webb and Jackson*, 1993; *Flesch et al.*, 1998; *Kung et al.*, 2004), and impulsive stimulated light scattering (*Chai et al.*, 1997), NRIXS provides additional information via the partial projected phonon density of states (DOS), such as the mean-square displacement of the iron atoms and average force constant of the

iron sub-lattice (*Sturhahn, 2004; Jackson et al., 2009*). Further, we supplement our experimental results from NRIXS with first-principles calculations to understand how the local site symmetry of the iron atoms may affect the DOS of enstatite. Finally, we combine the elastic properties of iron-bearing enstatite determined in this study with past experimental reports on candidate phases to construct shear velocity profiles of likely petrologies in Earth’s upper mantle. We compare these profiles to global and regional seismic studies, as well as to characteristics of the X-discontinuity.

## 4.2 Methodology

Powdered starting materials of OEN-structured  $(\text{Mg}, ^{57}\text{Fe})_2\text{Si}_2\text{O}_6$  with 13 mol %  $^{57}\text{Fe}_2\text{Si}_2\text{O}_6$  (hereafter referred to as En87) were prepared for high-pressure NRIXS experiments. The starting  $^{57}\text{Fe}_2\text{Si}_2\text{O}_6$  was 95%  $^{57}\text{Fe}$  enriched. The samples in this experiment were taken from the same run charge that was used in a nuclear resonant scattering study at ambient conditions (*Jackson et al., 2009*) and high-pressures (*Zhang et al., 2011*), where the distribution of Fe in the M1 and M2 sites were determined by synchrotron Mössbauer spectroscopy giving the formula:  $(\text{Mg}_{0.980}\text{Fe}_{0.020(5)})(\text{Mg}_{0.760}\text{Fe}_{0.240})\text{Si}_2\text{O}_6$  (*Zhang et al., 2011*). Two individual diamond anvil cells (DACs) were loaded with En87 for high-pressure XRD and NRIXS measurements. We describe the DAC preparations, experimental details, and first-principles calculations below.

### 4.2.1 X-ray diffraction

For the XRD measurements, one symmetric DAC was used. Two type-I diamonds with culets 300  $\mu\text{m}$  in diameter were mounted and aligned to form the anvils. A Re gasket was pre-indented to  $\sim 50$   $\mu\text{m}$  thick and a 125  $\mu\text{m}$  diameter hole was drilled in the center of the pre-indentation using an electrical discharge machine. A  $\sim 25$   $\mu\text{m}$  thick sample ( $\sim 30$   $\mu\text{m}$  in diameter) was first compacted out of the powder, and then loaded into the gasket hole with two ruby spheres ( $\sim 10$   $\mu\text{m}$  in diameter) surrounding the sample. The DAC was then Ne gas-loaded (*Rivers et al., 2008*). After gas loading, the diameter of sample chamber shrank to  $\sim 55$   $\mu\text{m}$ . The ruby spheres were used to determine the pressure in the sample chamber below 4.6 GPa (*Mao et al., 1986*), where Ne is in the liquid state (*Shimizu et al., 2005*). We estimate the uncertainty in pressure determined using the ruby fluorescence method by computing the standard deviation of the pressure given by the different rubies in the sample chamber before and after each XRD measurement. At pressures above 4.6 GPa, Ne crystallizes and in-situ Ne volumes were used to determine the pressure via the Ne equation of state (*Dewaele et al., 2008*). As the X-ray sampled the enstatite and the Ne at the same location, using Ne pressure gauge reduced the influence of potential pressure gradients in the sample chamber (*Boehler, 2000*). Based on the positions of Ne (111) and (200) diffraction peaks, we estimate the Ne pressure uncertainty to be 0.1 to 0.2 GPa from 5.1 to 19.1 GPa (Table 4.1).

The XRD measurements were carried out at beamline 12.2.2 of the Advanced Light Source at Lawrence Berkeley National Laboratory. The energy (30 keV) and resolution (1 eV) of the X-rays were determined by a high heat load monochromator, and a focus area of  $10\ \mu\text{m} \times 20\ \mu\text{m}$  (full width at half maximum) was achieved by a Kirkpatrick-Baez mirror and clean-up slits. A high resolution MAR image plate, located in the downstream direction of the DAC with a distance of about 0.5 m, was used to collect the XRD patterns. A  $\text{LaB}_6$  standard sample was used to calibrate the sample to image plate distance and correct the tilting of the image plate. The diffraction images were integrated into angular resolved chi files using Fit2D (*Hammersley et al.*, 1996) (Figure 4.1). Diffraction peaks in the  $2\theta$  range between 7 and 12 degrees can be indexed with enstatite peaks. We used the peaks in this  $2\theta$  range to fit the unit cell volume of En87 (labeled in Figure 4.1), as this range provided enough peaks for volume refinement, avoided the interference of peaks from other material such as Ne, and had a relatively flat background. The clean-up slits reduced, but did not eliminate, the influence of X-ray intensity in the tails of the focus area. This effect combined with Re's relatively strong atomic scattering factor (*Henke et al.*, 1993) thus lead to some contribution of the Re gasket to the XRD diffraction patterns (Figure 4.1a). Diffraction peaks in the angular resolved chi files were fit to a Gaussian shape, and their central position and full width at half maximum served as the input of the unit cell volume and associated uncertainty, respectively. The unit cell volume of the sample was refined using UnitCell (*Holland and Redfern*, 1997). In most cases, the volume uncertainty was estimated to be 3% of the unit cell volume, which is larger than the  $2\sigma$  errors provided by UnitCell. To determine the best-fit equations of state, the P-V data sets were analyzed using the EOS-FIT (V5.2) least-squares package (*Angel*, 2000) (Figures 4.2,4.3).

## 4.2.2 Nuclear resonant inelastic X-ray scattering

For the nuclear resonant inelastic x-ray scattering measurements (NRIXS), a panoramic DAC with 3 large radial openings separated by 120 degrees around the sample was used, so as to increase the detection area and therefore the signal. The panoramic DAC was modified with a  $90^\circ$  opening and cubic boron nitride backing plate on the downstream side, thus maximizing the range of available diffraction angles for in-situ XRD. Similar to the the DAC prepared for XRD measurements, two type-I diamonds with culets  $300\ \mu\text{m}$  in diameter were mounted and aligned to form the anvils. A Be gasket was used to decrease X-ray absorption in the radial direction. The gasket was pre-indented to  $\sim 50\ \mu\text{m}$  thick and a  $125\ \mu\text{m}$  diameter hole was drilled in the center of the pre-indentation using an electrical discharge machine. The gasket hole was then filled with amorphous boron epoxy to hold the pressure and ensure the sample maintained a relatively high thickness with increasing pressure. We mechanically drilled a  $\sim 50\ \mu\text{m}$  diameter hole into the epoxy insert and loaded a  $\sim 25\ \mu\text{m}$  thick sample ( $\sim 30\ \mu\text{m}$  in diameter, compacted out of the powder) into it. Neon was loaded into the sample chamber of the DAC at GSECARS at the APS (*Rivers et al.*, 2008). Two ruby spheres ( $\sim 10\ \mu\text{m}$

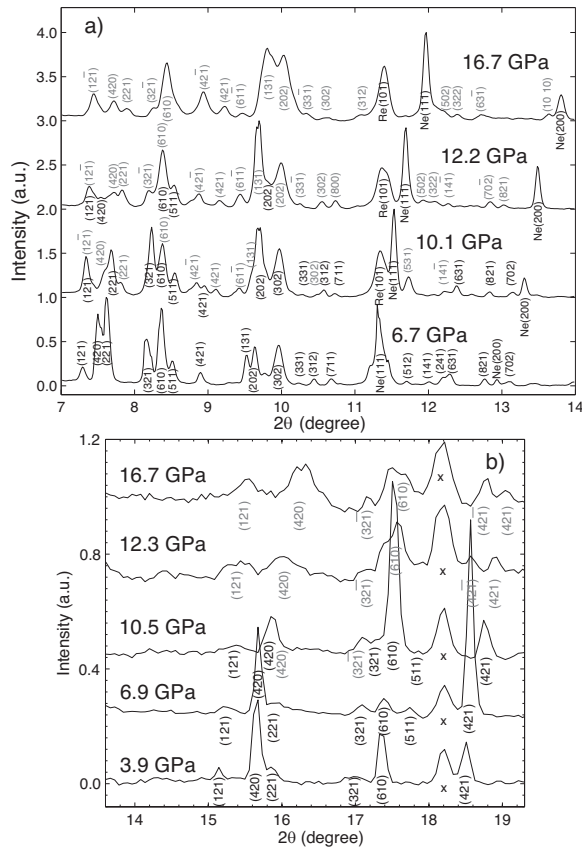


Figure 4.1: a) Select XRD patterns at different pressures taken at beamline 12.2.2 of the ALS ( $E=30$  keV). The  $hkl$  indices for the OEN phase (black) and HP phase (grey) are labeled near each peak. Ne and Re peaks are also labeled. b) Select in-situ XRD patterns taken at beamline 3-ID-B of the APS at the  $^{57}\text{Fe}$  nuclear resonance energy of 14.4125 keV. x: Ruby ( $\text{Al}_2\text{O}_3$ ) (104) peak. The background has been subtracted in each pattern.

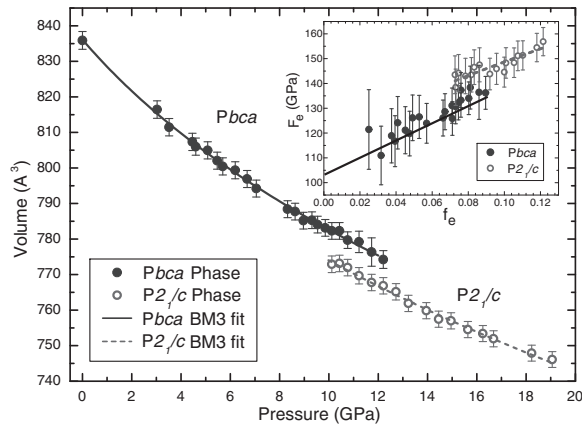


Figure 4.2: Unit cell volume as a function of pressure for En87 compressed using Ne as a pressure transmitting medium (Table 1). The best fit 3rd-order Birch-Murnaghan (BM3) equations of state for the two phases are shown as lines (see text for details). *Inset* normalized pressure ( $F_e$ ) versus Eulerian finite strain ( $f_e$ ) for the En87 sample. Lines are calculated from our reported BM3 EOS.

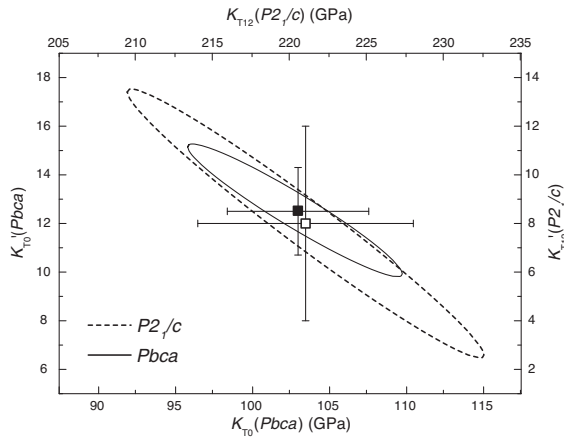


Figure 4.3: Confidence ellipses in  $K_T$  and  $K'_T$  for the fit of the BM3 EOS to the En87 P-V data (see text). Solid square and line:  $Pbca$ . Open square and dashed line:  $P2_1/c$ . Error bars are given at levels of  $1\sigma$ . The 68% confidence ellipses are calculated for two degrees of freedom (*Angel, 2000*).

in diameter) were placed around the En87 sample to monitor the pressure in the sample chamber (*Mao et al., 1986*), as Ne diffraction peaks were not visible in the sampled two-theta range (Figure 4.1b).

NRIXS experiments were performed at sector 3-ID-B of the Advanced Photon Source at Argonne National Laboratory. The energy bandwidth of the incident X-rays determines the resolution of the phonon spectra. The X-rays were prepared with bandwidths of 1 meV using a multiple-crystal Bragg reflection monochromator (*Toellner, 2000*). A Kirkpatrick-Baez mirror system was used to obtain a focal spot size of  $\sim 10 \times 10 \mu\text{m}^2$  at the full width at half maximum (*Zhao et al., 2004*). The storage ring was operated in low-emittance top-up mode with 24 bunches that were separated by 153 ns. For each spectrum, the monochromator was tuned from  $-75$  meV to  $+90$  meV around the nuclear resonance energy of  $^{57}\text{Fe}$  (14.4125 keV), with a step size of 0.25 meV and a collection time of 5 s per energy step (Figure 4.4a). The radiation emitted from the sample was observed with four avalanche photodiode detectors. Three detectors were placed around and close to the sample ( $\sim 2$  mm away) to collect the incoherent inelastic scattered photons, and the fourth detector was placed downstream ( $\sim 100$  cm) in the forward scattering direction, in order to obtain the resolution function independently. The counting rates were low due to the small thickness (in order to achieve pressure) and low  $^{57}\text{Fe}$  concentration. Therefore,  $\sim 10$  spectra per pressure were collected, and the average total counting rate in the highest Stokes peak was  $\sim 2.2$  counts/second. In-situ X-ray diffraction patterns ( $E=14.4125$  keV,  $\lambda=0.86025 \text{ \AA}$ ) were collected at sector 3-ID-B before and after each NRIXS compression point to determine the unit cell volume of the enstatite sample (Figure 4.1b). We use these volumes to compute the pressure via the best-fit BM3 EOS (see Section 3.1). We did not observe any indication of sample amorphization over the compression range investigated here. The NRIXS data were analyzed using the PHOENIX software package, and a quasi-harmonic

model was used to extract the partial phonon density of states (Figure 4.4b) from the measured raw NRIXS spectra (*Sturhahn, 2000*).

### 4.2.3 First-principles calculations

We employ density-functional theory (DFT) (*Hohenberg and Kohn, 1964; Kohn and Sham, 1965*) and density-functional perturbation theory (DFPT) (*Baroni et al., 1987, 2001; Gonze and Vigneron, 1989; Gonze et al., 1992, 2005*) to compute the phonon density of states of  $\text{Mg}_2\text{Si}_2\text{O}_6$  OEN. We employ Troullier-Martins-type pseudopotentials (*Troullier and Martins, 1991*) generated with the Fritz Haber Institute code (*Fuchs and Scheffler, 1999*), and the Generalized Gradient Approximation (GGA) in the Perdew-Burke-Erzerhof formulation (*Perdew et al., 1996*). All the calculations are static ( $T = 0$  K), and the phonons and DOS are computed in the quasi-harmonic approximation. We fully relax the crystal structure of OEN, minimizing both the residual interatomic forces and the residual non-hydrostatic stresses. We use a  $1 \times 2 \times 4$  special grid of high-symmetry  $\mathbf{k}$  points (*Monkhorst and Pack, 1976*) and a cutoff for the plane wave kinetic energy of 34 Hartrees (1Ha = 27.2116 eV). These parameters ensure an accuracy of the calculations better than 1 mHa in energy. We compute the phonons in the Brillouin-zone center for ambient pressure. The phonon density of states is built as a summation of the phonon band dispersion, which in turn is obtained using Fourier transform techniques of the interatomic force constants matrix at Gamma (*Gonze et al., 1992; Baroni et al., 2001*).

The DFT calculations are performed on pure  $\text{Mg}_2\text{Si}_2\text{O}_6$  compositions. Fe can enter the pyroxene structure on the M1 and/or M2 sites. Once the interatomic force constants matrix is computed for  $\text{Mg}_2\text{Si}_2\text{O}_6$ , we only alter the mass of the atom on the M1 or M2 sites corresponding to the desired amount of iron on that particular position. This is a standard procedure employed for studying isotope partitioning (*Schauble, 2004*). We assign the altered mass to be consistent with the composition of our sample studied by NRIXS. Thus 25% Fe on either M1 or M2 site in substitution to Mg yields a mass of 32.190. Using the new masses, we recompute the dynamical matrices and reconstruct the phonon density of states (Figures 4.5). The procedure ensures a first order approximation of the effect of iron on the total and Fe-partial phonon density of states. It has a relatively reduced computational cost and also presents the advantage of preserving the lattice symmetry.

## 4.3 Results

### 4.3.1 X-ray diffraction

We use XRD to determine the pressure-volume equation of state and to monitor the change of crystal symmetry of enstatite. Pressures are determined using the ruby fluorescence method (*Mao*

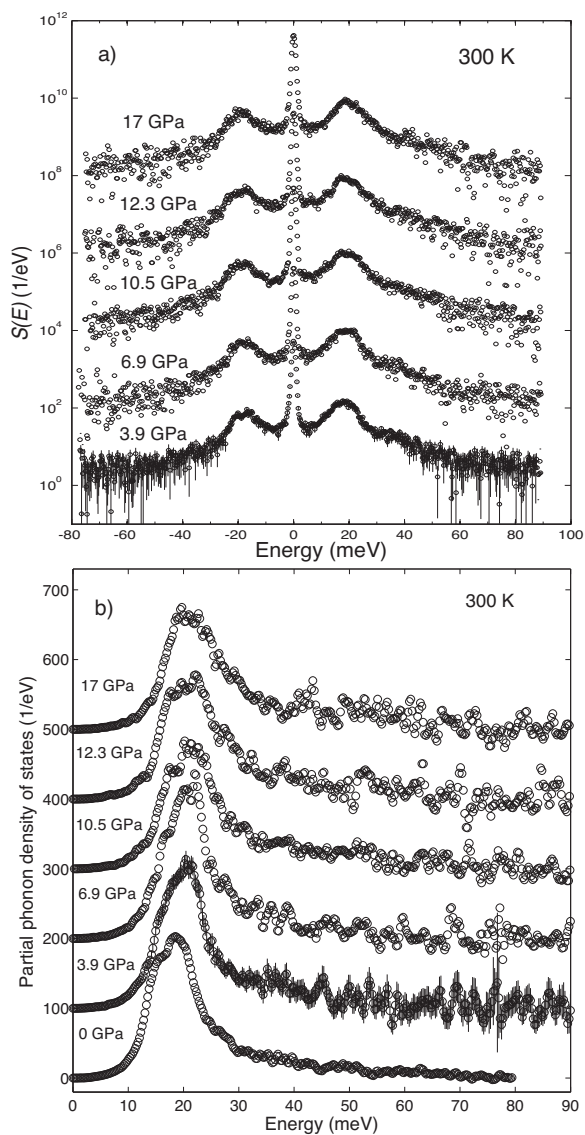


Figure 4.4: a: Select NRIXS spectra,  $D(E, V)$ , of En87. Data are shifted vertically. The errors in  $S(E)$  for 6.9, 10.5, 12.3 and 17 GPa are similar to the error of 3.9 GPa, but are not plotted for clarity. b: Partial projected phonon density of states of En87 at different pressures. Each spectrum is offset by 100 units in the vertical direction. Error bars for the ambient pressure data (*Jackson et al.*, 2009) are less than the size of the symbol. Errors for the high pressure data are similar to those of the 3.9 GPa data.

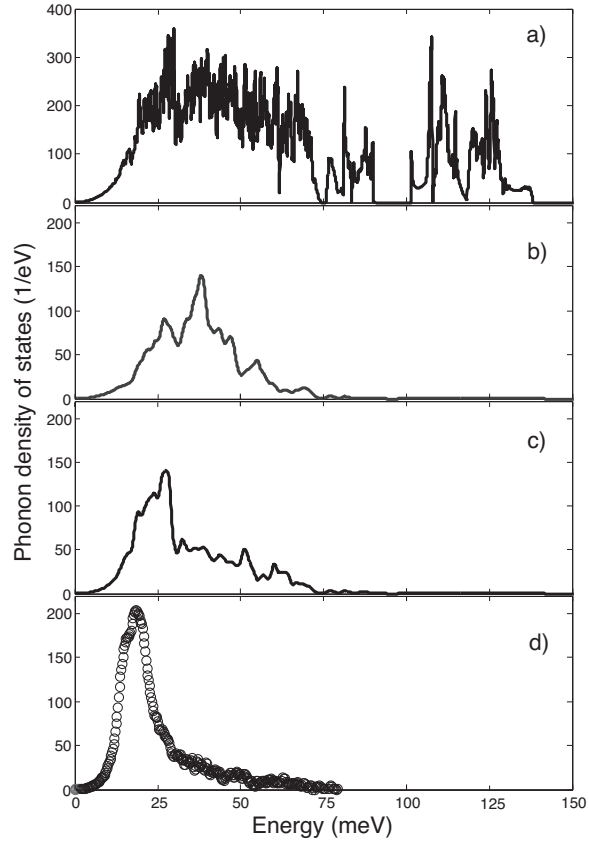


Figure 4.5: The DFT calculated phonon DOS (a-c, at 0 K) and measured Fe-partial projected phonon DOS for OEN at ambient pressure (d, at 300 K): a) total phonon DOS of  $\text{Mg}_2\text{Si}_2\text{O}_6$  OEN, b) partial phonon DOS for 25% Mg replaced by Fe on the M1 site, c) partial phonon DOS for 25% Mg replaced by Fe on the M2 site, and d) measured Fe-partial projected phonon DOS for En87 at 300 K (*Jackson et al.*, 2009).

*et al.*, 1986) (below 4.6 GPa where Ne is in the liquid state) and from the Ne unit cell volume using the BM3 EOS determined from *Dewaele et al.* (2008) (above 4.6 GPa). The pressures determined from each gauge agree up to 15 GPa then diverge. From the diffraction patterns, one structural transition can be identified between 10.1 GPa and 12.2 GPa. This transition pressure is consistent with previous experimental observations using synchrotron Mössbauer spectroscopy (*Zhang et al.*, 2011), XRD (*Kung et al.*, 2004; *Zhang et al.*, 2012) and ultrasonic interferometry (*Kung et al.*, 2004), and theoretical calculations (*Jahn*, 2008). Below 10.1 GPa, the diffraction peaks in the  $2\theta$  range between  $7^\circ$  and  $12^\circ$  can be indexed with *Pbca* symmetry. At pressures higher than 10.1 GPa, peaks from a new phase emerge in the XRD patterns, and at pressures higher than 12.2 GPa, the diffraction peaks indicate that the sample is converted to a new phase. In the  $2\theta$  range between  $7^\circ$  and  $12^\circ$  the diffraction peaks can be indexed using a monoclinic structure with space group  $P2_1/c$  (Figure 4.1), identified in a recent single crystal XRD study on  $(\text{Mg}_{1.74}\text{Fe}_{0.16}\text{Al}_{0.05}\text{Ca}_{0.04}\text{Cr}_{0.02})(\text{Si}_{1.94}\text{Al}_{0.06})\text{O}_6$  (*Zhang et al.*, 2012). Therefore, we adopt the  $P2_1/c$  structure as the structure for our high pressure phase. The  $P2_1/c$  structure is very similar to the  $P2_1ca$  structure, which is a suggested high-pressure symmetry for enstatite based on molecular dynamics simulations (*Jahn*, 2008). In our study, there is a density increase of  $1.2\pm 0.5\%$  at 10.1 GPa for the *Pbca* to  $P2_1/c$  transition, similar to theoretical results ( $\sim 1.3\%$ , *Jahn* (2008)) and a recent single crystal XRD study ( $1.9\pm 0.5\%$  over the pressure range of 12.66 to 14.26 GPa, *Zhang et al.* (2012)). The density increase for the *Pbca* to  $C2/c$  transition in the Mg end-member is reported to be 3 to 4%) (*Kung et al.*, 2004).

In order to determine the isothermal bulk modulus ( $K_T$ ) and the corresponding pressure derivative ( $K_T'$ ) of the En87 sample, a 3rd order Birch-Murnaghan equation of state was used to fit the P-V data set (Figure 4.2, Table 4.1). The OEN phase (*Pbca*) and the high pressure phase (hereafter referred as HP, space group  $P2_1/c$ ) were fit separately. For OEN, we obtained for the zero pressure unit cell volume ( $V_0$ ) the same value as our measured value ( $836\pm 3 \text{ \AA}^3$ ) and a zero-pressure bulk modulus ( $K_{T0}$ ) of  $103\pm 5$  GPa, roughly consistent with previous studies on OEN (Table 4.2) (*Hugh-Jones and Angel*, 1997; *Flesch et al.*, 1998; *Angel and Jackson*, 2002; *Kung et al.*, 2004). The disagreement with the study by *Chai et al.* (1997) is likely due to the fact that their sample contained more Al (Table 4.2). For the pressure derivative of the bulk modulus ( $K_{T0}'$ ), we obtained  $13\pm 2$ , consistent with the trend in the normalized pressure ( $F_e$ ) versus Eulerian finite strain ( $f_e$ ) (Figure 4.2). Although this value is higher than previous reports (Table 4.2), one must recognize the strong correlation between  $K_{T0}$  and  $K_{T0}'$  (Figure 4.3).

For the HP phase ( $P2_1/c$ ), the best fit volume at 12 GPa is  $767\pm 3 \text{ \AA}^3$ . The best fit bulk modulus of the  $P2_1/c$  phase at 12 GPa is  $220\pm 10$  GPa, significantly higher than the  $C2/c$ -structured Mg end member at the same pressure ( $168\pm 17$  GPa (*Shinmei et al.*, 1999),  $177\pm 6$  GPa (*Angel and Hugh-Jones*, 1994), and  $186\pm 1$  GPa (*Kung et al.*, 2005)). The best fit  $K_T'$  at 12 GPa is  $8\pm 4$ . The 68% confidence ellipses for the  $K_T$  and the  $K_T'$  fitting are shown in Figure 4.3. The confidence

Table 4.1: Unit cell volumes of the OEN phase ( $Pbca$ ) and the HP phase ( $P2_1/c$ ) as a function of pressure at room temperature determined from the XRD data refinements using the reflections shown in Figure 4.1a. Pressures were determined using the ruby fluorescence method (*Mao et al.*, 1986) (below 4.6 GPa), and from the Ne unit cell volume using the BM3 EOS from *Dewaele et al.* (2008) (above 4.6 GPa). For pressure determination, Ne (111) and (200) peaks were used. Values in parentheses indicate the uncertainty in the last significant digit.

Pressure (GPa)	Volume ( $\text{\AA}^3$ )	Pressure (GPa)	Volume ( $\text{\AA}^3$ )
OEN		HP	
0	836(3)	10.1(1)	773(2)
3.0(2)	816(2)	10.4(1)	773(2)
3.5(2)	811(2)	10.8(2)	772(2)
4.5(3)	807(2)	11.2(2)	770(2)
4.6(4)	806(2)	11.7(1)	768(2)
5.1(1)	805(2)	12.2(1)	767(2)
5.5(1)	802(2)	12.7(1)	765(2)
5.7(1)	800(2)	13.2(1)	762(2)
6.2(1)	799(2)	14.0(1)	760(2)
6.7(1)	797(2)	14.5(1)	757(2)
7.1(1)	794(2)	15.0(1)	757(2)
8.3(1)	788(2)	15.6(1)	755(2)
8.6(1)	788(2)	16.2(1)	753(2)
9.0(1)	785(2)	16.7(2)	752(2)
9.3(1)	785(2)	18.2(2)	748(2)
9.5(1)	784(2)	19.1(1)	746(2)
9.9(1)	783(2)	-	-
10.1(1)	782(2)	-	-
10.4(1)	782(2)	-	-
10.8(2)	780(2)	-	-
11.2(2)	779(3)	-	-
11.7(1)	776(4)	-	-
12.2(1)	774(3)	-	-

ellipses show that  $K_T$  and  $K_T'$  are strongly correlated (*Angel*, 2000). We note that our equations of state for both phases should not be extrapolated outside the measured pressure ranges for each phase (see Figure 4.3).

### 4.3.2 Nuclear resonant inelastic X-ray scattering and first-principles calculations

NRIXS measurements provide an independent method to examine the elastic properties of a sample. A quasi-harmonic model was used to extract the partial projected phonon density of states (DOS) (Figure 4.4) from the measured raw NRIXS spectra (*Sturhahn*, 2000). With increasing pressure, the DOS expands and shifts towards higher phonon energies, with subtle changes in shape. From the integration of DOS, one obtains parameters related to the  $^{57}\text{Fe}$ -participating vibrations in the En87 sample: the Lamb-Mössbauer factor,  $f_{LM}$  (related to the mean-square displacement of the iron atoms); the mean force constant,  $D_{ave}$ ; the vibrational free energy per atom,  $F_{vib}$ ; the vibrational

Table 4.2: Unit cell volume, isothermal bulk modulus and its pressure derivative of orthoenstatite (*Pbca*) at room pressure and temperature from different experimental studies.

	En100 <sup>[1]</sup>	En100 <sup>[2]</sup>	En100 <sup>[3]</sup>	En87 (This study)	En85 <sup>[4]</sup>	En83 <sup>[5]</sup>	En82 <sup>[6]</sup>
$V_0$ ( $\text{\AA}^3$ )	832.5(2)	832.9(1)	839(8)	836(3)	833.9(2)	833.12(6)	834.1(5)
$K_{T0}$ (GPa)	105.8(5)	109(4)*	104(2)*	103(5)	109(2)	112(1)	115.5(5)
$K'_T$	8.5(3)	6.6(7)*	10.9(5)*	13(2)	9(1)	7.4(4)	7.82
Method	XRD+BS	XRD+UI	UI	XRD	XRD	XRD	ISLS

[1] *Angel and Jackson* (2002),  $\text{Mg}_2\text{Si}_2\text{O}_6$ . [2] *Kung et al.* (2004),  $\text{Mg}_2\text{Si}_2\text{O}_6$ . [3] *Flesch et al.* (1998),  $\text{Mg}_2\text{Si}_2\text{O}_6$ . [4] *Hugh-Jones and Angel* (1997),  $(\text{Mg}_{0.85}\text{Fe}_{0.13}\text{Ca}_{0.02})_2(\text{Si}_{0.96}\text{Al}_{0.04})_2\text{O}_6$ . [5] *Hugh-Jones and Angel* (1997),  $(\text{Mg}_{0.83}\text{Fe}_{0.12}\text{Ca}_{0.006}\text{Al}_{0.04})_2(\text{Si}_{0.97}\text{Al}_{0.03})_2\text{O}_6$ . [6] *Chai et al.* (1997),  $(\text{Mg}_{1.63}\text{Fe}_{0.17}\text{Ca}_{0.04}\text{Mn}_{0.01})(\text{Al}_{0.12}\text{Cr}_{0.01})(\text{Si}_{1.89}\text{Al}_{0.11})\text{O}_6$ . Values in parentheses indicate the uncertainty in the last significant digit. Error presented in this study is  $1\sigma$ . BS: Brillouin spectroscopy; UI: ultrasonic interferometry; ISLS: impulsive stimulated light spectroscopy. (\*) indicates adiabatic values:  $K_{S0}$  is  $\sim 1\%$  higher than  $K_{T0}$ , (*Angel and Jackson*, 2002)

kinetic energy per atom,  $E_k$ ; the vibrational specific heat at constant volume per atom,  $c_V$  and the vibrational entropy per atom,  $S_{vib}$  (*Sturhahn*, 2000) (Table 4.3). A subset of these parameters show a minor change in the range of 10.1 to 12.2 GPa, thus indicating some level of sensitivity to the transition.

We compare the ambient phonon DOS from the NRIXS measurement (*Jackson et al.*, 2009) with the phonon density of states calculated from *ab initio* DFT (*Caracas and Gonze*, 2010). For this we consider three possible cases in the DFT calculations: pure  $\text{Mg}_2\text{Si}_2\text{O}_6$ , 25%Fe on the M1 site, and 25%Fe on the M2 site. The theoretical total phonon DOS and partial phonon DOS are shown in Figure 4.5. The measured partial phonon DOS from NRIXS is very similar to the DFT calculation of the partial phonon DOS where the Fe atoms are only in the M2 site (Figures 4.4,4.5): both have intense phonon peaks around 20 meV, and neither have large intensity around 40 meV. Therefore, the NRIXS data and DFT calculations suggest that the Fe occupation (or more accurate, that the heavier mass element) in the En87 sample is primarily in the M2 site, consistent with synchrotron and conventional Mössbauer studies that 92% of the  $^{57}\text{Fe}$  occupies the M2 site (*Zhang et al.*, 2011; *Jackson et al.*, 2009). Using PHOENIX, we input the various DFT computed phonon DOS and calculate the above-mentioned parameters at 0 K and 300 K for the different considerations of Fe-site occupancy (Table 4.4). Note that the average force constant is independent of temperature. It is not surprising that the parameters are not in good agreement with the experiments, as we consider heavy Mg as a proxy for Fe in our DFT calculations. It is possible to explore the possibility of scaling the DFT computed DOSs to obtain better agreement. However, this particular exercise would only make sense if the phonon DOSs were computed with Fe, rather than heavy Mg. And, of course, the absolute values of the free energy may be off significantly, but it is the volume derivative of the free energy that should be compared in this case, and that was not computed by DFT in this study.

Table 4.3: Thermodynamic parameters of the  $^{57}\text{Fe}$ -participating vibrations of En87 determined from NRIXS spectra at different pressures measured at 300 K.

Pressure (GPa)	$f_{LM}$	$F_{vib}$ (meV/atom)	$D_{ave}$ ( $\times 10^2\text{N/m}$ )	$E_k$ (meV/atom)	$c_V$ ( $k_B/\text{atom}$ )	$S_{vib}$ ( $k_B/\text{atom}$ )
0*	0.730(2)*	-8.4(3)	1.70(3)*, 1.70(3) <sup>†</sup>	14.01(7)*	2.75(1)*	3.60(1)*
3.9(2)	0.755(3)	-3(2)	1.85(27), 1.89(29) <sup>†</sup>	14.2(5)	2.72(5)	3.42(4)
6.9(4)	0.757(3)	-4(3)	1.70(33), 1.68(34) <sup>†</sup>	14.1(6)	2.74(6)	3.45(5)
10.5(7)	0.784(3)	4(2)	2.11(22), 2.31(22) <sup>†</sup>	14.4(4)	2.68(5)	3.19(4)
12.3(7)	0.784(3)	3(2)	2.10(27), 2.10(29) <sup>†</sup>	14.4(5)	2.69(5)	3.22(4)
17(1)	0.797(3)	7(2)	2.20(23), 1.91(24) <sup>†</sup>	14.5(4)	2.67(5)	3.09(4)

$f_{LM}$ : Lamb-Mössbauer factor,  $F_{vib}$ : free energy;  $D_{ave}$ : mean force constant (<sup>†</sup>: determined after refinement of the raw data),  $E_k$ : kinetic energy,  $c_V$ : vibrational specific heat,  $S_{vib}$ : vibrational entropy. All parameters were determined from the partial phonon DOS, unless otherwise noted. Uncertainties were determined using the PHOENIX software (*Sturhahn, 2000*). (\*): *Jackson et al. (2009)*.

Table 4.4: Thermodynamic parameters determined from the DFT computed phonon DOS, calculated at 0 K and 300 K using PHOENIX.

DFT phonon DOS	$f_{LM}$	$F_{vib}$ (meV/atom)	$D_{ave}$ ( $\times 10^2\text{N/m}$ )	$E_k$ (meV/atom)	$c_V$ ( $k_B/\text{atom}$ )	$S_{vib}$ ( $k_B/\text{atom}$ )
$\text{Mg}_2\text{Si}_2\text{O}_6$ total phonon DOS, Fig- ure 4.5a	NA	89.7, 72.6	10.31, 10.31	14.9, 19.2	0, 2.0	0, 1.7
25% Fe in the M1- site only, Fe-partial phonon DOS, Figure 4.5b	0.94, 0.86	57.5, 31.5	3.51, 3.51	9.4, 15.4	0, 2.5	0, 2.3
25% Fe in the M2- site only, Fe-partial phonon DOS, Figure 4.5c	0.93, 0.83	51.2, 20.4	3.09, 3.09	8.5, 15.1	0, 2.6	0, 2.7

$f_{LM}$ : Lamb-Mössbauer factor,  $F_{vib}$ : free energy;  $D_{ave}$ : mean force constant;  $E_k$ : kinetic energy,  $c_V$ : vibrational specific heat,  $S_{vib}$ : vibrational entropy. NA: not applicable. In the case of the total phonon DOS, the values represent contributions from all atoms in the lattice. For the partial phonon DOS, the values represent contributions from the  $^{57}\text{Fe}$ -participating vibrations. All parameters are determined using the PHOENIX software at 0 K and 300 K, respectively (*Sturhahn, 2000*).

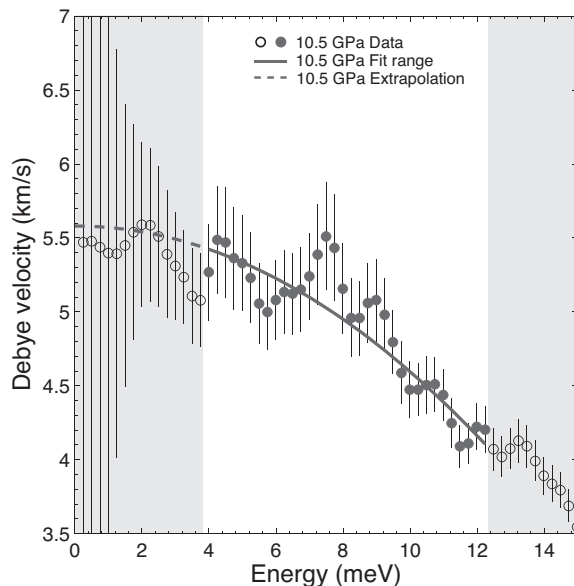


Figure 4.6: Debye sound velocity ( $V_D$ ) determination at 10.5 GPa. The fit (solid and dashed lines) was performed on the data (open circles) starting from 3.7 meV (determined by the resolution of the monochromator) and ending at 12.2 meV (determined by chi-squared analysis), then extrapolated to  $E=0$  to determine  $V_D$ . Gray regions show the data and associated uncertainties that were not used in the fit.

By analyzing the low energy region of the measured DOS, one can obtain the Debye sound velocity ( $V_D$ ). The Debye sound velocity is the isotropic sound velocity of the material, obtained from the region in the DOS where the dispersion of the acoustic modes is linear (or the DOS is parabolic) as a function of energy. The energy range that provided the best fit is from 3.7 meV to 12.2 meV (Figure 4.6). This range avoids the elastic peak (resolution function) at lower energies (*Sturhahn and Jackson, 2007; Jackson et al., 2009*). We compare the Debye sound velocity in this study with the calculated values from previous studies on enstatite (Figure 4.7a). For previous single-crystal studies (*Frisillo and Barsch, 1972; Duffy and Vaughan, 1988; Webb and Jackson, 1993; Chai et al., 1997*), the Debye sound velocity was determined numerically from averaging the elastic constants using Christoffel equation (*Sturhahn and Jackson, 2007*) or from the isotropic  $V_P$  and  $V_S$  values from experiments on powdered material (*Flesch et al., 1998; Kung et al., 2004*). One interesting feature is the decrease of  $V_D$  at around 12 GPa, which is observed in our data and *Kung et al. (2004)*.  $V_D$  decreases by about 0.2 km/s when pressure increases from 10.5 GPa to 12.3 GPa. The in-situ XRD pattern shows that there is a transition from the  $Pbca$  structure to a high-pressure phase, and Mössbauer spectroscopy data show a change in the trend of the hyperfine parameters of En87 (*Zhang et al., 2011*), so it is reasonable to conclude that the decrease in  $V_D$  is related to the structural transition.

By combining the Debye sound velocity from NRIXS and the bulk modulus from the P-V equation of state (all determined in this study on En87 from the same bulk sample), it is possible to extract

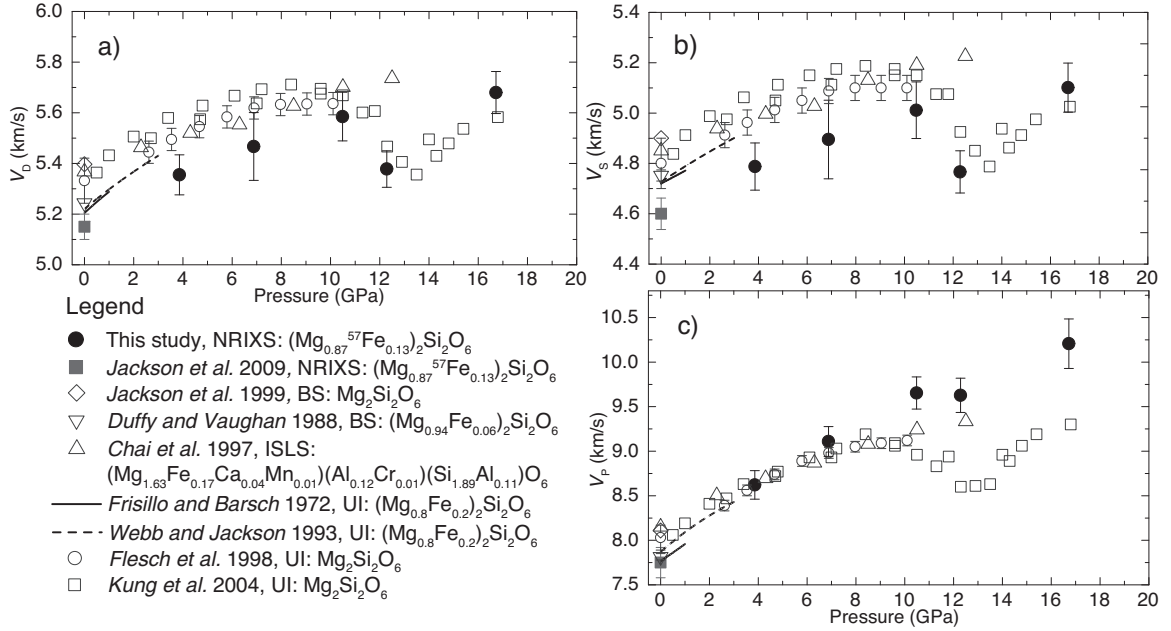


Figure 4.7: Sound velocities determined from this experiment (see Table 4.5) and from previous measurements (see Legend). a): Debye velocity ( $V_D$ ), b): shear velocity ( $V_S$ ), c): compressional velocity ( $V_P$ ). UI: ultrasonic interferometry, BS: Brillouin spectroscopy, ISLS: impulsive stimulated light spectroscopy.

Table 4.5: Elastic parameters of En87 determined from this study using XRD and NRIXS at different pressures.

Volume $\text{\AA}^3$	Density ( $\text{g/cm}^3$ )	Pressure (GPa)	$V_D$ (km/s)	$V_P$ (km/s)	$V_S$ (km/s)	$V_\Phi$ (km/s)	$\frac{V_P}{V_S}$	$\nu$	$K$ (GPa)	$\mu$ (GPa)
836(3)*	3.31(1)	0	5.12(5)	7.7(2)	4.63(5)	5.6(2)	1.669	0.220	103(5)	71(2)
811(2)	3.41(2)	3.9(2)	5.33(8)	8.6(2)	4.78(8)	6.6(2)	1.794	0.274	147(9)	78(2)
795(3)	3.48(3)	6.9(4)	5.5(1)	9.1(2)	4.9(1)	7.1(2)	1.862	0.297	177(9)	83(4)
782(2)	3.54(3)	10.5(7)	5.55(9)	9.6(2)	4.96(9)	7.7(3)	1.935	0.318	210(10)	87(3)
767(3)	3.61(3)	12.3(7)	5.38(7)	9.6(2)	4.79(7)	7.8(3)	2.001	0.332	220(10)	83(2)
752(3)	3.68(3)	17(1)	5.68(8)	10.2(3)	5.05(8)	8.4(5)	2.025	0.339	260(20)	94(3)

$V_D$ ,  $V_P$ ,  $V_S$ , and  $V_\Phi$ : Debye, compressional, shear, and bulk sound velocities, respectively.  $K$ : bulk modulus,  $\mu$ : shear modulus. Volume was determined by in-situ XRD at APS 3-ID-B (see text) and density was corrected for  $^{57}\text{Fe}$ -enrichment. Pressures up to 10.5 GPa were determined from the  $Pbca$  EOS (Table 4.2) and at 12.3 and 17

GPa, the  $P2_1/c$  EOS was used. Error determinations: volume - statistical, density - volume and microprobe uncertainties,  $K$  - BM3 fit at the  $1\sigma$  level, other parameters - PHOENIX software (Sturhahn, 2000). (\*): Jackson *et al.* (2009), recalculated  $V_P$ ,  $V_S$ ,  $K$ , and  $\mu$  using the  $Pbca$  EOS from this study.

the compressional ( $V_P$ ) and shear ( $V_S$ ) sound velocities of En87 as a function of pressure (Figure 4.7b & c). The compressional ( $V_P$ ) and shear ( $V_S$ ) sound velocity can be calculated from

$$\frac{3}{V_D^3} = \frac{1}{V_P^3} + \frac{2}{V_S^3} \quad (4.1)$$

$$\frac{K}{\rho} = V_P^2 - \frac{4}{3}V_S^2 \quad (4.2)$$

where  $\rho$  is the density (corrected for  $^{57}\text{Fe}$ -enrichment),  $K$  is the bulk modulus from the equation of state, and  $V_D$  is the Debye sound velocity from the NRIXS measurement. In the calculation, the in-situ XRD density and the bulk modulus from the best fit 3rd-order Birch-Murnaghan EOS are used. In this case, we assume  $K_{S0}$  can be approximated by  $K_{T0}$  ( $K_{S0}$  is  $\sim 1\%$  higher than  $K_{T0}$ , *Angel and Jackson* (2002)). The associated uncertainties in determining  $V_P$  and  $V_S$  from  $V_D$  and bulk modulus has been discussed in detail in *Sturhahn and Jackson* (2007).

We compare our results with previous studies (*Frisillo and Barsch*, 1972; *Duffy and Vaughan*, 1988; *Webb and Jackson*, 1993; *Chai et al.*, 1997; *Flesch et al.*, 1998; *Kung et al.*, 2004; *Jackson et al.*, 2009) (Figure 4.7b & c). Note that the ambient pressure results of En87 are from NRIXS measurements on a larger aggregate of the sample (*Jackson et al.*, 2009), from which a smaller portion of the sample was drawn for this study. Therefore, the room-pressure value of En87 is a very good representation of the average properties of En87 at this pressure. The values of En87 are consistent with a decrease in wave speed with the addition of iron at a given pressure, however there appears to be an inconsistency in the magnitude of the trend when comparing results from different techniques (*Duffy and Vaughan*, 1988; *Chai et al.*, 1997; *Flesch et al.*, 1998; *Kung et al.*, 2004; *Jackson et al.*, 2009, 1999). In the pressure range where we observe OEN ( $Pbca$ ), the  $V_D$ ,  $V_P$  and  $V_S$  increase from room-pressure to 10.5 GPa. These trends are consistent with previous measurements in this pressure range (*Frisillo and Barsch*, 1972; *Webb and Jackson*, 1993; *Chai et al.*, 1997; *Flesch et al.*, 1998; *Kung et al.*, 2004). The pressure derivative of the shear modulus for the  $Pbca$  phase is  $d\mu/dP = 1.7 \pm 0.1$  between 0 and 10.5 GPa.

Near the phase transition (10.5 GPa), our in-situ XRD pattern at sector 3-ID-B showed that the  $Pbca$  phase is dominant. A weak  $P2_1/c$  ( $32\bar{1}$ ) peak is present at this pressure, however there is not enough information to resolve its in-situ density nor the abundance of the  $P2_1/c$  phase. Therefore, we report the sound velocities at 10.5 GPa using the density and bulk modulus from the dominant  $Pbca$  phase. If one uses the density and bulk modulus of the  $P2_1/c$  phase, the compressional and shear velocities of En87 are within the uncertainties of the  $Pbca$  phase at 10.5 GPa.

At 12.3 GPa, the ( $42\bar{1}$ ) peak of the HP phase appears and  $V_D$  and  $V_S$  for  $P2_1/c$  show a drop in velocity (a decrease of  $\sim 0.2$  km/s,  $\sim 4\%$  in  $V_S$ ), rather than a smooth increase (Figure 4.7). A similar drop in  $V_S$  was observed in the Mg-end member using ultrasonic interferometry (*Kung et al.*,

2004). This behavior is likely related to the structural transition. Interestingly, we do not observe the same decrease in  $V_P$  as past studies have reported for the Mg-end member. The  $V_P$  value up to 12.3 GPa is similar to the values reported by *Chai et al.* (1997). In our XRD measurements performed on a sample from the same run charge (Figures 4.1,4.2), we find that the  $Pbca$ - $P2_1/c$  structural transition is associated with a volume reduction, which leads to a determined  $V_P$  value that shows a slight change in trend near the transition. We show that the Fe atoms are almost entirely in the M2 site, using a combination of Mössbauer spectroscopy, NRIXS, and DFT (Figure 4.5). Differences in Fe-concentration, Fe-ordering, and equations of state for the different enstatite samples could, in part, explain the differences in  $V_P$  between the studies.

### 4.3.3 Geophysical implications

Phase transitions of enstatite have been suggested as candidates for the seismic X-discontinuity in a depleted mantle (*Woodland and Angel*, 1997; *Woodland*, 1998; *Kung et al.*, 2004, 2005; *Akashi et al.*, 2009; *Jacobsen et al.*, 2010). In seismological studies, the X-discontinuity is characterized by a large depth variation, from 240 to 340 km (*Deuss and Woodhouse*, 2002; *Revenaugh and Jordan*, 1991; *Bagley and Revenaugh*, 2008), with reflections associated with a shear impedance increase of 3 to 7.5% (corresponding to a reflection coefficient 1.5 to 3.8% *Revenaugh and Jordan* (1991); *Bagley and Revenaugh* (2008)). The compressional impedance change for this discontinuity is not clear yet. In our study, we identify a transition occurring in enstatite, likely  $Pbca$ - $P2_1/c$ , between 10.1 and 12.2 GPa (a depth equivalent of 300-350 km) accompanied by a shear impedance drop of  $\sim 2\%$ . The shear impedance of the  $P2_1/c$  phase increases by  $\sim 8\%$  from 12.3 GPa to 17 GPa. The compressional impedance of enstatite slightly increases by  $\sim 2\%$  for the  $Pbca$ - $P2_1/c$  transition between 10.1 and 12.3 GPa, and it continues to increase by  $\sim 7\%$  from 12.3 GPa to 17 GPa. Molecular dynamics simulation (*Jahn*, 2008) suggests that the  $P2_1/c$  phase is metastable at high temperature, and multi-anvil experiments show that the HP-CEN phase is the stable polymorph of enstatite at 14 GPa and 1000 °C (*Kung et al.*, 2004). We explore the influence of iron-bearing  $Pbca$ -structured enstatite on upper mantle petrologic models, as well as the high-pressure phases of enstatite, and compare these results to seismic observations.

We now construct shear velocity profiles for candidate upper mantle assemblages that include  $Pbca$ -structured enstatite, HP-CEN, and the  $P2_1/c$ -structured enstatite. We use a finite strain method (*Duffy and Anderson*, 1989) to primarily assess the influence of  $Pbca$ -structured enstatite on seismic shear wave structures that have been reported. For the elastic moduli and associated pressure derivatives of enstatite, we use values from this study. We use the thermal expansion coefficient and linear temperature derivatives of the elastic moduli of the  $Pbca$  phase (*Jackson et al.*, 2007). Thermoelasticity data for olivine ( $(\text{Mg}_{0.9}\text{Fe}_{0.1})_2\text{SiO}_4$ ),  $C2/c$  HP-CEN, diopside and pyrope garnet ( $(\text{Mg}_{0.9}\text{Fe}_{0.1})_3\text{Al}_2(\text{SiO}_4)_3$ ) were taken from recent reports (*Wang et al.*, 1998; *Liu et al.*, 2005;

Table 4.6: Thermoelastic parameters of minerals used in the finite strain model.

Minerals	$\rho_0$ (g/cm <sup>3</sup> )	$K$ (GPa)	$\mu$ (GPa)	$K'$	$\mu'$	$dK/dT$ (GPa/K)	$d\mu/dT$ (GPa/K)	$\alpha_0$ (10 <sup>-6</sup> K <sup>-1</sup> )	$\alpha_1$ (10 <sup>-9</sup> K <sup>-2</sup> )	Reference
OEN	3.31(1) <sup>a</sup>	103(5) <sup>a</sup>	71(2) <sup>a</sup>	13(2) <sup>a</sup>	1.7(1) <sup>a</sup>	-0.0263(3) <sup>b</sup>	-0.0136(3) <sup>b</sup>	29.7 <sup>b</sup>	5.7 <sup>b</sup>	This study <sup>a</sup> , <i>Jackson et al. (2007)<sup>b</sup></i>
$P2_1/c$	3.61(3) <sup>a</sup>	220(10) <sup>a</sup>	83(2) <sup>a</sup>	8(4) <sup>a</sup>	2.5(5) <sup>a</sup>	-0.0263(3) <sup>b</sup>	-0.0136(3) <sup>b</sup>	29.7 <sup>b</sup>	5.7 <sup>b</sup>	This study at 12 GPa <sup>a</sup> , <i>Jackson et al. (2007)<sup>b</sup></i>
HP-CEN	3.46(1)	156(1)	99(1)	5.6(3)	1.5(1)	-0.017(1)	-0.015(1)	17.3(80)	16.4(11.7)	<i>Kung et al. (2005)</i> at 6.5 GPa
Olivine	3.342(2)	130.3(4)	77.4(2)	4.61(11)	1.61(4)	-0.0164(5)	-0.0130(3)	27.11	6.885	<i>Liu et al. (2005)</i>
Garnet	3.566(1) <sup>a</sup>	170.0(2) <sup>a</sup>	93.2(1) <sup>a</sup>	4.51(2) <sup>a</sup>	1.51(2) <sup>a</sup>	-0.0170(1) <sup>a</sup>	-0.0107(1) <sup>a</sup>	23(2) <sup>b</sup>	9.4(2.8) <sup>b</sup>	<i>Zou et al. (2012)<sup>a</sup></i> , <i>Wang et al. (1998)<sup>b</sup></i>
Diopside	3.277(5)	115.9(9)	72.8(4)	4.5(1.8)	1.7	-0.0123	-0.00998	26	10	<i>Isaak et al. (2006)</i>

Note: The DLA parameterization (*Duffy and Anderson, 1989*) was used to compute the shear velocity profiles in Figure 4.8. The thermal expansion coefficients ( $\alpha_0$  and  $\alpha_1$ ) were used to correct the densities and pressure derivatives of elastic moduli. For the high-pressure phases ( $P2_1/c$  and HP-CEN), the thermoelastic parameters were first projected back to ambient P-T values using the third order finite strain theory without a temperature correction, and then the projected ambient values were treated the same as the other phases. To compute the velocities of the rock, the average sound velocities were calculated using Voigt-Reuss-Hill procedure and the Hill average is plotted in 4.8.

*Kung et al., 2005; Isaak et al., 2006; Zou et al., 2012*) (Table 4.6). We use a 1400 °C adiabat in the calculation. Three different petrological models were considered: pyrolite-like with 57% olivine, 14% pyrope garnet, 12% diopside and 17% enstatite (volume ratio) (*Ringwood, 1991*); enstatite-enriched harzburgite with 50% olivine, 10% pyrope garnet and 40% enstatite (*Irifune and Ringwood, 1987; Hieronymus et al., 2007*); and piclogite-like with 16% olivine, 37% pyrope garnet, 23% diopside, 21% jadeite (assume to have the same elastic parameters as diopside), and 3% enstatite (*Bass and Anderson, 1984; Ita and Stixrude, 1992*) (Figure 4.8).

We find that the characteristic shear velocities for these three petrological models between 230 and 280 km depth are lower than the global average PREM model (*Dziewonski and Anderson, 1981*) and higher than the global average AK135 model (*Kennett et al., 1995*). It is noteworthy to point out that in this depth region, the average Earth models PREM and ak135 show significantly different wave speeds and gradients (Figure 4.8). The shear velocity of the petrological models are slightly lower than the shear structure beneath tectonically stable regions such as the eastern North American continent at depths above 300 km (SNA, *Grand and Helmberger (1984a)*). In the same depth range, they are significantly higher (>50 m/s) than the shear velocity structure beneath tectonically active regions such as the western United States (TNA, *Grand and Helmberger (1984a)*), the Pacific ocean (PAC06, *Tan and Helmberger (2007)*) and the northern Atlantic ocean (ATL, *Grand and Helmberger (1984b)*) (Figure 4.8). The calculated pressure derivative of the shear wave speed ( $dV_S/dP$ ) is about 0.03 km/s/GPa between 230 and 300 km for these three petrological models. This shear velocity gradient is higher than the average Earth model PREM, but lower than regional studies. Based on the phase diagram of enstatite (*Woodland, 1998*), we assume that the OEN phase ( $Pbca$ ) transitions into the HP-CEN phase ( $C2/c$ ) at 300 km ( $\sim 10$  GPa), accompanied by a shear velocity jump (*Kung et al., 2005*). It is possible to calculate the shear reflection coefficients for the different petrologies considered here from the shear velocity and density of OEN (this study) and HP-CEN (*Kung et al.,*

2005) using the following equation (Revenaugh and Jordan, 1991; Bagley and Revenaugh, 2008):

$$R = \frac{\rho_{HP-CEN} \times V_{HP-CEN} - \rho_{OEN} \times V_{OEN}}{\rho_{HP-CEN} \times V_{HP-CEN} + \rho_{OEN} \times V_{OEN}} \quad (4.3)$$

The shear reflection coefficients corresponding to different petrological compositions are 0.5% (pyrolite), 1.2% (enstatite-enriched harzburgite) and 0.1% (piclogite). The calculated shear reflection coefficients are lower than seismic observations for the "X-discontinuity" (1.5 to 3.5%) (Revenaugh and Jordan, 1991; Bagley and Revenaugh, 2008). Based on our XRD and NRIXS data, we also compute the shear velocity profile of the pyrolitic mantle speculating that the *Pbca* phase gradually transitions into the  $P2_1/c$  phase from 10 to 12 GPa (Figure 4.8). We note that the existence of the  $P2_1/c$  phase in the mantle remains speculative.

Although iron-bearing enstatite-rich phase assemblages may produce lower than average shear velocities, it appears that between 250 and 300 km depth in tectonically active regions, changes in candidate petrologic assemblages (i.e., pyrolite, piclogite, harzburgite) may not be enough to explain the very low shear velocities observed. Partial melting (Tan and Helmlberger, 2007) or a hydrated phase assemblage may help explain the non-pervasive distribution of the X-discontinuity (Jacobsen et al., 2010; Revenaugh and Jordan, 1991). However, observations of the X-discontinuity in regions expected to be dry, such as the underside region of subducted slabs will likely require alternative explanations than those considered here. Nevertheless, we find that phase assemblages containing considerable fractions of *Pbca*-structured iron-bearing enstatite can produce shear velocities that are lower than what is observed under stable tectonic regions (SNA, Grand and Helmlberger (1984a)) and the 1D Earth model PREM.

In this manuscript, we report the high pressure elasticity of  $^{57}\text{Fe}$  enriched En87 sample constrained by x-ray diffraction and nuclear resonant inelastic x-ray scattering experiments up to 19.1 GPa. A BM3 EOS fitting gives  $K_{T0}=103\pm 5$  GPa and  $K_{T0}'=13\pm 2$  for the *Pbca* phase. At 12 GPa, a BM3 EOS fitting gives  $K_{T12}=220\pm 10$  GPa with  $K_{T12}'=8\pm 4$  for the  $P2_1/c$  phase. A structural transition from *Pbca* phase to  $P2_1/c$  phase is observed between 10.1 and 12.2 GPa, associated with a shear velocity decrease by  $\sim 4\%$ . DFT calculations of the partial phonon DOS of enstatite are consistent with  $\text{Fe}^{2+}$  dominantly occupying the M2 site, consistent with experimental constraints on the iron-occupancy of our sample. By using the shear velocity determined from this study and a finite strain model, we compute shear velocity profiles for different upper mantle petrological compositions. The shear velocity jump associated with the *Pbca*- $C2/c$  transition has a shear reflection coefficient lower than that observed for the seismic "X-discontinuity". The low velocities reported in tectonically active regions are unlikely to be explained by the presence of enstatite alone and may require phase assemblages containing hydrous phases and/or partial melt. We find that candidate upper mantle phase assemblages containing *Pbca*-structured enstatite are associated with shear

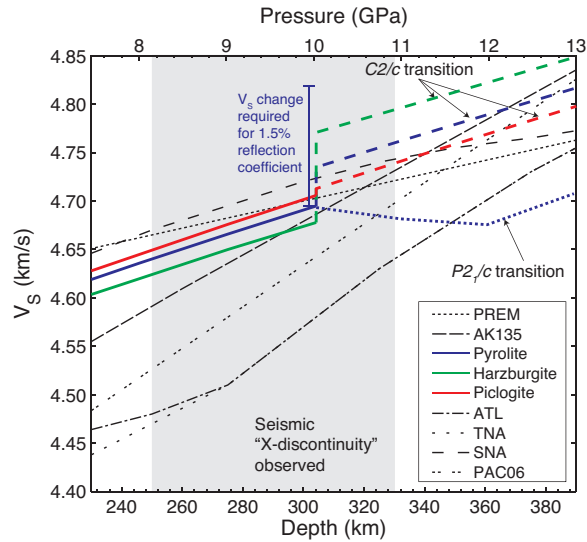


Figure 4.8: Comparison of calculated shear wave velocities from candidate upper mantle petrological models (1400 °C adiabat, see text) with seismic profiles. At  $P > 10$  GPa: dashed curve: assuming  $C2/c$  transition ((*Kung et al.*, 2005)); dotted curve: speculating that the  $P2_1/c$  transition occurs (this study). See text for details. Shaded region: seismic X-discontinuity observed (*Revenaugh and Jordan*, 1991; *Bagley and Revenaugh*, 2008). Global seismic models: PREM (230-390 km in depth, 7.5-13.0 GPa in pressure, interpolated between reported values), *Dziewonski and Anderson* (1981); AK135, *Kennett et al.* (1995). Regional seismic models: SNA, *Grand and Helmberger* (1984a); TNA, *Grand and Helmberger* (1984a); ATL, *Grand and Helmberger* (1984b); PAC06 (interpolated between reported values), *Tan and Helmberger* (2007). Blue scale at 300 km: shear velocity jump required for a seismic reflection with 1.5% reflection coefficient in a pyrolitic mantle (*Bagley and Revenaugh*, 2008).

velocity gradients that are higher than the average Earth model PREM, but lower than regional studies down to about 250 km depth.

## Chapter 5

# Fast temperature spectrometer for samples under extreme conditions

### 5.1 Introduction

Accurate and precise temperature determinations are among several important factors in obtaining reliable thermodynamic data for materials from experiments under extreme pressures and temperatures. In high pressure experiments conducted using the diamond-anvil cell (DAC), there are three common ways to reach high temperatures: laser heating (*Shen et al.*, 2001, 2005; *Meng et al.*, 2006; *Prakapenka et al.*, 2008), resistive heating (*Bassett et al.*, 1993; *Du et al.*, 2013a; *Zha et al.*, 2008) and shock-wave loading of precompressed samples (*Loubeyre et al.*, 2004; *Jeanloz et al.*, 2007). The latter method permits unique states of matter to be probed at high pressures and temperatures. However, the sample is typically destroyed, thus presenting reproducibility challenges (*Jeanloz et al.*, 2007). Heating by infrared lasers permits temperatures characteristic of Earth's deep interior to be reached (up to and exceeding 6500 K). Although resistive heating alone presents challenges in generating temperatures higher than 2000 K at high pressures (*Bassett et al.*, 1993; *Du et al.*, 2013a; *Zha et al.*, 2008), thermocouple-based temperature determinations provide fairly accurate and precise sample temperatures. Laser heating can be implemented in most DAC designs, while special gaskets, additional heaters and associated controllers are required for resistive heating (*Bassett et al.*, 1993; *Du et al.*, 2013a; *Zha et al.*, 2008). Laser heating is therefore often employed in high pressure experiments where temperatures greater than about 1200 K are desired.

Laser heating does present challenges. The temperature distribution in laser heating experiments can be inhomogeneous (*Boehler*, 2000; *Campbell*, 2008). Some recent progress has been made in increasing the spatial homogeneity, including laser heating from both sides (*Shen et al.*, 2001; *Prakapenka et al.*, 2008), combining different laser modes (*Shen et al.*, 2001), and adjustable laser geometry with beam-shaping optics (*Prakapenka et al.*, 2008). The second and less discussed chal-

---

<sup>0</sup>Revised over what was previously published as *Zhang et al.* (2015)

lenge is the stability of laser heating over a defined time period. The sample temperature in a laser heating experiment can fluctuate faster than in resistive heating experiments. Previous studies have documented temperature fluctuations of several hundred Kelvins (*Jeanloz and Heinz, 1984; Jeanloz and Kanner, 1996; Dewaele et al., 2007, 2010; Anzellini et al., 2013*) at a minimum of tens of Hz (*Jeanloz and Heinz, 1984*) during continuous wave laser heating. Experiments have shown that small ( $\sim 0.2\text{-}3\%$ ) temporal fluctuations in laser power are followed by large fluctuations in the temperature of the sample (*Jeanloz and Heinz, 1984*). It is also suggested that melting of the thermal insulation layer (*Dewaele et al., 2010*), changes in the thermal conductivity in the sample chamber (*Geballe and Jeanloz, 2012*) and changes in the laser coupler's reflectivity (*Geballe and Jeanloz, 2012*) may contribute to these large temperature fluctuations. Such fluctuations are not favorable for reliable temperature determinations of a laser-heated sample, and will inevitably increase the uncertainty of the temperature measurement.

There are a few approaches to address unstable temperature readouts in laser-heated DAC experiments. Closed-loop laser power feedback systems have proved to be effective in reducing the temperature fluctuation at a constant laser power (*Heinz et al., 1991; Shen et al., 2001*). However, this method is not suitable for experiments that involve ramping up the laser power every few seconds, such as that done for melting studies. For these types of experiments, it is preferred to determine the temperature of the sample at a frequency higher than the sample's temperature fluctuations and the accumulation time needed to diagnose certain material properties (in this case, melting). Currently, most temperature determination systems in laser-heated DAC experiments use charge-coupled device (CCD) chips as detectors. The CCD chip is either used in a spectrometer to fit the measured intensities to a temperature using Planck's law (*Shen et al., 2001; Zhao et al., 2004; Prakapenka et al., 2008*), or used to monitor the spatial distribution of the hotspot temperature by measuring the intensities of different wavelength bands (*Campbell, 2008; Du et al., 2013b*). However, conventional CCD spectrometers have some limitations, including a low dynamic range. The dynamic range of a modern CCD spectrometer is on the order of  $10^3\text{-}10^4$  for a single acquisition (e.g., Ocean Optics USB-4000), whereas the dynamic range of the photomultiplier tube is  $\sim 10^6$ . The large dynamic range is important for an accurate determination of the temperature. Another limitation of many CCD-based spectrometers is a slow reading rate. The conventional CCD chips for spectrometers usually have  $10^3\text{-}10^5$  pixels. To calculate the temperature using the CCD data, first one needs to read the intensity from the CCD chip, and then transfer the entire CCD image to the controlling computer to compute the temperature. In most CCD-equipped laser-heated DAC experiments at the synchrotron, the temperature readout frequency is at best on the order of 1 Hz (e.g., *Dewaele et al. (2007, 2010)* and *Anzellini et al. (2013)*). For laser-heated DAC experiments involving time-resolution and rapid temperature changes, a high-frequency accurate temperature readout system with a large dynamic range is highly desirable.

In this study, we present a new multi-wavelength **Fast Temperature Readout** (FasTeR) spectrometer operating in-line with nuclear resonant scattering and X-ray diffraction techniques at the Advanced Photon Source at Argonne National Laboratory. FasTeR is dedicated to experiments involving rapid temperature changes in the sample near its solidus(*Jackson et al.*, 2013), and is tailored to laser-heated DACs. The FasTeR spectrometer may be combined with other time-resolved measurements, such as time-domain thermorefectance(*Hsieh et al.*, 2009; *Chen et al.*, 2011; *Dalton et al.*, 2013), thermal diffusivity(*Beck et al.*, 2007), measurements using the dynamic diamond-anvil cell(*Velisavljevic et al.*, 2014), pulsed laser-heating(*Goncharov et al.*, 2010; *Yoo et al.*, 2012), high-speed shutter-based techniques(*Toellner et al.*, 2011), and perhaps even shock/ramp compression experiments(*Lyzena and Ahrens*, 1979; *Loubeyre et al.*, 2004; *Jeanloz et al.*, 2007).

## 5.2 Instrumentation

### 5.2.1 Experimental set-up

The fast temperature readout system described in this paper is installed at beamline 3-ID-B at the Advanced Photon Source of Argonne National Laboratory. It operates in parallel with nuclear resonance scattering (NRS) methods, X-ray diffraction (XRD), laser heating and a conventional charge-coupled-device (CCD)-based temperature readout system (Figure 5.1). Previous reports have described the experimental set-up for NRS and XRD studies at this beamline(*Zhao et al.*, 2004; *Gao et al.*, 2009; *Jackson et al.*, 2013), and the principles of NRS have been described before in detail(*Sturhahn*, 2004). In this study, we combine a new multi-wavelength **Fast Temperature Readout** (FasTeR) spectrometer with synchrotron Mössbauer spectroscopy (SMS), also known as nuclear resonant forward scattering, and X-ray diffraction to determine the melting temperature of  $^{57}\text{Fe}_{0.9}\text{Ni}_{0.1}$  at high pressure. In the following paragraphs, the details of the experimental set-up are described.

The X-rays are first monochromatized by a high heat-load diamond-crystal monochromator to a bandwidth of 1 eV, then filtered to the bandwidth of 1 meV using a silicon multiple-crystal Bragg reflection monochromator(*Toellner*, 2000). Two Kirkpatrick-Baez mirrors, one horizontal and the other vertical, are used to obtain a measured optimal X-ray focal spot size of  $\sim 10(\text{horizontal}) \times 11(\text{vertical}) \mu\text{m}^2$  at the full width at half maximum. The storage ring is operated in a low-emittance top-up mode with 24 bunches that are separated by 153 ns. Two ion chambers are placed in the upstream (IC1) and the downstream (IC3) sides of the sample stage to monitor the X-ray intensity before and after the sample (Figure 5.1, bottom tier). XRD measurements are carried out using a moveable mar345 Image Plate Detector System (Marresearch GmbH). The image plate is placed  $\sim 300\text{mm}$  away from the sample in the downstream direction. Ambient  $\text{CeO}_2$  is used to calibrate the position and tilt of the image plate. *In-situ* XRD patterns ( $E = 14.4125 \text{ keV}$ ,  $\lambda = 0.86025 \text{ \AA}$ ) are typically

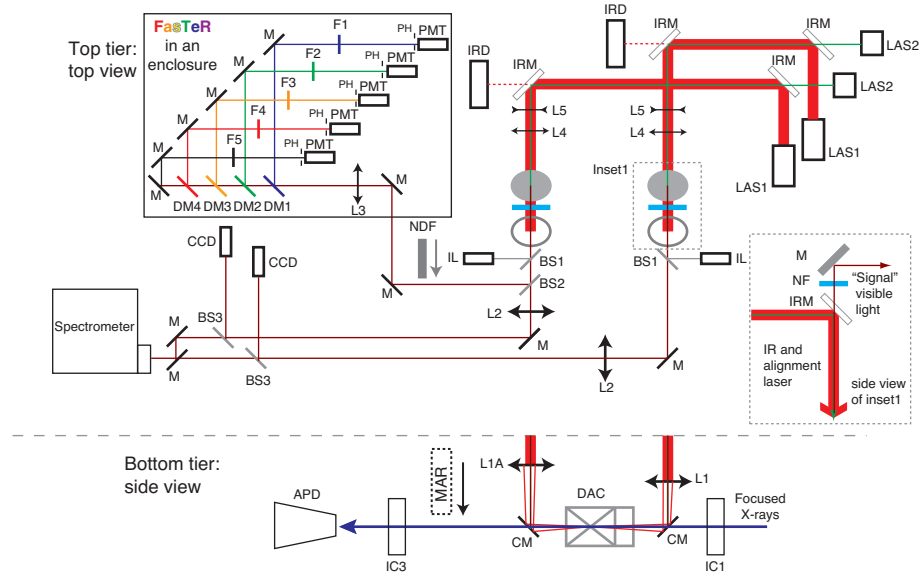


Figure 5.1: Design of the experimental set-up for laser-heating, nuclear resonant scattering, X-ray diffraction, and FasTeR at beamline 3-ID-B of the Advanced Photon Source at Argonne National Laboratory. LAS1: 100 W continuous fiber laser, 1064 nm (IPG Photonics). The power supplies are located outside of the experimental station. LAS2: 1 mW 532 nm alignment laser (Lasermate). IRM: 1064 nm coated infrared laser mirror (Newport). M: Al-coated flat mirror (ThorLabs). CM: amorphous carbon mirror with silver coating. IRD: infrared pindiode. NF: 1064 nm notch filter. L1: 100 mm focal-length apochromat lens (Sigma Optics). L1A: 77 mm focal-length apochromat lens (USLaser). L2: 1m focal-length achromat lens (Oriel). L3: 700 mm focal-length achromat lens (CVI Melles-Griot). L4: 100 mm focal-length planoconvex lens (ThorLabs). L5: -25 mm focal-length planoconcave lens (ThorLabs). L4 and L5 together form the beam size controller. IL: 18 W LED illuminator (Schott). BS1: 92-8 pellicle beamsplitter (ThorLabs). BS2: 50-50 metallic beamsplitter (OFR). BS3: 45-55 coated pellicle beam splitter (ThorLabs). DM1-4: dichroic beam splitters for different wavelength bands (Semrock). F1-5: bandpass filters for different wavelength bands (Semrock). PH: 50  $\mu\text{m}$  pinhole (Edmund optics). PMT: photo multiplier tube (Hamamatsu). NDF: optical density 2.0 neutral density filter (ThorLabs). CCD: charge-coupled device camera (Panasonic). Spectrometer:  $f/2.2$  broadband grating spectrometer with a  $1024 \times 250$  pixel front illuminated CCD (Princeton Instrument). IC1: ion chamber with Ne gas. IC3: ion chamber with Ar gas. APD: avalanche photodiode detector. MAR: X-ray image plate on a horizontal moving stage (Marresearch GmbH). DAC: diamond-anvil cell. The perspectives of the top tier and the bottom tier are perpendicular to each other.

collected at each compression point to obtain the unit-cell volume of the sample, which can then be used with an appropriate equation of state to determine the pressure of the sample.

The double-sided infrared (IR) laser heating system at beamline 3-ID-B is similar to systems installed at beamlines 16-ID-B (HPCAT) (*Meng et al.*, 2006) and 13-ID-D (GSE-CARS) (*Prakapenka et al.*, 2008) of the APS. Upgrades to the double-sided laser-heating system at 3-ID-B (*Zhao et al.*, 2004) are described here, and they include two randomly polarized, diode-pumped fiber lasers (IPG Photonics, 100 W each) with remote power control. These two lasers are single-mode continuous wave ytterbium-doped lasers working at a wavelength of 1064 nm. Located on a table above the X-ray beam (Figure 5.1, top tier), the IR laser heads with co-axial green alignment lasers (Lasermate, 532 nm, 1 mW) are guided to the sample position with mirrors. A pair of 100 mm focal length convex and -25 mm focal length concave lenses (ThorLabs) are used to regulate the divergence and size of the IR laser beams. The distance between the two lenses is controlled remotely by stepping motors, so that the IR laser hotspot diameter ( $\varnothing_{\text{laser}}$ ) is adjustable between approximately 15 and 50  $\mu\text{m}$ . The IR laser has a gaussian intensity profile. On the bottom tier, two different apochromats are used to focus the laser beams on the sample. These apochromats are optimized for both IR and visible light to minimize the chromatic aberration. The apochromat in the upstream direction of the sample (OptoSigma) has a focal length of 100 mm. In the downstream direction, an apochromat with a 77 mm focal length (USLaser) is used. A pair of amorphous graphite mirrors coated with silver are used to guide the IR laser beams. The amorphous graphite mirrors minimize the attenuation of the incident X-rays onto the sample. A conventional broadband grating charge-coupled device (CCD) spectrometer (1024 $\times$ 250 pixels, Princeton Instrument) determines the temperature from the upstream and downstream sides of the heated sample (*Zhao et al.*, 2004), thus monitoring the presence of axial surface temperature gradients.

### 5.2.2 Fast temperature readout spectrometer (FasTeR)

The design of the **Fast Temperature Readout** (FasTeR) spectrometer described here was originally developed for shock compression experiments (*Lyzenga and Ahrens*, 1979). FasTeR utilizes sensitive detectors at select wavelength ranges in the visible regime to sample the thermal radiation of hotspot in a laser-heated diamond anvil cell. The typical sizes of these hotspots are on the order of  $\sim 40 \mu\text{m}$ , significantly smaller than those in the shock wave experiments (*Lyzenga and Ahrens*, 1979). For example, the system by *Lyzenga and Ahrens* (1979) is capable of determining shock temperatures as fast as every  $\sim 10 \text{ ns}$ , with a field of view ( $\varnothing$ ) of  $1 \text{ mm}^2$ . The field of view for FasTeR ( $\varnothing_{\text{FasTeR}}$ ) is determined from the magnification ratio of the two apochromats (700mm : 77mm) and the 50  $\mu\text{m}$  pinhole in front of the detectors (Figure 5.1, inset 2), resulting in  $\varnothing_{\text{FasTeR}} = 6 \mu\text{m}$ . The intensity ratio between these different wavelength bands are computed and used with Planck's law to determine the temperature of the sample. The details of FasTeR are laid out in the following paragraphs.

The FasTeR spectrometer consists of an array of photomultiplier tubes (PMTs, Hamamatsu) as detectors. PMTs combine high gain, low noise, and high frequency response. They have a working frequency of 20 kHz, a radiant sensitivity of  $\sim 200$  V/nW, and a large dynamic range ( $\sim 10^6$ ). A neutral density filter (NDF, ThorLabs, optical density 2.0) can be moved in to the optical path in order to prevent saturation of the PMTs when the hotspot emission has a high intensity. The NDF gives two additional orders of magnitude to the total dynamic range of FasTeR, and it can be added remotely by computer control during an experiment.

The optical filters are essential in our temperature determination, because they define the transmission bands in the visible spectrum. To obtain five distinct, non-overlapping bands distributed between 350 nm and 850 nm, FasTeR uses four  $45^\circ$  dichroic mirrors (Semrock), one mirror (Newport) and five vertical incident bandpass filters (Semrock) (Figure 5.2). Each of these bands is  $\sim 40$  nm wide, with edges sharper than 5 nm. The transmission of each band is higher than 85%, and the signal of each band is collected by one individual PMT. The photocathodes of PMTs are selected to suit their corresponding optical transmission bands. Though the incident signal is passing through a  $45^\circ$  tilted infrared mirror which is 5 mm thick (Figure 5.1, inset 1), the chromatic aberration is very low for our FasTeR system, because each PMT detector is collecting the signal from only one transmission band, and each transmission band is  $\sim 40$  nm wide. The chromatic aberration in each band is smaller than  $4 \mu\text{m}$  on the detector side, which leads to a temperature error of less than 10 K. The optical signal received by each PMT is referred to as a "channel". Currently, there are five channels in the FasTeR system: the blue channel (B: 386-450 nm), green channel (G: 508-553 nm), orange channel (O: 601-631 nm), red channel (R: 671-709 nm), and infrared channel (I: 751-821 nm). From the convolution of Planck's law and the channel transmission, the theoretical intensity ratios between different channels can be calculated. See Section 5.2.3 for details on temperature calibration.

Stepping motors are used to align and focus the five PMTs to the same position. The resolution of the stepping motor is  $1 \mu\text{m}$  in three translational dimensions. During the aligning and focusing procedure, we place a  $25 \mu\text{m}$  pinhole at the measured X-ray focus position, and illuminate the pinhole uniformly from the back. We then scan the pinhole in three orthogonal directions (x,y,z), and fine-tune the position of the pinhole's image on the PMTs by adjusting the angles of the reflection mirrors and the positions of the PMTs, such that the signals are maximized when the pinhole is at the X-ray focus position. This procedure guarantees the alignment and focus of the FasTeR system with respect to the X-ray focus.

### 5.2.3 Calibration

Accurate determinations of temperature using FasTeR requires that the responses of each channel at different temperatures are known. To calibrate these responses, we use a frosted-glass tungsten

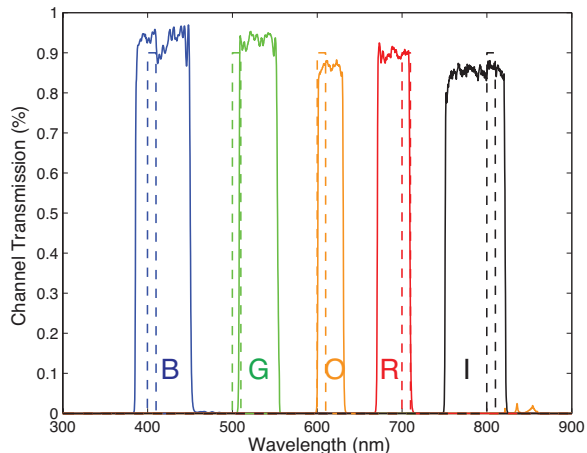


Figure 5.2: Wavelength-dependent channel transmission of the optical bandpass filters for FasTeR. B: blue channel (386-450 nm). G: green channel (508-553 nm). O: orange channel (601-631 nm). R: red channel (671-709 nm). I: infrared channel (751-821 nm). Solid curves: channel transmission used in experiments. These curves are based on the data provided by the manufacturer of the mirrors and filters. Dashed curves: example 10 nm bandwidth channel transmission used in simulation (please refer to Figure 5.7e-f for more details).

ribbon standard lamp with known radiance (Gigahertz-Optik). The working temperature range of this lamp is between 2000 K and 3200 K, and its temperature has been calibrated against the input current at the National Institute for Standards and Technology. During the calibration, we place a 25  $\mu\text{m}$  pinhole at the X-ray focus position. The standard lamp is fixed 10 cm away from the pinhole, illuminating the pinhole uniformly from the back. At a certain temperature of the standard lamp, an average intensity over 30 seconds is recorded as a particular channel's response. Calibrations with NDF in and out of the optical path are carried out independently. We measure the five channels' responses throughout the lamp's working temperature range (Figure 5.3).

To compute the hotspot temperature, we use the relative ratio between channels instead of the absolute intensity from each channel. The theoretical relative ratio curves between different channels at different temperatures are calculated from the integration of Planck's black body radiation function and the transmission band of each channel. The influence of the optical system is corrected by fitting the calculated theoretical relative ratio curve to the measured relative ratios from the calibration. In the experiments, the temperature is calculated so that the residual function,

$$R = \sum_{i=1}^4 c_i \left( \left( \frac{I_i}{I_{ref}} \right)_{measure} - \left( \frac{I_i(T)}{I_{ref}(T)} \right)_{theory} \right)^2 \quad (5.1)$$

where

$$c_i = \left( \frac{\sum I_i(T)}{I_i(T)} \right)_{theory}^2 \quad (5.2)$$

is minimized. In this equation, T is the temperature,  $I_i$  is the signal from channel  $i$  (unit: V),

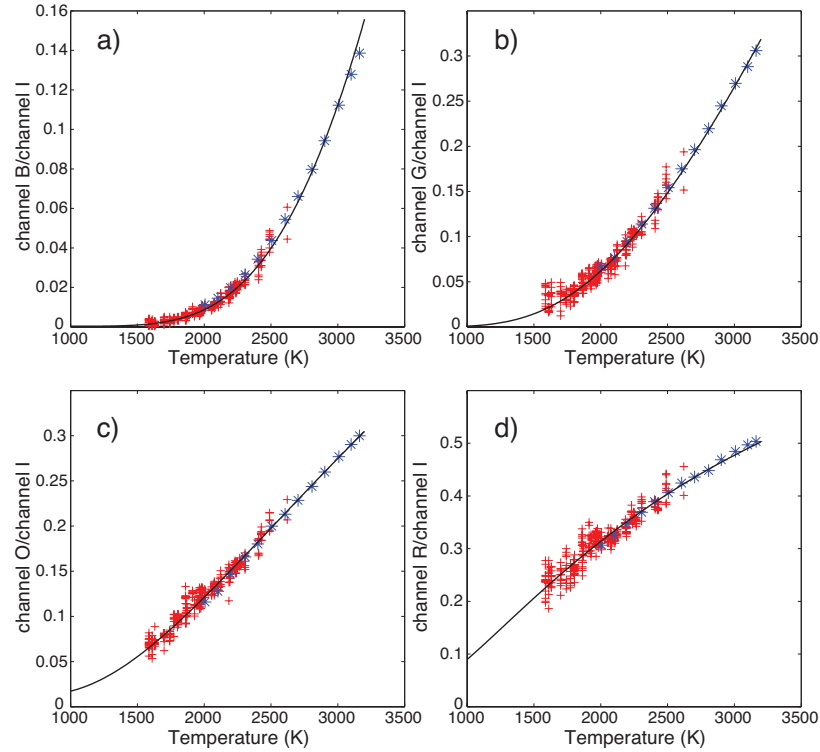


Figure 5.3: Calibration of intensity ratios from theoretical calculations (black curve) and the tungsten standard lamp (blue asterisk, temperature read from the lamp controller), and comparison with measured laser-heated hotspot (red cross, temperature read from the CCD spectrometer). NDF is out of the optical path during this specific calibration and laser heating. a): intensity ratio between channel B and channel I. b): intensity ratio between channel G and channel I. c): intensity ratio between channel O and channel I. d): intensity ratio between channel R and channel I. The intensities of different channels are measured simultaneously during the experiment. Wavelength ranges for each channel provided in the text and Figure 5.2.

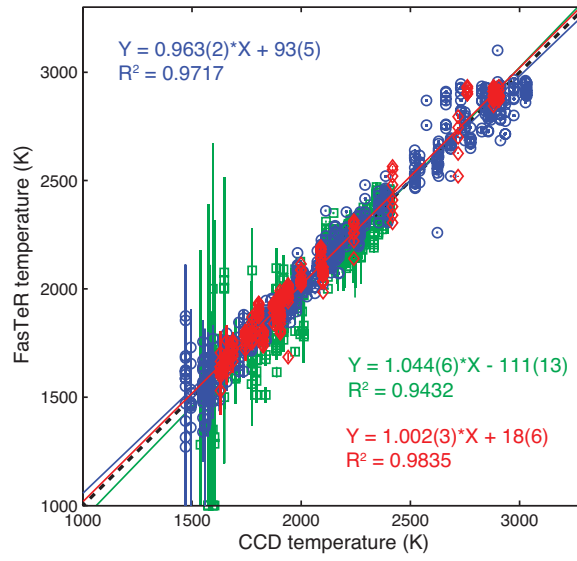


Figure 5.4: Comparison between the temperatures read by the CCD spectrometer (horizontal axis) and FasTeR (vertical axis) for three different heating runs. The samples are  $\text{Fe}_{0.9}\text{Ni}_{0.1}$  at  $P_{300K} = 29 \pm 2$  GPa (blue circles),  $\text{Fe}_{0.9}\text{Ni}_{0.1}$  at  $P_{300K} = 66 \pm 3$  GPa (green squares) and Fe at  $P_{300K} = 28 \pm 2$  GPa (red diamonds). The CCD spectrometer temperature's error is estimated to be 100 K (*Shen et al.*, 2001; *Zhao et al.*, 2004; *Lin et al.*, 2004) (not shown here for clarity), and the FasTeR temperature's error plotted here is the dark current fluctuation. The scattering error is then determined from the distribution of measured temperatures at a given CCD-determined temperature. Dashed line:  $Y=X$  identity line. Solid lines: linear regressions of the three datasets. Values in parentheses indicate the uncertainty in the last significant digit.

$c(i)$  is the weight constant of channel  $i$  so that the temperature determination doesn't weigh too much on one specific channel in the measured temperature range. Depending on the intensities of all channels,  $c(i)$  varies in different experiments.  $I_{ref}$  is the reference channel's intensity, which has the largest signal-to-noise ratio. In our measurements, the reference channel is the infrared channel (channel I). Using a computer acquisition sequence, the temperature is calculated and recorded as the experiment proceeds. Calibration of the CCD-based spectrometer at beamline 3-ID-B is also achieved using similar procedures.

Three different heating runs on Fe and  $\text{Fe}_{0.9}\text{Ni}_{0.1}$  samples, prepared in different DACs, are shown in Figure 5.4 to illustrate the point that the temperatures determined by FasTeR are in good agreement with those determined from the conventional CCD-based spectrometer in the explored range of 1500 to 3000 K. For the temperature error of each reported temperature from the FasTeR system, we consider three contributions. One contribution is the dark current fluctuation of each PMT, which is on the order of 0.2 mV. The dark current fluctuation is calculated so that the residual function,

$$R' = \sum_{i=1}^4 c_i \left( \left( \frac{I_i + \Delta I}{I_{ref} - \Delta I} \right)_{measure} - \left( \frac{I_i(T + \Delta T)}{I_{ref}(T + \Delta T)} \right)_{theory} \right)^2 \quad (5.3)$$

is minimized. In this equation,  $\Delta I = 0.2$  mV,  $\Delta T$  is the dark current fluctuation, and the other

parameters are the same as in Equation (5.1). The dark current fluctuation is the error of a single FasTeR reading, and it varies with the signal intensity of each PMT. The higher the intensity is, the smaller the dark current contribution is. At  $\sim 1500$  K, the dark current fluctuation can be as high as 300 K, whereas at temperatures higher than 2000 K, the dark current fluctuation is usually less than 10 K. In certain experiments, such as melting point determinations (see Section 5.3), the scattering error of the temperature determined by FasTeR is considered as the second contribution to the temperature error. While different types of data are recorded simultaneously at one rate, such as the integrated SMS delayed counts, ion chamber intensities, laser power, and CCD temperature every few seconds, FasTeR temperatures are recorded every  $\sim 10$  ms. For example, the FasTeR temperature corresponding to a particular SMS delayed count is the average of  $\sim 300$  FasTeR readings, and the standard deviation is reported as the scattering error. The scattering error is experiment-dependent. Both the dark current fluctuation and the scattering error are considered in the final temperature error determination. The third contribution we consider is the effect of chromatic aberration ( $\sim 10$  K, discussed in Section 5.2.2). During melting experiments at high pressures, the scattering error dominates for each FasTeR temperature. Typically, the largest differences between FasTeR and CCD-based temperatures are found at lower temperatures and temperatures near the melting point of the material. Due to FasTeR's large dynamic range, one does not need to change its integration time during heating. FasTeR's working temperature range can be adjusted by changing the gain of the PMTs.

#### 5.2.4 FasTeR sampling frequency

As its name implies, the FasTeR spectrometer features a temperature reading rate much faster than most conventional CCD-based systems. Currently, temperatures are well-determined at a readout rate of 100 Hz, up to 300 times faster than the conventional CCD at the same beamline. We compare the temperature readout rates between FasTeR and the conventional CCD spectrometer. Temperatures are recorded continuously by both systems during any given heating run, however more time is required to readout the intensities of a conventional CCD-based system. The time interval between two FasTeR readings is  $\sim 10$  ms, whereas the time interval between two CCD readings is  $\sim 3$  s. During one example melting experimental run, FasTeR records  $\sim 30,000$  measurements (downstream side), while only 46 measurements per side from the CCD are recorded (92 measurements in total).

We have also tested the sampling frequency of FasTeR with an optical chopper. In this test, an  $3000 \pm 100$  K illuminator is placed behind a  $200 \mu\text{m}$  pinhole, and the pinhole is located at the focal position of the FasTeR system. An optical chopper is placed in front of the pinhole, and interrupts the light from the pinhole periodically. The frequency of the optical chopper is adjustable in the range of 20 to 100 Hz. One can see that the sampling frequency of FasTeR can clearly distinguish the 100 Hz signal from the chopper (Figure 5.5). In this set-up, the sampling frequency of FasTeR

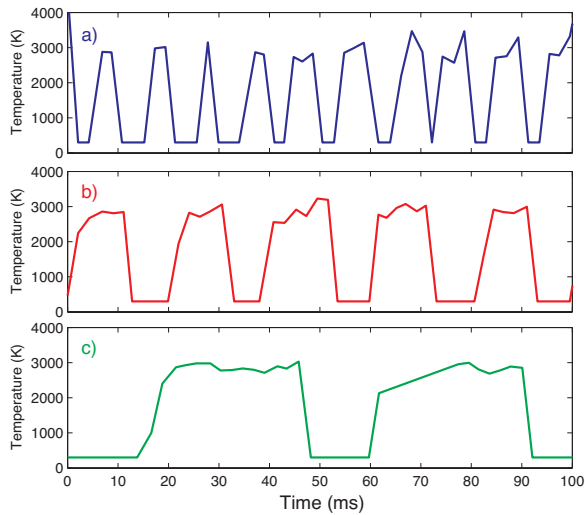


Figure 5.5: FasTeR’s time resolution tested with an optical chopper. The light source’s temperature is  $3000 \pm 100$  K. a): chopper frequency = 100 Hz. b): chopper frequency = 50 Hz. c): chopper frequency = 20 Hz. The fine structure of the temperature readouts is mostly due to the fact that the PMTs are not exactly synchronized (temporal offset  $\sim 1$  ms) with the optical chopper (temporal offset  $\sim 1$  ms).

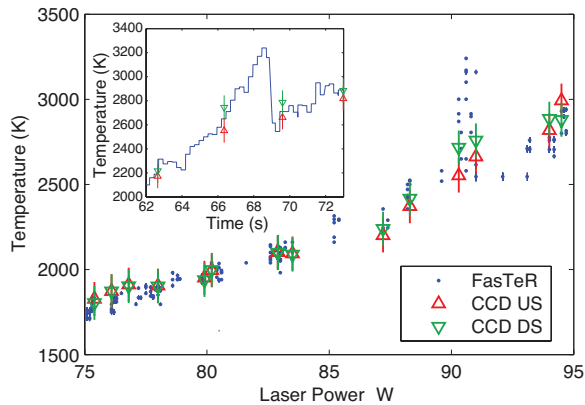


Figure 5.6: Transient temperature fluctuation as a function of laser power captured by the FasTeR system but not the CCD spectrometer. Temperatures read by the FasTeR system (blue dots, looking at the downstream side) and the CCD spectrometer (upstream side: red normal triangles; downstream side: green reversed triangles). Inset: temperature as a function of time, zoomed in to the rapid fluctuation (blue curve: FasTeR temperatures). The plateaus of the FasTeR temperatures come from the select time resolution of the analog-digital converter for this specific experiment (5 Hz). The FasTeR system’s sampling rate is 100 Hz. Sample:  $fcc\text{-Fe}_{0.9}\text{Ni}_{0.1}$ ,  $P_{300K} = 39 \pm 2$  GPa.

reaches  $\sim 400$  Hz, as determined from the number of measured temperatures divided by the duration of the measurement (recorded in the FasTeR data file). The fluctuations and spikes in the signal arise from the phase shift between the PMTs and optical chopper ( $\sim 1$  ms) and of each PMT ( $\sim 1$   $\mu$ s) that is recorded in series during an experiment. In continuous wave laser-heating scenarios, the temperature fluctuation rate can be on the order of  $10^4$  K/s (Jeanloz and Kavner, 1996), which could come from large changes in thermal conductivity or changes in the reflectivity of the sample during melting (Jeanloz and Heinz, 1984; Jeanloz and Kavner, 1996; Geballe and Jeanloz, 2012). In this study, we observe a transient temperature fluctuation: the temperature of the sample changes by about 600 K within 2 seconds (Figure 5.6). This temperature fluctuation indicates a change in the coupling between the laser and the sample and is likely associated with melting (Geballe and Jeanloz, 2012). FasTeR catches this rapid temperature fluctuation, whereas the conventional CCD spectrometer does not, because this temperature fluctuation coincides with the data transferring period between the two CCD readings. This case demonstrates that the FasTeR spectrometer is capable of capturing such fluctuations and thus obtaining a more accurate assessment of the sample's temperature during time-resolved experiments.

### 5.2.5 Simulating FasTeR

In order to understand the new FasTeR instrument in terms of its performance, response, and design modifications, we have performed several simulations. To this end, we have developed simulation software called SIMFaster, which is written in MatLab. SIMFaster uses the channel transmission of the FasTeR system,  $\mathcal{O}_{\text{laser}}$ ,  $\mathcal{O}_{\text{FasTeR}}$  and  $\mathcal{O}_{\text{CCD}}$  as its inputs (Figure 5.7a). For simulating the temperature determined from FasTeR, SIMFaster convolves the black body radiation curve with the channel transmissions, integrates over  $\mathcal{O}_{\text{FasTeR}}$  to obtain the intensity of each detector, and fits the intensity ratios between different channels to calculate the temperature.

We present several simulations with variations of the various  $\mathcal{O}$ . We first start with a simulation using the typical values for the various  $\mathcal{O}$  in our experimental set-up and optimized conditions ( $\mathcal{O}_{\text{laser}} = 35$   $\mu$ m,  $\mathcal{O}_{\text{CCD}} = 10$   $\mu$ m,  $\mathcal{O}_{\text{FasTeR}} = 6$   $\mu$ m, where FasTeR and the CCD spectrometer are aligned to the center of the hotspot) (Figure 5.7a,b). One can see that the temperature offset between the FasTeR system and the CCD spectrometer is temperature dependent, where the temperature difference is about 60 K at 3000 K. These offsets are due to the difference between the  $\mathcal{O}_{\text{FasTeR}}$  and the  $\mathcal{O}_{\text{CCD}}$  (Figure 5.7c). When there is no difference between  $\mathcal{O}_{\text{FasTeR}}$  and the  $\mathcal{O}_{\text{CCD}}$ , there is no temperature offset. Similarly, the  $\mathcal{O}_{\text{laser}}$  also affects the temperature offset when the  $\mathcal{O}_{\text{FasTeR}}$  and the  $\mathcal{O}_{\text{CCD}}$  are not equal (Figure 5.7d). The smaller the  $\mathcal{O}_{\text{laser}}$  is, the larger the temperature offset will be. Such simulations are necessary to evaluate if and when any of the components drift during an experiment.

Another important application of the simulation software is the assessment of system design

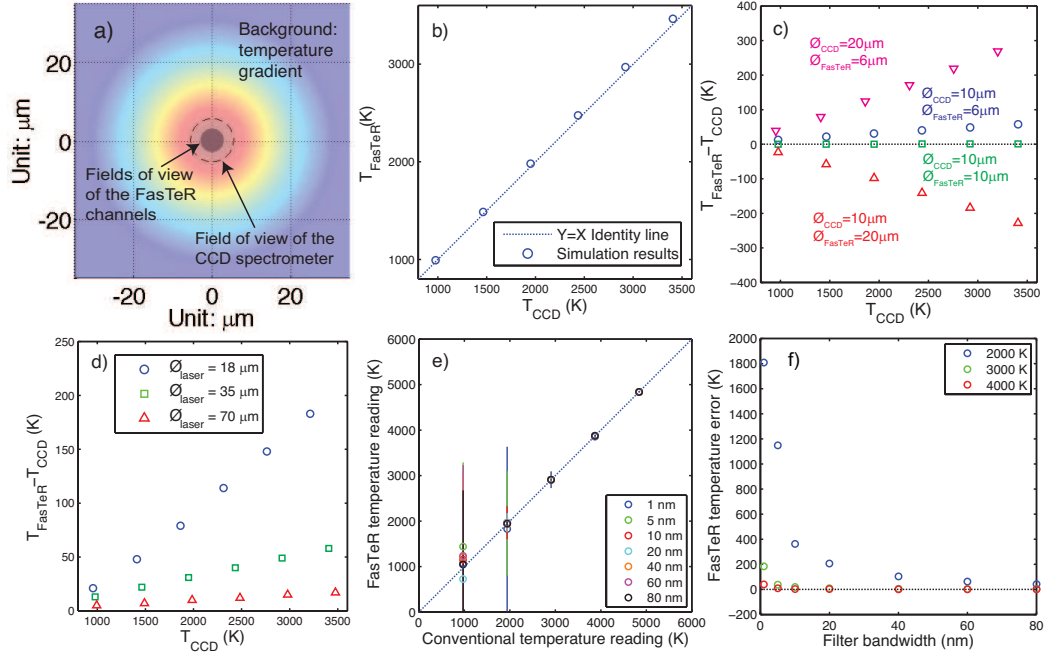


Figure 5.7: a): One example of the simulation conditions:  $\varnothing_{\text{laser}} = 35\mu\text{m}$  (background),  $\varnothing_{\text{CCD}} = 10\mu\text{m}$  (dashed circle at the center),  $\varnothing_{\text{FasTeR}} = 6\mu\text{m}$  (grey filled circle at the center). b): Comparison of temperatures determined by FasTeR and the CCD spectrometer from simulations using SIMFaster. Simulation conditions are the same as in a). Dashed line is the  $Y=X$  identity line. Temperature differences are the result of the mismatch in field of views for FasTeR and the CCD spectrometers. c): Influence of select variations of the  $\varnothing_{\text{FasTeR}}$  and the  $\varnothing_{\text{CCD}}$ . The  $\varnothing_{\text{laser}}$  is fixed at  $35\mu\text{m}$ . Blue circles:  $\varnothing_{\text{CCD}} = 10\mu\text{m}$ ,  $\varnothing_{\text{FasTeR}} = 6\mu\text{m}$ . Green squares:  $\varnothing_{\text{CCD}} = 10\mu\text{m}$ ,  $\varnothing_{\text{FasTeR}} = 10\mu\text{m}$ . Red triangles up:  $\varnothing_{\text{CCD}} = 10\mu\text{m}$ ,  $\varnothing_{\text{FasTeR}} = 20\mu\text{m}$ . Magenta triangles down:  $\varnothing_{\text{CCD}} = 20\mu\text{m}$ ,  $\varnothing_{\text{FasTeR}} = 6\mu\text{m}$ . d): Influence of varying the  $\varnothing_{\text{laser}}$ . The  $\varnothing_{\text{CCD}}$  is fixed at  $10\mu\text{m}$ , and the  $\varnothing_{\text{FasTeR}}$  is fixed at  $6\mu\text{m}$ . Blue circles:  $\varnothing_{\text{laser}} = 35\mu\text{m}$ . Green squares:  $\varnothing_{\text{laser}} = 18\mu\text{m}$ . Red triangles up:  $\varnothing_{\text{laser}} = 70\mu\text{m}$ . e) and f): Comparison of the temperature reading (e) and error (f) using different channel bandwidths. The  $\varnothing_{\text{CCD}}$  and the  $\varnothing_{\text{FasTeR}}$  are fixed at  $10\mu\text{m}$ ,  $\varnothing_{\text{laser}} = 35\mu\text{m}$ , and all detectors share the same noise level.

changes. To this end, we assess the influence of the transmission bandwidth of the optical filter system (Figure 5.7e,f). Using SIMFaster, we assume that both the  $\mathcal{O}_{\text{FasTeR}}$  and the  $\mathcal{O}_{\text{CCD}}$  are  $10 \mu\text{m}$ ,  $\mathcal{O}_{\text{laser}} = 35 \mu\text{m}$ , and all the detectors share the same noise level. We adjust the detector noise level so that the temperature error is 100 K at  $\max(T_{\text{laser}}) = 2000 \text{ K}$  when the transmission bandwidth = 40 nm, which is close to our experimental condition. Numerical simulation shows that narrowing the transmission bandwidth has little effect on the temperature reading (Figure 5.7e), but will significantly increase the error of temperature determination (Figure 5.7f), because the total intensity collected by the detector is proportional to the transmission bandwidth. Thus, it would only make sense to use narrower bandwidth filters (less than about 40 nm) for experiments that involve a much brighter thermal flux than those presented here.

### 5.3 Melting of $^{57}\text{Fe}_{0.9}\text{Ni}_{0.1}$ at high pressure

As a demonstration of the FasTeR system, we have determined the melting point of  $^{57}\text{Fe}_{0.9}\text{Ni}_{0.1}$  at  $P_{300\text{K}} = 29 \pm 2 \text{ GPa}$ . The high pressure environment is provided by a symmetric-type piston cylinder diamond-anvil cell. Two Type-I diamonds with  $300 \mu\text{m}$  culets are mounted and aligned to form the anvils. A Re gasket is pre-indented to  $\sim 45 \mu\text{m}$  thick, and a  $110 \mu\text{m}$  diameter hole is drilled in the center of the pre-indentation using a laser drilling system located at GSE-CARS, APS. A 95% isotopically-enriched  $^{57}\text{Fe}_{0.9}\text{Ni}_{0.1}$  foil with a thickness of  $15 \mu\text{m}$  is cut into  $60 \times 80 \mu\text{m}^2$  rectangular sections and cleaned. Dehydrated KCl is pressed into transparent flakes and loaded together with the  $^{57}\text{Fe}_{0.9}\text{Ni}_{0.1}$  foil in a sandwich configuration into the Re gasket. The KCl serves as both a pressure-transmitting medium and a thermal insulator. The sample is dehydrated in a vacuum furnace at  $100 \text{ }^\circ\text{C}$ . A few ruby spheres ( $\sim 10 \mu\text{m}$  in diameter) are placed away from the sample and used as pressure markers (Mao *et al.*, 1986). The *in-situ* XRD patterns collected at 3-ID-B indicate that the pressurized  $^{57}\text{Fe}_{0.9}\text{Ni}_{0.1}$  sample is hexagonally-close packed (*hcp*) at 300 K. We constrain the sample's pressure at ambient temperature using both ruby fluorescence and *in-situ* X-ray diffraction. The pressure of this sample at 300 K is thus determined to be  $29 \pm 2 \text{ GPa}$ . For all the example heating runs (e.g., Figures 5.4 and 5.6), the samples were prepared and analyzed in this fashion.

The synchrotron Mössbauer spectroscopy (SMS) experiments to determine melting are similar to those described in Jackson *et al.* (2013). First, the X-ray and laser focal areas are aligned. Then, the sample pressure at 300 K is constrained by collecting *in-situ* X-ray diffraction images and using *hcp* Fe's equation of state (Dewaele *et al.*, 2006). The thermal pressure of the sample is constrained from the diffraction patterns with and without laser heating, where we use *fcc* Fe's equation of state at high temperatures (Komabayashi and Fei, 2010). After an XRD image is collected at 300 K, a 300 K SMS spectrum is collected at the location where the melting measurement is going to be carried out.

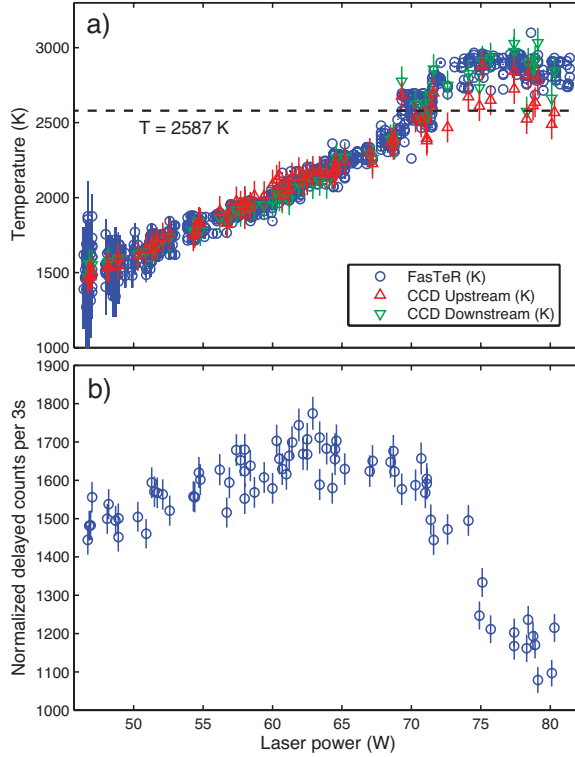


Figure 5.8: Temperature and normalized delayed counts as functions of the laser power. a): Temperature as a function of the laser power. Blue circles: temperatures read by the FasTeR system. Red and Green triangles: best-fit temperatures, determined using the SpecT code (*Shen et al.*, 2001), from the upstream and downstream directions. FasTeR error bar: dark current fluctuation (see text). CCD spectrometer error bar: 100 K. b): Normalized SMS delayed counts per 3s as a function of the laser power. The delayed counts are normalized with respect to the incident X-ray intensity. Error bars are given by the square-root of measured delayed counts. The laser power is read from the laser controller module. The laser output power fluctuation is within 0.5%. The sample's pressure at 300 K is  $P_{300K} = 29 \pm 2$  GPa. Note that the melting point of KCl at 30 GPa is  $3410 \pm 50$  K (*Boehler et al.*, 1996).

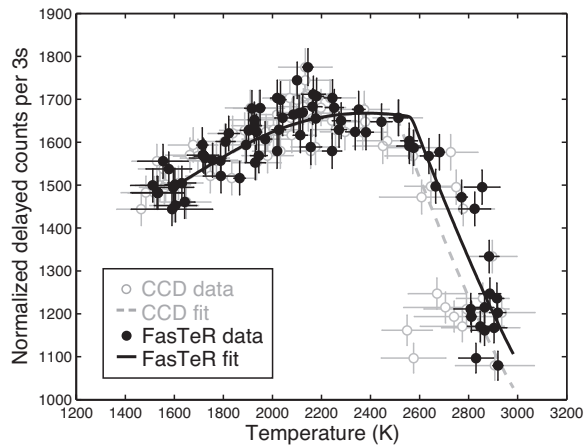


Figure 5.9: Determining the melting temperature of  $\text{Fe}_{0.9}\text{Ni}_{0.1}$  at  $P_{300\text{K}}=29\pm 2$  GPa. Black solid dots: temperatures determined from the FasTeR system. Grey empty circles: temperatures determined from the CCD spectrometer. Black curve: best-fit theoretical curve using the FasTeR data. Grey dashed curve: best-fit theoretical curve using the CCD data. For the FasTeR data,  $\sim 300$  measurements are represented in each temperature value plotted. The error bars of the temperatures are the scattering uncertainties of the  $\sim 300$  FasTeR measurements. Each CCD data point represents the average of the upstream and the downstream CCD temperatures in one measurement, and its error bar is assumed to be the quadrature sum of the front/back temperature gradient and the uncertainty of the temperature reading. The best-fit melting points are  $2587\pm 109$  K for the FasTeR data, and  $2534\pm 112$  K for the CCD data. The best-fit theoretical curves, the melting points and their errors come from SIMX. See text for details on the fitting procedure.

We then preheat the sample and balance the upstream and downstream temperatures at around 1500 K, so that the sample is heated uniformly. Then, we collect a SMS spectrum at this temperature. The hot SMS spectrum provides the effective thickness of the sample at a reference temperature and is used in the fitting routine of the data to determine the melting point. Immediately after collecting the high temperature SMS spectrum, we begin the computer-controlled sequence of a melting run. In this sequence, the laser power is ramped up every 3 seconds and many parameters are recorded, such as the integrated SMS delayed counts, laser power, the intensities of the ion chambers and the temperatures from FasTeR and the CCD spectrometer. The intensity recorded by ion chamber #3 (IC3) is proportional to the total incident X-ray intensity. The integrated SMS delayed signal over 3 seconds is then normalized with respect to the reading of IC3. More details of the data analysis can be found in *Jackson et al. (2013)*. The temperature and the normalized delayed counts are plotted as a function of laser power in Figure 5.8. Immediately after a melting run is completed and the laser power is shut off, the sample is scanned in both x and y directions to verify proper alignment of the X-ray and IR laser focal areas. Finally, an ambient temperature SMS spectrum and an XRD pattern are collected at the same location to constrain the effective thickness and sample pressure after the melting run.

The temperature of the sample is recorded simultaneously by the FasTeR system while ramping up the laser power. Since the FasTeR system has a sampling frequency much higher than that for

SMS, the FasTeR temperature corresponding to each SMS data point is reported as the average of the FasTeR temperature during the integration time (3 s/pt). The CCD temperature corresponding to each SMS data point is reported as the average of the upstream and the downstream CCD temperatures. In each step, there is one upstream CCD temperature and one downstream CCD temperature recorded. The CCD temperatures are fitted using the SpecT code (*Shen et al.*, 2001).

The melting point is determined by fitting the normalized SMS delayed signal as a function of the sample temperature using the SIMX module of the MINUTI software package (Figure 5.9). The melting temperatures with the best fit are 2587 K for the FasTeR data and 2534 for the CCD data, with fitting errors of 22 K and 32 K, respectively. We report the error of the melting point determined from FasTeR as the quadrature sum of the SIMX fitting error (22 K), the average axial surface temperature difference determined from the CCD (35 K), the chromatic aberration (10 K), and the appropriate level of uncertainty assessed from the spectroradiometric method and detailed balance principle (100 K) (*Sturhahn and Jackson*, 2007). The error for the melting temperature determined from the CCD temperatures are computed similarly. Thus, the melting temperatures are  $2587 \pm 109$  K for the FasTeR data, and  $2534 \pm 112$  K for the CCD data.

If one uses the laser power vs. temperature approach to determine melting, i.e. locating the temperature plateau or change in trend as a function of laser power (*Boehler et al.*, 1990; *Boehler*, 1993), a value of  $2864 \pm 219$  K is obtained from FasTeR temperatures. This melting point criteria is based on the premise that the molten phase likely has a higher thermal conductivity or reflectivity than the solid phase (*Geballe and Jeanloz*, 2012). Because the laser's spot size is typically larger than the X-ray's sampling volume and provided there are finite temperature/pressure gradients, the plateau criteria will likely overestimate the melting temperature, as it requires a relatively large volume of the sample to change its thermal conductivity or reflectivity. The method we present here, that is monitoring the atomic dynamics using synchrotron Mössbauer spectroscopy, requires that only the material in the sampled X-ray volume melt, which is a small fraction of the laser's spot size.

We compare our melting point of  $^{57}\text{Fe}_{0.9}\text{Ni}_{0.1}$  at  $P_{300\text{K}} = 29 \pm 2$  GPa with previous studies on pure Fe and an Fe-Ni-Si alloy at similar pressures. Our value of  $2587 \pm 109$  K is close to the reported melting point of pure Fe from *Shen et al.* (2004) ( $2550 \pm 50$  K at  $P_{300\text{K}} = 28$  GPa) and *Jackson et al.* (2013) ( $2500 \pm 115$  K at  $P_{300\text{K}} = 28 \pm 3$  GPa), but higher than the melting point reported by *Boehler et al.* for pure Fe ( $\sim 2400$  K at  $\sim 30$  GPa) (*Boehler et al.*, 1990). Our melting point of  $^{57}\text{Fe}_{0.9}\text{Ni}_{0.1}$  is higher than the melting point of  $\text{Fe}_{0.78}\text{Ni}_{0.04}\text{Si}_{0.18}$  (*Morard et al.* (2011),  $2440 \pm 150$  K at  $P_{300\text{K}} = 28 \pm 1$  GPa), although within mutual reported uncertainties.

## 5.4 Conclusions

A multi-wavelength fast temperature readout spectrometer named FasTeR has been developed at beamline 3-ID-B of the Advanced Photon Source. Working together with nuclear resonant scattering and X-ray diffraction techniques and double-sided laser-heating in the diamond-anvil cell, the FasTeR spectrometer consists of an array of photomultiplier tubes and optical dichroic filters. The benefits of this system are that it features a fast readout rate, high sensitivity, large dynamic range, well-constrained focus, and a relatively simple and inexpensive design. A software tool, SIMFaster, has been developed to simulate FasTeR and assess design configurations.

Example heating runs on different samples have been demonstrated. In this study, experiments were conducted up to about 3000 K, and we see no barrier for the FasTeR spectrometer to determine temperatures higher than 3000 K. Well calibrated, the temperatures determined outside of the vicinity of melting from FasTeR are generally in good agreement with results from the conventional CCD spectrometer.

Dedicated to monitoring the atomic dynamics under extreme conditions, FasTeR overcomes some of the drawbacks of a conventional CCD-based system. Specifically, FasTeR is capable of capturing transient temperature fluctuations, at least on the order of 300 K per s, due to its relatively large dynamic range ( $\sim 10^6$ ). FasTeR's maximum temperature readout rate sampled in this study is 400 Hz, orders of magnitude higher than the CCD-based temperature reading system at the same beamline. We have combined FasTeR with synchrotron Mössbauer spectroscopy to determine the melting temperature of  $^{57}\text{Fe}_{0.9}\text{Ni}_{0.1}$  at high pressure.

The characteristics of FasTeR would also benefit temperature determinations for studies that utilize ultra-fast techniques, such as time-domain thermoreflectance(*Hsieh et al.*, 2009; *Chen et al.*, 2011; *Dalton et al.*, 2013), thermal diffusivity(*Beck et al.*, 2007), measurements using the dynamic diamond-anvil cell(*Velisavljevic et al.*, 2014), pulsed laser-heating(*Goncharov et al.*, 2010; *Yoo et al.*, 2012) and measurements utilizing high-speed periodic shutters(*Toellner et al.*, 2011). The principle design of the FasTeR system is also suitable for shock/ramp compression experiments(*Lyzenga and Ahrens*, 1979; *Loubeyre et al.*, 2004; *Jeanloz et al.*, 2007).

## Chapter 6

# Temperature of Earth's core constrained from melting of Fe and Fe<sub>0.9</sub>Ni<sub>0.1</sub> at high pressures

### 6.1 Introduction

Cosmochemical and seismological studies suggest that Earth's core is primarily composed of iron with ~5-10 wt% nickel, plus ~10 wt% light elements, such as sulfur, oxygen, silicon and carbon (*McDonough and Sun, 1995; Li and Fei, 2003; Deuss, 2014; Hirose et al., 2013*). The core consists of a solid inner section surrounded by a convecting, liquid outer layer (*Lehmann, 1936*). Experiments show that the inclusion of light elements tends to lower the melting point of Fe-rich alloys (e.g., *Boehler 1992; Fei and Bertka 2005; Stewart et al. 2007; Chen et al. 2008; Andrault et al. 2009; Asanuma et al. 2010; Terasaki et al. 2011*, and references therein). The melting temperatures of pure iron and iron alloyed with a few percent nickel therefore provide the basis for understanding expected temperatures in the core. The temperature of the core at the core-mantle boundary (CMB) provides constraints on the heat flow across this boundary and thus affects the age determination of the inner core (*Labrosse et al., 2001*), influences the evolution of the geodynamo (*Olson, 2013*), and controls the temperature gradient within the thermal boundary layer above the CMB (*Anderson, 1990; Lay et al., 2008*).

Among the four crystalline forms of Fe, the high-pressure phases face-centered cubic (*fcc*) and hexagonal close packed (*hcp*) are the primary foci of this study. The melting curve of *fcc* Fe constrains the *fcc-hcp*-liquid ( $\gamma$ - $\epsilon$ -l) triple point, an essential reference point for the melting curve of the *hcp* phase under large compression. However, the high pressure melting curves of *fcc*- and *hcp*-Fe are still controversial, leading to estimated temperatures at the inner core-outer core boundary ranging from 4850 K to 7800 K (*Williams et al., 1987; Boehler et al., 1990; Shen et al., 1998; Jackson et al.,*

---

<sup>0</sup>Revised over what was previously published as *Zhang et al. (2016)*

2013; *Anzellini et al.*, 2013; *Aquilanti et al.*, 2015). In particular, studies of the high pressure melting curve of *fcc*- and *hcp*-Fe-Ni alloys are not available.

Several experimental methods have been used to explore the high pressure melting curves of metals, among which the laser heated diamond anvil cell (LH-DAC) is the most common (e.g., *Boehler* 1993; *Errandonea et al.* 2001; *Shen et al.* 2004; *Dewaele et al.* 2007, 2010; *Jackson et al.* 2013; *Anzellini et al.* 2013; *Zhang et al.* 2015). In LH-DAC experiments, the temperature determination is usually less accurate and precise than the pressure determination. One major contribution to the temperature uncertainty in LH-DAC experiments are rapid temporal fluctuations (10-100 Hz) of the sample temperature during the experiment (*Jeanloz and Heinz*, 1984; *Zhang et al.*, 2015). These fluctuations are likely a result of the coupling between laser light and sample surface, and at temperatures close to a sample's melting point  $\sim 0.3\%$  of laser power fluctuation can lead to temperature fluctuations of up to 200 K (*Jeanloz and Heinz*, 1984; *Jeanloz and Kavner*, 1996). Also slower (1 Hz) temperature fluctuations of several hundreds of Kelvin have been reported for samples near their melting points (*Dewaele et al.*, 2007, 2010; *Anzellini et al.*, 2013; *Zhang et al.*, 2015). This magnitude of temperature fluctuation presents a challenge for accurately and precisely determining the melting temperature of a sample.

Melting experiments in a LH-DAC typically ramp up the laser power quickly (seconds to minutes) to convert the sample from solid to liquid. Therefore, a fast temperature readout system whose sampling frequency exceeds that of the melting diagnostic is necessary to obtain reliable sample temperatures with high precision. We have developed a multi-wavelength temperature readout spectrometer named FasTeR to address this issue (*Zhang et al.*, 2015). The FasTeR system features a well-calibrated sampling rate of 100 Hz (and up to at least 400 Hz) with large dynamic range, high sensitivity, and a well-constrained optical aperture. This new system is located at beamline 3-ID-B of the Advanced Photon Source (APS) at Argonne National Laboratory, IL and described in detail elsewhere (*Zhang et al.*, 2015).

In this study, we combine the LH-DAC, the FasTeR spectrometer, and synchrotron Mössbauer spectroscopy to constrain the high pressure melting curves of *fcc*- and *hcp*-structured  $^{57}\text{Fe}_{0.9}\text{Ni}_{0.1}$  and  $^{57}\text{Fe}$  up to pressures of 125 GPa. The Mössbauer signal that scatters from the sample prior to melting is sensitive to the movement of the iron nuclei (*Singwi and Sjölander*, 1960; *Boyle et al.*, 1961), and thus provides a unique diagnostic for the solid-liquid transition of Fe-rich materials (*Jackson et al.*, 2013).

## 6.2 Experiments

### 6.2.1 Sample preparation

The Fe-Ni sample used in this study was synthesized at Caltech. Individual pieces of Ni and 95%-enriched  $^{57}\text{Fe}$  are selected with an accuracy of 1.0 mg to produce 50 mg of  $\text{Fe}_{0.9}\text{Ni}_{0.1}$ . The Fe and Ni pieces are arc-melted in an argon atmosphere, then cold rolled to a physical thickness of about 13  $\mu\text{m}$ . The elemental composition of the Fe-Ni sample is determined by a JEOL JXA-8200 electron probe micro-analyzer (EPMA) at Caltech's Microanalysis Center. Quantitative data are acquired in focused mode, using wavelength-dispersive spectrometry, operating at 15 kV accelerating voltage and 20 nA beam current. Pure Fe, Ni and Re metal standards are used for the analysis. No elements other than Fe and Ni are detected within the uncertainty. EPMA analysis of 25 sampled regions gives an average composition of  $\text{Fe}_{0.91(1)}\text{Ni}_{0.09(1)}$  for the  $^{57}\text{Fe}$ -Ni alloy, where the numbers in parentheses indicate the uncertainties in the last digit, hereafter referred to as  $\text{Fe}_{0.9}\text{Ni}_{0.1}$  for simplicity. The 95% isotopically enriched  $^{57}\text{Fe}$  and  $\text{Fe}_{0.9}\text{Ni}_{0.1}$  foils with thicknesses ranging from 9 to 15  $\mu\text{m}$  are cut into rectangular sections with an EDM and cleaned. The sizes of the sections range from about  $55 \times 55 \mu\text{m}^2$  to  $80 \times 80 \mu\text{m}^2$ . The  $^{57}\text{Fe}$  samples used in this study are cut from the same larger foils used in a previous melting study (*Jackson et al.*, 2013).

In each melting run, a symmetric DAC is used to provide the high pressure environment. Two quarter-carat Type-I diamonds with culet sizes ranging from beveled 250 to 300  $\mu\text{m}$  in diameter are mounted on backing plates (WC or cBN) and aligned to form the anvils. A Re gasket is pre-indented to  $\sim 45 \mu\text{m}$  thickness, and to form the sample chamber, a hole is drilled in the center of the pre-indentation using an EDM or a laser drilling system. The sample chamber's size ranges from 80 to 115  $\mu\text{m}$  in diameter, depending on the diamond culet size. Dehydrated KCl is pressed into transparent flakes and loaded together with an individual pre-cut  $^{57}\text{Fe}_{0.9}\text{Ni}_{0.1}$  or  $^{57}\text{Fe}$  foil in a sandwich configuration into the sample chamber. The KCl serves as both a pressure-transmitting medium and thermal insulation. A few ruby spheres ( $\sim 10 \mu\text{m}$  in diameter) are placed away from the sample and used as pressure markers (*Mao et al.*, 1986). The DAC is first purged in a chamber filled with purified Ar gas and then heated in a vacuum furnace before closing to remove oxygen and moisture. After the DAC is sealed, pressure is increased to the approximate desired range and laser annealed to about 1500 K before the X-ray experiments. The laser annealing is essential to determine sample coupling behavior with the IR laser and to relax any stresses induced by cold compression. When possible, X-ray diffraction is collected *in-situ* to constrain the pressure of the sample.

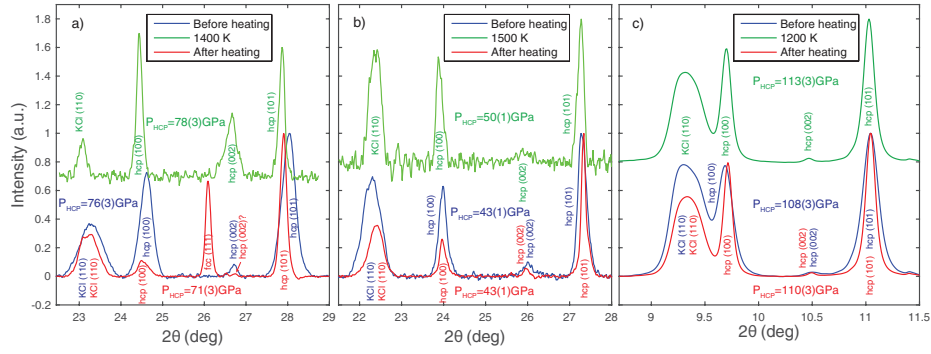


Figure 6.1: X-ray diffraction patterns collected before (300 K, blue), during (green) and after (300 K, red) typical melting runs. Panels a,c and b show results for  $\text{Fe}_{0.9}\text{Ni}_{0.1}$  and Fe, respectively. Diffraction patterns in panels a and b are collected at APS 3-ID-B with an X-ray wavelength of 0.086026 nm corresponding to an energy of 14.4125 keV (1 meV bandwidth). Panel c shows data collected at APS 13-ID-D with an X-ray wavelength of 0.0344 nm corresponding to an energy of 36.0 keV (1 eV bandwidth). The X-ray focal spots are aligned to the melted areas on the sample.

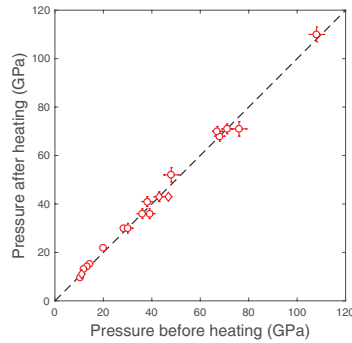


Figure 6.2: Comparison of the pressures determination at 300 K using XRD of pre-heated samples (horizontal axis) and post-melted samples (vertical axis). The black dashed line is the identity line. Circles:  $\text{Fe}_{0.9}\text{Ni}_{0.1}$ . Diamonds: Fe. Pressures are calculated from *fcc*- and *hcp*-iron's equation of state (Dewaele *et al.*, 2006; Komabayashi, 2014).

### 6.2.2 Synchrotron Mössbauer spectroscopy measurements

The dynamics of the iron atoms are used as a diagnostic to detect melting and are probed using nuclear resonant forward scattering, also known as synchrotron Mössbauer spectroscopy (SMS) (*Jackson et al.*, 2013). As explained previously, the observed time-delayed signal is caused by coherent elastic scattering of synchrotron X-rays while traversing a sample containing  $^{57}\text{Fe}$  or another accessible nuclear resonant isotope (*Jackson et al.*, 2013). The emission of the SMS signal occurs into the direction of the incident X-rays and is independent of the spatial positions of atoms. The strength of the SMS signal is primarily determined by the effective thickness of the sample traversed by the X-rays. The effective thickness,  $\eta$ , is a dimensionless number given as the product of the numerical density of the  $^{57}\text{Fe}$  nuclei,  $\rho$ , the physical thickness of the sample,  $d$ , the nuclear resonant cross section,  $\sigma = 2.56 \times 10^{-22}\text{m}^2$  for  $^{57}\text{Fe}$ , and the dimensionless temperature-dependent Lamb-Mössbauer factor,  $f$

$$\eta = \rho d \sigma f \quad . \quad (6.1)$$

The experiments are carried out at beamline 3-ID-B of the APS, which uniquely features nuclear resonant scattering techniques coupled with *in-situ* double-sided laser heating, a new FasTeR temperature measurements system, conventional CCD-based spectrometers, and X-ray diffraction (*Zhao et al.*, 2004; *Gao et al.*, 2009; *Jackson et al.*, 2013; *Zhang et al.*, 2015). The storage ring is operated in low-emittance top-up mode with 24 bunches that are separated by 153 ns. The energy (14.4125 keV) and resolution (1 meV) of the X-rays are determined by a silicon high resolution monochromator (*Toellner*, 2000), and a focus area of  $\sim 10 \times 11 \mu\text{m}^2$  (full width at half maximum) is achieved by a Kirkpatrick-Baez mirror system (*Eng et al.*, 1998; *Zhang et al.*, 2015). In-situ X-ray diffraction images are collected on the compressed samples at the same beamline to obtain the crystal symmetry and pressure of the sample (Figs. 6.1 and 6.2). This is achieved by moving a high resolution MAR image plate (Marresearch GmbH), located 0.3 m downstream of the DAC, into the X-ray path. Some diffraction patterns are collected at APS beamline 13-ID-D using a MARCCD detector (Rayonix) (Fig. 6.1c), where 36.0 keV X-rays with 1 eV bandwidth are focused to  $\sim 3 \times 3 \mu\text{m}^2$ .  $\text{CeO}_2$  and  $\text{LaB}_6$  standards are used to calibrate the sample to image plate distance and correct for the tilt of the image plate at 3-ID-B and 13-ID-D. The diffraction images are integrated into angular resolved files using the DIOPTAS software (*Prescher and Prakapenka*, 2015).

After a diffraction image is collected, the image plate is moved out of the X-ray path for the series of SMS measurements that constrain the melting point. The SMS signal is captured by an avalanche photodiode detector placed  $\sim 0.5$  m downstream of the sample. For each melting run, a high-statistical quality reference SMS spectrum is collected for about 10 minutes at 300 K at the sample position where the melting measurement will be carried out. The sample is then scanned in

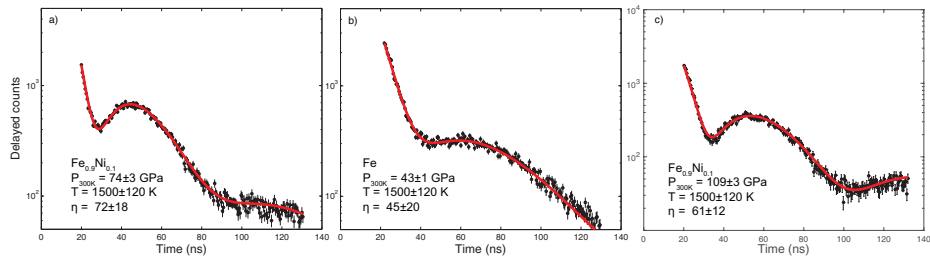


Figure 6.3: SMS spectra of  $^{57}\text{Fe}_{0.9}\text{Ni}_{0.1}$  and  $^{57}\text{Fe}$  at high pressures and high temperatures. Each spectrum is collected for about 10 minutes. The SMS spectra provide the time window and are fitted to the profile given by Equation (6.2) to determine the effective thickness. The red curves show the best-fits. The temperature shown here is determined from an average of the upstream and downstream CCD and FasTeR spectrometers over the data collection time. Pressures and their errors at 300 K are shown. a):  $^{57}\text{Fe}_{0.9}\text{Ni}_{0.1}$  at  $P_{300\text{K}}=74\pm 3$  GPa and  $1500\pm 120$  K. The best-fit effective thickness is  $72\pm 18$ . b):  $^{57}\text{Fe}$  at  $P_{300\text{K}}=43\pm 1$  GPa and  $1500\pm 120$  K. The best-fit effective thickness is  $45\pm 20$ . c):  $^{57}\text{Fe}_{0.9}\text{Ni}_{0.1}$  at  $P_{300\text{K}}=109\pm 3$  GPa and  $1500\pm 120$  K. The best-fit effective thickness is  $61\pm 12$ .

both x and y directions to record sample topography with respect to alignment of the X-ray and IR laser focal areas. Then, we preheat the sample to about 1500 K, balancing the laser power upstream and downstream to achieve similar CCD readout temperatures, thus suggesting a uniformly heated sample. Another high-statistical quality SMS spectrum is collected at this elevated temperature (Fig. 6.3). This particular SMS spectrum provides the timing window and effective thickness of the sample at a reference elevated temperature immediately preceding the melting run, both necessary for later determination of the melting point.

Before discussing the next sequence of events for melting temperature determination, we describe the profile,  $S(t, \eta)$ , of the time resolved delayed counts, the SMS spectrum. The SMS spectrum depends on the level splitting of the resonant nuclei, the effective thickness of the sample,  $\eta$  (as described above), and the time,  $t$ , relative to the excitation by the X-ray pulse. For *fcc* and *hcp* Fe and  $\text{Fe}_{0.9}\text{Ni}_{0.1}$ , it is known that the nuclear levels of  $^{57}\text{Fe}$  are un-split (*Macedo and Keune, 1988*). Therefore  $S$  reduces to

$$S(t, \eta) = \eta^2 e^{-t/\tau} \frac{J_1^2(\sqrt{\eta t/\tau})}{\eta t/\tau}, \quad (6.2)$$

where  $J_1$  is the first order Bessel function of the first kind, and  $\tau$  is the life time of the excited nuclear state (141 ns for  $^{57}\text{Fe}$ ) (e.g., *Sturhahn 2000; Jackson et al. 2013*). The sample's effective thickness at 1500 K, which is also the initial effective thickness for the melting run, is then obtained by fitting the measured SMS spectrum to the profile given by Equation (6.2).

Melt detection using SMS aims at measuring the effective thickness as defined by Equation (6.1) as a function of temperature. In the liquid state, the Lamb-Mössbauer factor and thus the effective thickness vanishes. In an experiment, the measurement of the time-integrated SMS signal is therefore

sufficient if the nuclear level splitting is known as in our case. The measured time-integrated SMS signal is then given by

$$I(\eta) = A e^{-\mu d} \sum_{n=0}^{\infty} \int_{t_1+nt_B}^{t_2+nt_B} S(t', \eta) dt' \quad . \quad (6.3)$$

Here  $t_1$  and  $t_2$  are the beginning and end of the accessible time window,  $t_B$  is the time interval between subsequent X-ray pulses (given by the synchrotron operation mode, here  $t_B=153$  ns),  $n$  is indexing X-ray pulses into the past,  $A$  is a scaling factor that depends on experimental conditions such as spectral X-ray flux incident on the sample,  $d$  is the physical thickness of the sample,  $\mu$  is the electronic absorption coefficient of the sample material,  $S$  is the profile of the SMS spectrum specified in Equation (6.2), and  $\eta$  is the temperature-depended effective thickness of the sample (*Jackson et al.*, 2013).

After collecting a high temperature SMS spectrum, we immediately proceed to a computer-controlled acquisition sequence, which constitutes the melting run. In this sequence, the laser power is ramped up every 3 seconds while recording salient parameters, such as laser power, time-integrated SMS spectrum (delayed counts), X-ray intensities upstream and downstream of the sample via ionization chambers, and temperature readouts from FasTeR and the CCD spectrometer. The downstream X-ray intensity is used to normalize the time-integrated SMS spectrum which accounts for the electronic absorption term in Equation (6.3) and for potential upstream X-ray intensity fluctuations. As described in *Zhang et al.* (2015), the temperature of the sample is recorded simultaneously by the FasTeR system and by upstream/downstream CCD spectrometers. Since the FasTeR system has a high sampling frequency, the FasTeR temperature is reported as the average of about 300 samplings for each 3 s interval. The temperature obtained from the CCD-based spectrometer is measured once for each 3 s interval using the Spect code (*Shen et al.*, 2001) and is reported as the average of upstream and downstream temperatures. The CCD-based spectrometer in this study tends to underestimate the sample temperature compared to the FasTeR measurement, because the CCD-based spectrometer has a slightly larger aperture (*Zhang et al.*, 2015). Therefore, the temperatures determined from the FasTeR system are used in determination of the melting temperatures (Tables 6.1 & 6.2, Section 3.2). Sample temperature and normalized time-integrated delayed counts are shown as a function of laser power for three typical melting runs in Figure 6.4. One can see that the duration of a melting run typically ranges from about two to four minutes.

Immediately after a melting run is completed on a localized region of the sample, the laser power is shut off, and a SMS spectrum is acquired. The sample is then scanned in both x and y directions to assess whether sample topography has changed with respect to scans before the melting run (i.e., to re-confirm that the sample area is relatively flat). Finally, we determine the sample pressure using in situ XRD (or ex situ ruby fluorescence) to document a potential pressure drift during the experiment.

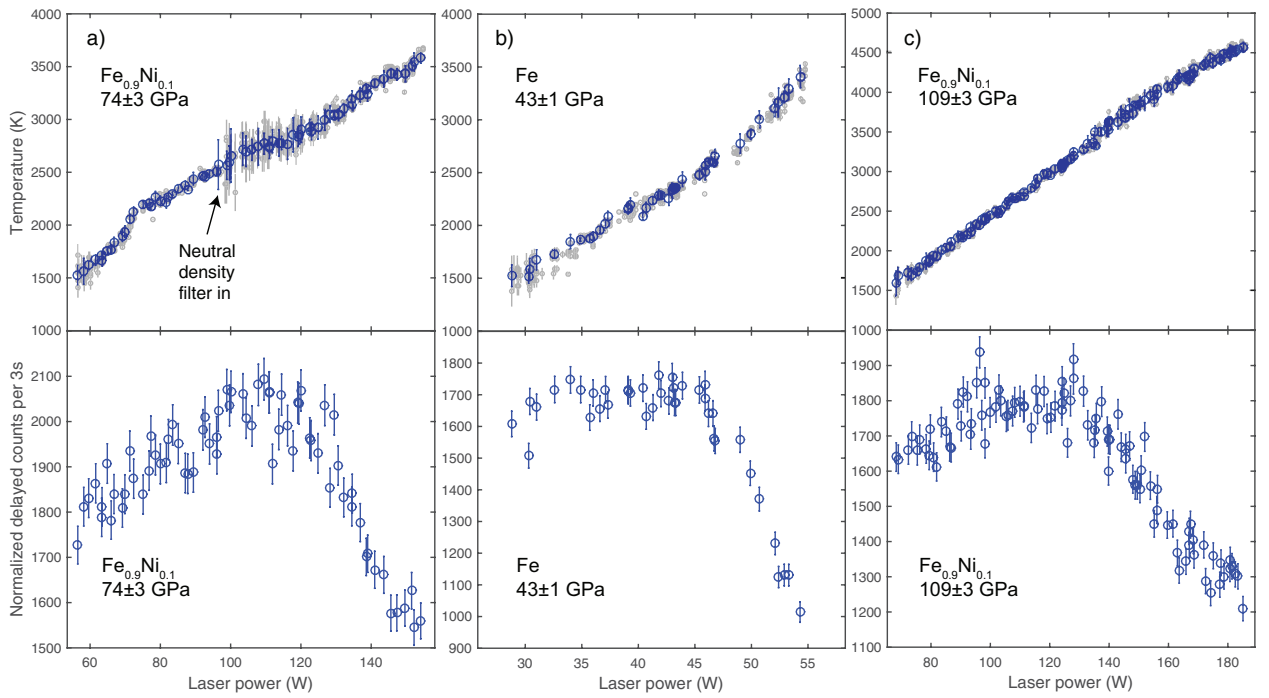


Figure 6.4: Temperatures and time-integrated normalized delayed counts as a function of laser power. Sample composition, pressure and pressure error at 300 K are indicated in each panel. Temperatures are determined by the FasTeR system. Both un-binned (light grey) and binned (blue) temperatures are shown in the top panels. Binned temperatures and their standard deviations are used in determining the melting temperatures (Figure 6.6). The melting run in panel a required insertion of a neutral density filter at  $\sim 100$  W laser power to avoid saturation. Panels a and c display data corresponding to melting runs D1R9 and D4R3 in Table 6.1. Panel b display data corresponding to melting run D6R6 in Table 6.2. The duration of a melting run typically ranges from about two to four minutes.

The pressure of the sample at 300 K is reported as the average of the pressures determined before and after heating. We also examine the Ni/Fe atomic ratios of the melted and unmelted regions on one Fe<sub>0.9</sub>Ni<sub>0.1</sub> sample (recovered from D1R9, Tab. 6.1) using the EPMA facility at Caltech. The average Ni/Fe atomic ratio for the unmelted regions is  $9.91 \times 10^{-2} \pm 6.5 \times 10^{-3}$  (25 data points), and the average Ni/Fe atomic ratio for the melted regions is  $9.51 \times 10^{-2} \pm 1.19 \times 10^{-2}$  (18 data points). The Ni/Fe atomic ratios in the melted regions have more scatter because the melted regions have more relief at the surface. Within our experimental uncertainty, there is no clear evidence for nickel segregation in the melted regions.

## 6.3 Results and Discussion

### 6.3.1 Thermal contribution to the pressure

In all of our experiments, *hcp*-structured Fe and Fe<sub>0.9</sub>Ni<sub>0.1</sub> are observed at 300 K. The thermal equations of state from *Komabayashi* (2014) and *Dewaele et al.* (2006) are used to calculate the pressures for *fcc*- and *hcp*-phases, respectively. The pressures determined from ruby fluorescence and XRD are consistent within their relatively large error bars. Pressure uncertainties determined from the rubies are large due to their spread in values around the sample chamber and/or changes during a melting run. The quoted uncertainty for pressure determined using XRD can be large due to the limited number of accessible diffraction peaks at 14.4125 keV, despite the use of cBN backing plates. The final pressure we report is that determined from XRD (when available), measured at the same location on the sample where it is melted. In some of the melting runs, we collect a series of diffraction images, first at 300 K before heating, then at high temperatures to constrain the trend of thermal contribution to pressure, and finally at 300 K after heating, to constrain potential pressure drifts (Fig. 6.1, Section 2.2).

In order to determine the thermal pressure contribution at the sample's melting point, we assume that: *fcc*-Fe and *fcc*-Fe<sub>0.9</sub>Ni<sub>0.1</sub> share the same thermoelastic parameters as *hcp*-Fe and *hcp*-Fe<sub>0.9</sub>Ni<sub>0.1</sub>; thermal pressure is only a function of temperature. The first assumption has been adopted by an XRD study using resistive heating (*Komabayashi et al.*, 2009) and is observed in LH-DAC XRD experiments (*Anzellini et al.*, 2013). The addition of ~10% Ni is suggested to have minor effect on the thermal pressure determination (*Komabayashi et al.*, 2012). The second assumption is supported by nuclear resonant inelastic scattering experiments on *hcp*-Fe at high pressures which report a weak volume dependence of the vibrational thermal pressure up to 171 GPa (*Murphy et al.*, 2011).

At the melting temperature  $T_m$ , the sample's pressure can be written as

$$P(T_m) = P(T_0) + P_{th}(T_m) \quad , \quad (6.4)$$

where  $P(T_0)$  is the pressure at reference temperature  $T_0 = 300$  K. The thermal pressure

$$P_{th}(T_m) = a(T_m - T_0) + c(T_m^2 - T_0^2) \quad (6.5)$$

has two contributions: a linear term arising from the harmonic component of the vibrational thermal pressure; a quadratic term originating from the anharmonic and electronic components (*Anderson*, 1980; *Dewaele et al.*, 2006; *Murphy et al.*, 2011). Values of  $a = (4.6 \pm 0.5) \times 10^{-3}$  GPa/K and  $c = (0.2 \pm 3.4) \times 10^{-6}$  GPa<sup>2</sup>/K<sup>2</sup> are obtained from a best fit to data from our high P-T diffraction measurements (Figs. 6.1 and 6.5).

For reference, we also show thermal pressures determined from recent high pressure and tem-

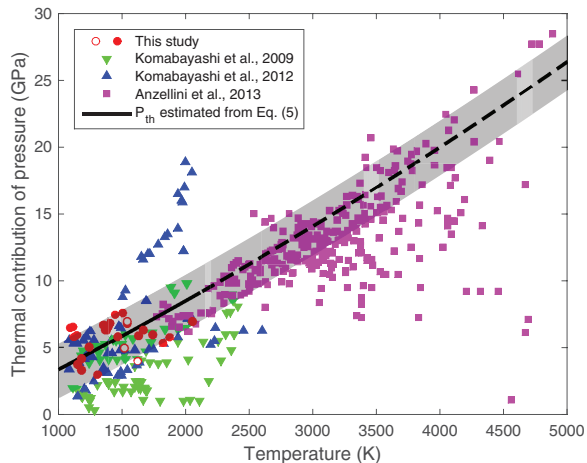


Figure 6.5: Thermal pressure derived from XRD data at high pressure and temperature. Pressures of the data points at 300 K range from 10 GPa to 150 GPa. Solid circles (this study): XRD data taken at 13-ID-D. Empty circles (this study): XRD data taken at 3-ID-B. Black curve (this study): thermal contribution to pressure estimated from Equation (6.5). Grey shaded region: estimated uncertainty of the thermal contribution to pressure. The dashed part of the curve is extrapolated. Resistive heating and optical spectroscopy temperature reading are used in *Komabayashi et al.* (2009, 2012). *fcc*- and *hcp*-Fe’s equations of state from *Komabayashi* (2014) and *Dewaele et al.* (2006) are used to determine the pressure.

perature XRD studies on Fe and Fe-Ni (*Komabayashi et al.*, 2009, 2012; *Anzellini et al.*, 2013). A subset of the data from *Komabayashi et al.* (2009, 2012) and *Anzellini et al.* (2013) shows signs of relaxation during heating as pressure changes significantly when temperature is increased. Because *Anzellini et al.* (2013) didn’t provide the volumes (pressures) of the Fe sample at 300 K, we cannot directly compare their thermal pressures with our results. Instead, we compare the relative pressure change between two different elevated temperatures. We assume that in each heating run from *Anzellini et al.* (2013) the thermal pressure of the first data point follows Equation (6.5), and the thermal pressures of subsequent data points in the same heating run are calculated by integration of subsequent relative pressure changes. The thermal pressure trend as a function of temperature defined by Equation (6.5) is slightly higher than that observed by *Anzellini et al.* (2013) (Fig. 6.5). In general, the thermal pressures observed in these studies are about half of the constant-volume values for *hcp*-Fe from an *ab initio* calculation (*Dewaele et al.*, 2006) and nuclear resonant inelastic X-ray scattering measurements (*Murphy et al.*, 2011). A similar effect was reported for laser-heated platinum in an argon medium (*Goncharov et al.*, 2010). Based on the scatter in these independent measurements, we assess a reasonable error estimate on the thermal pressure (Tables 6.1 & 6.2).

### 6.3.2 Melting temperature determination

The melting temperatures of Fe and  $\text{Fe}_{0.9}\text{Ni}_{0.1}$  are determined by fitting the measurable quantity, namely normalized delayed counts, as a function of sample temperature using the SIMX module

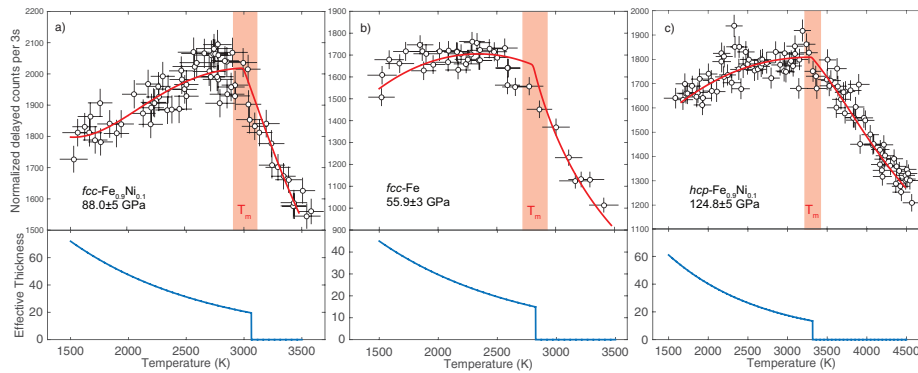


Figure 6.6: Time-integrated normalized delayed counts (top panels) and calculated effective thicknesses (bottom panels) as a function of temperature for typical melting runs. Panels a and c display data corresponding to melting runs D1R9 and D4R3 in Table 6.1. Panel b displays data corresponding to melting run D6R6 in Table 6.2. Sample composition and pressure are indicated in each panel. Pressure values include the thermal contribution at the melting point, and temperatures are determined using the FasTeR spectrometer. The solid curves result from fits using the SIMX module of the MINUTI software package. Best-fit melting temperatures are indicated as the red bands in the figure. Best-fit melting temperatures are: panel a,  $T_m = 3059 \pm 106$  K,  $\chi^2 = 1.4 \pm 0.1$ ; panel b,  $T_m = 2835 \pm 114$  K,  $\chi^2 = 1.5 \pm 0.2$ ; panel c,  $T_m = 3317 \pm 104$  K,  $\chi^2 = 1.1 \pm 0.1$ .

of the MINUTI software package (Fig. 6.6). The effective thickness of the sample is determined immediately before the melting run begins, at around 1500 K (Fig. 6.3). The laser’s hotspot profile is estimated from optical observation, and the X-ray focus profile is determined by knife-edge scanning. Both profiles are provided as inputs to SIMX to determine the effective thickness distribution weighted by the X-ray intensity distribution. From Equations (6.2) and (6.3) and the assumption of zero effective thickness of melted material, SIMX calculates the normalized delayed intensity as a function of sample temperature and provides a fit to the measured data. For the fitting procedure, uncertainties of temperature and of the time-integrated normalized delayed counts must be provided. The latter are simply given as the square root of accumulated counts in the collection span (3 s in our case), and the temperature uncertainties are the sum of the standard deviation of all FasTeR readings during the 3 s collection span (Fig. 6.4), the root-mean-square value of the dark current fluctuation, and chromatic aberration, as described in detail previously (Zhang *et al.*, 2015). These uncertainties are displayed in Figure 6.6. The fitting error of the melting point, along with its associated reduced  $\chi^2$  value from SIMX are reported in Tables 6.1 & 6.2. The uncertainty for a melting temperature is reported as the quadrature sum of the SIMX fitting error, the temperature difference of values given by the upstream and downstream CCD-based spectrometers, chromatic aberration of the CCD system (about 10 K), and the appropriate level of uncertainty assessed from the spectroradiometric method and detailed balance principle (100 K) (Sturhahn and Jackson, 2007; Zhang *et al.*, 2015). The melting temperatures, pressures, and all associated parameters obtained in this study are summarized in Tables 6.1 & 6.2.

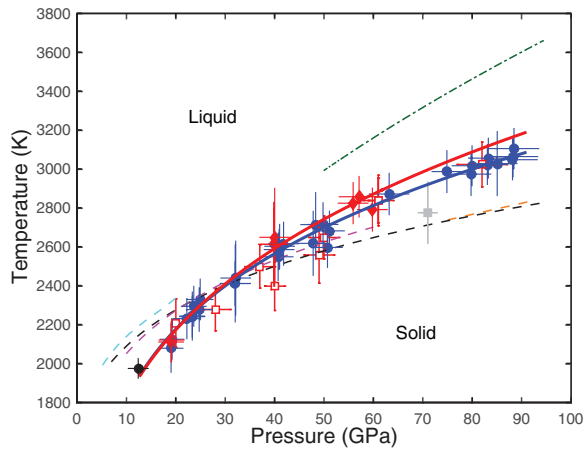


Figure 6.7: Melting points of *fcc*-structured Fe and  $\text{Fe}_{0.9}\text{Ni}_{0.1}$ . Solid blue circles and red diamonds (this study):  $\text{Fe}_{0.9}\text{Ni}_{0.1}$  and Fe. Blue and red solid curves (this study): best-fits for  $\text{Fe}_{0.9}\text{Ni}_{0.1}$  and Fe using Equation (6.6). The following studies include thermal contributions: empty squares (*Jackson et al.*, 2013), dark green dash-dotted curve (*Anzellini et al.*, 2013), orange dashed curve (*Aquilanti et al.*, 2015), grey square: shock compression (*Ahrens et al.*, 2002). Black solid circle: *Strong et al.* (1973), corrected with thermal contribution of pressure using Equation (6.5). The following studies did not consider thermal pressure: black dashed curve (*Boehler et al.*, 1990; *Boehler*, 1993), magenta dashed curve (*Shen et al.*, 1998, 2004), cyan dashed curve (*Liu and Bassett*, 1975). All experiments except for *Ahrens et al.* (2002) were carried out with laser-heated diamond anvil cells.

### 6.3.3 Melting curves of the *fcc*-phases and triple points

Melting temperatures and pressures obtained in this study (Tables 6.1 & 6.2) are now used to construct melting curves of *fcc*-structured Fe and  $\text{Fe}_{0.9}\text{Ni}_{0.1}$  (Figure 6.7). The reported pressures include the 300 K value and the high temperature contribution. The 300 K pressures are determined before and after the melting runs on annealed samples by X-ray diffraction (or ruby fluorescence), and the high temperature contributions are calculated from Equation (6.5) as outlined in Section 3.1. At ambient pressure, a very narrow two-phase field, reported to be less than 10 K wide (*Cacciamani et al.*, 2010), exists for *fcc*- $\text{Fe}_{0.9}\text{Ni}_{0.1}$  and liquid. However, the precision of our high-pressure measurements is not sufficient to identify such a coexistence region.

The shape of the melting curve has been modeled previously using the empirical Simon-Glatzel equation (*Murphy et al.*, 2011; *Anzellini et al.*, 2013)

$$T_m = T_{m0} \left( \frac{P_m - P_{m0}}{x} + 1 \right)^y, \quad (6.6)$$

where melting points ( $P_m$ ,  $T_m$ ) are related to a reference melting point ( $P_{m0}$ ,  $T_{m0}$ ), and  $x, y$  are adjustable, material specific parameters. In our study, the best-fit parameters are:  $T_{m0}=2194\pm 100$  K,  $P_{m0}=21.4\pm 0.9$  GPa,  $x=20\pm 5$  GPa, and  $y=0.25\pm 0.04$  for Fe;  $T_{m0}=2199\pm 100$  K,  $P_{m0}=21.5\pm 0.7$  GPa,  $x=18\pm 3$  GPa, and  $y=0.22\pm 0.02$  for  $\text{Fe}_{0.9}\text{Ni}_{0.1}$ . The corresponding melting curves are shown in Figure 6.7. Considering uncertainties, these melting curves overlap in the tails of their one sigma

confidence regions.

The  $\gamma$ - $\epsilon$ -l triple points of Fe and  $\text{Fe}_{0.9}\text{Ni}_{0.1}$  are constrained by the  $\gamma$ - $\epsilon$  phase boundary reported in previous studies. *Komabayashi et al.* (2009) and *Komabayashi et al.* (2012) measured the  $\gamma$ - $\epsilon$  boundary of Fe and an Fe-9.7 wt% Ni alloy using resistively-heated DACs and X-ray diffraction. They reported the slope of the phase boundary  $dP/dT$  as 0.0394 GPa/K (at 88 GPa, 2800 K) for Fe and as 0.0426 GPa/K (at 61.8 GPa, 1992 K) for Fe-9.7 wt% Ni alloy, respectively. In principle, a  $\gamma$ - $\epsilon$ -l triple point is not meaningful for an alloy such as  $\text{Fe}_{0.9}\text{Ni}_{0.1}$ , because melting should be described by a solidus and liquidus. Within our experimental resolution however, the solidus and liquidus of  $\text{Fe}_{0.9}\text{Ni}_{0.1}$  coincide and are addressed as the melting curve of  $\text{Fe}_{0.9}\text{Ni}_{0.1}$ . Accordingly we define a quasi  $\gamma$ - $\epsilon$ -l triple point for  $\text{Fe}_{0.9}\text{Ni}_{0.1}$  as the intersection of  $\gamma$ - $\epsilon$  phase boundary and melting curve. By combining the *fcc*-*hcp* boundaries from *Komabayashi et al.* (2009, 2012) and our *fcc* melting curves, the  $\gamma$ - $\epsilon$ -l triple points of Fe and  $\text{Fe}_{0.9}\text{Ni}_{0.1}$  are calculated to be  $110\pm 5$  GPa,  $3345\pm 120$  K and  $116\pm 5$  GPa,  $3260\pm 120$  K, respectively (Fig. 6.8). The triple point of Fe is found at higher temperature and lower pressure than the quasi triple point of  $\text{Fe}_{0.9}\text{Ni}_{0.1}$ , a trend suggested by ambient pressure experiments (see *Cacciamani et al.* 2010 and references therein).

### 6.3.4 Melting curves of the *hcp*-phases

Two melting experiments are carried out for  $\text{Fe}_{0.9}\text{Ni}_{0.1}$  at pressures above 100 GPa. The pressure of the  $\text{Fe}_{0.9}\text{Ni}_{0.1}$  sample at room temperature is  $109\pm 3$  GPa, determined by XRD (Tab. 6.1). The same sample is melted twice at two locations, spatially separated by  $\sim 20$   $\mu\text{m}$ . The best-fit melting temperatures of the two runs are  $3383\pm 102$  K and  $3317\pm 104$  K as determined by SIMX. The thermal contribution according to Equation (6.5) is included to provide pressures at melting as  $125\pm 3$  GPa and  $124.8\pm 3$  GPa, respectively (Fig. 6.8). These melting points are at higher pressures and temperatures than the quasi  $\gamma$ - $\epsilon$ -l triple point, and we can infer that melting of the *hcp*-phase of  $\text{Fe}_{0.9}\text{Ni}_{0.1}$  was observed in these two melting runs. In order to extrapolate the high pressure melting curves of *hcp*-structured Fe and  $\text{Fe}_{0.9}\text{Ni}_{0.1}$  to inner core conditions, we apply the Simon-Glatzel Equation (6.6) and the (quasi) triple points determined earlier as anchor points,  $T_{m0}$  and  $P_{m0}$ . The other two parameters in the Simon-Glatzel equation are obtained from the phonon density-of-states of *hcp*-Fe measured by nuclear resonant inelastic X-ray scattering by a procedure outlined in section 4 of *Murphy et al.* (2011). This method makes the reasonable assumption that the vibrational behavior of *hcp*-structured Fe and  $\text{Fe}_{0.9}\text{Ni}_{0.1}$  are very similar. Then the best-fit parameters in the Simon-Glatzel equation are:  $x = 171\pm 20$  GPa,  $y = 0.63\pm 0.08$  for *hcp*- $\text{Fe}_{0.9}\text{Ni}_{0.1}$ , and  $x = 167\pm 20$  GPa,  $y = 0.64\pm 0.08$  for *hcp*-Fe. These melting curves, which are shown in Figure 6.8, predict for *hcp*- $\text{Fe}_{0.9}\text{Ni}_{0.1}$  a melting temperature of  $3370\pm 120$  K at 125 GPa, demonstrating consistency with the measured values of  $3383\pm 102$  K and  $3317\pm 104$  K.

Melting curves of Fe-Ni alloys at high pressures were not reported previously, but a comparison

Table 6.1: Experimental results and melting points of  $\text{Fe}_{0.9}\text{Ni}_{0.1}$  determined by synchrotron Mössbauer spectroscopy.

<i>fcc-Fe<sub>0.9</sub>Ni<sub>0.1</sub></i>										
Run number	Volume <sup>a</sup> (cc/mol)	P <sub>XRD</sub> (GPa)	P <sub>ruby</sub> (GPa)	P <sub>m</sub> (GPa)	Density <sup>b</sup> g/cm <sup>3</sup>	Effective thickness	SIMX reduced $\chi^2$	SIMX fitting error (K)	Time window (ns)	T <sub>m</sub> (K)
D1R2	6.38±0.02	10.1±0.4	10±1	19.0±2.4	8.93±0.03	89±20	0.7±0.3	72	10.1-124.6	2081±123
D1R1	6.38±0.02	10.1±0.4	10±1	19.2±2.4	8.93±0.03	124±22	0.9±0.2	22	10.1-124.6	2127±102
D10R4	NA	NA	12.5±0.8	22.2±2.8	(9.0±0.1)	100±22	0.9±0.2	26	16.1-136.0	2233±103
D10R1	NA	NA	13.6±0.5	23.3±2.5	(9.07±0.05)	43±15	1.0±0.3	71	18.0-137.3	2246±123
D10R3	NA	NA	13.6±0.5	23.3±2.5	(9.07±0.05)	53±26	1.2±0.2	29	12.3-135.2	2243±104
D10R2	NA	NA	13.6±0.5	23.6±2.5	(9.07±0.05)	70±17	0.7±0.2	22	12.3-135.2	2296±102
D9R2	NA	NA	14.7±0.6	24.7±2.6	(9.12±0.07)	45±26	0.9±0.2	48	12.5-136.2	2279±111
D9R1	NA	NA	14.7±0.6	24.9±2.6	(9.12±0.07)	73±42	0.6±0.2	30	11.2-136.2	2331±104
D7R2	NA	NA	21.3±1	32.0±3	(9.4±0.1)	35±15	1.1±0.4	100	18.9-135.7	2411±141
D7R3	NA	NA	21.3±1	32.0±3	(9.4±0.1)	55±25	0.8±0.4	38	19.0-136.1	2410±107
D7R1	NA	NA	21.3±1	32.1±3	(9.4±0.1)	31±11	1.9±0.6	130	19.6-135.7	2423±164
D9R5	NA	NA	29.3±1	40.7±3	(9.6±0.1)	61±9	1.5±0.3	84	15.8-135.9	2530±131
D9R3	NA	NA	29.3±1	40.9±3	(9.6±0.1)	63±15	0.8±0.1	21	15.9-136.5	2574±103
D9R4	NA	NA	29.3±1	41.0±3	(9.6±0.1)	70±14	1.1±0.2	62	16.1-135.4	2602±112
D1R5	5.95±0.05	30.0±1	30.0±3	41.8±3	9.6±0.1	106±35	2.1±0.3	57	18.2-139.5	2645±115
D1R3	5.92±0.04	36.0±1	38.0±2	47.8±3	9.8±0.1	16±9	1.1±0.3	130	15.8-135.8	2619±164
D1R4	5.92±0.04	36.0±1	38.0±2	48.3±3	9.8±0.1	16±9	2.9±0.4	130	15.8-135.8	2715±164
D3R1	5.76±0.04	37.5±1	39.0±3	49.8±3	9.9±0.1	43±20	1.1±0.3	48	19.3-132.7	2716±111
D8R1	5.76±0.04	39.0±1	37.5±2	50.7±3	9.9±0.1	68±18	1.3±0.2	21	16.4-139.5	2598±102
D8R2	5.76±0.04	39.0±1	37.5±2	51.1±3	9.9±0.1	45±26	1.0±0.2	14	18.0-139.5	2683±101
D1R6	5.62±0.06	50.0±2	52.0±3	63.2±4	10.2±0.2	102±19	1.4±0.2	55	16.1-132.6	2882±114
D8R5	5.44±0.05	61.0±1	63.0±3	74.9±3	10.5±0.1	76±13	1.3±0.2	55	16.1-133.4	2966±114
D1R10	5.38±0.04	66.0±2	66.8±3	79.8±4	10.6±0.1	64±30	1.4±0.2	44	15.9-130.5	2974±109
D1R11	5.38±0.04	66.0±2	66.8±3	80.0±4	10.6±0.1	74±14	1.2±0.1	19	16.0-131.5	3017±102
D8R3	5.37±0.05	69.0±2	63.0±3	83.1±4	10.7±0.1	82±14	0.7±0.2	22	16.0-135.6	3023±102
D8R4	5.37±0.05	69.0±2	63.0±3	83.3±4	10.7±0.1	72±13	1.2±0.2	21	16.0-135.9	3056±102
D4R1	5.34±0.03	71.0±2	71.0±2	85.1±4	10.7±0.1	90±24	4.9±0.4	130	17.9-132.8	3028±164
D1R9	5.28±0.04	74.0±3	74.3±2	88.0±5	10.8±0.2	72±15	1.4±0.1	36	15.9-136.3	3059±106
D1R8	5.28±0.04	74.0±3	74.3±2	88.2±5	10.8±0.2	109±18	1.6±0.2	66	16.0-136.3	3061±114
D1R7	5.28±0.04	74.0±3	74.3±2	88.5±5	10.8±0.2	104±18	1.2±0.1	38	15.7-136.1	3103±107

<i>hcp-Fe<sub>0.9</sub>Ni<sub>0.1</sub></i>										
Run number	Volume <sup>a</sup> (cc/mol)	P <sub>XRD</sub> (GPa)	P <sub>ruby</sub> (GPa)	P <sub>m</sub> (GPa)	Density <sup>b</sup> g/cm <sup>3</sup>	Effective thickness	SIMX reduced $\chi^2$	SIMX fitting error (K)	Time window (ns)	T <sub>m</sub> (K)
D4R3	4.96±0.04	109.0±3	112.0±5	124.8±5	11.5±0.1	61±12	1.1±0.1	27	19.6-132.5	3317±104
D4R2	4.96±0.04	109.0±3	112.0±5	125.0±5	11.5±0.1	64±13	1.1±0.1	19	19.6-132.4	3383±102

*quasi  $\gamma$ - $\epsilon$ -l triple point*

P: 116±5 GPa

T: 3260±120 K

DXY = DAC X Run Y. <sup>a</sup>: In some melting runs the limited angular access of backing plates prevented diffraction peaks to be observed (NA: not applicable), therefore pressures are determined from fluorescence of ruby spheres. <sup>b</sup>:

Values in parentheses are calculated from pressure via the *fcc*-Fe (Komabayashi (2014)) or *hcp*-Fe (Dewaele *et al.* (2006)) equations of state. P<sub>m</sub> is determined by adding the thermal contribution (Equation 6.5) at the melting temperature to the pressure at 300 K.

Table 6.2: Experimental results and melting points of Fe determined by synchrotron Mössbauer spectroscopy.

<i>fcc-Fe</i>										
Run number	Volume <sup>a</sup> (cc/mol)	P <sub>XRD</sub> (GPa)	P <sub>ruby</sub> (GPa)	P <sub>m</sub> (GPa)	Density <sup>b</sup> g/cm <sup>3</sup>	Effective thickness	SIMX reduced $\chi^2$	SIMX fitting error (K)	Time window (ns)	T <sub>m</sub> (K)
D10R5	6.42±0.04	10.0±0.5	11.1±1	19.0±2.5	8.88±0.05	49±12	1.7±0.4	25	15.8-135.7	2116±103
D10R6	6.42±0.04	10.0±0.5	11.1±1	19.1±2.5	8.88±0.05	53±12	2.2±0.4	43	15.8-135.8	2123±119
D6R1	NA	NA	28.0±1	39.8±3	(9.6±0.1)	27±11	0.9±0.2	190	17.8-136.4	2614±215
D6R2	NA	NA	28.0±1	39.8±3	(9.6±0.1)	28±10	0.6±0.2	150	18.0-135.6	2614±180
D6R3	NA	NA	28.0±1	40.0±3	(9.6±0.1)	18±11	1.4±0.3	230	17.8-135.7	2650±251
D6R6	5.70±0.03	43.0±1	42.3±2	55.9±3	10.0±0.1	49±14	1.5±0.2	54	21.1-136.3	2835±114
D6R5	5.69±0.03	44.0±2	42.3±2	57.1±4	10.0±0.2	47±15	0.9±0.2	29	21.0-136.5	2858±104
D6R4	5.65±0.03	47.0±1	42.3±2	59.8±3	10.1±0.1	53±14	0.5±0.1	45	21.2-135.6	2792±110

 *$\gamma$ - $\epsilon$ -l triple point*

P: 110±5 GPa

T: 3345±120 K

DXY = DAC X Run Y. <sup>a</sup>: In some melting runs the limited angular access of backing plates prevented diffraction peaks to be observed (NA: not applicable), therefore pressures are determined from fluorescence of ruby spheres. <sup>b</sup>:

Values in parentheses are calculated from pressure via the *fcc*-Fe (Komabayashi (2014)) or *hcp*-Fe (Dewaele *et al.* (2006)) equations of state. P<sub>m</sub> is determined by adding the thermal contribution (Equation 6.5) at the melting temperature to the pressure at 300 K.

of the obtained melting curves for Fe with previous studies is possible. A wide range of criteria were used in those studies to determine melting: *Liu and Bassett* (1975) and *Boehler et al.* (1990) measured the resistivity of Fe at different temperatures; *Williams et al.* (1987), *Boehler et al.* (1990), and *Boehler* (1993) monitored the surface properties of Fe, such as optical reflectivity, texture and convective motion; diffuse scattering observed in an XRD setup has been used recently (*Shen et al.*, 1998, 2004; *Anzellini et al.*, 2013); X-ray absorption spectroscopy is used to monitor the phase transitions of Fe (*Aquilanti et al.*, 2015).

These methods have different sensitivities to the onset of melting. Monitoring the surface properties is not sensitive to the interior of the sample, and can be dependent on sample-specific surface and interface properties. X-ray based methods, such as monitoring diffuse scattering (X-ray diffraction), short-range coordination environment (X-ray absorption), and atomic dynamics (synchrotron Mössbauer spectroscopy), are more sensitive to the entire scattering volume of the sample. Thermal diffuse scattering is sensitive to the average electronic arrangement of the material during the X-ray diffraction exposure time (*Shen et al.*, 2004; *Dewaele et al.*, 2007, 2010; *Anzellini et al.*, 2013). The presence of melt is identified by the appearance of broad diffuse rings in the X-ray diffraction pattern characterizing the disappearance of long range coordination environments in the melt. The thermal diffuse scattering signal must be discriminated against a relatively large background signal and likely requires a large volume of melt in the scattering volume. X-ray absorption spectroscopy monitors the average short-range coordination of the absorbing atoms rendering a subtle change upon melting.

Synchrotron Mössbauer spectroscopy is sensitive only to the resonant nuclei in the sample and is a background free diagnostic method when used in combination with time discrimination techniques. The intensity of the time-integrated signal from synchrotron Mössbauer spectroscopy reflects the microscopic range of movement of the iron nuclei. As the solid sample transitions to a liquid state, atoms experience an enhanced freedom of motion. For the iron nuclei this results in the absence of recoil-free scattering events. The Mössbauer signal, which is a consequence of recoil-free scattering, consequently disappears in the liquid state and drops markedly in a solid-liquid mixture (*Singwi and Sjölander*, 1960; *Boyle et al.*, 1961; *Jackson et al.*, 2013; *Zhang et al.*, 2015). These significant differences in criteria may explain the higher melting temperatures reported for Fe using thermal diffuse scattering (Figs. 6.7, 6.8), as they are likely to represent upper bounds. The marked drop in the Mössbauer signal reliably captures the first melt to form in the sampled volume. In combination with well-calibrated temperature data from the FasTeR instrument, high-quality melting temperatures for Fe and  $\text{Fe}_{0.9}\text{Ni}_{0.1}$  can be obtained.

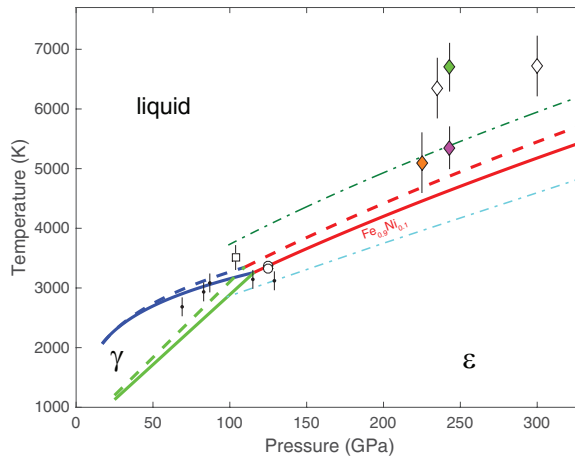


Figure 6.8: Phase boundaries of Fe and  $\text{Fe}_{0.9}\text{Ni}_{0.1}$ . Dashed curves and solid curves are for Fe and  $\text{Fe}_{0.9}\text{Ni}_{0.1}$ , respectively (this study), where the  $\gamma$ - $\epsilon$  boundaries of Fe and  $\text{Fe}_{0.9}\text{Ni}_{0.1}$  are adapted from *Komabayashi et al.* (2009, 2012). The empty circles are for  $hcp\text{-Fe}_{0.9}\text{Ni}_{0.1}$  (this study, error bars are smaller than the symbols). Dash-dotted curves: Fe  $\epsilon$ -l boundary (dark green: *Anzellini et al.* 2013, cyan: *Boehler* 1993). Black dots: Fe solid-liquid boundary, (*Boehler et al.*, 2008). Empty square:  $hcp\text{-Fe}$  in LH-DAC, XRD (*Ma et al.*, 2004). Diamonds:  $hcp\text{-Fe}$ , shock compression experiments (orange: *Nguyen and Holmes* 2004, magenta: *Brown and McQueen* 1986, green: *Bass et al.* 1987, empty: *Yoo et al.* 1993).

### 6.3.5 Implications for the temperature in Earth's core

The high pressure melting curves of  $fcc$  and  $hcp$  structured Fe and  $\text{Fe}_{0.9}\text{Ni}_{0.1}$  constrained in this study allow us to predict the temperature in Earth's core. It is commonly assumed that addition of light elements to Fe depresses the melting point of iron alloys (*Alfè et al.*, 2002). Therefore the melting temperatures of  $hcp\text{-Fe}$  and  $hcp\text{-Fe}_{0.9}\text{Ni}_{0.1}$  at 330 GPa serve as an upper bound for the temperature at Earth's inner core-outer core boundary ( $T_{\text{ICB}}$ ) (*Lehmann*, 1936; *Terasaki et al.*, 2011). An extrapolation of our melting curves for  $hcp\text{-Fe}$  and  $hcp\text{-Fe}_{0.9}\text{Ni}_{0.1}$  predicts upper bounds for  $T_{\text{ICB}}$  of  $5700 \pm 200$  K and  $5500 \pm 200$  K, respectively (Fig. 6.8). In this study, we assume that  $hcp\text{-Fe}_{0.9}\text{Ni}_{0.1}$  is a more likely base composition for the core than pure  $hcp\text{-Fe}$ , and consequently we proceed with  $hcp\text{-Fe}_{0.9}\text{Ni}_{0.1}$ 's melting curve to constrain the upper bound of  $T_{\text{ICB}}$ .

The thermal profile in the core is commonly derived from an adiabatic model, for which the temperature gradient in the outer core is given by (*Poirier*, 2000)

$$\frac{\partial T}{\partial z} = \frac{g\gamma_{th}}{\Phi} T \quad , \quad (6.7)$$

where  $T$  is temperature,  $z$  is depth,  $g$  is gravitational acceleration,  $\gamma_{th}$  is the thermodynamic Grüneisen parameter, and  $\Phi$  is the seismic parameter. We use the gravitational acceleration data from the PREM model (*Dziewonski and Anderson*, 1981) and the seismic parameter from the AK135 global seismic model (*Kennett et al.*, 1995). For compressed liquid iron,  $\gamma_{th}$  was reported as

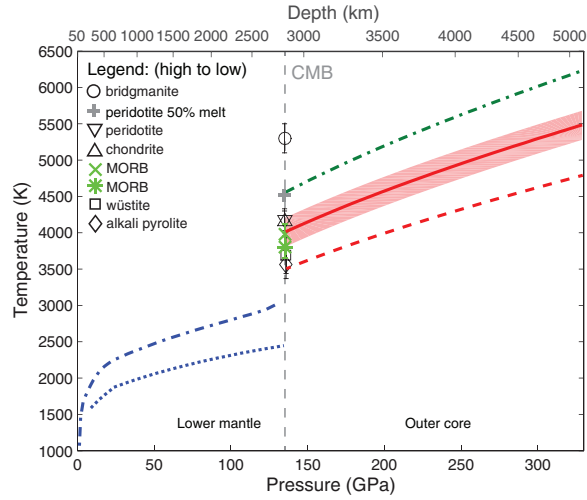


Figure 6.9: Proposed thermal profiles of Earth's interior and melting points of minerals. Blue curves: proposed geotherms (dotted: *Brown and Shankland* 1981; dashed: *Stacey* 1977). Red solid curve: outer core temperature profile calculated from inferred melting temperature of  $hcp\text{-Fe}_{0.9}\text{Ni}_{0.1}$  at 330 GPa, this study, red shaded region gives error estimate. Red dashed curve: outer core temperature profile calculated from our study and accounting a 700 K melting point depression at the ICB from light elements (*Alfè et al.*, 2002). Dark green dash-dotted curve: outer core temperature profile calculated from inferred melting temperature of  $hcp\text{-Fe}$  at 330 GPa (*Anzellini et al.*, 2013). Circle: bridgmanite melting point (*Akins et al.*, 2004). Gray cross: peridotite containing about 50% melt (*Tateno et al.*, 2014). Reversed triangle: peridotite solidus (*Fiquet et al.*, 2010). Triangle: chondrite solidus (*Andrault et al.*, 2011). Green cross: MORB solidus (*Pradhan et al.*, 2015), extrapolated value from data between 44 and 128 GPa. Green asterisk: MORB solidus (*Andrault et al.*, 2014). Square: wüstite melting point (*Fischer and Campbell*, 2010), extrapolated value from data between 0 and 77 GPa. Diamond: alkali pyrolite solidus (*Nomura et al.*, 2014). The depth scale is taken from the Preliminary Reference Earth Model (*Dziewonski and Anderson*, 1981).

ranging between 1.56 at 257 GPa and 1.47 at the ICB from shock-compression experiments (*Brown and McQueen, 1986*) and calculated as ranging between 1.5 and 1.53 in the outer core (*Alfè et al., 2002*). After combining these results into an average, we use  $\gamma_{th} = 1.51$  and, with *hcp*-Fe<sub>0.9</sub>Ni<sub>0.1</sub>'s melting point of  $5500 \pm 200$  K at the ICB, we obtain a temperature of  $4000 \pm 200$  K at the core side of the CMB at  $z = 2891$  km,  $P = 136$  GPa (Fig. 6.9).

The temperature of  $4000 \pm 200$  K that we obtain for the core side of the CMB is slightly lower than the solidus temperature of peridotitic ( $4180 \pm 150$  K, *Fiquet et al. 2010*) and chondritic lower mantle assemblages ( $4150 \pm 150$  K, *Andrault et al. 2011*) at 135 GPa (albeit in the mutual uncertainties). The extrapolated melting point of wüstite at  $P = 136$  GPa is 3690 K (*Fischer and Campbell, 2010*). A very low solidus temperature of an alkali-rich pyrolitic sample was reported to be  $3570 \pm 200$  K at the CMB (*Nomura et al., 2014*). The alkalic pyrolite starting material contains a significant amount of volatile elements (400 ppm water,  $\sim 0.4$  wt% Na<sub>2</sub>O and  $\sim 0.05$  wt% K<sub>2</sub>O) not present in other experiments (*Fiquet et al., 2010; Andrault et al., 2011*), and volatile elements are known to depress the solidus temperatures of mantle assemblages (*Hirschmann et al., 1998; Corgne et al., 2003; Andrault et al., 2011*).

We conduct similar calculations with the melting curve of *hcp*-Fe reported by *Anzellini et al. (2013)*. Their melting temperature at 330 GPa is  $6230 \pm 500$  K, which corresponds to a temperature of 4560 K at the core-mantle boundary using the adiabat described above. This temperature is much higher than the solidus of peridotitic (*Fiquet et al., 2010; Nomura et al., 2014*) and chondritic (*Andrault et al., 2011*) phase assemblages at the CMB, suggesting that roughly half of the base of the mantle should be molten (*Tateno et al., 2014*) (Fig. 6.9).

Although the Earth's core is mainly composed of an iron-nickel alloy, the seismologically inferred density requires the presence of light elements to balance the density deficit. Therefore, the lower bound on the temperature profile in the core depends on the species of light elements and how these elements affect the melting behavior of iron and iron-nickel alloys. Experimental and theoretical investigations suggest that light elements such as S, O, and Si alloyed with iron could depress the melting point of iron by up to 700 K at the ICB (e.g., *Alfè et al. 2002*). If one considers a relatively extreme melting point depression of 700 K on the temperature at the ICB inferred from *hcp*-Fe<sub>0.9</sub>Ni<sub>0.1</sub>'s melting point of 5500 K (this study), then the temperature at the ICB would be 4800 K. If the adiabat is unchanged with the addition of light elements, then the core-side CMB temperature could be as low as 3500 K (Fig. 6.9). *Terasaki et al. (2011)* measured the phase relations of a candidate core-alloy of atomic composition Fe<sub>75</sub>O<sub>5</sub>S<sub>20</sub> up to 157 GPa and concluded that, assuming its existence in Earth's core and comparing to previous studies on pure iron, the CMB temperature could be  $3600 \pm 200$  K. We have observed that alloying about 10wt% nickel to iron could result in a melting point depression relative to pure iron of about 290 K or about 5 % at the ICB. Thus it is conceivable that the melting temperatures of light element alloys of *hcp*-Fe<sub>0.9</sub>Ni<sub>0.1</sub> would

be further depressed than the values considered in *Terasaki et al.* (2011) .

One major implication of the temperature constraints considered here is the effect on phase relations at the base of the mantle. Fits to seismic waves that sample the base of the mantle suggest ultra-low velocity zones ranging from 10's to 100 km in width and height (*Berryman, 2000; Ni and Helmberger, 2001; Lay et al., 2004; McNamara et al., 2010; Sun et al., 2013; Thorne et al., 2013*). These features are often attributed to partial melt of lower mantle materials (*Williams and Garnero, 1996; Berryman, 2000; Lay et al., 2004; Labrosse et al., 2007; Hier-Majumder, 2008*). A recent dynamic compression study suggests that a peridotitic lowermost mantle rock is unlikely to produce an equilibrium partial melt that is sufficiently dense to match seismic inferences of about +5 to 14 % density anomalies (*Thomas and Asimow, 2013*). A similarly compelling explanation of seismic observations is solid material with low seismic velocities, such as Fe-rich (Mg,Fe)O magnesiowüstite (*Wicks et al., 2010; Bower et al., 2011; Sun et al., 2013; Rost, 2013*). These hypotheses could be assessed by examination of the solidus temperatures reported for candidate mantle phases and assemblages at the CMB in comparison with the temperature ranges reported for this region. The presence of partial melts at the base of the mantle is feasible if a sufficient amount of light elements would depress the solidus of silicate phase assemblages, so that the geotherm of the lowermost mantle intersects the solidus at just the right value and angle to generate a reasonable amount of melt.

## 6.4 Conclusion

The melting points of *fcc*- and *hcp*-structured  $\text{Fe}_{0.9}\text{Ni}_{0.1}$  and Fe have been measured up to 125 GPa. We carried out these measurements with LH-DACs using newly developed techniques involving synchrotron Mössbauer spectroscopy, the FasTeR spectrometer, and the MINUTI software package. The SIMX module in MINUTI is used to reliably fit a melting point to the observed signal. We place the  $\gamma$ - $\epsilon$ -1 triple point of Fe at  $110\pm 5$  GPa and  $3345\pm 120$  K, and the quasi triple point of  $\text{Fe}_{0.9}\text{Ni}_{0.1}$  at  $116\pm 5$  GPa and  $3260\pm 120$  K. With the (quasi)  $\gamma$ - $\epsilon$ -1 triple points and the thermophysical parameters of *hcp*-Fe determined from a nuclear resonant inelastic X-ray scattering dataset (*Murphy et al., 2011*), we constructed high pressure melting curves of *hcp*-structured Fe and  $\text{Fe}_{0.9}\text{Ni}_{0.1}$ . We suggest that the upper bound of Earth's inner-core outer-core boundary temperature is given by *hcp*- $\text{Fe}_{0.9}\text{Ni}_{0.1}$ 's melting point, rather than by pure iron. With an ICB temperature of  $5500\pm 200$  K for *hcp*- $\text{Fe}_{0.9}\text{Ni}_{0.1}$ , we use an adiabatic thermal model to derive the upper bound for the temperature on the core side of the CMB as  $4000\pm 200$  K. This temperature is lower than the solidus of typical lower mantle assemblages. With the addition of light elements such as a combination of sulfur, oxygen, and silicon, the core-side CMB temperature could be as low as 3500 K. These newly constrained temperature bounds will help determine the range of permissible phase assemblages and transport properties at the core-mantle and inner core-outer core boundaries.

## Chapter 7

# Concluding remarks

In this thesis, I summarize the high pressure nuclear resonant scattering experiments on iron-bearing materials that I have involved in since 2008. Iron-bearing minerals are broadly distributed in the Earth, from the crust to the core (e.g., *Sturhahn and Jackson 2007, Frost 2008, Fiquet et al. 2008* and references therein), and their elastic (e.g., *Zhang et al. 2013a*) and thermodynamic (e.g., *Jackson et al. 2013*) properties under extreme P-T conditions are of general importance to the geodynamic modeling (e.g., *Bower et al. 2011*) and the interpretation of seismic-wave observations (e.g., *Zhang et al. 2013a*). An accurate laboratory determination of these properties provides constraints to determine the composition (e.g., *Zhang et al. 2013a*) and temperature of Earth's interior (e.g., *Jackson et al. 2013*). Nuclear resonant scattering is an advanced synchrotron based spectroscopic technique, which helps further our understanding of candidate materials in Earth's interior, including but not limited to site-specific chemical environment (*Zhang et al., 2011*), elasticity (*Zhang et al., 2013a*) and melting temperature (*Jackson et al., 2013*). The principles of nuclear resonant scattering and X-ray diffraction, and the details of our experiments are summarized in Chapters 1 and 2. For the geophysical part, the first mineral discussed in this thesis is enstatite (Chapters 3 & 4), which is believed to be one of the major components in the upper mantle. Other examples include iron and iron-nickel alloy, which are relevant to the cores of terrestrial planets (Chapters 5 & 6).

### 7.1 Earth's upper mantle

Enstatite is an abundant silicate mineral in the upper mantle, and recent studies suggest it endures several structural transitions at high pressures (*Zhang et al., 2011, 2012; Dera et al., 2013; Zhang et al., 2013b; Finkelstein et al., 2014*). Chapter 3 focuses on the pressure induced structural transitions of enstatite. Nuclear resonant scattering is capable of detecting subtle changes in the mineral's hyperfine parameters, and can therefore be sensitive to the transitions occurring in minerals under pressure. The site-specific hyperfine behavior of iron in a  $^{57}\text{Fe}$ -enriched powdered enstatite sample has been explored using synchrotron Mössbauer spectroscopy and diamond

anvil cells in two independent experiments with different pressure media (NaCl and Ne). The  $(\text{Mg}_{0.980}\text{Fe}_{0.020(5)})(\text{Mg}_{0.760}\text{Fe}_{0.240})\text{Si}_2\text{O}_6$  sample is pressurized up to 36 GPa at ambient temperature, and this chemical formula is determined by fitting synchrotron Mössbauer spectra. Analyses of data sets reveal a discontinuity in the hyperfine parameters between 10 and 12 GPa, indicative of a structural transformation in enstatite. On the other hand, the structural transitions are different in the two independent experiments, because the behaviors of the hyperfine parameters deviate from each other, which probably come from the pressure media. The NaCl pressure medium produces a larger non-hydrostatic stress environment than the Ne medium (*You et al.*, 2009). The hyperfine parameters of the iron sites, such as the isomer shift and the quadrupole splitting, have been measured as functions of pressure in both pressure media. The site-specific behaviors and their relation with the local stress conditions are explored. The M1 site is smaller in volume than the M2 site, and the M2-site distorts more quickly with pressure than the M1 site. Recent researches show that some of the candidate high pressure structural transitions of enstatite are metastable (*Kung et al.*, 2004; *Jahn*, 2008; *Zhang et al.*, 2012; *Finkelstein et al.*, 2014), and this study provides information about how the local stress environment can influence the high pressure behavior of enstatite.

Chapter 4 focuses on the elastic properties of iron-bearing enstatite at high pressures. The research methods include X-ray powder diffraction (XRD), nuclear resonant inelastic X-ray scattering (NRIXS) and first principle calculation. The same synthetic powdered  $^{57}\text{Fe}$ -enriched  $(\text{Mg}_{0.980}\text{Fe}_{0.020(5)})(\text{Mg}_{0.760}\text{Fe}_{0.240})\text{-Si}_2\text{O}_6$  enstatite is explored by XRD and NRIXS. The *Pbca*-structured enstatite sample was compressed in fine pressure increments for our XRD measurements and one structural transition between 10.1 and 12.2 GPa is identified from the XRD data, resulting a  $P2_1/c$  phase at high pressures. The partial phonon density of states (DOS) is derived from the raw nuclear resonant inelastic X-ray scattering data up to 17 GPa, and from the low-energy region of the DOS, the Debye sound velocity is determined. We use the equation of state determined from XRD and Debye sound velocity to compute the isotropic compressional and shear wave velocities of enstatite at different pressures. We combine density-functional theory with nuclear resonant scattering to understand the local site symmetry of the Fe atoms in our sample, and the calculation is consistent with our synchrotron Mössbauer spectroscopy study, showing that Fe atoms dominantly occupy the M2 site. The *Pbca-P2<sub>1</sub>/c* transition is associated with a  $\sim 4\%$  shear velocity softening. Besides elasticity, other thermodynamic parameters at different pressures are also accessed from the NRIXS data.

The experimental data is used to answer some questions with geophysical interest. The structural transitions of enstatite is usually associated with the mantle X-discontinuity (*Woodland*, 1998; *Kung et al.*, 2004; *Akashi et al.*, 2009). The sound velocity measurement in this study indicates that the *Pbca-P2<sub>1</sub>/c* transition can't explain the X-discontinuity, which has a shear impedance increase of 3 to 7.5% (*Revenaugh and Jordan*, 1991). The *Pbca-C2/c* transition of enstatite alone is not enough

to cover the shear impedance increase of X-discontinuity. Therefore, other possibilities, such as structural transition of silica (*Woodland, 1998*) or incorporation of water in mantle assemblages (*Jacobsen et al., 2010*) also contribute to the X-discontinuity. On the other hand, currently it is difficult to assess the stress environment in the mantle, especially near the subduction region. The structural transition of enstatite in the non-hydrostatic environment may be responsible for some geophysical phenomena close to the subduction.

## 7.2 Cores of terrestrial planets

The cores of terrestrial planets are associated with not only high pressure, but also high temperature. So to simulate the environment of the cores, we need to heat the sample, and to constrain the temperature of the sample well. Laser heated diamond anvil cell is capable of generating pressure-temperature conditions similar to the core environment, but it usually associates with a rapid temperature fluctuation. To capture the sample's transient temperature fluctuations and reduce uncertainties in melting temperatures, we develop a Fast Temperature Readout spectrometer named FasTeR in-line with nuclear resonant scattering measurements under extreme conditions at Sector 3-ID-B of the Advanced Photon Source at Argonne National Laboratory. Chapter 5 describes the FasTeR system in detail. Dedicated to determining the sample's temperature near its melting point, FasTeR features a fast readout rate (about 100 Hz), high sensitivity, large dynamic range and well-constrained focus. FasTeR is capable of reading out temperatures about 1 to 2 magnitudes faster than the conventional CCD spectrometer, without sacrificing accuracy, and is especially suitable for dynamic measurements at extreme conditions.

Recently, synchrotron Mössbauer spectroscopy (SMS) has been shown to be a powerful probe in determining the solid-liquid boundary of iron-bearing materials (e.g., *Jackson et al. 2013*). The characteristic SMS time signal vanishes when melting occurs. This process is described by the Lamb-Mössbauer factor, a quantity that is directly related to the mean-square displacement of the Fe atoms. FasTeR has been successfully combined with SMS measurements on compressed Fe and  $\text{Fe}_{0.9}\text{Ni}_{0.1}$  to determine the melting curves by monitoring the dynamics of the atoms. Chapter 6 focuses on the melting studies and their geophysical implications. The melting temperatures of *fcc*-structured Fe and  $\text{Fe}_{0.9}\text{Ni}_{0.1}$  is determined at high pressures. The melting curve of *fcc*-Fe is slightly higher than the melting curve of *fcc*- $\text{Fe}_{0.9}\text{Ni}_{0.1}$ , but the difference is smaller than the uncertainty. The pressure dependence of the melting temperature of *fcc*-structured Fe and  $\text{Fe}_{0.9}\text{Ni}_{0.1}$  can be described using the Simon-Glatzel equation:  $T_M = T_{M0}(\frac{P_M - P_{M0}}{x} + 1)^y$ . By intersecting the melting curves of *fcc*-structured Fe and  $\text{Fe}_{0.9}\text{Ni}_{0.1}$  with the the corresponding  $\gamma$ - $\epsilon$  boundaries (*Komabayashi et al., 2009, 2012*), the  $\gamma$ - $\epsilon$ -l triple point of  $\text{Fe}_{0.9}\text{Ni}_{0.1}$  is determined as  $116 \pm 5$  GPa and  $3260 \pm 120$  K, and  $110 \pm 5$  GPa and  $3345 \pm 120$  K for Fe. With the  $\gamma$ - $\epsilon$ -l triple points of Fe and  $\text{Fe}_{0.9}\text{Ni}_{0.1}$ , and the

thermophysical parameters of *hcp*-Fe determined from a NRIXS measurement (*Murphy et al.*, 2011), the high pressure melting curves of *hcp*-structured Fe and  $\text{Fe}_{0.9}\text{Ni}_{0.1}$  can be computed. Further SMS melting data are collected for *hcp*  $\text{Fe}_{0.9}\text{Ni}_{0.1}$  to confirm its melting curve. We suggest that the upper bound of Earth's inner-core outer-core boundary temperature is given by *hcp*- $\text{Fe}_{0.9}\text{Ni}_{0.1}$ 's melting point, rather than by pure iron. With an ICB temperature of  $5500\pm 200$  K for *hcp*- $\text{Fe}_{0.9}\text{Ni}_{0.1}$ , we use an adiabatic thermal model to derive the upper bound for the temperature on the core side of the CMB as  $4000\pm 200$  K. This temperature is lower than the solidus of typical lower mantle assemblages. With the addition of light elements such as a combination of sulfur, oxygen, and silicon, the core-side CMB temperature could be as low as 3500 K. Therefore, given the melting curves of candidate dominant core materials presented here, light element melting point depressions, and reported phase relations of volatile-free lower mantle assemblages, the solid-state assemblages are more likely to be present at Earth's core-mantle boundary. These newly constrained temperature bounds will help determine the range of permissible phase assemblages and transport properties at the core-mantle and inner core-outer core boundaries.

## Appendix A

# Appendix

Table A.1 summarizes all the high pressure experiments related to this thesis between 2008 and 2015. The first two beamtimes (2008 October and 2009 March) are related to Chapter 3. The next two beamtimes (2009 July and 2011 February) are related to Chapter 4. All the other seven beamtimes (2012 April, 2012 June, 2013 February, 2013 July, 2013 November, 2014 February and 2015 June) are related to Chapters 5 and 6.

Table A.1: Detailed experimental information of all high pressure experiments in this thesis.

Dates	Beamline	DAC	Sample	Technique	Pressure medium	Pressures (300 K)	Laser heating?
2008/10/09-2008/10/07	APS 3-ID-B	DAC1	En87	SMS	NaCl	0-36 GPa	No
2009/03/30-2009/03/31	APS 16-ID-D	DAC8	En87	SMS	Ne	4.1-26.8 GPa	No
2009/07/28-2009/08/01	ALS 12.2.2	DAC8	En87	XRD	Ne	0-19.1 GPa	No
2011/02/06-2011/02/12	APS 3-ID-B	DAC13	En87	NRIXS+XRD	Ne	3.9-17 GPa	No
2012/04/08	APS 3-ID-B	DAC9	$^{57}\text{Fe}_{0.9}\text{Ni}_{0.1}$	SMS melting	KCl	14.7 GPa	Yes
2012/04/09	APS 3-ID-B	DAC10	$^{57}\text{Fe}_{0.9}\text{Ni}_{0.1}$	SMS melting	KCl	13.6 GPa	Yes
2012/06/06	APS 3-ID-B	DAC1	$^{57}\text{Fe}_{0.9}\text{Ni}_{0.1}$	SMS melting+XRD	KCl	10.1 GPa	Yes
2013/02/09	APS 3-ID-B	DAC10	$^{57}\text{Fe}_{0.9}\text{Ni}_{0.1}$	SMS melting	KCl	12.5 GPa	Yes
2013/02/10	APS 3-ID-B	DAC9	$^{57}\text{Fe}_{0.9}\text{Ni}_{0.1}$	SMS melting	KCl	29.3 GPa	Yes
2013/02/11	APS 3-ID-B	DAC1	$^{57}\text{Fe}_{0.9}\text{Ni}_{0.1}$	SMS melting	KCl	36.0 GPa	Yes
2013/07/26	APS 3-ID-B	DAC1	$^{57}\text{Fe}_{0.9}\text{Ni}_{0.1}$	SMS melting	KCl	30.0 GPa	Yes
2013/07/27	APS 3-ID-B	DAC8	$^{57}\text{Fe}_{0.9}\text{Ni}_{0.1}$	SMS melting	KCl	39.0 GPa	Yes
2013/07/28	APS 3-ID-B	DAC1	$^{57}\text{Fe}_{0.9}\text{Ni}_{0.1}$	SMS melting	KCl	50.0 GPa	Yes
2013/07/29	APS 3-ID-B	DAC6	$^{57}\text{Fe}$	SMS melting	KCl	28.0 GPa	Yes
2013/11/16	APS 3-ID-B	DAC7	$^{57}\text{Fe}_{0.9}\text{Ni}_{0.1}$	SMS melting	KCl	21.3 GPa	Yes
2013/11/16	APS 3-ID-B	DAC10	$^{57}\text{Fe}$	SMS melting	KCl	10.0 GPa	Yes
2013/11/17	APS 3-ID-B	DAC1	$^{57}\text{Fe}_{0.9}\text{Ni}_{0.1}$	SMS melting+XRD	KCl	74.0 GPa	Yes
2013/11/18	APS 3-ID-B	DAC8	$^{57}\text{Fe}_{0.9}\text{Ni}_{0.1}$	SMS melting	KCl	69.0 GPa	Yes
2013/11/20	APS 3-ID-B	DAC6	$^{57}\text{Fe}$	SMS melting+XRD	KCl	47.0 GPa	Yes
2014/02/06	APS 3-ID-B	DAC1	$^{57}\text{Fe}_{0.9}\text{Ni}_{0.1}$	SMS melting	KCl	66.0 GPa	Yes
2014/02/10	APS 3-ID-B	DACcp4	$^{57}\text{Fe}_{0.9}\text{Ni}_{0.1}$	SMS melting	KCl	71.0 GPa	Yes
2015/06/14	APS 13-ID-D	DAC3	$^{57}\text{Fe}_{0.9}\text{Ni}_{0.1}$	XRD	KCl	37.5 GPa	Yes
2015/06/15	APS 13-ID-D	DACcp4	$^{57}\text{Fe}_{0.9}\text{Ni}_{0.1}$	XRD	KCl	109.0 GPa	Yes
2015/06/17	APS 3-ID-B	DAC3	$^{57}\text{Fe}_{0.9}\text{Ni}_{0.1}$	SMS melting	KCl	37.5 GPa	Yes
2015/06/18	APS 3-ID-B	DACcp4	$^{57}\text{Fe}_{0.9}\text{Ni}_{0.1}$	SMS melting	KCl	109.0 GPa	Yes
2015/06/18	APS 3-ID-B	DACcp4	$^{57}\text{Fe}_{0.9}\text{Ni}_{0.1}$	SMS melting	KCl	109.0 GPa	Yes

SMS: synchrotron Mössbauer spectroscopy. XRD: X-ray diffraction. NRIXS: nuclear resonant inelastic X-ray scattering. En87:  $(\text{Mg}_{0.980}^{57}\text{Fe}_{0.020})(\text{Mg}_{0.760}^{57}\text{Fe}_{0.240})\text{Si}_2\text{O}_6$ .

# Bibliography

- Ahrens, T. J., K. G. Holland, and G. Q. Chen (2002), Phase diagram of iron, revised-core temperatures, *Geophysical Research Letters*, *29*(7), 1150.
- Akahama, Y., and H. Kawamura (2006), Pressure calibration of diamond anvil raman gauge to 310 GPa, *Journal of Applied Physics*, *100*(4), 043516, doi:<http://dx.doi.org/10.1063/1.2335683>.
- Akashi, A., Y. Nishihara, E. Takahashi, Y. Nakajima, Y. Tange, and K. Funakoshi (2009), Ortho-*enstatite*/clino-*enstatite* phase transformation in MgSiO<sub>3</sub> at high pressure and high temperature determined by in situ X-ray diffraction: Implications for nature of the X-discontinuity, *Journal of Geophysical Research-Solid Earth*, *114*(B4), B04,206.
- Akins, J. A., S.-N. Luo, P. D. Asimow, and T. J. Ahrens (2004), Shock-induced melting of MgSiO<sub>3</sub> perovskite and implications for melts in Earth's lowermost mantle, *Geophysical Research Letters*, *31*(14), L14,612, doi:10.1029/2004GL020237.
- Alfè, D., M. Gillan, and G. Price (2002), Composition and temperature of the Earth's core constrained by combining ab initio calculations and seismic data, *Earth and Planetary Science Letters*, *195*(1-2), 91 – 98, doi:[http://dx.doi.org/10.1016/S0012-821X\(01\)00568-4](http://dx.doi.org/10.1016/S0012-821X(01)00568-4).
- Anderson, D. L. (2007), *New Theory of the Earth*, Cambridge University Press.
- Anderson, O. L. (1980), An experimental high-temperature thermal equation of state bypassing the Grüneisen parameter, *Physics of the Earth and Planetary Interiors*, *22*(3-4), 165–172.
- Anderson, O. L. (1990), The high-pressure triple points of iron and their effects on the heat flow from the Earth's core, *Journal of Geophysical Research: Solid Earth*, *95*(B13), 21,697–21,707, doi:10.1029/JB095iB13p21697.
- Andrault, D., N. Bolfan-Casanova, O. Ohtaka, H. Fukui, H. Arima, M. Fialin, and K. Funakoshi (2009), Melting diagrams of Fe-rich alloys determined from synchrotron in situ measurements in the 15-23 GPa pressure range, *Physics of the Earth and Planetary Interiors*, *174*(1-4), 181–191.
- Andrault, D., N. Bolfan-Casanova, G. L. Nigro, M. A. Bouhifd, G. Garbarino, and M. Mezouar (2011), Solidus and liquidus profiles of chondritic mantle: Implication for melting of the

- earth across its history, *Earth and Planetary Science Letters*, *304*(1-2), 251 – 259, doi: <http://dx.doi.org/10.1016/j.epsl.2011.02.006>.
- Andrault, D., G. Pesce, M. A. Bouhifd, N. Bolfan-Casanova, J.-M. Hnot, and M. Mezouar (2014), Melting of subducted basalt at the core-mantle boundary, *Science*, *344*(6186), 892–895, doi: 10.1126/science.1250466.
- Angel, R. J. (2000), Equations of state, *High-Temperature and High-Pressure Crystal Chemistry*, *41*, 35–59.
- Angel, R. J., and D. A. Hugh-Jones (1994), Equations of state and thermodynamic properties of enstatite pyroxenes, *Journal of Geophysical Research-Solid Earth*, *99*(B10), 19,777–19,783.
- Angel, R. J., and J. M. Jackson (2002), Elasticity and equation of state of orthoenstatite, MgSiO<sub>3</sub>, *American Mineralogist*, *87*(4), 558–561.
- Antonangeli, D., et al. (2011), Spin crossover in ferropicrinite at high pressure: A seismologically transparent transition, *Science*, *331*(6013), 64–67, doi:10.1126/science.1198429.
- Anzellini, S., A. Dewaele, M. Mezouar, P. Loubeyre, and G. Morard (2013), Melting of iron at Earth's inner core boundary based on fast X-ray diffraction, *Science*, *340*(6131), 464–466.
- Aquilanti, G., A. Trapananti, A. Karandikar, I. Kantor, C. Marini, O. Mathon, S. Pascarelli, and R. Boehler (2015), Melting of iron determined by x-ray absorption spectroscopy to 100 GPa, *Proceedings of the National Academy of Sciences*, *112*(39), 12,042–12,045, doi: 10.1073/pnas.1502363112.
- Asanuma, H., E. Ohtani, T. Sakai, H. Terasaki, S. Kamada, T. Kondo, and T. Kikegawa (2010), Melting of iron-silicon alloy up to the core-mantle boundary pressure: implications to the thermal structure of the earth's core, *Physics and Chemistry of Minerals*, *37*(6), 353–359.
- Badro, J. (2014), Spin transitions in mantle minerals, *Annual Review of Earth and Planetary Sciences*, *42*(1), 231–248, doi:10.1146/annurev-earth-042711-105304.
- Bagley, B., and J. Revenaugh (2008), Upper mantle seismic shear discontinuities of the Pacific, *Journal of Geophysical Research-Solid Earth*, *113*(B12), B12,301.
- Baroni, S., P. Giannozzi, and A. Testa (1987), Green's-function approach to linear response in solids, *Physical Review Letters*, *58*(18), 1861–1864.
- Baroni, S., S. de Gironcoli, A. Dal Corso, and P. Giannozzi (2001), Phonons and related crystal properties from density-functional perturbation theory, *Review of Modern Physics*, *73*(2), 515–562.

- Bartels, R. A., and D. E. Schuele (1965), Pressure derivatives of the elastic constants of NaCl and KCl at 295 K and 195 K, *Journal of Physics and Chemistry of Solids*, *26*(3), 537–549, doi: 10.1016/0022-3697(65)90130-7.
- Bass, J. D., and D. L. Anderson (1984), Composition of the upper mantle: geophysical tests of two petrological models, *Geophysical Research Letters*, *11*(3), 237–240.
- Bass, J. D., B. Svendsen, and T. J. Ahrens (1987), The temperature of shock compressed iron, *High-Pressure Research in Mineral Physics: A Volume in Honor of Syun-iti Akimoto*, pp. 393–402.
- Bassett, W. A., A. H. Shen, M. Bucknum, and I.-M. Chou (1993), A new diamond anvil cell for hydrothermal studies to 2.5 GPa and from -190 to 1200 °C, *Review of Scientific Instruments*, *64*(8), 2340–2345.
- Beck, P., A. F. Goncharov, V. V. Struzhkin, B. Militzer, H.-K. Mao, and R. J. Hemley (2007), Measurement of thermal diffusivity at high pressure using a transient heating technique, *Applied Physics Letters*, *91*(18), 181,914.
- Berryman, J. G. (2000), Seismic velocity decrement ratios for regions of partial melt in the lower mantle, *Geophysical Research Letters*, *27*(3), 421–424, doi:10.1029/1999GL008402.
- Boehler, R. (1992), Melting of the Fe-FeO and the Fe-FeS systems at high pressure: Constraints on core temperatures, *Earth and Planetary Science Letters*, *111*(2-4), 217–227.
- Boehler, R. (1993), Temperatures in the earth's core from melting-point measurements of iron at high static pressures, *Nature*, *363*(6429), 534–536.
- Boehler, R. (2000), High-pressure experiments and the phase diagram of lower mantle and core materials, *Reviews of Geophysics*, *38*(2), 221–245.
- Boehler, R., N. von Bagen, and A. Chopelas (1990), Melting, thermal expansion, and phase transitions of iron at high pressures, *Journal of Geophysical Research: Solid Earth*, *95*(B13), 21,731–21,736.
- Boehler, R., M. Ross, and D. B. Boercker (1996), High-pressure melting curves of alkali halides, *Physical Review B*, *53*, 556–563.
- Boehler, R., D. Santamaría-Pérez, D. Errandonea, and M. Mezouar (2008), Melting, density, and anisotropy of iron at core conditions: new x-ray measurements to 150 GPa, in *Journal of Physics: Conference Series*, vol. 121, p. 022018, IOP Publishing.
- Bower, D. J., J. K. Wicks, M. Gurnis, and J. M. Jackson (2011), A geodynamic and mineral physics model of a solid-state ultralow-velocity zone, *Earth and Planetary Science Letters*, *303*(3-4), 193–202, doi:10.1016/j.epsl.2010.12.035.

- Boyle, A. J. F., D. S. P. Bunbury, C. Edwards, and H. E. Hall (1961), The mössbauer effect in tin from 120k to the melting point, *Proceedings of the Physical Society*, *77*(1), 129.
- Bragg, W. L. (1913), The diffraction of short electromagnetic waves by a crystal, *Proceedings of the Cambridge Philosophical Society*, *17*, 4357.
- Bragg, W. L. (1967), Nobel lecture: The diffraction of X-rays by crystals, in *Nobel Lectures, Physics 1901-1921*, Elsevier Publishing Company, Amsterdam.
- Brown, J. M., and R. G. McQueen (1986), Phase transitions, Grüneisen parameter, and elasticity for shocked iron between 77 GPa and 400 GPa, *Journal of Geophysical Research: Solid Earth*, *91*(B7), 7485–7494, doi:10.1029/JB091iB07p07485.
- Brown, J. M., and T. J. Shankland (1981), Thermodynamic parameters in the earth as determined from seismic profiles, *Geophysical Journal of the Royal Astronomical Society*, *66*(3), 579–596, doi:10.1111/j.1365-246X.1981.tb04891.x.
- Cacciamani, G., A. Dinsdale, M. Palumbo, and A. Pasturel (2010), The Fe-Ni system: Thermodynamic modelling assisted by atomistic calculations, *Intermetallics*, *18*(6), 1148 – 1162.
- Cameron, M., and J. J. Papike (1981), Structural and chemical variations in pyroxenes, *American Mineralogist*, *66*(1-2), 1–50.
- Campbell, A. J. (2008), Measurement of temperature distributions across laser heated samples by multispectral imaging radiometry, *Review of Scientific Instruments*, *79*(1), 015,108.
- Caracas, R., and X. Gonze (2010), Lattice dynamics and thermodynamical properties, in *Thermodynamic Properties of Solids: Experiment and Modeling*, edited by S. L. Chaplot, R. Mittal, and N. Choudhury, pp. 291–315, Wiley-VCH Verlag, Weinheim.
- Catalli, K., et al. (2010), Spin state of ferric iron in mgsio<sub>3</sub> perovskite and its effect on elastic properties, *Earth and Planetary Science Letters*, *289*(1-2), 68 – 75, doi:10.1016/j.epsl.2009.10.029.
- Chai, M., J. M. Brown, and L. J. Slutsky (1997), The elastic constants of an aluminous orthopyroxene to 12.5 GPa, *Journal of Geophysical Research-Solid Earth*, *102*(B7), 14,779–14,785.
- Chen, B., J. Li, and S. A. Hauck (2008), Non-ideal liquidus curve in the Fe-S system and Mercury’s snowing core, *Geophysical Research Letters*, *35*(7), L07,201.
- Chen, B., W.-P. Hsieh, D. G. Cahill, D. R. Trinkle, and J. Li (2011), Thermal conductivity of compressed H<sub>2</sub>O to 22 GPa: A test of the leibfried-schlmann equation, *Physical Review B*, *83*, 132,301.

- Chen, B., J. M. Jackson, W. Sturhahn, D. Zhang, J. Zhao, J. K. Wicks, and C. A. Murphy (2012), Spin crossover equation of state and sound velocities of  $(\text{Mg}_{0.65}\text{Fe}_{0.35})\text{O}$  ferropericlase to 140 GPa, *Journal of Geophysical Research: Solid Earth*, *117*(B8), B08,208, doi:10.1029/2012JB009162.
- Chu, R., B. Schmandt, and D. V. Helmberger (2011), Juan de Fuca subduction zone from a mixture of tomography and waveform modeling, *Journal of Geophysical Research-Solid Earth and Planets*, *117*(B3), B03,304.
- Chu, R., B. Schmandt, and D. V. Helmberger (2012), Upper mantle P velocity structure beneath the Midwestern United States derived from triplicated waveforms, *Geochemistry, Geophysics, Geosystems*, *13*, Q0AK04.
- Corgne, A., N. L. Allan, and B. J. Wood (2003), Atomistic simulations of trace element incorporation into the large site of  $\text{MgSiO}_3$  and  $\text{CaSiO}_3$  perovskites, *Physics of the Earth and Planetary Interiors*, *139*(1-2), 113 – 127, doi:http://dx.doi.org/10.1016/S0031-9201(03)00148-1, diffusion and Partitioning in Planetary Interiors.
- Dalton, D. A., W.-P. Hsieh, G. T. Hohensee, D. G. Cahill, and A. F. Goncharov (2013), Effect of mass disorder on the lattice thermal conductivity of MgO periclase under pressure, *Scientific Reports*, *3*, 2400.
- Dera, P., G. J. Finkelstein, T. S. Duffy, R. T. Downs, Y. Meng, V. Prakapenka, and S. Tkachev (2013), Metastable high-pressure transformations of orthoferrosilite fs82, *Physics of the Earth and Planetary Interiors*, *221*(0), 15 – 21, doi:http://dx.doi.org/10.1016/j.pepi.2013.06.006.
- Deuss, A. (2014), Heterogeneity and anisotropy of Earth's inner core, *Annual Review of Earth and Planetary Sciences*, *42*(1), 103–126, doi:10.1146/annurev-earth-060313-054658.
- Deuss, A., and J. H. Woodhouse (2002), A systematic search for mantle discontinuities using SS-precursors, *Geophysical Research Letters*, *29*(8), 1249–1252.
- Dewaele, A., P. Loubeyre, F. Occelli, M. Mezouar, P. I. Dorogokupets, and M. Torrent (2006), Quasihydrostatic equation of state of iron above 2mbar, *Physical Review Letters*, *97*, 215,504.
- Dewaele, A., M. Mezouar, N. Guignot, and P. Loubeyre (2007), Melting of lead under high pressure studied using second-scale time-resolved x-ray diffraction, *Physical Review B*, *76*, 144,106.
- Dewaele, A., F. Datchi, P. Loubeyre, and M. Mezouar (2008), High pressure-high temperature equations of state of neon and diamond, *Physical Review B*, *77*(9), 094,106.
- Dewaele, A., M. Mezouar, N. Guignot, and P. Loubeyre (2010), High melting points of tantalum in a laser-heated diamond anvil cell, *Physical Review Letters*, *104*, 255,701.

- Domeneghetti, M., and G. Steffen (1992), M1, M2 site populations and distortion parameters in synthetic Mg-Fe orthopyroxenes from Mössbauer spectra and X-ray structure refinements, *Physics and Chemistry of Minerals*, *19*(5), 298–306, doi:10.1007/BF00204007.
- Dorfman, S. M., Y. Meng, V. B. Prakapenka, and T. S. Duffy (2013), Effects of Fe-enrichment on the equation of state and stability of (Mg,Fe)SiO<sub>3</sub> perovskite, *Earth and Planetary Science Letters*, *361*(0), 249–257, doi:http://dx.doi.org/10.1016/j.epsl.2012.10.033.
- Du, Z., L. Miyagi, G. Amulele, and K. K. M. Lee (2013a), Efficient graphite ring heater suitable for diamond-anvil cells to 1300 K, *Review of Scientific Instruments*, *84*(2), 024,502.
- Du, Z., G. Amulele, B. L. Robin, and K. K. M. Lee (2013b), Mapping temperatures and temperature gradients during flash heating in a diamond-anvil cell, *Review of Scientific Instruments*, *84*(7), 075,111.
- Dubrovinsky, L., N. Dubrovinskaia, V. B. Prakapenka, and A. M. Abakumov (2012), Implementation of micro-ball nanodiamond anvils for high-pressure studies above 6 Mbar, *Nature communications*, *3*, 1163.
- Duffy, T. S., and D. L. Anderson (1989), Seismic velocities in mantle minerals and the mineralogy of the upper mantle, *Journal of Geophysical Research-Solid Earth and Planets*, *94*(B2), 1895–1912.
- Duffy, T. S., and M. T. Vaughan (1988), Elasticity of enstatite and its relationship to crystal-structure, *Journal of Geophysical Research-Solid Earth and Planets*, *93*(B1), 383–391.
- Dyar, M. D., R. L. Klima, D. Lindsley, and C. M. Pieters (2007), Effects of differential recoil-free fraction on ordering and site occupancies in Mössbauer spectroscopy of orthopyroxenes, *American Mineralogist*, *92*(2-3), 424–428.
- Dziewonski, A. M., and D. L. Anderson (1981), Preliminary reference earth model, *Physics of the Earth and Planetary Interiors*, *25*, 297–356.
- Eeckhout, S. G., E. De Grave, C. A. McCammon, and R. Vochten (2000), Temperature dependence of the hyperfine parameters of synthetic P2<sub>1</sub>/c Mg-Fe clinopyroxenes along the MgSiO<sub>3</sub>-FeSiO<sub>3</sub> join, *American Mineralogist*, *85*(7-8), 943–952.
- Eng, P. J., M. Newville, M. L. Rivers, and S. R. Sutton (1998), Dynamically figured kirkpatrick baez x-ray microfocusing optics, *Proc. SPIE*, *3449*, 145–156, doi:10.1117/12.330342.
- Errandonea, D., B. Schwager, R. Ditz, C. Gessmann, R. Boehler, and M. Ross (2001), Systematics of transition-metal melting, *Physical Review B*, *63*, 132,104.
- Fei, Y., and C. Bertka (2005), The interior of mars, *Science*, *308*(5725), 1120–1121.

- Finkelstein, G. J., P. K. Dera, and T. S. Duffy (2014), Phase transitions in orthopyroxene (en90) to 49 gpa from single-crystal X-ray diffraction, *Physics of the Earth and Planetary Interiors*, doi:<http://dx.doi.org/10.1016/j.pepi.2014.10.009>.
- Fiquet, G., F. Guyot, and J. Badro (2008), The Earth's lower mantle and core, *Elements*, 4(3), 177–182.
- Fiquet, G., A. L. Auzende, J. Siebert, A. Corgne, H. Bureau, H. Ozawa, and G. Garbarino (2010), Melting of peridotite to 140 Gigapascals, *Science*, 329(5998), 1516–1518.
- Fischer, R. A., and A. J. Campbell (2010), High-pressure melting of wüstite, *American Mineralogist*, 95(10), 1473–1477.
- Flesch, L. M., B. S. Li, and R. C. Liebermann (1998), Sound velocities of polycrystalline MgSiO<sub>3</sub>-orthopyroxene to 10 GPa at room temperature, *American Mineralogist*, 83(5-6), 444–450.
- Frisillo, A. L., and G. R. Barsch (1972), Measurement of single-crystal elastic-constants of bronzite as a function of pressure and temperature, *Journal of Geophysical Research*, 77(32), 6360–6384.
- Frost, D. J. (2008), The upper mantle and transition zone, *Elements*, 4(3), 171–176.
- Frost, D. J., and F. Langenhorst (2002), The effect of Al<sub>2</sub>O<sub>3</sub> on Fe-Mg partitioning between magnesiowüstite and magnesium silicate perovskite, *Earth and Planetary Science Letters*, 199(1-2), 227–241, doi:[http://dx.doi.org/10.1016/S0012-821X\(02\)00558-7](http://dx.doi.org/10.1016/S0012-821X(02)00558-7).
- Fuchs, M., and M. Scheffler (1999), Ab initio pseudopotentials for electronic structure calculations of poly-atomic systems using density-functional theory, *Computer Physics Communications*, 119(1), 67 – 98.
- Gao, L., B. Chen, M. Lerche, E. E. Alp, W. Sturhahn, J. Zhao, H. Yavas, and J. Li (2009), Sound velocities of compressed Fe<sub>3</sub>C from simultaneous synchrotron X-ray diffraction and nuclear resonant scattering measurements, *Journal of Synchrotron Radiation*, 16(6), 714–722.
- Geballe, Z. M., and R. Jeanloz (2012), Origin of temperature plateaus in laser-heated diamond anvil cell experiments, *Journal of Applied Physics*, 111(12), 123,518.
- Goncharov, A. F., V. B. Prakapenka, V. V. Struzhkin, I. Kantor, M. L. Rivers, and D. A. Dalton (2010), X-ray diffraction in the pulsed laser heated diamond anvil cell, *Review of Scientific Instruments*, 81(11), 113,902.
- Gonze, X., and J. P. Vigneron (1989), Density-functional approach to nonlinear-response coefficients of solids, *Physical Review B*, 39(18), 13,120–13,128.

- Gonze, X., D. C. Allan, and M. P. Teter (1992), Dielectric tensor, effective charges, and phonons in  $\alpha$ -quartz by variational density-functional perturbation theory, *Physical Review Letters*, *68*(24), 3603–3606.
- Gonze, X., G. M. Rignanese, and R. Caracas (2005), First-principles studies of the lattice dynamics of crystals, and related properties, *Zeitschrift für Kristallographie*, *220*(5-6), 458–472.
- Grand, S. P., and D. V. Helmberger (1984a), Upper mantle shear structure of North America, *Geophysical Journal of the Royal Astronomical Society*, *76*, 399–438.
- Grand, S. P., and D. V. Helmberger (1984b), Upper mantle shear structure beneath the Northwest Atlantic Ocean, *Journal of Geophysical Research-Solid Earth*, *89*(B13), 11,465–11,475.
- Grocholski, B., S.-H. Shim, W. Sturhahn, J. Zhao, Y. Xiao, and P. C. Chow (2009), Spin and valence states of iron in  $(\text{Mg}_{0.8}\text{Fe}_{0.2})\text{SiO}_3$  perovskite, *Geophysical Research Letters*, *36*(24), L24,303, doi:10.1029/2009GL041262.
- Hammersley, A. P., S. O. Svensson, M. Hanfland, A. N. Fitch, and D. Hausermann (1996), Two-dimensional detector software: From real detector to idealised image or two-theta scan, *High Pressure Research*, *14*(4-6), 235–248.
- Heinz, D. L., and R. Jeanloz (1984), The equation of state of the gold calibration standard, *Journal of Applied Physics*, *55*(4), 885–893, doi:http://dx.doi.org/10.1063/1.333139.
- Heinz, D. L., J. S. Sweeney, and P. Miller (1991), A laser heating system that stabilizes and controls the temperature: Diamond anvil cell applications, *Review of Scientific Instruments*, *62*(6), 1568–1575.
- Henke, B. L., E. M. Gullikson, and J. C. Davis (1993), X-ray interactions: Photoabsorption, scattering, transmission, and reflection at  $E = 50\text{--}30,000$  eV,  $Z = 1\text{--}92$ , *Atomic Data and Nuclear Data Tables*, *54*(2), 181–342.
- Hier-Majumder, S. (2008), Influence of contiguity on seismic velocities of partially molten aggregates, *Journal of Geophysical Research: Solid Earth*, *113*(B12), B12,205, doi:10.1029/2008JB005662.
- Hieronymus, C. F., Z. H. Shomali, and L. B. Pedersen (2007), A dynamical model for generating sharp seismic velocity contrasts underneath continents: Application to the Sorgenfrei-Tornquist Zone, *Earth and Planetary Science Letters*, *262*(1-2), 77–91.
- Hirose, K., S. Labrosse, and J. Hernlund (2013), Composition and state of the core, *Annual Review of Earth and Planetary Sciences*, *41*(1), 657–691, doi:10.1146/annurev-earth-050212-124007.

- Hirschmann, M. M., M. S. Ghiorso, L. E. Wasylenki, P. D. Asimow, and E. M. Stolper (1998), Calculation of peridotite partial melting from thermodynamic models of minerals and melts. i. review of methods and comparison with experiments, *Journal of Petrology*, *39*(6), 1091–1115, doi:10.1093/петroj/39.6.1091.
- Hohenberg, P., and W. Kohn (1964), Inhomogeneous electron gas, *Physical Review*, *136*(3B), B864–B871.
- Holland, T. J. B., and S. A. T. Redfern (1997), Unit cell refinement from powder diffraction data: The use of regression diagnostics, *Mineralogical Magazine*, *61*(1), 65–77.
- Holmes, N. C., J. A. Moriarty, G. R. Gathers, and W. J. Nellis (1989), The equation of state of platinum to 660 GPa (6.6 Mbar), *Journal of Applied Physics*, *66*(7), 2962–2967, doi: <http://dx.doi.org/10.1063/1.344177>.
- Hsieh, W.-P., B. Chen, J. Li, P. Keblinski, and D. G. Cahill (2009), Pressure tuning of the thermal conductivity of the layered muscovite crystal, *Physical Review B*, *80*, 180,302.
- Hugh-Jones, D., T. Sharp, R. Angel, and A. Woodland (1996), The transition of orthoferrosilite to high-pressure *c2/c* clinoferrosilite at ambient temperature, *European Journal of Mineralogy*, *8*(6), 1337–1345.
- Hugh-Jones, D., A. Chopelas, and R. Angel (1997), Tetrahedral compression in (Mg,Fe)SiO<sub>3</sub> orthopyroxenes, *Physics and Chemistry of Minerals*, *24*(4), 301–310.
- Hugh-Jones, D. A., and R. J. Angel (1994), A compressional study of MgSiO<sub>3</sub> orthoenstatite up to 8.5-GPa, *American Mineralogist*, *79*(5-6), 405–410.
- Hugh-Jones, D. A., and R. J. Angel (1997), Effect of Ca<sup>2+</sup> and Fe<sup>2+</sup> on the equation of state of MgSiO<sub>3</sub> orthopyroxene, *Journal of Geophysical Research-Solid Earth*, *102*(B6), 12,333–12,340.
- Hugh-Jones, D. A., A. B. Woodland, and R. J. Angel (1994), The structure of high-pressure *c2/c* ferrosilite and crystal-chemistry of high-pressure *c2/c* pyroxenes, *American Mineralogist*, *79*(11-12), 1032–1041.
- Iizuka, R., H. Kagi, and K. Komatsu (2010), Comparing ruby fluorescence spectra at high pressure in between methanol-ethanol pressure transmitting medium and its deuteride, in *Journal of Physics: Conference Series*, vol. 215, p. 012177.
- Ingalls, R. (1964), Electric-field gradient tensor in ferrous compounds, *Physical Review*, *133*, A787–A795, doi:10.1103/PhysRev.133.A787.

- Irifune, T., and A. E. Ringwood (1987), Phase transformations in a harzburgite composition to 26 GPa: implications for dynamical behaviour of the subducting slab, *Earth and Planetary Science Letters*, *86*(2-4), 365–376.
- Isaak, D. G., I. Ohno, and P. C. Lee (2006), The elastic constants of monoclinic single-crystal chrome-diopside to 1,300 k, *Physics and Chemistry of Minerals*, *32*, 691–699.
- Ita, J., and L. Stixrude (1992), Petrology, elasticity, and composition of the mantle transition zone, *Journal of Geophysical Research-Solid Earth*, *97*(B5), 6849–6866.
- Ito, E., and E. Takahashi (1989), Postspinel transformations in the system  $\text{Mg}_2\text{SiO}_4\text{-Fe}_2\text{SiO}_4$  and some geophysical implications, *Journal of Geophysical Research: Solid Earth*, *94*(B8), 10,637–10,646, doi:10.1029/JB094iB08p10637.
- Jackson, J. M., S. V. Sinogeikin, and J. D. Bass (1999), Elasticity of  $\text{MgSiO}_3$  orthoenstatite, *American Mineralogist*, *84*(4), 677–680.
- Jackson, J. M., S. V. Sinogeikin, M. A. Carpenter, and J. D. Bass (2004), Novel phase transition in orthoenstatite, *American Mineralogist*, *89*(1), 239–244.
- Jackson, J. M., W. Sturhahn, G. Shen, J. Zhao, M. Y. Hu, D. Errandonea, J. D. Bass, and Y. Fei (2005), A synchrotron Mössbauer spectroscopy study of  $(\text{Mg,Fe})\text{SiO}_3$  perovskite up to 120 GPa, *American Mineralogist*, *90*(1), 199–205.
- Jackson, J. M., S. V. Sinogeikin, S. D. Jacobsen, H. J. Reichmann, S. J. Mackwell, and J. D. Bass (2006), Single-crystal elasticity and sound velocities of  $(\text{Mg}_{0.94}\text{Fe}_{0.06})\text{O}$  ferropericlaase to 20 GPa, *Journal of Geophysical Research: Solid Earth*, *111*(B9), B09,203, doi:10.1029/2005JB004052.
- Jackson, J. M., S. V. Sinogeikin, and J. D. Bass (2007), Sound velocities and single-crystal elasticity of orthoenstatite to 1073 K at ambient pressure, *Physics of the Earth and Planetary Interiors*, *161*(1-2), 1–12.
- Jackson, J. M., E. A. Hamecher, and W. Sturhahn (2009), Nuclear resonant X-ray spectroscopy of  $(\text{Mg,Fe})\text{SiO}_3$  orthoenstatites, *European Journal of Mineralogy*, *21*(3), 551–560.
- Jackson, J. M., et al. (2013), Melting of compressed iron by monitoring atomic dynamics, *Earth and Planetary Science Letters*, *362*(0), 143–150.
- Jacobsen, S. D., et al. (2008), Compression of single-crystal magnesium oxide to 118 GPa and a ruby pressure gauge for helium pressure media, *American Mineralogist*, *93*(11-12), 1823–1828.
- Jacobsen, S. D., Z. X. Liu, T. B. Ballaran, E. F. Littlefield, L. Ehm, and R. J. Hemley (2010), Effect of  $\text{H}_2\text{O}$  on upper mantle phase transitions in  $\text{MgSiO}_3$ : Is the depth of the seismic X-discontinuity

- an indicator of mantle water content?, *Physics of the Earth and Planetary Interiors*, 183(1-2), 234–244.
- Jahn, S. (2008), High-pressure phase transitions in MgSiO<sub>3</sub> orthoenstatite studied by atomistic computer simulation, *American Mineralogist*, 93(4), 528–532.
- Jayaraman, A. (1983), Diamond anvil cell and high-pressure physical investigations, *Rev. Mod. Phys.*, 55, 65–108, doi:10.1103/RevModPhys.55.65.
- Jeanloz, R., and D. L. Heinz (1984), Experiments at high temperature and pressure: Laser heating through the diamond cell, *Le Journal de Physique Colloques*, 45(C8), 83–92.
- Jeanloz, R., and A. Kavner (1996), Melting criteria and imaging spectroradiometry in laser-heated diamond-cell experiments, *Philosophical Transactions of the Royal Society A: Mathematical, Physical and Engineering Sciences*, 354(1711), 1279–1305.
- Jeanloz, R., P. M. Celliers, G. W. Collins, J. H. Eggert, K. K. M. Lee, R. S. McWilliams, S. Brygoo, and P. Loubeyre (2007), Achieving high-density states through shock-wave loading of pre-compressed samples, *Proceedings of the National Academy of Sciences*, 104(22), 9172–9177, doi: 10.1073/pnas.0608170104.
- Kennett, B. L. N., E. R. Engdahl, and R. Buland (1995), Constraints on seismic velocities in the earth from traveltimes, *Geophysical Journal International*, 122(1), 108–124.
- Kirby, S. H., and L. A. Stern (1993), Experimental dynamic metamorphism of mineral single crystals, *Journal of Structural Geology*, 15(9-10), 1223–1240, doi:10.1016/0191-8141(93)90165-7.
- Klima, R. L., C. M. Pieters, and M. D. Dyar (2007), Spectroscopy of synthetic Mg-Fe pyroxenes I: Spin-allowed and spin-forbidden crystal field bands in the visible and near-infrared, *Meteoritics & Planetary Science*, 42(2), 235–253, doi:10.1111/j.1945-5100.2007.tb00230.x.
- Kohn, W., and L. J. Sham (1965), Self-consistent equations including exchange and correlation effects, *Physical Review*, 140(4A), A1133–A1138.
- Komabayashi, T. (2014), Thermodynamics of melting relations in the system Fe-FeO at high pressure: Implications for oxygen in the Earth's core, *Journal of Geophysical Research: Solid Earth*, 119(5), 4164–4177, doi:10.1002/2014JB010980, 2014JB010980.
- Komabayashi, T., and Y. Fei (2010), Internally consistent thermodynamic database for iron to the Earth's core conditions, *Journal of Geophysical Research: Solid Earth*, 115(B3), B03,202.
- Komabayashi, T., Y. Fei, Y. Meng, and V. Prakapenka (2009), In-situ x-ray diffraction measurements of the  $\gamma - \epsilon$  transition boundary of iron in an internally-heated diamond anvil cell, *Earth and Planetary Science Letters*, 282(1-4), 252–257.

- Komabayashi, T., K. Hirose, and Y. Ohishi (2012), In situ X-ray diffraction measurements of the fcc-hcp phase transition boundary of an Fe-Ni alloy in an internally heated diamond anvil cell, *Physics and Chemistry of Minerals*, *39*(4), 329–338.
- Kung, J., B. Li, T. Uchida, Y. Wang, D. Neuville, and R. C. Liebermann (2004), In situ measurements of sound velocities and densities across the orthopyroxene high-pressure clinopyroxene transition in MgSiO<sub>3</sub> at high pressure, *Physics of the Earth and Planetary Interiors*, *147*(1), 27–44.
- Kung, J., B. Li, T. Uchida, and Y. Wang (2005), In-situ elasticity measurement for the unquenchable high-pressure clinopyroxene phase: Implication for the upper mantle, *Geophysical Research Letters*, *32*(1), L01,307.
- Kung, J., B. Li, and R. C. Liebermann (2006), Ultrasonic observations of elasticity changes across phase transformations in MgSiO<sub>3</sub> pyroxenes, *Journal of Physics and Chemistry of Solids*, *67*(9-10), 2051–2055.
- Kunimoto, T., and T. Irifune (2010), Pressure generation to 125 GPa using a 6-8-2 type multi-anvil apparatus with nano-polycrystalline diamond anvils, *Journal of Physics: Conference Series*, *215*(1), 012,190.
- Labrosse, S., J.-P. Poirier, and J.-L. L. Mouël (2001), The age of the inner core, *Earth and Planetary Science Letters*, *190*(3-4), 111 – 123, doi:[http://dx.doi.org/10.1016/S0012-821X\(01\)00387-9](http://dx.doi.org/10.1016/S0012-821X(01)00387-9).
- Labrosse, S., J. Hernlund, and N. Coltice (2007), A crystallizing dense magma ocean at the base of the Earth's mantle, *Nature*, *450*(7171), 866–869.
- Lavina, B., P. Dera, and R. T. Downs (2014), Modern x-ray diffraction methods in mineralogy and geosciences, *Reviews in Mineralogy and Geochemistry*, *78*(1), 1–31.
- Lay, T., E. J. Garnero, and Q. Williams (2004), Partial melting in a thermo-chemical boundary layer at the base of the mantle, *Physics of the Earth and Planetary Interiors*, *146*(3-4), 441 – 467, doi:<http://dx.doi.org/10.1016/j.pepi.2004.04.004>.
- Lay, T., J. Hernlund, and B. A. Buffett (2008), Core-mantle boundary heat flow, *Nature Geoscience*, *1*(1), 25–32.
- LeFevre, L. V., and D. V. Helmberger (1989), Upper mantle p velocity structure of the canadian shield, *Journal of Geophysical Research-Solid Earth*, *94*(B12), 17,749–17,765.
- Lehmann, I. (1936), P<sup>''</sup>, *Publications du Bureau Central Sismologique International*, *A14*, S.87–115.

- Li, J., and Y. Fei (2003), Experimental constraints on core composition, *Treatise on Geochemistry*, 2, 521–546.
- Li, J., W. Sturhahn, J. M. Jackson, V. V. Struzhkin, J. F. Lin, J. Zhao, H.-K. Mao, and G. Shen (2006), Pressure effect on the electronic structure of iron in (Mg,Fe)(Si,Al)O<sub>3</sub> perovskite: a combined synchrotron Mössbauer and X-ray emission spectroscopy study up to 100GPa, *Physics and Chemistry of Minerals*, 33(8-9), 575–585, doi:10.1007/s00269-006-0105-y.
- Lin, C., Z. Li, and S. S. Hafner (1993), Local electronic states of Fe<sup>2+</sup> ions in orthopyroxene, *American Mineralogist*, 78(1-2), 8–15.
- Lin, C.-C. (2003), Pressure-induced metastable phase transition in orthoenstatite (MgSiO<sub>3</sub>) at room temperature: a Raman spectroscopic study, *Journal of Solid State Chemistry*, 174(2), 403–411, doi:10.1016/S0022-4596(03)00278-0.
- Lin, C. M., J. L. Chao, and C.-C. Lin (2005), Metastable phase transition of orthoenstatite (MgSiO<sub>3</sub>) under high pressure, *Solid State Sciences*, 7(3), 293–297, doi:10.1016/j.solidstatesciences.2004.10.005.
- Lin, J.-F., W. Sturhahn, J. Zhao, G. Shen, H.-K. Mao, and R. J. Hemley (2004), Absolute temperature measurement in a laser-heated diamond anvil cell, *Geophysical Research Letters*, 31(14), L14,611.
- Lin, J.-F., et al. (2008), Intermediate-spin ferrous iron in lowermost mantle post-perovskite and perovskite, *Nature geoscience*, 1(10), 688–691.
- Liu, L., and W. A. Bassett (1975), The melting of iron up to 200 kbar, *Journal of Geophysical Research*, 80(26), 3777–3782.
- Liu, L.-G. (1975), Post-oxide phases of forsterite and enstatite, *Geophysical Research Letters*, 2(10), 417–419, doi:10.1029/GL002i010p00417.
- Liu, W., J. Kung, and B. Li (2005), Elasticity of San Carlos olivine to 8 GPa and 1073 K, *Geophysical Research Letters*, 32(16), L16,301.
- Loubeyre, P., et al. (2004), Coupling static and dynamic compressions: first measurements in dense hydrogen, *High Pressure Research*, 24(1), 25–31, doi:10.1080/08957950310001635792.
- Lyzenga, G. A., and T. J. Ahrens (1979), Multiwavelength optical pyrometer for shock compression experiments, *Review of Scientific Instruments*, 50(11), 1421–1424.
- Ma, Y., M. Somayazulu, G. Shen, H. kwang Mao, J. Shu, and R. J. Hemley (2004), In situ X-ray diffraction studies of iron to earth-core conditions, *Physics of the Earth and Planetary Interiors*,

- 143-144(0), 455 – 467, doi:<http://dx.doi.org/10.1016/j.pepi.2003.06.005>, new Developments in High-Pressure Mineral Physics and Applications to the Earth's Interior.
- Macedo, W. A. A., and W. Keune (1988), Magnetism of epitaxial fcc-Fe(100) films on Cu(100) investigated in situ by conversion-electron Mössbauer spectroscopy in ultrahigh vacuum, *Phys. Rev. Lett.*, *61*, 475–478, doi:10.1103/PhysRevLett.61.475.
- Mao, H. K., J. Xu, and P. M. Bell (1986), Calibration of the ruby pressure gauge to 800-kbar under quasi-hydrostatic conditions, *Journal of Geophysical Research-Solid Earth and Planets*, *91*(B5), 4673–4676.
- McCammon, C., I. Kantor, O. Narygina, J. Rouquette, U. Ponkratz, I. Sergueev, M. Mezouar, V. Prakapenka, and L. Dubrovinsky (2008), Stable intermediate-spin ferrous iron in lower-mantle perovskite, *Nature Geoscience*, *1*(10), 684–687.
- McCammon, C. A., and C. Tennant (1996), High-pressure Mössbauer study of synthetic clinoferrrosilite, FeSiO<sub>3</sub>, *Mineral Spectroscopy: A Tribute to RG Burns, Geochemical Society, Special publication*, *5*, 281–288.
- McDonough, W. F., and S.-S. Sun (1995), The composition of the earth, *Chemical geology*, *120*(3), 223–253.
- McNamara, A. K., E. J. Garnero, and S. Rost (2010), Tracking deep mantle reservoirs with ultra-low velocity zones, *Earth and Planetary Science Letters*, *299*(1-2), 1 – 9, doi: <http://dx.doi.org/10.1016/j.epsl.2010.07.042>.
- Meng, Y., G. Shen, and H. K. Mao (2006), Double-sided laser heating system at HPCAT for in situ x-ray diffraction at high pressures and high temperatures, *Journal of Physics: Condensed Matter*, *18*(25), S1097.
- Monkhorst, H. J., and J. D. Pack (1976), Special points for brillouin-zone integrations, *Physical Review B*, *13*(12), 5188–5192.
- Morard, G., D. Andrault, N. Guignot, J. Siebert, G. Garbarino, and D. Antonangeli (2011), Melting of Fe-Ni-Si and Fe-Ni-S alloys at megabar pressures: implications for the core-mantle boundary temperature, *Physics and Chemistry of Minerals*, *38*(10), 767–776.
- Mössbauer, R. L. (1962), Recoilless nuclear resonance absorption of Gamma radiation: A new principle yields gamma lines of extreme narrowness for measurements of unprecedented accuracy, *Science*, *137*(3532), 731–738, doi:10.1126/science.137.3532.731.
- Murakami, M., K. Hirose, K. Kawamura, N. Sata, and Y. Ohishi (2004), Post-perovskite phase transition in MgSiO<sub>3</sub>, *Science*, *304*(5672), 855–858, doi:10.1126/science.1095932.

- Murphy, C. A., J. M. Jackson, W. Sturhahn, and B. Chen (2011), Melting and thermal pressure of hcp-Fe from the phonon density of states, *Physics of the Earth and Planetary Interiors*, 188(1-2), 114–120.
- Murphy, C. A., J. M. Jackson, and W. Sturhahn (2013), Experimental constraints on the thermodynamics and sound velocities of hcp-Fe to core pressures, *Journal of Geophysical Research-Solid Earth*, 118(5), 1999–2016.
- Nakajima, Y., D. J. Frost, and D. C. Rubie (2012), Ferrous iron partitioning between magnesium silicate perovskite and ferropericlasite and the composition of perovskite in the earth's lower mantle, *Journal of Geophysical Research: Solid Earth*, 117(B8), B09,151, doi:10.1029/2012JB009151.
- Nestola, F., T. B. Ballaran, T. Balić-Žunić, L. Secco, and A. Dal Negro (2008), The high-pressure behavior of an Al- and Fe-rich natural orthopyroxene, *American Mineralogist*, 93(4), 644–652.
- Nguyen, J. H., and N. C. Holmes (2004), Melting of iron at the physical conditions of the earth's core, *Nature*, 427(6972), 339–342.
- Ni, S., and D. V. Helmberger (2001), Probing an ultra-low velocity zone at the core mantle boundary with P and S waves, *Geophysical Research Letters*, 28(12), 2345–2348, doi:10.1029/2000GL012766.
- Nomura, R., K. Hirose, K. Uesugi, Y. Ohishi, A. Tsuchiyama, A. Miyake, and Y. Ueno (2014), Low core-mantle boundary temperature inferred from the solidus of pyrolite, *Science*, 343(6170), 522–525, doi:10.1126/science.1248186.
- Olson, P. (2013), The new core paradox, *Science*, 342(6157), 431–432, doi:10.1126/science.1243477.
- Pasternak, M. P., R. D. Taylor, R. Jeanloz, and S. R. Bohlen (1992), Magnetic ordering transition in  $\text{Mg}_{0.9}\text{Fe}_{0.1}\text{SiO}_3$  orthopyroxene, *American Mineralogist*, 77(9-10), 901–903.
- Perdew, J. P., K. Burke, and M. Ernzerhof (1996), Generalized gradient approximation made simple, *Phys. Rev. Lett.*, 77, 3865–3868.
- Poirier, J.-P. (2000), *Introduction to the Physics of the Earth's Interior*, Cambridge University Press.
- Pradhan, G. K., G. Fiquet, J. Siebert, A.-L. Auzende, G. Morard, D. Antonangeli, and G. Garbarino (2015), Melting of MORB at core-mantle boundary, *Earth and Planetary Science Letters*, 431, 247 – 255, doi:http://dx.doi.org/10.1016/j.epsl.2015.09.034.
- Prakapenka, V. B., A. Kubo, A. Kuznetsov, A. Laskin, O. Shkurikhin, P. Dera, M. L. Rivers, and S. R. Sutton (2008), Advanced flat top laser heating system for high pressure research at GSECARS: application to the melting behavior of germanium, *High Pressure Research*, 28(3), 225–235.

- Prescher, C., and V. B. Prakapenka (2015), DIOPTAS: a program for reduction of two-dimensional x-ray diffraction data and data exploration, *High Pressure Research*, *35*(3), 223–230.
- Prescher, C., F. Langenhorst, L. S. Dubrovinsky, V. B. Prakapenka, and N. Miyajima (2014), The effect of Fe spin crossovers on its partitioning behavior and oxidation state in a pyrolytic Earth’s lower mantle system, *Earth and Planetary Science Letters*, *399*(0), 86–91, doi: <http://dx.doi.org/10.1016/j.epsl.2014.05.011>.
- Reed, R. (1992), Reading out CCDs: Where does the time go?, *NOAO Newsletter*, *30*.
- Revenaugh, J., and T. H. Jordan (1991), Mantle layering from ScS reverberations. 3. the upper mantle, *Journal of Geophysical Research-Solid Earth*, *96*(B12), 19,781–19,810.
- Reynard, B., J. D. Bass, and J. Brenizer (2010), High-temperature elastic softening of orthopyroxene and seismic properties of the lithospheric upper mantle, *Geophysical Journal International*, *181*(1), 557–566.
- Ringwood, A. E. (1979), Composition and origin of the earth, in *The Earth: Its Origin, Structure and Evolution*, edited by M. W. McElhinny, pp. 1–58, Academic Press, New York.
- Ringwood, A. E. (1991), Phase transformations and their bearing on the constitution and dynamics of the mantle, *Geochimica et Cosmochimica Acta*, *55*(8), 2083–2110.
- Rivers, M., V. B. Prakapenka, A. Kubo, C. Pullins, C. M. Holl, and S. D. Jacobsen (2008), The COMPRES/GSECARS gas-loading system for diamond anvil cells at the Advanced Photon Source, *High Pressure Research*, *28*(3), 273–292.
- Rost, S. (2013), Deep earth: Core-mantle boundary landscapes, *Nature Geoscience*, *6*(2), 89–90.
- Rubie, D., F. Nimmo, and H. Melosh (2007), Formation of earth’s core, in *Treatise on Geophysics*, edited by G. Schubert, pp. 51–90, Elsevier, Amsterdam, doi:<http://dx.doi.org/10.1016/B978-044452748-6.00140-1>.
- Schauble, E. A. (2004), Applying stable isotope fractionation theory to new systems, *Reviews in Mineralogy and Geochemistry*, *55*(1), 65–111.
- Shen, G., H.-K. Mao, R. J. Hemley, T. S. Duffy, and M. L. Rivers (1998), Melting and crystal structure of iron at high pressures and temperatures, *Geophysical Research Letters*, *25*(3), 373–376.
- Shen, G., M. L. Rivers, Y. Wang, and S. R. Sutton (2001), Laser heated diamond cell system at the Advanced Photon Source for in situ x-ray measurements at high pressure and temperature, *Review of Scientific Instruments*, *72*(2), 1273–1282.

- Shen, G., V. B. Prakapenka, M. L. Rivers, and S. R. Sutton (2004), Structure of liquid iron at pressures up to 58 GPa, *Physical Review Letters*, *92*, 185,701.
- Shen, G., V. B. Prakapenka, P. J. Eng, M. L. Rivers, and S. R. Sutton (2005), Facilities for high-pressure research with the diamond anvil cell at GSECARS, *Journal of Synchrotron Radiation*, *12*(5), 642–649.
- Shimizu, H., H. Imaeda, T. Kume, and S. Sasaki (2005), High-pressure elastic properties of liquid and solid neon to 7 GPa, *Physical Review B*, *71*, 014,108–014,112.
- Shinmei, T., N. Tomioka, K. Fujino, K. Kuroda, and T. Irifune (1999), In situ X-ray diffraction study of enstatite up to 12 GPa and 1473 K and equations of state, *American Mineralogist*, *84*(10), 1588–1594, doi:10.1103/PhysRevB.71.014108.
- Singwi, K. S., and A. Sjölander (1960), Resonance absorption of nuclear gamma rays and the dynamics of atomic motions, *Phys. Rev.*, *120*, 1093–1102, doi:10.1103/PhysRev.120.1093.
- Stacey, F. D. (1977), A thermal model of the earth, *Physics of the Earth and Planetary Interiors*, *15*(4), 341–348, doi:http://dx.doi.org/10.1016/0031-9201(77)90096-6.
- Stevenson, D. J. (1981), Models of the earth's core, *Science*, *214*(4521), 611–619, doi:10.1126/science.214.4521.611.
- Stewart, A. J., M. W. Schmidt, W. van Westrenen, and C. Liebske (2007), Mars: A new core-crystallization regime, *Science*, *316*(5829), 1323–1325.
- Strong, H. M., R. E. Tuft, and R. E. Hanneman (1973), The iron fusion curve and  $\gamma$ - $\delta$ -l triple point, *Metallurgical Transactions*, *4*(11), 2657–2661, doi:10.1007/BF02644272.
- Sturhahn, W. (2000), CONUSS and PHOENIX: Evaluation of nuclear resonant scattering data, *Hyperfine Interactions*, *125*(1-4), 149–172.
- Sturhahn, W. (2004), Nuclear resonant spectroscopy, *Journal of Physics-Condensed Matter*, *16*(5), S497–S530.
- Sturhahn, W., and J. M. Jackson (2007), Geophysical applications of nuclear resonant scattering, in *Advances in High-Pressure Mineralogy: GSA Special Paper 421*, pp. 157–174.
- Sturhahn, W., J. M. Jackson, and J.-F. Lin (2005), The spin state of iron in minerals of Earth's lower mantle, *Geophysical Research Letters*, *32*(12), L12,307, doi:10.1029/2005GL022802.
- Sun, D., D. V. Helmberger, J. M. Jackson, R. W. Clayton, and D. J. Bower (2013), Rolling hills on the core-mantle boundary, *Earth and Planetary Science Letters*, *361*(0), 333–342, doi:http://dx.doi.org/10.1016/j.epsl.2012.10.027.

- Tan, Y., and D. V. Helmberger (2007), Trans-Pacific upper mantle shear velocity structure, *Journal of Geophysical Research-Solid Earth*, *112*(B8), B08,301.
- Taran, M. N., and K. Langer (2003), Single-crystal high-pressure electronic absorption spectroscopic study of natural orthopyroxenes, *European Journal of Mineralogy*, *15*(4), 689–695, doi: 10.1127/0935-1221/2003/0015-0689.
- Tateno, S., K. Hirose, Y. Ohishi, and Y. Tatsumi (2010), The structure of iron in Earth’s inner core, *Science*, *330*(6002), 359–361, doi:10.1126/science.1194662.
- Tateno, S., K. Hirose, and Y. Ohishi (2014), Melting experiments on peridotite to lowermost mantle conditions, *Journal of Geophysical Research: Solid Earth*, *119*(6), 4684–4694, doi: 10.1002/2013JB010616.
- Terasaki, H., S. Kamada, T. Sakai, E. Ohtani, N. Hirao, and Y. Ohishi (2011), Liquidus and solidus temperatures of a Fe-O-S alloy up to the pressures of the outer core: Implication for the thermal structure of the Earth’s core, *Earth and Planetary Science Letters*, *304*(3), 559–564.
- Thomas, C. W., and P. D. Asimow (2013), Direct shock compression experiments on premolten forsterite and progress toward a consistent high-pressure equation of state for CaO-MgO-Al<sub>2</sub>O<sub>3</sub>-SiO<sub>2</sub>-FeO liquids, *Journal of Geophysical Research: Solid Earth*, *118*(11), 5738–5752, doi: 10.1002/jgrb.50374.
- Thorne, M. S., E. J. Garnero, G. Jahnke, H. Igel, and A. K. McNamara (2013), Mega ultra low velocity zone and mantle flow, *Earth and Planetary Science Letters*, *364*, 59 – 67, doi: <http://dx.doi.org/10.1016/j.epsl.2012.12.034>.
- Toellner, T. S. (2000), Monochromatization of synchrotron radiation for nuclear resonant scattering experiments, *Hyperfine Interactions*, *125*(1-4), 3–28.
- Toellner, T. S., E. E. Alp, T. Graber, R. W. Henning, S. D. Shastri, G. Shenoy, and W. Sturhahn (2011), Synchrotron Mössbauer spectroscopy using high-speed shutters, *Journal of Synchrotron Radiation*, *18*(2), 183–188, doi:10.1107/S090904951003863X.
- Troullier, N., and J. Martins (1991), Efficient pseudopotentials for plane-wave calculations, *Physical Review B*, *43*, 1993–2006.
- Tschauner, O., and C. Ma (2014), Bridgmanite, IMA 2014-017. CNMNC Newsletter No. 21, August 2014, page 798, *Mineralogical Magazine*, *78*, 797–804.
- Velisavljevic, N., et al. (2014), Time-resolved x-ray diffraction and electrical resistance measurements of structural phase transitions in zirconium, *Journal of Physics: Conference Series*, *500*(3), 032,020.

- Wang, L., N. Moon, Y. Zhang, W. R. Dunham, and E. J. Essene (2005), Fe-Mg order-disorder in orthopyroxenes, *Geochimica et Cosmochimica Acta*, *69*(24), 5777–5788, doi:10.1016/j.gca.2005.08.011.
- Wang, L., W. Yang, Y. Xiao, B. Liu, P. Chow, G. Shen, W. L. Mao, and H.-k. Mao (2011), Application of a new composite cubic-boron nitride gasket assembly for high pressure inelastic x-ray scattering studies of carbon related materials, *Review of Scientific Instruments*, *82*(7), 073,902, doi:10.1063/1.3607994.
- Wang, Y., D. J. Weidner, J. Zhang, G. D. Gwanrnesia, and R. C. Liebermann (1998), Thermal equation of state of garnets along the pyrope-majorite join, *Physics of the Earth and Planetary Interiors*, *105*(1-2), 59–71.
- Webb, S. L., and I. Jackson (1993), The pressure-dependence of the elastic-moduli of single-crystal ortho-pyroxene ( $\text{Mg}_{0.8}\text{Fe}_{0.2}\text{SiO}_3$ ), *European Journal of Mineralogy*, *5*(6), 1111–1119.
- Weidner, D. J., H. Wang, and J. Ito (1978), Elasticity of orthoenstatite, *Physics of the Earth and Planetary Interiors*, *17*(2), 7–13.
- Wicks, J. K., J. M. Jackson, and W. Sturhahn (2010), Very low sound velocities in iron-rich (Mg,Fe)O: Implications for the core-mantle boundary region, *Geophysical Research Letters*, *37*(15), doi:10.1029/2010GL043689.
- Williams, Q., and E. J. Garnero (1996), Seismic evidence for partial melt at the base of earth's mantle, *Science*, *273*(5281), 1528–1530, doi:10.1126/science.273.5281.1528.
- Williams, Q., R. Jeanloz, J. Bass, B. Svendsen, and T. J. Ahrens (1987), The melting curve of iron to 250 Gigapascals - a constraint on the temperature at Earth's center, *Science*, *236*(4798), 181–182.
- Woodland, A. B. (1998), The orthorhombic to high-P monoclinic phase transition in Mg-Fe pyroxenes: Can it produce a seismic discontinuity?, *Geophysical Research Letters*, *25*(8), 1241–1244.
- Woodland, A. B., and R. J. Angel (1997), Reversal of the orthoferrosilite-high-P clinoferrosilite transition, a phase diagram for  $\text{FeSiO}_3$  and implications for the mineralogy of the Earth's upper mantle, *European Journal of Mineralogy*, *9*(2), 245–254.
- Yamazaki, D., E. Ito, T. Yoshino, N. Tsujino, A. Yoneda, X. Guo, F. Xu, Y. Higo, and K. Funakoshi (2014), Over 1 Mbar generation in the Kawai-type multianvil apparatus and its application to compression of  $(\text{Mg}_{0.92}\text{Fe}_{0.08})\text{SiO}_3$  perovskite and stishovite, *Physics of the Earth and Planetary Interiors*, *228*(0), 262–267, doi:http://dx.doi.org/10.1016/j.pepi.2014.01.013, high-Pressure Research in Earth Science: Crust, Mantle, and Core.

- Yang, H. X., and S. Ghose (1995), High-temperature single-crystal X-ray diffraction studies of the ortho-ortho phase-transition in enstatite,  $\text{Mg}_2\text{Si}_2\text{O}_6$  at 1360 K, *Physics and Chemistry of Minerals*, *22*(5), 300–310.
- Yoo, C. S., N. C. Holmes, M. Ross, D. J. Webb, and C. Pike (1993), Shock temperatures and melting of iron at earth core conditions, *Physical Review Letters*, *70*, 3931–3934.
- Yoo, C.-S., H. Wei, R. Dias, G. Shen, J. Smith, J.-Y. Chen, and W. Evans (2012), Time-resolved synchrotron X-ray diffraction on pulse laser heated iron in diamond anvil cell, *Journal of Physics: Conference Series*, *377*(1), 012,108.
- You, S.-J., L.-C. Chen, and C.-Q. Jin (2009), Hydrostaticity of pressure media in diamond anvil cells, *Chinese Physics Letters*, *26*(9), 096,202.
- Zha, C.-S., K. Mibe, W. A. Bassett, O. Tschauner, H.-K. Mao, and R. J. Hemley (2008), P-V-T equation of state of platinum to 80 GPa and 1900 K from internal resistive heating/x-ray diffraction measurements, *Journal of Applied Physics*, *103*(5), 054,908.
- Zhang, D., J. M. Jackson, W. Sturhahn, and Y. Xiao (2011), Local structure variations observed in orthoenstatite at high pressures, *American Mineralogist*, *96*(10), 1585–1592.
- Zhang, D., J. M. Jackson, B. Chen, W. Sturhahn, J. Zhao, J. Yan, and R. Caracas (2013a), Elasticity and lattice dynamics of enstatite at high pressure, *Journal of Geophysical Research: Solid Earth*, *118*(8), 4071–4082, doi:10.1002/jgrb.50303.
- Zhang, D., J. M. Jackson, J. Zhao, W. Sturhahn, E. E. Alp, T. S. Toellner, and M. Y. Hu (2015), Fast temperature spectrometer for samples under extreme conditions, *Review of Scientific Instruments*, *84*(1), 013,105.
- Zhang, D., J. M. Jackson, J. Zhao, W. Sturhahn, E. E. Alp, M. Y. Hu, T. S. Toellner, C. A. Murphy, and V. B. Prakapenka (2016), Temperature of Earth's core constrained from melting of Fe and  $\text{Fe}_{0.9}\text{Ni}_{0.1}$  at high pressures, *Earth and Planetary Science Letters*, *447*, 72 – 83, doi: <http://dx.doi.org/10.1016/j.epsl.2016.04.026>.
- Zhang, J. S., P. Dera, and J. D. Bass (2012), A new high-pressure phase transition in natural Fe-bearing orthoenstatite, *American Mineralogist*, *97*(7), 1070–1074.
- Zhang, J. S., B. Reynard, G. Montagnac, R. C. Wang, and J. D. Bass (2013b), Pressure-induced Pbc $\rightarrow$ P2 $_1$ /c phase transition of natural orthoenstatite: Compositional effect and its geophysical implications, *American Mineralogist*, *98*(5-6), 986–992, doi:10.2138/am.2013.4345.

- Zhang, L., J. Stanek, S. S. Hafner, H. Ahsbahs, H. F. Grünsteudel, J. Metge, and R. Rüffer (1999),  $^{57}\text{Fe}$  nuclear forward scattering of synchrotron radiation in hedenbergite  $\text{CaFeSi}_2\text{O}_6$  at hydrostatic pressures up to 68 GPa, *American Mineralogist*, *84*, 447–453.
- Zhang, L., et al. (2014), Disproportionation of  $(\text{Mg,Fe})\text{SiO}_3$  perovskite in earths deep lower mantle, *Science*, *344* (6186), 877–882, doi:10.1126/science.1250274.
- Zhao, J. Y., W. Sturhahn, J. F. Lin, G. Y. Shen, E. E. Alp, and H. K. Mao (2004), Nuclear resonant scattering at high pressure and high temperature, *High Pressure Research*, *24* (4), 447–457.
- Zhuravlev, K., J. Jackson, A. Wolf, J. Wicks, J. Yan, and S. Clark (2010), Isothermal compression behavior of  $(\text{Mg,Fe})\text{O}$  using neon as a pressure medium, *Physics and Chemistry of Minerals*, *37* (7), 465–474, doi:10.1007/s00269-009-0347-6.
- Zou, Y., T. Irifune, G. S., M. L. Whitaker, T. Shinmei, H. Ohfuji, R. Negishi, and Y. Higo (2012), Elasticity and sound velocities of polycrystalline  $\text{Mg}_3\text{Al}_2(\text{SiO}_4)_3$  garnet up to 20 GPa and 1700 K, *Journal of Applied Physics*, *112* (1), 014,910.